SEMICONDUCTORS VOLUME 32, NUMBER 10 OCTOBER 1998

ATOMIC STRUCTURE AND NON-ELECTRONIC PROPERTIES OF SEMICONDUCTORS

Activation and distribution of silicon implanted in gallium arsenide as a result of isothermal radiation annealing

V. M. Ardyshev

Tomsk Polytechnical University, 634061 Tomsk, Russia

M. V. Ardyshev

Tomsk State University, 634034 Tomsk, Russia

(Submitted March 23, 1998; accepted for publication April 2, 1998)
Fiz. Tekh. Poluprovodn. **32**, 1153–1157 (October 1998)

The method of capacitance–voltage characteristics is used to investigate the concentration profiles $n(x)$ of ^{28}Si, implanted in GaAs [$E=50$ and 75 keV, $F=(1.88-6.25)\times10^{12}\,\mathrm{cm}^{-2}$] after ‘‘photonic’’ and ‘‘electronic’’ annealing with a protective dielectric coating covering the surface and without it. It is shown that in contrast to thermal annealing (800 °C, 30 min), after photonic and electronic annealing diffusive redistribution of silicon into the interior of the GaAs sample is observed. The diffusion coefficient D and degree of activation η increase as the temperature is increased in the case of photonic annealing and as the power is increased in the case of electronic annealing. The values of the activation energy of the processes for D and η for radiation annealing (photonic and electron) are lower than the corresponding values for thermal annealing. The values of D and η after photonic and electronic annealing without the protective dielectric coating are higher than with it.
[S1063-7826(98)00110-0]

INTRODUCTION

It is known that radiation annealing of implanted GaAs takes place at temperatures above 800 °C over a time of a few seconds.[1,2] At such temperatures the dominant role in the processes of activation and distribution of the impurity is accorded to thermal effects while the influence of ionization in speeding up these processes is assumed to be negligible.[3] On the other hand, the brief duration of the anneal makes it possible to perform it without using protective coatings.[1,2,4] At the same time, at temperatures above 450 °C arsenic evaporates, and the concentration of vacancies in the sublattice of the GaAs sample increases substantially in the skin layer. Arsenic vacancies, which are nonradiative recombination centers,[5] can lead to changes in the impurity concentration profiles.

In this paper we report the results of an experimental study of the behavior of silicon in Si-implanted GaAs during radiation anneals with a dielectric coating that protects the implanted surface and without such protective coating.

EXPERIMENTAL PROCEDURE

Measurements were performed on wafers of semi-insulating GaAs, $370\pm20\,\mu$m in thickness, oriented in the (100) plane, with a resistivity greater than $10^7\,\Omega\cdot$cm and a dislocation density no greater than $5\times10^4\,\mathrm{cm}^{-2}$. The chromium concentration in the material did not exceed $10^{16}\,\mathrm{cm}^{-3}$. Before implantation the wafers were processed in the etchant $H_2SO_4:H_2O_2:H_2O=1:1:10$.

A $6.25\times10^{12}\,\mathrm{cm}^{-2}$ dose of ^{28}Si ions with an energy of 50 keV were implanted, followed by a $1.88\times10^{12}\,\mathrm{cm}^{-2}$ dose of 75-keV ions and a $4.37\times10^{12}\,\mathrm{cm}^{-2}$ dose, also of 75-keV ions, at 300 K in a vacuum of 6×10^{-6} Pa. To eliminate axial and planar channeling,[6] the wafers were placed in such a way that the angle α between the surface normal and the direction of the ion beam in the plane parallel to the base cut was 10°. The wafers were then rotated in the clockwise direction about the [100] axis through an angle $\beta=35°$. A film of SiO_2 doped with samarium ($N_{\mathrm{Sm}}=6-12$ at. %) was deposited on one part of the wafer using the technique described in Ref. 7. The other part was not coated. ‘‘Electron’’ annealing (EA) with the dielectric coating and without it was performed on a ‘‘Modul’″ setup[8] with an electron beam energy of 10 keV and power density $6.8-8.8\,\mathrm{W/cm}^2$ for 10 and 12 s in a vacuum of 10^{-5} Pa. ‘‘Photonic’’ annealing (PA) of samples without the dielectric coating was performed on an ‘‘Impul’s-5’’ setup in a stream of nitrogen (the dew point was held at or below -65 °C) with the help of halogen lamps with 1-kW power each, over the temperature range 805–925 °C for 10 s. For comparison, photonic anneals were performed on coated samples at 870 °C. Thermal annealing (TA) of coated samples was performed at 800 °C for 30 min in a stream of hydrogen. After each anneal the dielectric coating was removed by cleaning the wafer surface to form

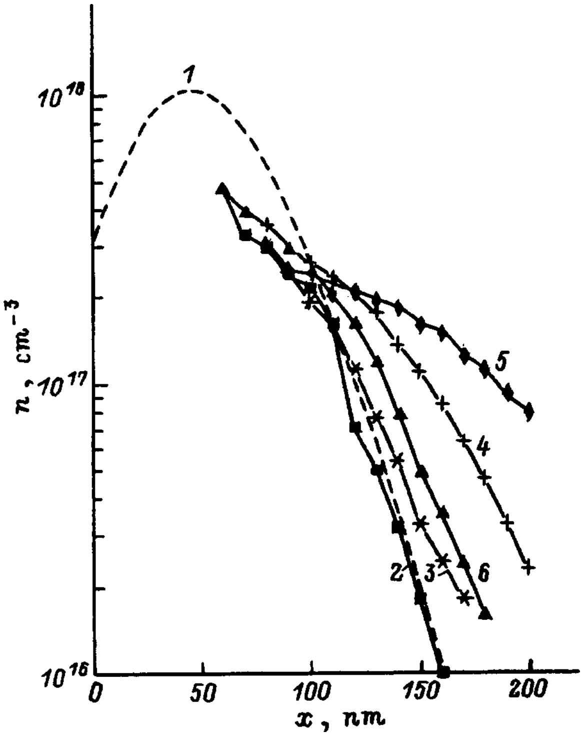

FIG. 1. Calculated profile of the implanted silicon concentration (*1*) ($E_1 = 50$ keV, $F_1 = 6.25 \times 10^{12}$ cm^{-2} and $E_2 = 75$ keV, $F_2 = 1.78 \times 10^{12}$ cm^{-2}) and electron concentration profiles obtained by photonic annealing at 805 °C (*2*), 825 °C (*3*), 870 °C (*4*), and 925 °C (*5*) without the protective dielectric coating, and at 870 °C with the dielectric coating (*6*).

Schottky barriers (SB) with dimensions $100 \times 100\,\mu$m^2 which were metallized on the basis of the alloy AuGe + 14%Ni. The method of capacitance–voltage characteristics was used to measure the electron concentration profiles.

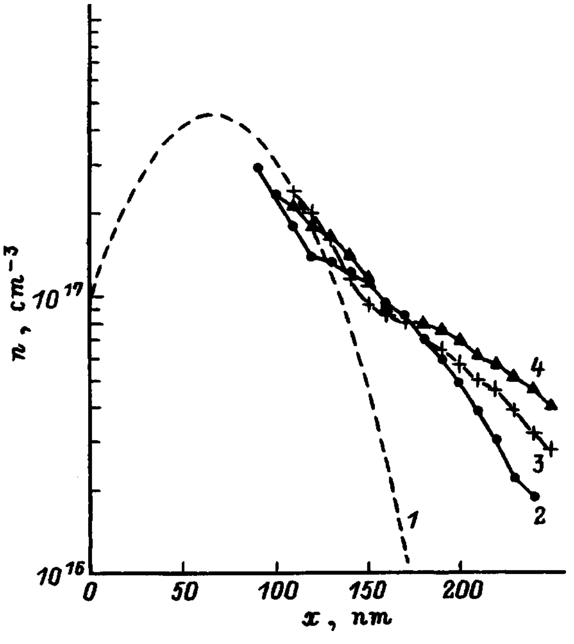

FIG. 2. Calculated profile of the implanted silicon concentration (*1*) ($E = 75$ keV, $F = 4.4 \times 10^{12}$ cm^{-2}) and electron concentration profiles obtained by electronic annealing (6.8 W/cm^2) (*2*), (7.2 W/cm^2) (*3*), 7.6 W/cm^2 (*4*) without the protective dielectric coating.

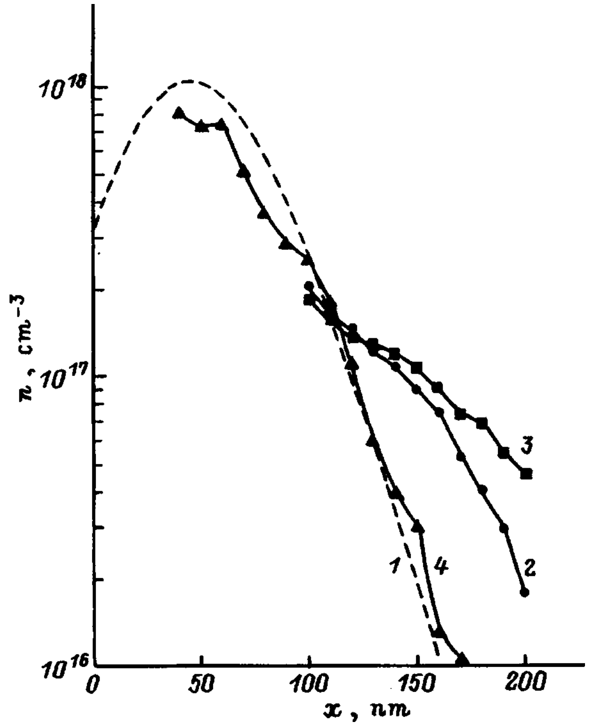

FIG. 3. Calculated profile of the implanted silicon concentration (*1*) ($E_1 = 50$ keV, $F_1 = 6.25 \times 10^{12}$ cm^{-2} and $E_2 = 75$ keV, $F_2 = 1.78 \times 10^{12}$ cm^{-2}) and electron concentration profiles obtained by electronic annealing with the protective dielectric coating (7.6 W/cm^2) (*2*), (8.8 W/cm^2) (*3*), and by thermal annealing (800 °C, 30 min) (*4*).

EXPERIMENTAL RESULTS AND DISCUSSION

Figures 1–3 show experimental electron concentration profiles obtained after PA (Fig. 1) and after EA (Figs. 2 and 3), and calculated profiles of the implanted impurity concentration based on values of R_p and ΔR_p determined by secondary-ion mass-spectroscopy (SIMS).[9] For comparison, a typical profile of the electron concentration after TO is plotted in Fig. 3 (curve *4*).

It can be seen that after PA and EA the electron concentration profiles $n(x)$ lie deeper (a "broadening" of the profiles is observed) than the calculated profile and the profile obtained by TA. As the temperature is increased in the case of PA, and the power in the case of electronic annealing, the thickness of the layer with electrically active silicon grows. In addition, for PA (Fig. 1, curve *6*) and EA (Fig. 3, curves *2* and *3*) of GaAs with a protective dielectric coating the electron concentration profiles are concentrated nearer to the surface in comparison with the profile in GaAs that has been annealed without a protective coating (Figs. 1 and 2). After EA (Fig. 2), in contrast to PA (Fig. 1), segments of rapid (segment I) and slow (segment II) variation of $n(x)$ are observed. The boundary between these segments shifts into the interior of the GaAs sample as the power is increased in the case of EA: from 120 nm at 6.8 W/cm^2 (Fig. 2, curve *2*) to 160 nm at 7.6 W/cm^2 (Fig. 2, curve *4*). For EA in the case of coated samples, this peculiarity in the behavior of $n(x)$ is not observed (Fig. 3).

From a comparison of the measured concentration profile $n(x)$ after TA (Fig. 3, curve *4*) with the calculated con-

TABLE I. Values of the diffusion parameters and the degree of electrical activation of silicon in GaAs for different types of annealing.

Type of annealing	$P, W/cm^2$	T, °C	D, cm^2/s	η, %	Remarks
TA	–	800	2.3×10^{-15}	71.2	With dielectric coating
EA	6.8	–	–	74.5	Without dielectric coating (segment I)
	7.2	–	5.1×10^{-13}	88.9	
	7.6	–	1.18×10^{-12}	95.4	
	6.8	–	2.7×10^{-12}	78.2	Without dielectric coating (segment II)
	7.2	–	4.1×10^{-12}	81.9	
	7.6	–	6.1×10^{-12}	88.1	
	7.6	–	1.35×10^{-12}	56.3	With dielectric coating
	8.8	–	3.8×10^{-12}	65.5	
PA	–	805	4.1×10^{-13}	61.0	Without dielectric coating
	–	825	6.4×10^{-13}	63.2	
	–	870	1.5×10^{-12}	76.8	
	–	925	5.0×10^{-12}	89.9	
	–	870	4.9×10^{-13}	71.1	With dielectric coating

centration profile (Fig. 3, curve *1*) it follows that channeling of silicon ions was essentially absent during implantation. It can thus be concluded that the observed "broadening" is not associated with channelization.

Assuming that the distribution of electrically active Si after PA and EA is due to diffusion processes, the dependence $n(x)$ can be represented in the form[10]

$$n(x)=\eta\cdot F[(2\pi)^{1/2}(\Delta R_p^2+2Dt)^{1/2}]^{-1}\times\exp[-(x-R_p)^2(2\Delta R_p^2+4Dt)^{-1}], \tag{1}$$

where F is the implantation dose, η is the degree of electrical activity of silicon, D is the diffusion coefficient of silicon, and t is the annealing time.

We used formula (1) together with the experimental data to estimate D and η (Table I).

The following conclusions follow from Table I: 1) the diffusion coefficient for PA and for EA is $2-3$ times greater than for TA; for EA (power greater than 7.2 W/cm^2) of uncoated samples the degree of activation of silicon is higher on segment I than on segment II of $n(x)$; 3) for PA and EA of coated samples, D and η are lower than their values after radiation annealing for the uncoated samples; 4) as the power is increased in the case of EA, and the temperature in the case of PA, the diffusion coefficient and the degree of activation of the implanted silicon grow.

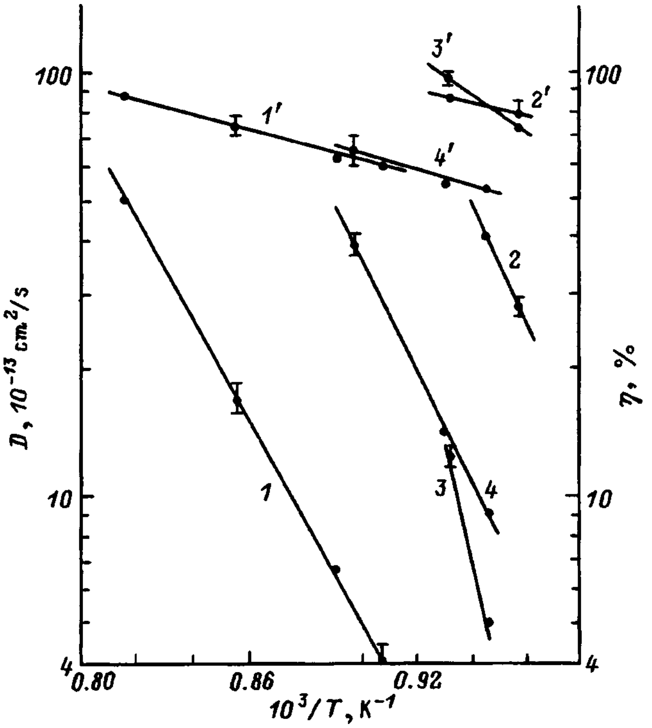

FIG. 4. Diffusion coefficient (*1–4*) and degree of electrical activation of silicon (*1'–4'*) plotted as functions of the inverse temperature for photonic annealing without the protective dielectric coating (*1,1'*), and for electronic annealing without the protective dielectric coating (segment II, *2,2'*; segment I, *3, 3'*) and with the dielectric coating (*4, 4'*).

Figure 4 plots D and η as functions of the inverse temperature for PA and EA. The temperature for EA was calculated with the help of the equation

$$\rho\cdot C\cdot d\cdot dT/dt=P-2\times\varepsilon\cdot\sigma(T^4-T_0^4), \tag{2}$$

where ρ, C, and d are the density, specific heat, and thickness of the GaAs wafers, respectively, T and T_0 are the temperature of the sample when acted on by the electron beam for a time t and its initial temperature, respectively, P is the power directed on the sample, ε is the reflectivity of GaAs, and σ is the Stefan–Boltzmann constant.

It can be seen that the dependence of D and η on the inverse temperature takes the form of straight lines. The values of activation energy E_a for D and η determined from their slopes along with the values of the pre-exponential factor D_0 are given in Table II.

The following conclusions follow from the results presented above: 1) For EA (segment II) and for PA the values

TABLE II. Values of the activation energy and pre-exponential factor for D and η for the investigated forms of radiation annealing.

	Form of annealing							
	EA without protective coating (segment I)		EA without protective coating (segment II)		EA with protective coating		PA with protective coating	
Parameter	D	η	D	η	D	η	D	η
E_a, eV	5.74	0.79	2.60 ± 0.05	0.38 ± 0.09	2.7	0.4	2.56 ± 0.01	0.31 ± 0.04
D_0, cm^2/s	–	–	8.85	–	5.8	–	0.173	–

of E_a for D are roughly 0.7 eV lower than the value 3.3 eV (Ref. 11) for thermal diffusion of silicon; for η the activation energy under these annealing conditions is also less than E_a (0.5 eV, Ref. 12) for purely thermal activation of silicon. 2) For EA the pre-exponential factor D_0 in the dependence $D(T^{-1})$ is greater than its value for PA. 3) The lowest values of E_a for η are observed for PA and for EA [segment II of $n(x)$]. The highest values of E_a for η correspond to activation of silicon on segment I of $n(x)$ for EA (Table II).

If we wish to trace out the radiation-stimulated mechanism of speeded-up annealing[13,14] and if we assume that vacancies in both GaAs sublattices are centers of nonradiative recombination,[5] then it is necessary to assume that a high concentration of these vacancies is present in the starting material, and also that when GaAs is radiation-annealed without a protective coating the newly formed arsenic vacancies (V_{As}) migrate to significant depths ($200-250$ nm) in the annealing time ($10-12$ s). The first assumption probably holds since the total vacancy concentration in GaAs single crystals can reach values $\sim 10^{19}\,\mathrm{cm}^{-3}$ (Ref. 15). The second assumption also holds as a result of the decreased value of the activation energy E_a of the diffusion of vacancies into the interior of the GaAs sample as a result of of radiation, as has been observed for silicon.

Taking this circumstance into account, the results can be explained in the following way. Under the action of radiation, electron–hole pairs are created. They participate in the process of nonradiative recombination at the vacancies in both sublattices of the virgin GaAs, and also at the arsenic vacancies V_{As}, which are formed as a result of the evaporation of arsenic during radiation annealing of GaAs without a protective insulating coating. In this context, the energy E_R, which is converted into the energy of vibrations of the atoms (including the implanted impurity) surrounding the recombination center, merits special attention. If the height of the barrier for TA is equal to E_T, then under the action of radiation the activation energy of processes of migration and electrical activation of the impurity can be lowered by the amount E_T-E_R (Ref. 16). The electron–hole pairs thus hasten, through the recombination process, the migration of the impurity and its distribution at the vacant sites of the gallium sublattice. Since the recombination rate depends on the concentration of recombination centers, the efficiency of the given process will be higher in samples with high V_{As} concentration, as has been observed in experiments on the annealing of GaAs without a protective insulating coating.

CONCLUSIONS

1. After ‘‘photonic’’ annealing and after ‘‘electron’’ annealing as opposed to thermal annealing, a diffusive redistribution of silicon into the interior of gallium arsenide samples is observed. As the temperature is increased in the case of photonic annealing, and the power in the case of electronic annealing, the diffusion D and the degree of electrical activation of the impurity η are observed to grow.

2. When GaAs samples are radiation-annealed with the implanted surface not protected by a insulating coating, the values of D and η are larger.

3. After electronic annealing without the protective film, a segment of rapid variation (near the surface) and a segment of slow variation (at depths $x > 120-160$ nm) of the electron concentration profile $n(x)$ are observed. After electronic annealing (power greater than 7.2 W/cm^2) the value of η on the rapid segment is greater than on the slow segment.

We wish to express our gratitude to L. A. Kozlova for her assistance with the experiments and V. S. Budishevskiĭ for performing the ‘‘electron’’ anneal.

[1] A. V. Chernyaev, *Method of Ion Implantation in the Fabrication of GaAs-based Devices and Integrated Circuits* [in Russian] (Radio i Svyaz’, Moscow, 1990).

[2] *Neutron Transmutation Doping of Semiconductors*, edited by J. M. Meese (Plenum Press, New York, 1979; Mir, Moscow, 1988)

[3] A. V. Dvurechenskiĭ, G. A. Kachurin *et al.*, *Pulsed Annealing of Semiconductor Materials* [in Russian] (Nauka, Moscow, 1982).

[4] I. Kazuhiko, Y. Masahiro *et al.*, Jpn. J. Appl. Phys. **22**, L299 (1983).

[5] S. Y. Chiang and G. L. Pearson, J. Appl. Phys. **46**, 2986 (1975).

[6] V. M. Ardyshev, L. A. Kozlova *et al.*, Author’s Certificate No. 235899, registered 01.04.86.

[7] V. V. Titov, in *Obzory po élektron. tekhn., Ser. Poluprovodn. Prib.* [Electronic Engineering Reviews, Series: Semiconductor Devices] **1**, No. 10 (223), 62 (1974).

[8] Yu. E. Kreĭndel’, N. I. Lebedeva *et al.*, Pis’ma Zh. Tekh. Fiz. **8**, 1465 (1982) [Sov. Tech. Phys. Lett. **8**, 630 (1982)].

[9] D. H. Lee and R. M. Matbon, Appl. Phys. Lett. **30**, 327 (1977).

[10] MOP–SBIS. *Modeling of Circuit Elements and Production Processes* [in Russian, translated from the English and edited by R. A. Suris] (Radio i Svyaz’, Moscow, 1988).

[11] T. T. Lavrishchev and S. S. Khludkov, in *Gallium Arsenide* [in Russian] (Tomsk State Univ. Press, Tomsk, 1974), No. 5, p. 57.

[12] B. M. Goryunov, E. I. Zorin *et al.*, in *Gallium Arsenide* [in Russian] (Tomsk State Univ. Press, Tomsk, 1974), No. 4, p. 102.

[13] V. M. Lenchenko, Fiz. Tverd. Tela (Leningrad) **11**, 799 (1969) [Sov. Phys. Solid State **11**, 649 (1969)].

[14] D. V. Lang and L. C. Kimerling, Phys. Rev. Lett. **33**, 489 (1974).

[15] M. G. Mil’vidskiĭ and V. B. Osvenskiĭ, *Structural Defects in Single-Crystal Semiconductors* [in Russian] (Metallurgiya, Moscow, 1984).

[16] L. C. Kimerling, IEEE Trans. Nucl. Sci. **N5–23**, 1497 (1976).

Translated by Paul F. Schippnick

Equilibrium of native point defects in tin dioxide

K. P. Bogdanov, D. Ts. Dimitrov, O. F. Lutskaya, and Yu. M. Tairov

St. Petersburg State Electrical Engineering University, 197376 St. Petersburg, Russia

(Submitted April 14, 1998; accepted for publication April 20, 1998)
Fiz. Tekh. Poluprovodn. **32**, 1158–1160 (October 1998)

A model of electrically active and neutral native point defects in SnO_2 is developed. Thermodynamic analysis of the equilibrium of the native point defects makes it possible to construct the phase diagram $P_{O_2}-T-x$ of lead dioxide. The contradiction between *n*-type monopolar conductivity and the two-sided homogeneity region of the SnO_2 phase is resolved. © *1998 American Institute of Physics.* [S1063-7826(98)00210-5]

Tin dioxide is a wideband semiconductor, whose properties depend dramatically on the oxygen pressure during synthesis.[1] Undoped SnO_2 possesses only electronic conductivity.[1,2] However, thermogravimetric studies of deviation of the phase composition from stoichiometric as a function of temperature and oxygen pressure show that SnO_2 has a two-sided homogeneity region.[3] This contradiction can be resolved only by way of a thermodynamic analysis of the equilibrium of electrically active and neutral native point defects in SnO_2.

Despite the wide use of this material, the results of studies of its properties are also of a contradictory nature. This pertains to the phase diagram in the system Sn–O_2 (Refs. 4 and 5) and to the available data in the literature on the energy spectrum of levels in the band gap. Using various methods of investigation, the authors of Refs. 6–8 found donor levels with activation energies in the range from 0.2 to 1.9 eV, whose physical nature has not been reliably identified. Efforts to explain the presence of *n*-type conductivity in SnO_2 in terms of measurements of the electrical conductivity as a function of the oxygen partial pressure at different temperatures are presented in Ref. 9. The author of this paper assumed that the conductivity in the temperature interval $830-1226$ K is due to singly and doubly charged oxygen vacancies. The authors of Ref. 8 conclude that the main types of defects in tin dioxide are interstitial metal ions and complex anion vacancies.

However, we have not been able to find in the literature a complete and noncontradictory model of native defects in SnO_2 which takes into account all of the peculiarities of this material. The reason for this, in our opinion, is the absence of a thermodynamic analysis of the equilibrium of electrically active and neutral native defects in SnO_2 in a wide range of temperatures and oxygen pressures. The goal of our study, which involves such an analysis, was to create a model of the native point defects in tin dioxide based on the electrical properties of this material and on the results of thermogravimetric studies of the homogeneity region of SnO_2.

The choice of the point defect model in SnO_2 rests on the results of a thermogravimetric analysis[3] and on the data for the energy levels in the band gap, taken from Ref. 6. As the main defect type we chose Schottky defects and Frenkel' defects in the tin sublattice, and also the appearance of Sn vacancies during processing of stoichiometric tin dioxide in oxygen. Interstitial tin and vacancies in the oxygen sublattice are responsible for *n*-type conductivity in SnO_2, and vacancies in the tin sublattice for *p*-type conductivity. The processes of formation and ionization of these defects, and also the equilibrium constants of the corresponding reactions, are formulated in the following equations:

$$0 \rightarrow e^- + h^+ + \Delta E_i, \quad K_i = np, \quad \Delta E_i = 3.5\,\text{eV}; \tag{1}$$

$$0 \rightarrow V_{Sn} + 2V_O + \Delta H_S,$$
$$K_S = [V_{Sn}][V_O]^2, \quad \Delta H_S = 10\,\text{eV}; \tag{2}$$

$$Sn_{Sn} + V_i \rightarrow Sn_i + V_{Sn} + \Delta H_F,$$
$$K_F = [V_{Sn}][Sn_i], \quad \Delta H_F = 6.5\,\text{eV}; \tag{3}$$

$$O_2 \rightarrow V_{Sn} + 2O_O + \Delta H_{O_2V},$$
$$K_{O_2V} = [V_{Sn}]/P_{O_2}, \quad \Delta H_{O_2V} = 1\,\text{eV}; \tag{4}$$

$$V_O \rightarrow V_O^+ + e^- + E_O, \quad K_O = \frac{[V_O^+]n}{[V_O]}, \quad E_O = 0.75\,\text{eV}; \tag{5}$$

$$V_O^+ \rightarrow V_O^{2+} + e^- + E_{O_2}, \quad K_{O_2} = \frac{[V_O^{2+}]n}{[V_O^+]}, \quad E_{O_2} = 1.4\,\text{eV}; \tag{6}$$

$$Sn_i \rightarrow Sn_i^+ + e^- + E_{Sn_i}, \quad K_{Sn_i} = \frac{[Sn_i^+]n}{[Sn_i]}, \quad E_{Sn_i} = 1.8\,\text{eV}; \tag{7}$$

$$V_{Sn} \rightarrow V_{Sn}^- + h^+ + E_{Sn}, \quad K_{Sn} = \frac{[V_{Sn}^-]p}{[V_{Sn}]}, \quad E_{Sn} = 2.1\,\text{eV}. \tag{8}$$

The temperature dependence of the energy of formation of the defects is assumed to be analogous to that of the width of the band gap. As an example, we calculate the energy characteristics of these processes at $T = 1223$ K. The energies of formation of the Schottky and Frenkel' defects were calculated by the crystal-chemical method.[2] The ionization energies of the defects in Eqs. (5)–(8) were taken from Refs. 6 and 8. The pre-exponential factor in the temperature depen-

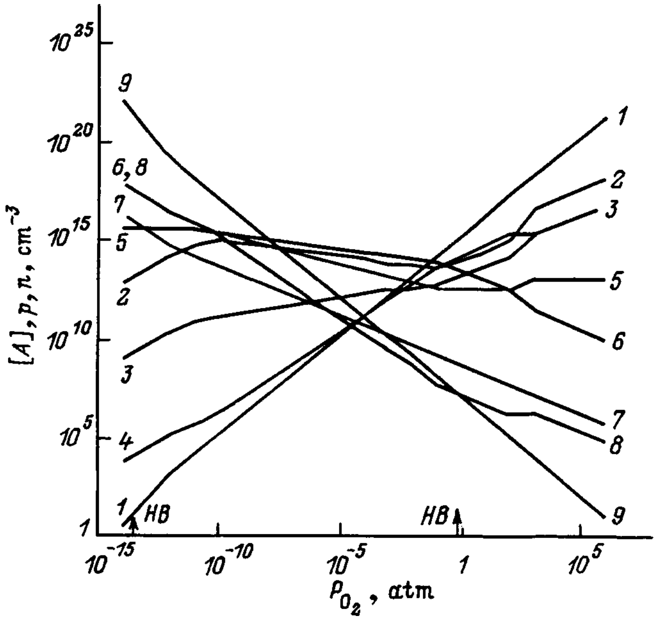

FIG. 1. Equilibrium diagram of the native point defects in SnO$_2$ at $T=1223$ K; $[A],p,n$ are the concentrations of the A defects and the charge carriers. The curves plot the concentrations of the following species: *1* — $[V_{\mathrm{Sn}}]$, *2* — $[V_{\mathrm{O}}^{2+}]$, *3* — p, *4* — $[V_{\mathrm{Sn}}^{-}]$, *5* — $[V_{\mathrm{O}}^{+}]$, *6* — n, *7* — $[V_{\mathrm{O}}]$, *8* — $[\mathrm{Sn}_i^{+}]$, *9* — $[\mathrm{Sn}_i]$. The arrows labeled *HB* mark the boundaries of the homogeneity region.

dence of the equilibrium constants of reactions (1), (5)–(8) (entropy term) was calculated by a method of statistical physics.[10] We calculated the entropy and enthalpy of process (4) from the results of thermogravimetric studies.[3]

In addition to the above equations, we included the equations of electrical neutrality and material balance

$$n+[V_{\mathrm{Sn}}^{-}]=p+[V_{\mathrm{O}}^{+}]+2[V_{\mathrm{O}}^{2+}]+[\mathrm{Sn}_i^{+}], \qquad (9)$$

$$\Delta=[V_{\mathrm{O}}]+[V_{\mathrm{O}}^{+}]+[V_{\mathrm{O}}^{2+}] -2\{[V_{\mathrm{Sn}}]+[V_{\mathrm{Sn}}^{-}]-[\mathrm{Sn}_i]-[\mathrm{Sn}_i^{+}]\}. \qquad (10)$$

The combined system of equations (1)–(10) was solved by the Brower method, the sense of which consists in approximating the equation of electrical neutrality (9) for various regions of the oxygen pressure with allowance for only the largest terms in the given region. We considered the following regions of approximation of the equation of electrical neutrality for an ionic semiconductor:

$$\mathrm{I}—n=[\mathrm{Sn}_i^{+}], \quad \mathrm{II}—n=[V_{\mathrm{O}}^{+}], \quad \mathrm{III}—n=2[V_{\mathrm{O}}^{2+}]$$

$$\mathrm{IV}—[V_{\mathrm{Sn}}^{-}]=2[V_{\mathrm{O}}^{2+}], \quad \mathrm{V}—[V_{\mathrm{Sn}}^{-}]=p.$$

For the indicated regions we calculated the point defect and charge carrier concentrations as functions of the oxygen pressure for $T=800-1700$ K. As an example, we present results of the calculation for $T=1223$ K in Fig. 1, where the arrows labeled *HB* indicate the boundaries of the homogeneity region (BHR) of the SnO$_2$ phase. It can be seen from Fig. 1 that the predominant type of defect within the limits of the homogeneity region of SnO$_2$ for realistic oxygen pressures is doubly ionized oxygen vacancies V_{O}^{2+} (curve *2*).

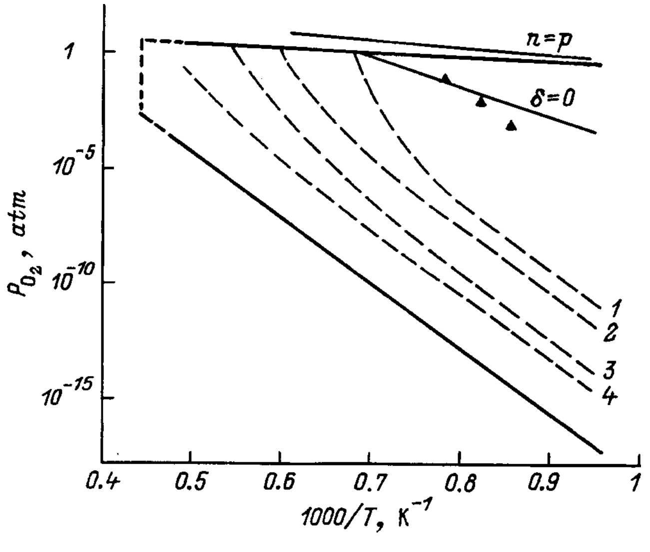

FIG. 2. Phase diagram of lead dioxide $P_{\mathrm{O}_2}-T-x$. The dashed lines are isoconcentrates of the composition for deviations δ in atomic fractions: *1* — $10^{-6.75}$, *2* — 10^{-6}, *3* — $10^{-4.5}$, *4* — 10^{-3}. The filled triangles plot experimental data from Ref. 3.

From the results of a thermodynamic analysis of the dependence of the point defect $[A]$ and charge carrier $[p,n]$ concentrations on the oxygen partial pressure P_{O_2} and temperature T we constructed the phase diagram of tin dioxide $P_{\mathrm{O}_2}-T-x$, shown in Fig. 2. In the construction of the three-phase equilibrium line we used the projection of the $T-x$ phase diagram of the system Sn–O$_2$ from Ref. 4. In this diagram, to the left of the SnO$_2$ phase no stable SnO phase is found, and SnO$_2$ (solid) and Sn (liquid, solid) coexist in equilibrium. The right-hand boundary of the SnO$_2$ homogeneity region corresponds to SnO$_2$–O$_2$ equilibrium. Thus, we obtain the right-hand boundary from the oxygen pressure above tin dioxide saturated with oxygen. The left-hand boundary is the tin vapor pressure above pure tin plotted as a function of temperature and converted to an oxygen pressure through the dissociation constant of SnO$_2$.

Figure 2 plots the temperature dependence of the oxygen pressure $P_{\mathrm{O}_2}^{\delta=0}$ above the stoichiometric tin dioxide phase (the line $\delta=0$), and also the dependence $P_{\mathrm{O}_2}^{\mathrm{inv}}(T)$ — the line $n=p$. These lines were constructed from the results of a thermodynamic analysis of the equilibrium of the native point defects and charge carriers in a wide range of oxygen pressures and temperatures. From the $P_{\mathrm{O}_2}-T-x$ diagram it can be seen that $P_{\mathrm{O}_2}^{\mathrm{inv}}$ and $P_{\mathrm{O}_2}^{\delta=0}$ do not coincide. This has to do with the fact that all types of defects, including electrically neutral defects, contribute to $P_{\mathrm{O}_2}^{\delta=0}(T)$, whereas the main contribution to $P_{\mathrm{O}_2}^{\mathrm{inv}}(T)$ comes from the electrically active defects. Note that the line $n=p$ is located in region IV corresponding to the equality $[V_{\mathrm{Sn}}^{-}]=2[V_{\mathrm{O}}^{2+}]$, and was obtained from the condition $n=p$, while the line $\delta=0$ lies in a different approximation region of the electrical neutrality equation (III), specifically, in the region $n=2[V_{\mathrm{O}}^{2+}]$. Thus, stoichiometric composition of the SnO$_2$ phase ($\delta=0$) does not coincide with the composition corresponding to inversion of conductivity type in SnO$_2$. The boundary line of the homogeneity region on the oxygen side turned out to lie between the lines $\delta=0$ and $n=p$. Thus, within the limits of the homogeneity region in the investigated temperature interval the SnO_2 phase has *n*-type conductivity, but can have an excess oxygen content relative to the stoichiometric composition (SnO_{2+x}). In this case, the excess oxygen is found in the electrically neutral state. Thus it can be either interstitial oxygen or a vacancy in the Sn sublattice which creates a deep acceptor level.

In the $P_{O_2}-T-x$ diagram we have also plotted lines of equal deviation of the phase composition (δ) from stoichiometry in atomic fractions (isoconcentrates *1–4*). The variation of the slope of the isoconcentrate in the high-temperature region is found to be in agreement with the data.[3] For comparison we have also plotted the results of thermogravimetric studies from Ref. 3 for $\delta=0$ (shown as points). Special note should be made of the fact that according to the data of Ref. 3, an oxygen excess in the SnO_2 phase is possible only for temperatures $T<1423$ K. At higher temperatures only a metal excess is possible in the SnO_2 phase. This result agrees with the temperature dependence of the oxygen pressure above the stoichiometric SnO_2 phase. The satisfactory agreement of the data of Ref. 3 with our results, and also the monopolar conductivity of SnO_2 within the limits of the homogeneity region of this phase confirm the validity of our model of electrically active and neutral native point defects in SnO_2.

[1] V. M. Vaĭnshteĭn and V. I. Fistul', Itogi Nauki i Tekh., Ser.: Élektronika i Ee Primeneniya [Progress of Science and Technology, Series: Electronics and Its Applications], No. 4, 108 (1973).

[2] P. Kofstad, *Nonstoichiometry, Diffusion and Electrical Conductivity in Binary Metal Oxides* (Wiley-Interscience, New York, 1972; Mir, Moscow, 1975).

[3] H. Koinuma, J. Shimoyama, J. Mizusaki, M. Kawasaki, and K. Fueki, in *Extended Abstracts of the 18th International Conference on Solid State Devices and Materials* (Tokyo, Japan, 1986), p. 763.

[4] Yu. V. Levinskiĭ, *P–T–x Phase Diagrams of Binary Metallic Systems* [in Russian] (Metallurgiya, Moscow, 1990).

[5] I. S. Kulikov, *Thermodynamics of Oxides* [in Russian] (Metallurgiya, Moscow, 1986).

[6] J. E. Houston and E. E. Kohnke, J. Appl. Phys. **36**, 3931 (1965).

[7] D. E. Dyshel', Neorg. Mater. **32**, 59 (1996).

[8] V. O. Shvalev and V. G. Teplov, Poverkhnost': Fizika, Khimiya, Mekhanika [Surface: Physics, Chemistry, Mechanics], No. 1, 98 (1991).

[9] J. Rudolph, Techn. Wis. Abhandl. Osram., **2**, 86 (1963).

[10] F. A. Kroger, *The Chemistry of Imperfect Crystals* (North-Holland, Amsterdam, 1964).

Translated by Paul F. Schippnick

SEMICONDUCTORS VOLUME 32, NUMBER 10 OCTOBER 1998

Arsenic cluster superlattice in gallium arsenide grown by low-temperature molecular-beam epitaxy

V. V. Chaldyshev, V. V. Preobrazhenskiĭ, M. A. Putyato, and B. R. Semyagin

Institute of Semiconductor Physics, Siberian Branch of the Russian Academy of Sciences, 630090 Novosibirsk, Russia

N. A. Bert, A. E. Kunitsyn, Yu. G. Musikhin, and V. V. Tret'yakov

A. F. Ioffe Physicotechnical Institute, Russian Academy of Sciences, 194021 St. Petersburg, Russia

P. Werner

Max-Plank-Institute of Microstructure Physics, D-06120 Halle, Germany

(Submitted May 27, 1998; accepted for publication May 28, 1998)
Fiz. Tekh. Poluprovodn. **32**, 1161–1164 (October 1998)

Molecular-beam epitaxy at 200 °C is used to grow an InAs/GaAs superlattice containing 30 InAs delta-layers with a nominal thickness of 1 monolayer, separated by GaAs layers of thickness 30 nm. It is found that the excess arsenic concentration in such a superlattice is $0.9\times 10^{20}\,\mathrm{cm}^{-3}$. Annealing the samples at 500 and 600 °C for 15 min leads to precipitation of the excess arsenic mainly into the InAs delta-layers. As a result, a superlattice of two-dimensional sheets of nanoscale arsenic clusters, which coincides with the superlattice of the InAs delta-layers in the GaAs matrix, is obtained. © *1998 American Institute of Physics.* [S1063-7826(98)00310-X]

Gallium arsenide, grown by molecular-beam epitaxy (MBE) at low temperatures $T\sim 200\,^\circ\mathrm{C}$ (LT-GaAs), has attracted significant attention because of its large electrical resistance, high breakdown voltage, and record-short lifetime of nonequilibrium charge carriers.[1–5] The primary peculiarity of LT-GaAs is an excess of arsenic As (up to 1.5 at. %), which is captured in the growing layer during low-temperature epitaxy. During annealing at a sufficiently high temperature $T\geqslant 500\,^\circ\mathrm{C}$ the excess arsenic forms clusters built into the GaAs matrix. In ordinary LT-GaAs the clusters are randomly distributed over the entire volume of the epitaxial film. It has been shown, however, that the spatial distribution of the arsenic clusters can be controlled with the help of indium delta-doping.[6–8] In this case, heterogeneous creation of excess arsenic clusters on the InAs delta-layers leads to the formation of two-dimensional sheets of clusters.

Our aim was to construct a multiperiod superlattice of two-dimensional sheets of arsenic clusters separated by a GaAs matrix not containing any clusters. To create the two-dimensional sheets of clusters we used indium delta-doping.

An InAs/GaAs superlattice was grown by molecular-beam epitaxy at 200 °C in a two-chambered ''Katun'' MBE setup on a substrate of semi-insulating gallium arsenide of diameter 50 mm and orientation (100). The superlattice consisted of 30 periods. The nominal thickness of the InAs delta-layers was one monolayer (ML). The thickness of the GaAs layers was 30 nm. The structure was divided into three parts. One of those parts was not subjected to any processing. The other two were annealed at 500 and 600 °C, respectively, for 15 min on the MBE setup with excess arsenic pressure.

The average indium concentration in the structure was measured by x-ray structural micro-analysis (XSMA). This method was also used to estimate the excess arsenic concentration in the samples.[4] For a more accurate measurement of the excess arsenic we used measurements of optical absorption in the near-IR due to $\mathrm{As_{Ga}}$ antistructural defects.[9–11] The microstructure of the samples before and after annealing was investigated by transmission electron microscopy (TEM) of cross sections. To prepare the samples, we used the usual procedure of mechanical grinding and polishing with subsequent etching by Ar^+ ions.[4,12] The studies were performed in the diffraction regime and in the high-resolution regime with the help of Philips EM 420 and JEM 4000 electron microscopes.

Figure 1 shows a dark-field electron-microscope image of a cross section of a structure in which periodic contrast is observed in the form of thin dark lines. The positions of the dark contrast lines coincide with the expected positions of the InAs delta-layers in the superlattice. The period of the superlattice turned out to be equal to $T_{SL}=28\pm 1$ nm. This value is in good agreement with the data of earlier studies utilizing the method of high-resolution x-ray diffraction ($T_{SL}=28\pm 2$ nm).[13]

XSMA showed that the average indium concentration in the structure is 1.1 ± 0.1 mol.%. Allowing for the fact that the superlattice period $T_{SL}=28$ nm, the thickness of the InAs layers should be 0.3 nm, i.e., ~ 1 ML. However, electron-microscope studies in the high-resolution regime showed (Fig. 2) that the thickness of the indium-containing layers is 4 ML. The difference between the nominal layer thickness and the observed (using TEM) layer thickness is probably due to small-scale relief in the growth surface.[12]

According to the XSMA estimate, the excess arsenic concentration in the InAs/GaAs superlattice grown at 200 °C turned out to be on the order of 0.6 at. %. Figure 3 shows

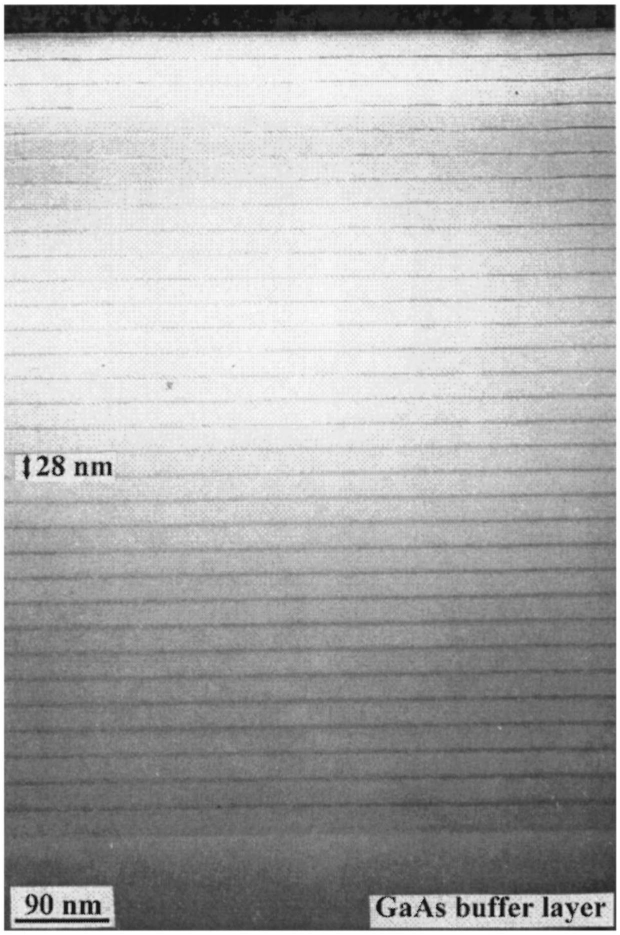

FIG. 1. Dark-field electron-microscope image of a cross section of an InAs/GaAs superlattice grown at low temperature; (200) reflection. The dark contrast corresponds to delta-layers of InAs. The sample was not annealed.

optical absorption spectra in the wavelength range 0.9 $-1.2\,\mu$m, measured at 300 K, for an InAs/GaAs superlattice before and after annealing. It can be seen that the absorption coefficient in the unannealed sample at 1 μm wavelength is equal to $1.2\times10^4\,\mathrm{cm}^{-1}$, which corresponds according to Martin's calibration[14] to a concentration of antistructural arsenic defects of $0.9\times10^{20}\,\mathrm{cm}^{-3}$ and an excess arsenic concentration of 0.8 at. %. This latter value is in satisfactory agreement with data on the relaxation of the lattice parameter of the structure upon annealing,[13] from which it follows that the arsenic excess is equal to 0.7 at. %.

During annealing the concentration of antistructural defects decreases substantially (Fig. 3) and the excess arsenic forms clusters. Figure 4 shows an electron-microscope image of a cross section of the sample after annealing at 500 °C. It can be seen that most of the clusters are accumulated into two-dimensional sheets, whose positions coincide with the positions of the InAs delta-layers. The actual thickness of the two-dimensional layers of clusters is 5–6 nm. Note that a considerable fraction of the clusters are located between the two-dimensional sheets and form a disordered system. It is important that the mean size (diameter) of the clusters in the two-dimensional sheets (∼3 nm) is larger than the mean size of the clusters between sheets (∼2.5 nm). This difference should lead to the result that during Ostwald ripening, upon increasing the duration or temperature of the anneal, the clusters located between the two-dimensional sheets will tend to dissolve.[8,15,16]

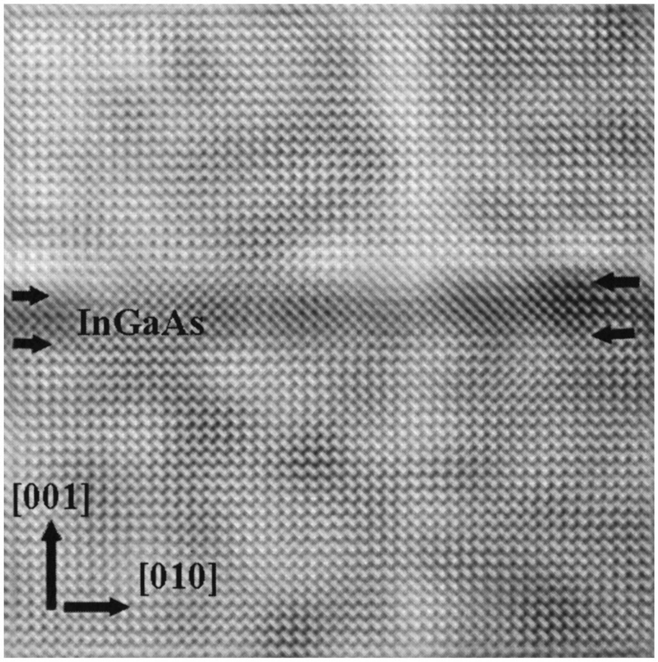

FIG. 2. High-resolution electron-microscope image of an InAs delta-layer in a GaAs matrix grown at low temperature. The nominal indium content in the layer is one monolayer. The sample was not annealed.

Figure 5 shows an electron-microscope image of a cross section of a structure annealed at 600 °C. It can be seen that the mean size of the clusters has increased to ∼6 nm, but in the electron-microscope images of the clusters one observes the characteristic moiré pattern, which reflects the difference between their atomic structure and the structure of the GaAs matrix.[17,18] The cluster concentration after annealing at 600 °C is significantly lower than after annealing at 500 °C, and is equal to $\sim2\times10^{11}\,\mathrm{cm}^{-2}$ in each two-dimensional

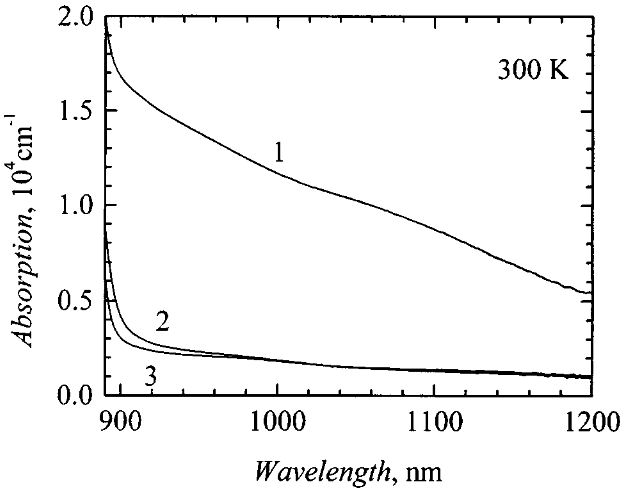

FIG. 3. Optical absorption spectra of an InAs/GaAs superlattice grown at low temperature, before annealing (*1*) and after annealing at 500 (*2*) and 600 °C (*3*) for 15 min.

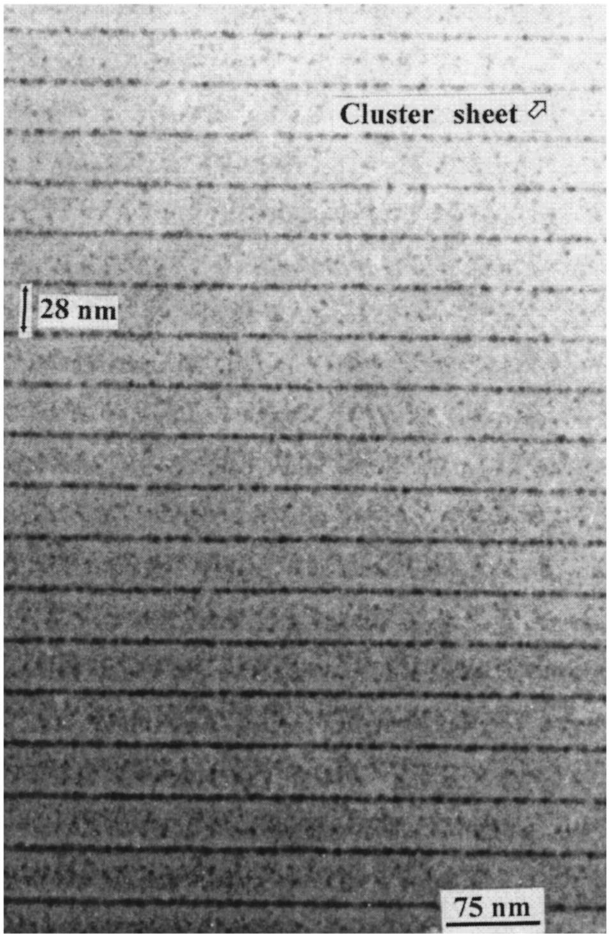

FIG. 4. Light-field electron-microscope image of a cross section of an InAs/GaAs superlattice grown at low temperature and annealed at 500 °C. The positions of the two-dimensional sheets of clusters correspond to the positions of the InAs delta-layers.

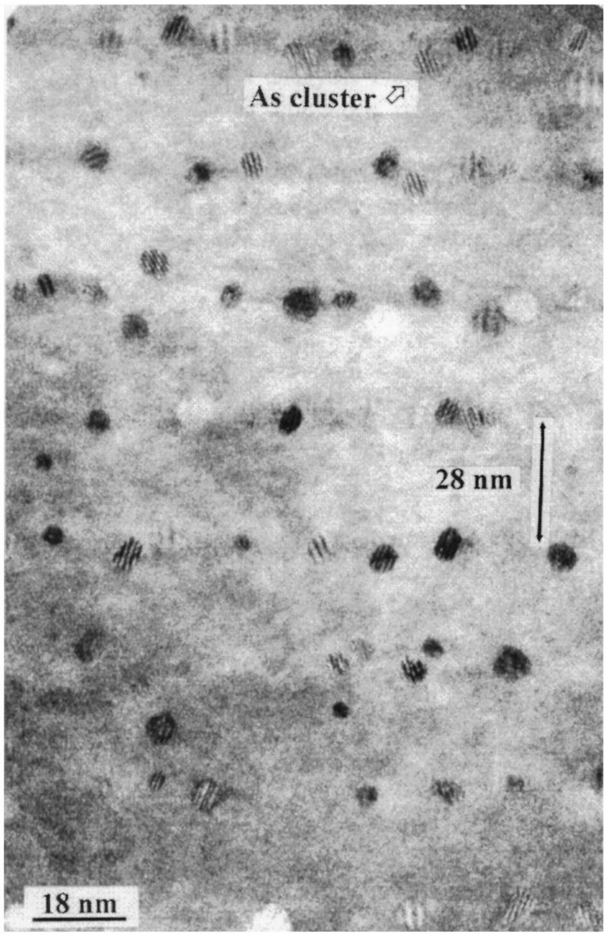

FIG. 5. Light-field electron-microscope image of a cross section of an InAs/GaAs superlattice grown at low temperature and annealed at 600 °C. The positions of the two-dimensional sheets of clusters correspond to the positions of the InAs delta-layers.

sheet. In this case the As clusters located between the two-dimensional sheets have mostly dissolved as a result of Ostwald ripening, and the two-dimensional sheets contain more than 90% of the clusters. The remaining uncoalesced large-scale clusters have reached the size of the clusters in the two-dimensional sheets. This is a consequence of the difference in the kinetics of Ostwald ripening (coalescence) in two-dimensional and three-dimensional systems.[15] According to the Lifshitz–Slezov theory[16] and the results of experimental studies,[15] such large-scale clusters between the two-dimensional sheets cannot be eliminated by further increasing the temperature or the anneal times.

As was shown in Ref. 15, the actual thickness of the two-dimensional sheets of arsenic clusters is close to double the mean diameter of the clusters. The increase in the thickness of the sheets during Ostwald ripening (coalescence) is due to nonequilibrium growth of the clusters in different directions, depending on the local environment of each cluster, and to diffusion smearing of the InAs delta-layers, which is significantly enhanced due to the large concentration of intrinsic point defects.[12] After the anneal at 600 °C the thickness of the two-dimensional sheets of clusters reached ~12 nm. Further increases in the temperature or duration of the anneal should lead to further growth of the thickness of the sheets of clusters. As a result, when the thickness of the sheets of clusters reaches one period of the superlattice (28 nm), the ordered system of two-dimensional sheets of clusters should transition to a disordered system of clusters, described by the Lifshitz–Slezov theory.[16] Such a transition was observed for arsenic clusters in GaAs in Ref. 15.

In summary, we have used low-temperature molecular-beam epitaxy to grow an InAs/GaAs superlattice containing 30 periods of thickness 28 nm each. The superlattice contained 0.8 at. % excess arsenic. Annealing of such a superlattice led to the formation of a periodic structure of two-dimensional sheets of nanoscale arsenic clusters. As a result of annealing at 500 °C for 15 min, the thickness of the two-dimensional sheets of clusters was reduced to a thickness corresponding to much less than one period of the superlattice; however, a fraction of the clusters are now located between the two-dimensional sheets. Such clusters for the most part dissolve when the annealing temperature is raised to 600 °C. As a result, more than 90% of the clusters are now concentrated in the two-dimensional sheets. In this case, however, the thickness of the two-dimensional sheets of clusters is increased to ~12 nm.

This work was carried out with the support of the Russian Ministry of Science (within the programs ''Fullerenes and atomic clusters'' and ''Physics of solid-state nanostructures''), the Russian Fund for Fundamental Research, and the Deutsche Forschungsgesellschaft.

[1] F. W. Smith, A. R. Calawa, C. L. Chen, M. J. Mantra, and L. J. Mahoney, Electron. Dev. Lett. **9**, 77 (1988).

[2] M. Kaminska, Z. Liliental-Weber, E. R. Weber, T. George, J. B. Kortright, F. W. Smith, B. Y. Tsaur, and A. R. Calawa, Appl. Phys. Lett. **54**, 1831 (1989).

[3] M. R. Melloch, K. Mahalingam, N. Otsuka, J. M. Woodall, and A. C. Warren, J. Cryst. Growth **111**, 39 (1991).

[4] N. A. Bert, A. I. Veĭnger, M. D. Vilisova, S. I. Goloshchapov, I. V. Ivonin, S. V. Kozyrev, A. E. Kunitsyn, L. G. Lavrent'eva, D. I. Lubyshev, V. V. Preobrazhenskiĭ, B. R. Semyagin, V. V. Tret'yakov, V. V. Chaldyshev, and M. P. Yakubenya, Fiz. Tverd. Tela (St. Petersburg) **35**, 2609 (1993) [Phys. Solid State **35**, 1289 (1993)].

[5] J. K. Luo, H. Thomas, D. V. Morgan, D. Westwood, and R. H. Williams, Semicond. Sci. Technol. **9**, 2199 (1994).

[6] T. M. Cheng, C. V. Chang, A. Chin, M. F. Huang, and J. H. Huang, Appl. Phys. Lett. **64**, 2517 (1994).

[7] N. A. Bert, V. V. Chaldyshev, D. I. Lubyshev, V. V. Preobrazhenskiĭ, and B. R. Semyagin, Fiz. Tekh. Poluprovodn. **29**, 2242 (1995) [Semiconductors **29**, 1170 (1995)].

[8] N. A. Bert, V. V. Chaldyshev, N. N. Faleev, A. E. Kunitsyn, D. I. Lubyshev, V. V. Preobrazhenskii, B. R. Semyagin, and V. V. Tret'yakov, Semicond. Sci. Technol. **12**, 51 (1997).

[9] X. Liu, A. Prasad, J. Nishio, E. R. Weber, Z. Liliental-Weber, and W. Walukiewicz, Appl. Phys. Lett. **67**, 279 (1995).

[10] N. A. Bert, V. V. Chaldyshev, A. E. Kunitsyn, Yu. G. Musihin, N. N. Faleev, V. V. Tret'yakov, V. V. Preobrazhenskii, M. A. Putyato, and B. R. Semyagin, Appl. Phys. Lett. **70**, 3146 (1997).

[11] V. V. Chaldyshev, A. E. Kunitsyn, V. V. Preobrazhenskiĭ, M. A. Putyato, B. R. Semyagin, V. V. Tret'yakov, and N. N. Faleev, Fiz. Tekh. Poluprovodn. **32**, 778 (1998) [Semiconductors **32**, 692 (1998)].

[12] N. A. Bert, Yu. G. Musikhin, V. V. Preobrazhenskiĭ, M. A. Putyato, B. R. Semyagin, A. A. Suvorova, V. V. Chaldyshev, N. N. Faleev, and P. Werner, Fiz. Tekh. Poluprovodn. **32**, 769 (1998) [Semiconductors **32**, 683 (1998)].

[13] N. N. Faleev, V. V. Chaldyshev, A. E. Kunitsyn, V. V. Preobrazhenskiĭ, M. A. Putyato, B. R. Semyagin, and V. V. Tret'yakov, Fiz. Tekh. Poluprovodn. **32**, 24 (1998) [Semiconductors **32**, 19 (1998)].

[14] M. Martin, Appl. Phys. Lett. **39**, 747 (1981).

[15] V. V. Chaldyshev, N. A. Bert, V. V. Preobrazhenskii, M. A. Putyato, and B. R. Semyagin, Mater. Sci. Eng., A **238**, 148 (1997).

[16] I. M. Lifshitz and V. V. Slezov, Zh. Éksp. Teor. Fiz. **35**, 479 (1958) [Sov. Phys. JETP **8**, 331 (1959)].

[17] Z. Liliental-Weber, A. Claverie, J. Washburn, F. Smith, and R. Calawa, Appl. Phys. A **53**, 141 (1991).

[18] N. A. Bert and V. V. Chaldyshev, Fiz. Tekh. Poluprovodn. **30**, 1889 (1996) [Semiconductors **30**, 988 (1996)].

Translated by Paul F. Schippnick

SEMICONDUCTORS VOLUME 32, NUMBER 10 OCTOBER 1998

ELECTRONIC AND OPTICAL PROPERTIES OF SEMICONDUCTORS

Photoconductivity of copper-compensated gallium phosphide

N. N. Pribylov, S. I. Rembeza, A. I. Spirin, V. A. Buslov, and S. A. Sushkov

Voronezh State Technological University, 394026 Voronezh, Russia

(Submitted July 14, 1997; accepted for publication December 23, 1997)
Fiz. Tekh. Poluprovodn. **32**, 1165–1169

Autocompensation effects in GaP after diffusive copper doping, amphotericity of electrical activity of the copper impurity, and the kinetics of interband photoconductivity and infrared quenching are explained in terms of a model of reconstruction of the bonds between the copper impurity and its immediate environment. In this picture, the acceptor state is associated with substitutional Cu atoms with tetrahedral coordination, while the donor state is associated with Cu atoms bonded to only two of the four phosphorus atoms. © *1998 American Institute of Physics.* [S1063-7826(98)00410-4]

INTRODUCTION

The behavior of copper impurity in gallium phosphide has been probed by a number of authors[1–7] using various photoconductivity methods. The main interest in GaP : Cu stemmed from the high sensitivity of the material to radiation in the short-wavelength region of the visible spectrum, which is attributable to the presence on the copper impurity of a deep level in the band gap with high asymmetry of the capture cross sections for electrons and holes.[1]

The presence of self-compensation in gallium phosphide due to diffusive copper doping was established elsewhere:[2] Regardless of the type of conductivity of the starting material after its doping, samples with resistivities from 10^4 to $10^{14}\,\Omega\cdot\text{cm}$ at 300 K were obtained.

The results of different authors, which were generalized in Ref. 3, are comparable: All reports mention the presence of the dominant ''*A*'' states in the energy band $E=E_v+(0.5-0.55)$ eV and sometimes the presence of ''*B*'' states in the energy range $E_v+(0.68-0.82)$ eV. Assigning the *B* level to copper is open to discussion since the concentrations of the *A* and *B* levels in the investigated samples were not correlated.[3]

Since the nature of the *B* level has not yet been determined and since its influence on the photoelectric properties of GaP : Cu has not been investigated, a study of the photoconductivity of this material with different copper doping levels is of interest.

EXPERIMENTAL PROCEDURE

The starting samples of gallium phosphide consisted of wafers with thickness 1 mm, cut from single crystals grown by the Czochralski method and doped with tellurium with an electron concentration of $4\times10^{17}\,\text{cm}^{-3}$ and Hall mobility $130\,\text{cm}^2/(\text{V}\cdot\text{s})$. Diffusive saturation of the samples with copper was carried out in evacuated quartz cells from layers of the metal sputtered onto both surfaces. The doping temperature was varied in the range 800–1200 °C, and the doping time, from 8 to 24 h. At the end of the anneals the samples were quenched by throwing the cells into water. The samples were processed with abrasive powders and then polished and etched in a mixture of hydrofluoric and nitric acids. Indium contacts, deposited on as-grown samples, ensured linear current–voltage characteristics (CVC) over a wide range of applied voltages. The highest-resistance samples were obtained in the temperature interval 800–930 °C. At room temperature their resistivity stood at $3\times10^{10}\,\Omega\cdot\text{cm}$.

Photoconductivity spectra were measured for both ordinary and Raman excitations. In the first case monochromatic radiation from a single source was directed upon the surface at normal incidence; to record the Raman spectra, we used radiation from two monochromators incident at an angle of roughly 45°. The modulation technique was used to record the photoconductivity. The current signal was amplified and synchronously detected by a selective phase-sensitive UNIPAN 232B nanovoltmeter with subsequent recording on a measurement–calculational complex built into an SDL-2 spectrometer, or on a tape cassette. A 1-kW NARVA halogen lamp and a xenon gas-discharge lamp served as the radiation sources. All measurements were performed in the constant-field regime. As the voltage source in the case of the high-resistance samples we used a stabilized power supply for the UBPV-1 photomultiplier.

MAIN EXPERIMENTAL RESULTS

1. *Photoconductivity spectra of* GaP : Cu *samples.* The room-temperature photoconductivity of the samples (Fig. 1) in the long-wavelength region of the spectrum is characterized by an impurity band with a 0.7eV threshold, whose maximum is at 1.05 eV, which extends to photon energies ~2 eV, where an abrupt growth of the photocurrent takes place right up to the edge of the band of the intrinsic transitions. Because the sum of the threshold energies of the bands is close to the width of the band gap of gallium phosphide,

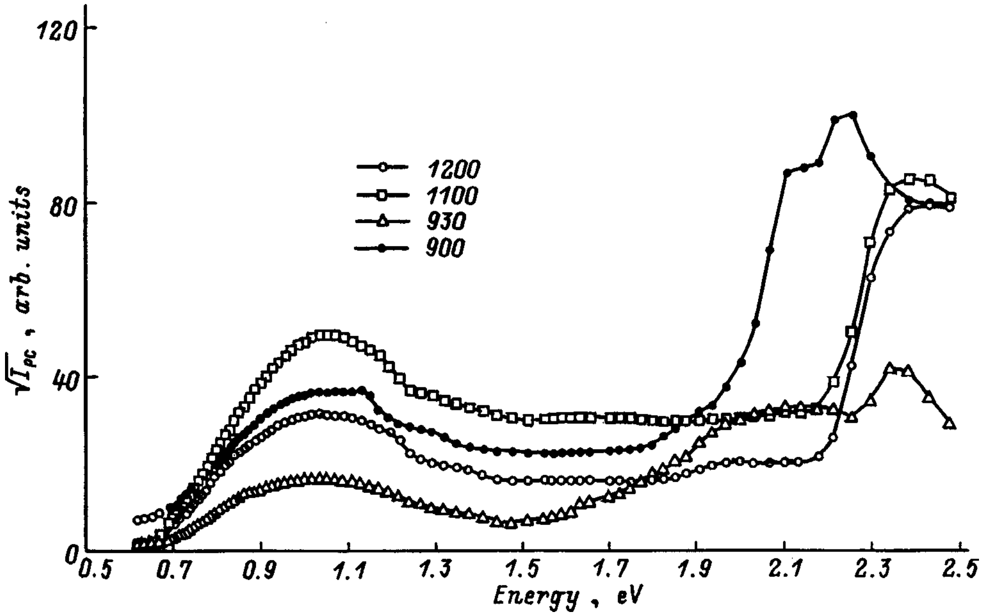

FIG. 1. Photoconductivity spectra of GaP : Cu samples doped with copper at various temperatures.

we can assume that they are connected with the *B* level which lies in the lower part of the band gap and which is partially filled with electrons.

The form of the photocurrent spectra for Raman excitation depends strongly on the intensity of either of the photon fluxes: It is possible to decrease the modulated current as well as to vary its phase, i.e., to obtain quenching of the intrinsic photoconductivity shown in Fig. 2. It can be seen that in the long-wavelength part of the spectrum unmodulated interband illumination reveals a new band with threshold near 0.6 eV. This result clearly confirms the presence in the investigated samples of centers which sensitize the intrinsic photoconductivity. Also, the observed thresholds are close to those of other authors.[4,5]

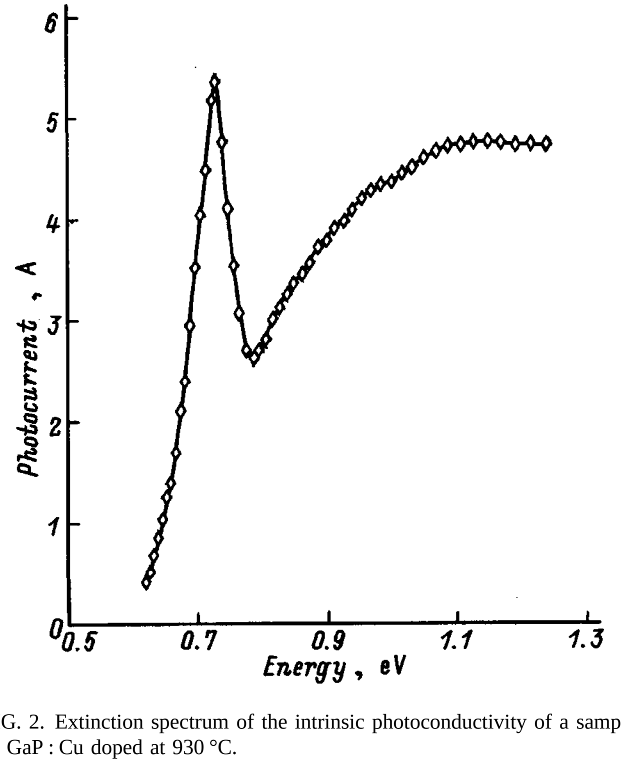

FIG. 2. Extinction spectrum of the intrinsic photoconductivity of a sample of GaP : Cu doped at 930 °C.

2. *Relaxation of the intrinsic photoconductivity.* The kinetics of variation of the photoconductivity (see Fig. 3) depends on the excitation intensity. After holding the samples in the dark, switching on unmodulated light with wavelength 547 nm ($h\nu = 2.27\,\mathrm{eV} > E_g$) leads first to rapid, and then to slow growth of the photocurrent up to its steady-state value. We found that the rate of growth of the photocurrent in the initial segment depends on the time between switching the light off and switching it back on. The form of this dependence is shown in the inset in Fig. 3. After switching the light off, the current in the sample circuit is observed to decay exponentially nearly to its dark value with a time constant of 1.2 s. If the light is switched back on immediately after the dark photocurrent is reached, rapid growth of the photocurrent to its steady-state value is observed. Thus, the samples show evidence of a memory effect at room temperature.

3. *Kinetics of infrared quenching of the intrinsic photoconductivity.* The effect of infrared quenching of the intrinsic photoconductivity is observed in the investigated samples. The kinetics of quenching was recorded at photon energies of 0.7 and 1.24 eV, which excite holes only from the *A* level in the first case and from both levels in the second. For the same quenching depth, which is achieved by varying the width of the monochromator slits, relaxation of the photocurrent within the limits of error of the recording devices does not depend on the photon energy (Fig. 4). Switching off the infrared excitation results in a still greater decrease of the current in the sample circuit with subsequent slow recovery. The rate of growth of the photocurrent after infrared quenching is independent of the intensity and duration of the infrared excitation and depends only on the depth of quenching of the intrinsic photoconductivity, and for a constant level of

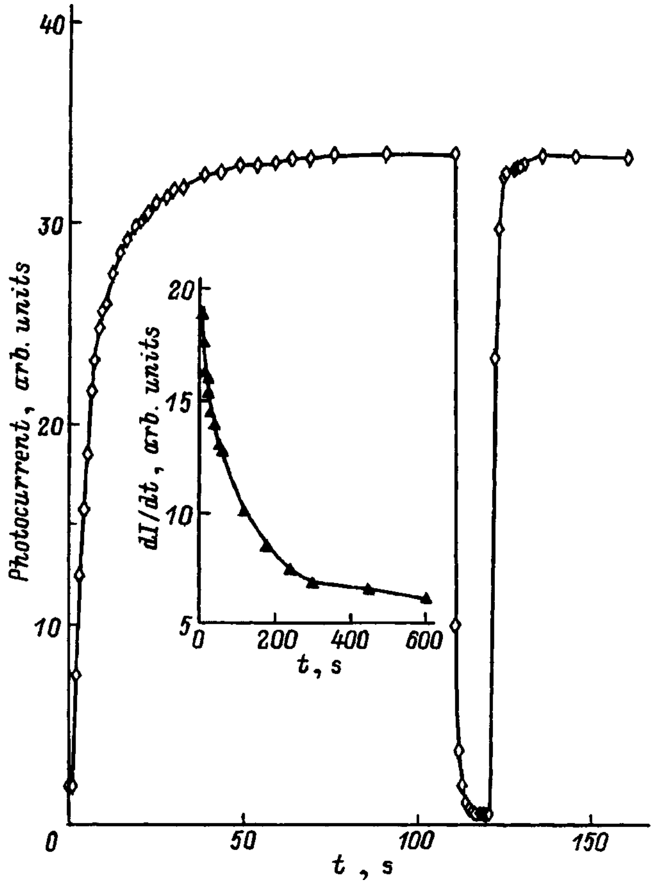

FIG. 3. Kinetics of the intrinsic photoconductivity of a sample of GaP : Cu doped at 930 °C. The inset plots the dependence of the rate of growth of the photocurrent (dI/dt) in arbitrary units as a function of storage time of the sample in the dark at room temperature.

intrinsic light is significantly lower than after holding the sample in the dark.

DISCUSSION OF EXPERIMENTAL RESULTS

In the experimental results presented in the preceding section, anomalies in the properties of the investigated GaP : Cu samples are obvious. These anomalies are expressed in the strong dependence of the photocurrent growth kinetics on the dark storage time of the sample and the greater rate of decay of the photoconductivity over its growth rate. This phenomenon was observed in Ref. 1, but was not specifically discussed. A qualitative explanation of the observed photoconductivity effects is possible on the basis of the following assumptions:

– As a result of copper doping, two energy levels can arise in the gallium-phosphide band gap: the lower one, an acceptor level—the A level, and the upper one, a donor level—the B level, whose states are denoted, depending on the presence or absence of electrons in them, as A^-, B^0, and A^0, B^+, respectively;

– the neutral acceptor state of the copper impurity (A^0) and the neutral donor state of the copper impurity (B^0) are equivalent in charge and can be obtained, one from the other, by changing the type of conductivity of the material.

Compensation of either type of conductivity is defined in terms of the quasichemical reaction

$$B^+ + e_{cB} \leftrightarrows A^- + p_{vB}, \tag{1}$$

from which it follows that an excess of electrons in the band gap leads to a prevalence of the acceptor states A^-, and an excess of holes is compensated for at the expense of the donor properties of the B^0 states.

On the basis of the above assumptions the kinetics of growth of the intrinsic photoconductivity (Fig. 1) is governed by the following factors: photogeneration of electron–hole pairs at the commencement of excitation cannot deliver a significant concentration of free charge carriers because the holes are efficiently captured by the A^- states, and because electrons are captured by the B^+ states. The presence of shallow donors in the initial samples accounts for the fact that the concentration of the A^- states exceeds that of the B^+ states and filling of the latter by electrons occurs earlier than filling of the A level by holes. Generation of additional pairs leads to an increase in the electron concentration in the conduction band and an increase in their lifetime due to continuing localization of holes at the lower level. We link the very

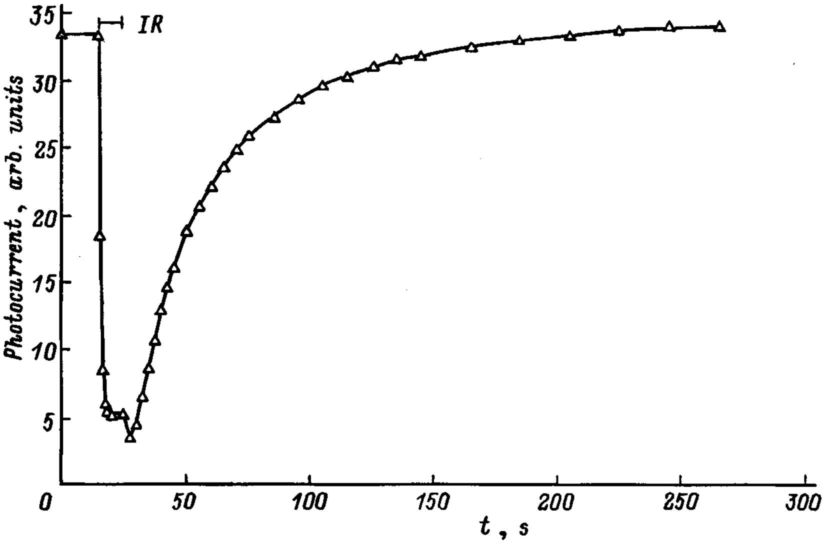

FIG. 4. Kinetics of extinction and recovery of the intrinsic photoconductivity in the sample doped at 930 °C.

slow growth of the photocurrent observed directly after the brief segment of rapid growth with the processes by which the neutral B^0 states transition into neutral A^0 states. This reconstruction is dictated by the photogenerated electrons, which govern the conductivity of the sample. As a result, the number of B levels decreases with a corresponding increase in the number of A levels. Increasing the concentration of A^0 centers increases the thermal generation of holes from this level into the valence band and results in saturation of the photocurrent. After the light is switched off, the thermally generated holes recombine with electrons, which leads to a rapid decrease of the photocurrent and to the establishment of a p-type conductivity of the sample, which stimulates a reversal of the direction of reaction (1). The high rate of growth of the photocurrent after quickly switching the light back on is governed by the redistribution of the density of states between the B and A levels in favor of the latter, and also by the fact that the rate of capture of holes by the A level is substantially greater than the rate of capture of electrons by the B level. If there is a pause between removal and restoration of the light, the kinetics of growth of segment 1, which reflects the restoration of the equilibrium distribution of the copper states, changes in a way that depends on the length of this pause. The time constant of this process, found from Fig. 3 (inset), is approximately 135 s.

The kinetics illustrated in Fig. 4 is explained by the fact that infrared radiation generates only holes, and increasing its intensity leads to an inversion of the dominant carrier type if the rate of optical generation of holes exceeds the rate of thermal generation of holes. As a result of recombination, the current falls precipitously, the sample acquires p-type conductivity, and the balance of reaction (1) shifts to the left, which leads to a redistribution of the density of states between the A and B levels in favor of the latter. After removing the infrared illumination, recombination of electron–hole pairs proceeds mainly through the B level due to the low concentration of sensitizing A centers. However, with localization of some of the holes at the A level, the type of conductivity of the sample changes and B^0 states accumulate. The rate of reconstruction of donor states into acceptor states is governed by the competition of the mechanisms of electron–hole pair recombination at the center and by the energy losses needed for the reconstruction $A \Leftrightarrow B$. The transformation of acceptor states into donor states brought about by infrared illumination of the centers is quite rapid.

We do not know of any electron-spin-resonance studies of the electronic structure of copper impurity states in III–V compounds; we can therefore discuss possible reasons for the donor properties of the B^0 centers only by analogy with known models for amphoteric impurities (Pt and Au in Si, Refs. 8 and 9). In our case, the copper acceptor state is realized upon its isovalent substitution for gallium by virtue of the fact that one electron from the filled d shell of the impurity is excited to a level of the valence electrons and another is accepted from the lattice. The copper donor state is realized by formation of a center, which consists of a copper ion bound to only two of the four atoms of its phosphorus environment with the two remaining phosphorus atoms closing their valence electrons on each other. The given center should have lower point symmetry due to the displacement of a Cu ion from a gallium site in the [110] direction. The possibility of lowering the point symmetry of a copper center in a gallium vacancy has been experimentally demonstrated for GaAs (Ref. 10). Polarization of photoluminescence has also been observed in GaP : Cu (Ref. 7).

[1] B. Goldstein and S. S. Perlman, Phys. Rev. **148**, 715 (1966).
[2] R. G. Schulze and P. E. Petersen, J. Appl. Phys. **45**, 5307 (1974).
[3] P. O. Fagerström, H. G. Grimmeiss, and H. H. Titze, J. Appl. Phys. **49**, 3341 (1978).
[4] H. G. Grimmeiss and H. Scholz, Philips Res. Rep. **20**, 107 (1965).
[5] H. G. Grimmeiss and B. Monemar, Phys. Solid State **19**, 505 (1973).
[6] B. Monemar, H. P. Gislason, P. J. Dean, and D. C. Herbert, Phys. Rev. B **25**, 7719 (1982).
[7] I. A. Buyanova, S. S. Ostapenko, and M. K. Sheĭnkman, Fiz. Tekh. Poluprovodn. **20**, 1791 (1986) [Sov. Phys. Semicond. **20**, 1123 (1986)].
[8] H. H. Woodbury and G. W. Ludwig, Phys. Rev. **126**, 466 (1962).
[9] N. T. Bagraev and V. A. Mashkov, JETP Lett. **39**, 251 (1984).
[10] N. S. Averkiev, V. A. Vetrov, A. A. Gutkin, I. A. Merkulov, L. P. Nikitin, I. I. Remina, and N. G. Romanov, Fiz. Tekh. Poluprovodn. **20**, 1617 (1986) [Sov. Phys. Semicond. **20**, 1014 (1986)].

Translated by Paul F. Schippnick

SEMICONDUCTORS VOLUME 32, NUMBER 10 OCTOBER 1998

Accumulation of electrons in GaAs layers grown at low temperatures and containing arsenic clusters

P. N. Brunkov, V. V. Chaldyshev, N. A. Bert, A. A. Suvorova, and S. G. Konnikov

A. F. Ioffe Physicotechnical Institute, Russian Academy of Sciences, 194021 St. Petersburg, Russia

A. V. Chernigovskiĭ

St. Petersburg State Technical University, 195251 St. Petersburg, Russia

V. V. Preobrazhenskiĭ, M. A. Putyato, B. R. Semyagin

Institute of Semiconductor Physics, Siberian Branch of the Russian Academy of Sciences,
630090 Novosibirsk, Russia

(Submitted February 10, 1998; accepted for publication February 11, 1998)
Fiz. Tekh. Poluprovodn. **32**, 1170–1174 (October 1998)

Capacitance spectroscopy was used to investigate the properties of Au/GaAs Schottky barriers in structures in which a thin layer of gallium arsenide grown at low temperature (LT-GaAs) and containing As clusters was sandwiched between two uniformly copper-doped layers of n-GaAs grown at standard temperatures. We detected electron accumulation in the LT-GaAs layer surrounded by two depletion regions in the adjacent n-GaAs layers. Emission of electrons from the LT-GaAs layer at 300 K results in an extended plateau in the capacitance–voltage characteristic. It is found that the presence of the 0.1 μm thick LT-GaAs layer sandwiched between the two much thicker n-GaAs layers results in an increase in the breakdown electric field to values as high as 230 kV/cm, which is much higher than typical values for standard Au/n-GaAs structures. © *1998 American Institute of Physics.* [S1063-7826(98)00510-9]

INTRODUCTION

Gallium arsenide grown by molecular-beam epitaxy at low temperatures $T<300\,^\circ$C (LT-GaAs) has attracted wide attention because of its high resistivity, high breakdown voltage, and record-short lifetime of nonequilibrium charge carriers.[1–5] The most striking feature of LT-GaAs is an arsenic excess (up to 1.5 at. %) incorporated into the growing layer during low-temperature epitaxy. This excess gives rise to a high concentration of point defects such as that of the antisite defect $\mathrm{As}_{\mathrm{Ga}}$, of interstitial arsenic As_i, and of gallium vacancy V_{Ga} and their complexes. Annealing of LT-GaAs at high temperatures ($T>500\,^\circ$C) leads to the formation of nanoscale As clusters, which are built into the GaAs matrix. Such clusters, like point defects, should be electrically active and can influence the electronic properties of the material.

In our study we used capacitance spectroscopy to investigate Au/GaAs Schottky-barrier structures in which a thin layer of LT-GaAs containing As clusters was sandwiched between two uniformly doped n-GaAs layers grown at standard temperatures. Our goal was to study the influence of the thin LT-GaAs layer on the electrical properties of the structure.

SAMPLES AND EXPERIMENTAL TECHNIQUE

The investigated samples were grown by molecular-beam epitaxy in a ''Katun'″ two-chamber setup on n^+-GaAs substrates with (100) orientation. The samples consisted of a layer of n-GaAs(Si) (thickness $\sim 0.5\,\mu$m, growth temperature 580 °C, electron concentration $2\times 10^{16}\,\mathrm{cm}^{-3}$), a layer of LT-GaAs (thickness $\sim 0.1\,\mu$m, growth temperature 200 °C), and a layer of n-GaAs(Si) (thickness $\sim 0.5\,\mu$m, growth temperature 580 °C, electron concentration $2\times 10^{16}\,\mathrm{cm}^{-3}$). Growth of the upper n-GaAs layer of the structure for 0.5 h led to annealing of the LT-GaAs layer and formation of arsenic clusters in it.

The crystal structure of the samples was investigated by transmission electron microscopy (TEM) in cross sections and in the growth plane. A Philips EM 420 electron microscope was used having an accelerating voltage of 100 keV.

The Schottky barriers were formed by sputtering Au onto the surface of the samples. The diameter of the Schottky contacts was 0.35 mm. Capacitance–voltage ($C-V$) characteristics were measured at frequencies in the range 100 Hz–1 MHz in the temperature range $77-300$ K. The amplitude of the measured signal was 25 mV. Also, the dependence of the conductivity (G) on the reverse bias was investigated.

Electrochemical $C-V$ profiling was done using the standard technique at a frequency of 3 kHz (Ref. 6).

RESULTS

Figures 1a and 1b show electron-microscope images of a cross section of one of the investigated structures. It can be seen that the LT-GaAs layer containing arsenic clusters has a thickness of $\sim 0.1\,\mu$m and is sandwiched in between two n-GaAs layers which do not contain clusters. The cluster density in the layer is $\sim 4\times 10^{11}\,\mathrm{cm}^{-2}$, and their average diameter is ~ 10 nm.

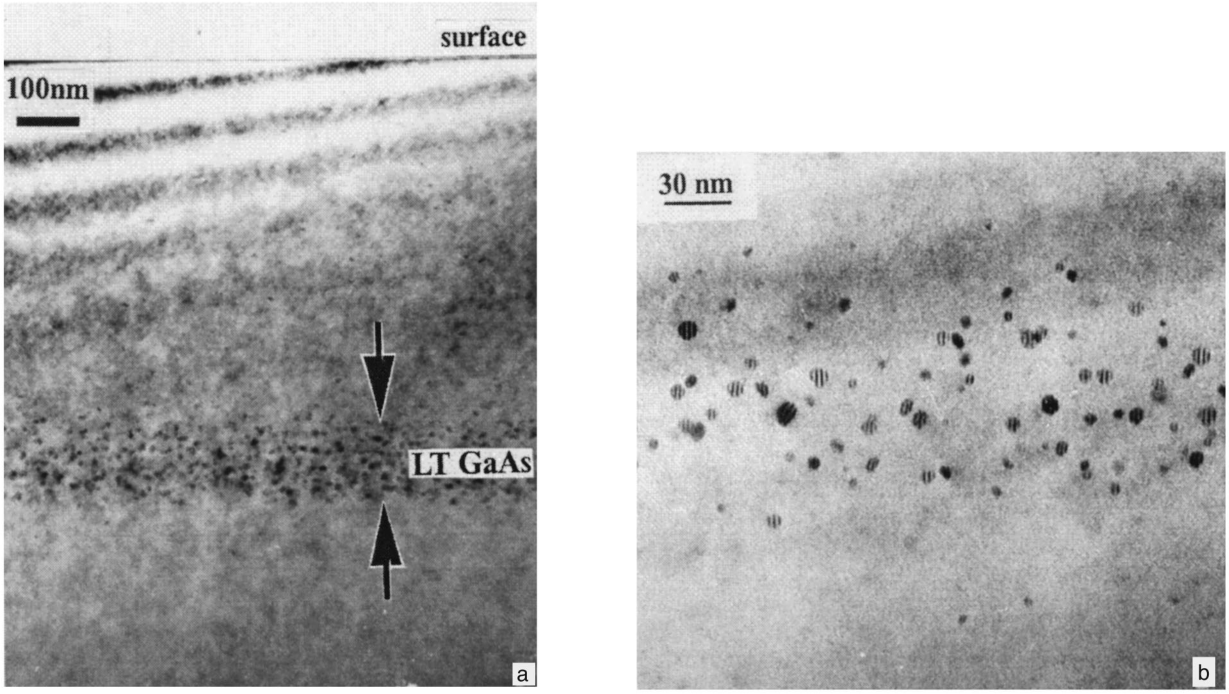

FIG. 1. a — Light-field TEM image ($g=220$) of a cross section of the structure *n*-GaAs/*LT*-GaAs/*n*-GaAs. b — magnified TEM image of a thin layer of *LT*-GaAs containing arsenic clusters.

Capacitance–voltage characteristics of a Au/*n*-GaAs/*LT*-GaAs/*n*-GaAs/n^+-GaAs structure, measured at a frequency of 10 kHz at 94 and 300 K are shown in Fig. 2a.

At 300 K, as the reverse bias is increased, the capacitance at first decreases rapidly, (at -2 V) falls precipitously, and then remains almost constant over a wide voltage interval. The region of quasiconstant capacitance extends from -2 to -12 V. With further increase of the reverse bias, the capacitance gradually decreases. At voltages around -25 V electrical breakdown is observed.

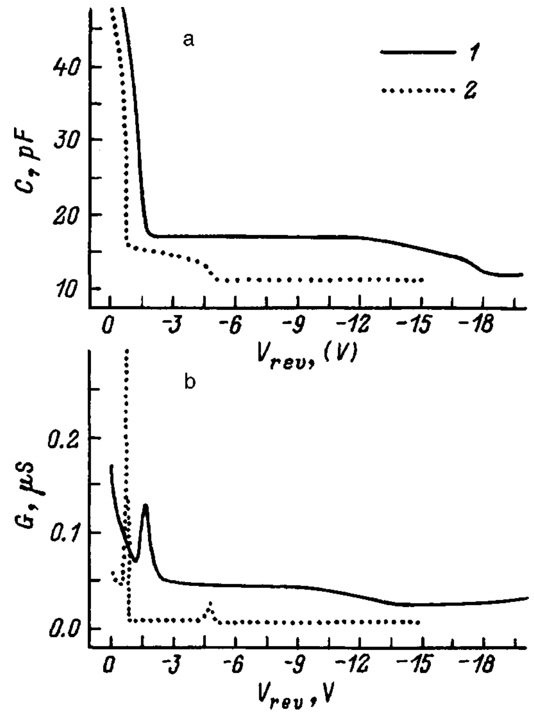

FIG. 2. $C-V$ (a) and $G-V$ (b) characteristics of the structure Au/*n*-GaAs/*LT*-GaAs/*n*-GaAs/n^+-GaAs, measured at 10 kHz at 300 K (*1*) and 94 K (*2*).

As the temperature is decreased, the wide plateau in the $C-V$ characteristics gradually narrows. At 95 K the plateau is not observed, and the precipitous fall of the capacitance at -2 V is followed by a gradual decrease (Fig. 2a). Note that the observed peculiarities of the $C-V$ characteristics at 300 and 94 K are not associated with leakage currents. As can be seen from Fig. 2b, the conductivity of the structure for reverse biases is small. The conductivity peaks are connected with the abrupt changes in the capacitance with increase of the reverse bias.

Employing the depletion-layer approximation, we calculated the free-carrier distribution profiles ($N_{CV}-W$) from the $C-V$ characteristics:

$$N_{CV}(W)=\frac{C^3}{q\varepsilon\varepsilon_0\left(\dfrac{dC}{dV}\right)},\qquad W=A\,\frac{\varepsilon\varepsilon_0}{C}, \tag{1}$$

where q is the charge of the electron, ε_0 is the dielectric constant of the vacuum, ε is the dielectric constant of the semiconductor, W is the width of the space charge region, and A is the area of the Schottky barrier. Profiles calculated for 300 and 94 K are shown in Fig. 3a.

As can be seen from Fig. 3a, the electron concentration near the surface ($W<0.35\,\mu$m) is $\sim 2.5\times10^{16}\,\mathrm{cm}^{-3}$, which is in line with what is expected given the level of doping of the upper *n*-GaAs layer. A depletion layer, which includes the *LT*-GaAs layer and the adjacent *n*-GaAs layers, is observed in the region $0.35<W<0.75\,\mu$m. Beyond the limits

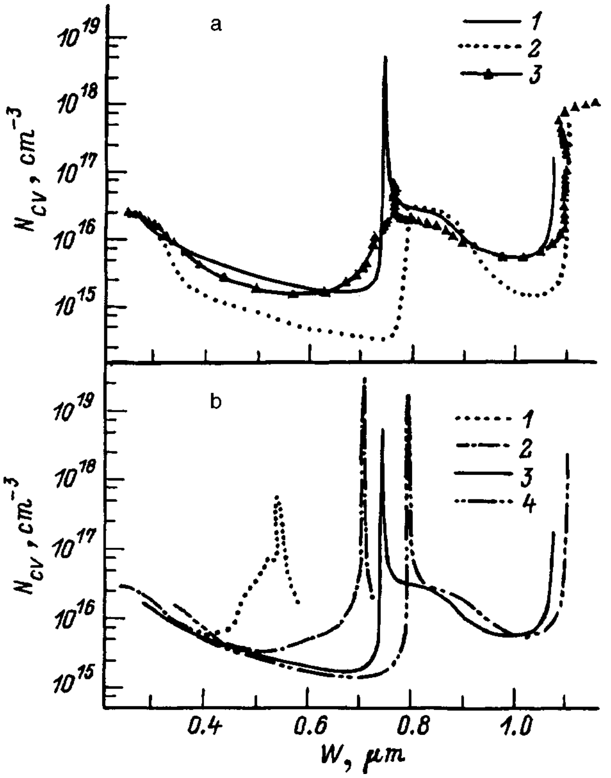

FIG. 3. a — Comparison of the $N_{CV}-W$ characteristics calculated from $C-V$ measurements at 10 kHz at 300 K (*1*) and 94 K (*2*) with the electrochemical profile (*3*). b — $N_{CV}-W$ characteristics calculated from $C-V$ measurements at 300 K at different frequencies: 100 Hz (*1*), 1 kHz (*2*), 10 kHz (*3*), 1 MHz (*4*).

of the depletion layer the electron concentration again reaches values near $2.5\times10^{16}\,\mathrm{cm}^{-3}$, which corresponds to the doping level of the lower *n*-GaAs layer. With further increase in *W*, we see another depletion region which is probably caused by defects in the metallurgical boundary between the substrate and the epitaxial film. Immediately beyond this depletion region the carrier concentration rises abruptly to $\sim2\times10^{18}\,\mathrm{cm}^{-3}$, which corresponds to doping level of the n^+-GaAs substrate. The carrier concentration depth profile inferred from the $C-V$ measurements is in good agreement with the charge-carrier concentration profile obtained independently by electrochemical profiling (see Fig. 3a).

The $N_{CV}-W$ profile calculated at 300 K is distinguished by the presence of a narrow peak which is due to the emission of electrons and which corresponds to the plateau in the $C-V$ characteristics (Fig. 3a). In the range of measurement frequencies from 1 MHz to 10 kHz this peak is located at the edge of the depletion region induced by the LT-GaAs layer. However, at lower measurement frequencies the peak shifts into the middle of the depletion layer, and at the very lowest frequencies ($\sim$100 Hz) its position corresponds to the geometric position of the LT-GaAs layer in the structure (Fig. 3b). Note that at 94 K the plateau in the $C-V$ characteristics is not observed and the emission peak in the $N_{CV}-W$ profiles is absent at all of the frequencies at which measurements were made.

DISCUSSION

Our studies show that the presence of the thin LT-GaAs layer leads to a significant increase in the electrical breakdown voltage of a Schottky diode. The breakdown electrical field strength, averaged over the structure, amounts to $\sim$230 V/cm, which corresponds to values characteristic of thick LT-GaAs layers,[7] and substantially exceeds values characteristic of ordinary *n*-GaAs and stoichiometric semi-insulating GaAs.

The observed behavior of the $C-V$ and $N_{CV}-W$ characteristics indicates an accumulation of electrons within the LT-GaAs layer and depletion around it.[8–10] The presence of built-in depletion regions leads to the appearance of a jump in the $C-V$ characteristics at -2 V, when these regions begin to overlap with the space charge region of the Schottky barrier which expands as the reverse bias is raised.

Accumulation of electrons in the LT-GaAs layer can take place both at deep-level defects and at arsenic clusters. The parameters of the deep levels characteristic of LT-GaAs were previously investigated by deep-level transient spectroscopy (DLTS) and the temperature-dependent conductivity method.[11–15] Such levels are $EL2$ (0.73 eV), $EB4$ (0.65 eV), and $EL3$ (0.57 eV). Studies using a scanning tunneling microscope showed[16] that the arsenic clusters also create levels deep in the GaAs band gap. The indicated electron levels are compensated in part by acceptors such as gallium vacancies.[17] The concentration of compensating acceptors in LT-GaAs is very large and in the unannealed material reaches $10^{18}\,\mathrm{cm}^{-3}$, which significantly exceeds the concentration of dopant-silicon shallow donors $(2\times10^{16}\,\mathrm{cm}^{-3})$. It may be expected that the concentration of compensating acceptors remains high also after annealing of the LT-GaAs layers despite conversion of most of the point defects formed by the arsenic excess into nanoscale clusters. In such a case, accumulation of charge in the LT-GaAs layer takes place due to transitions of electrons into the deep electronic levels (which are created by point defects or clusters) from the shallow donor levels of the adjacent *n*-GaAs layers. As a result, the LT-GaAs layer is surrounded by space charge regions. Assuming that the concentration of compensating deep levels in the LT-GaAs layer is much greater than the concentration n of the shallow donors in the *n*-GaAs layers, the width of the depletion region is

$$\Delta W = 2\sqrt{\frac{2\varepsilon\varepsilon_0\Delta V}{qn}} + d_{LT}, \tag{2}$$

where ΔV is the contact potential difference, and $d_{LT}=0.1\,\mu$m is the width of the LT-GaAs layer. Setting $\Delta V\approx0.5$ V, we obtain $\Delta W\approx0.4\,\mu$m, which corresponds to the experimentally determined width of the depletion region (Fig. 3a).

Thus, our $C-V$ studies show that the LT-GaAs layer accumulates electrons and induces space charge regions in the adjacent *n*-GaAs layers. An external bias should, in general, lead to emission of the accumulated charge. However, since the levels at which the electrons are trapped are located deep in the GaAs band gap, the emission rate should depend strongly on the temperature. At low temperatures the emission rate is extraordinarily low and at 94 K we did not observe the characteristic plateau in the $C-V$ characteristics even when the frequency was lowered to 100 Hz. At room temperature the emission rate is quite high; however, even in this case quasi-equilibrium does not have enough time to establish itself at high frequency. As a result, the peak in the $N_{CV}-W$ characteristic due to electron emission is shifted relative to the geometric position of the LT-GaAs layer toward the edge of the depletion region (Fig. 3a).[18] A situation similar to quasi-equilibrium can be realized by lowering the measurement frequency from 1 MHz to 100 Hz. In this case, the capacitance increases from 17 pF to 26 pF in the region of the plateau and the peak in the $N_{CV}-W$ characteristic shifts toward the geometrical position of the LT-GaAs layer (Fig. 3b).

The concentration of emitted electrons n_e can be estimated from the width of the plateau of quasiconstant capacitance in the $C-V$ characteristics from the relation[10]

$$n_e = C^* \Delta U / Aq, \tag{3}$$

where C^* is the value of the quasiconstant capacitance in the plateau, and ΔU is the width of the plateau. Substituting experimental data from Fig. 2a and noting that the area of the barrier $A = 1.1 \times 10^{-3}$ cm^2, we obtain $n_e \approx 1 \times 10^{12}$ cm^{-2}.

The concentration n_a of electrons accumulated in the LT-GaAs layer can be estimated from the width of the depletion region and the known level of doping with shallow donors:

$$n_a = n \Delta W = 0.8 \times 10^{12}\ \mathrm{cm}^{-2}. \tag{4}$$

The estimates obtained using formulas (3) and (4) show that $n_e \approx n_a$; i.e., at room temperature, using an external bias it is possible to achieve emission of the electrons accumulated in the LT-GaAs layer in its initial state.

CONCLUSIONS

Our study of Au/n-GaAs/LT-GaAs/n-GaAs Schottky-barrier structures shows that the presence of a thin LT-GaAs layer sandwiched between two much thicker n-GaAs layers leads to a significant increase in the electrical breakdown voltage in comparison with the breakdown voltage observed in standard Au/n-GaAs structures.

On the basis of our study of the capacitance–voltage characteristics of the Schottky barriers we have found that the presence of the thin LT-GaAs layer containing a system of deep-level point defects and nanoscale arsenic clusters leads to the accumulation in it of charge carriers and the formation of depletion regions in the adjacent n-GaAs layers. In the $C-V$ characteristics at 300 K we have discovered a wide plateau of quasiconstant capacitance. This plateau is most likely due to emission of electrons from the deep levels and arsenic clusters in the LT-GaAs layer. The concentration of accumulated electrons was found to be close to that of the emitted electrons: $\sim 1 \times 10^{12}$ cm^{-2}. At low temperatures (94 K) electron emission has not been observed experimentally.

This work was supported by the Russian Fund for Fundamental Research and by the Russian Ministry of Science (within the context of the programs ''Fullerenes and atomic clusters'' and ''Physics of solid-state nanostructures'').

[1] F. W. Smith, A. R. Calawa, C. L. Chen, M. J. Mantra, and L. J. Mahoney, Electron Dev. Lett. **9**, 77 (1988).

[2] M. Kaminska, Z. Liliental-Weber, T. George, J. B. Kortright, F. W. Smith, B. Y. Tsaur, and A. R. Calawa, Appl. Phys. Lett. **54**, 1831 (1989).

[3] M. R. Melloch, K. Mahalingam, N. Otsuka, J. M. Woodall, and A. C. Warren, J. Cryst. Growth **111**, 39 (1991).

[4] N. A. Bert, A. I. Veĭnger, M. D. Vilisova, S. I. Goloshchanov, I. V. Ivonin, S. V. Kozyrev, A. E. Kunitsyn, L. G. Lavrent'eva, D. I. Lubyshev, V. V. Preobrazhenskiĭ, B. R. Semyagin, V. V. Tret'yakov, V. V. Chaldyshev, and M. P. Yakubenya, Fiz. Tverd. Tela (St. Petersburg) **35**, 2609 (1993) [Phys. Solid State **35**, 1289 (1993)].

[5] J. K. Luo, H. Thomas, D. V. Morgan, D. Westwood, and R. H. Williams, Semicond. Sci. Technol. **9**, 2199 (1994).

[6] P. Blood, Semicond. Sci. Technol. **1**, 7 (1986).

[7] E. R. Brown, K. A. McIntosh, K. B. Nichols, and C. L. Dennis, Appl. Phys. Lett. **66**, 285 (1995).

[8] P. N. Brunkov, S. G. Konnikov, V. M. Ustinov, A. E. Zhukov, A. Yu. Egorov, V. M. Maksimov, N. N. Ledentsov, and P. S. Kop'ev, Fiz. Tekh. Poluprovodn. **30**, 924 (1996) [Semiconductors **30**, 492 (1996)].

[9] P. N. Brounkov, T. Benyattou, and G. Guillot, J. Appl. Phys. **80**, 864 (1996).

[10] K. Kreher, Phys. Status Solidi A **135**, 597 (1993).

[11] D. C. Look, D. C. Walters, M. O. Manasreh, J. R. Sizelove, C. E. Stutz, and K. R. Evans, Phys. Rev. B **42**, 3578 (1990).

[12] H. Fujioka, E. R. Weber, and A. K. Verma, Appl. Phys. Lett. **66**, 2834 (1995).

[13] D. C. Look, Z. Q. Fang, H. Yamamoto, J. R. Sizelove, M. G. Mier, and E. Stutz, J. Appl. Phys. **76**, 1029 (1994).

[14] C. H. Goo, W. S. Lau, T. C. Chong, and L. S. Tan, Appl. Phys. Lett. **69**, 2543 (1996).

[15] T. C. Lin and T. Okumura, Jpn. J. Appl. Phys. **35**, 1630 (1996).

[16] S. Hong, R. Reifenberger, D. B. Janes, D. McInturff, and J. M. Woodal, Appl. Phys. Lett. **68**, 2258 (1996).

[17] J. Gebauer, R. Krause-Rehberg, S. Eichler, M. Luysberg, H. Sohn, and E. R. Weber, Appl. Phys. Lett. **71**, 638 (1997).

[18] P. N. Brounkov, N. N. Faleev, Yu. G. Musikhin, A. A. Suvorova, A. F. Tsatsul'nikov, V. M. Maximov, A. Yu. Egorov, A. E. Zhukov, V. M. Ustinov, N. N. Ledentsov, P. S. Kop'ev, and S. G. Konnikov, Inst. Phys. Conf. Ser. **155** (IOP, Bristol, 1997), p. 841.

Translated by Paul F. Schippnick

SEMICONDUCTORS VOLUME 32, NUMBER 10 OCTOBER 1998

Study of GaN thin layers subjected to high-temperature rapid thermal annealing

N.I. Katsavets

ZAO ''Semiconductor Devices,'' 192281 St. Petersburg, Russia

G. M. Laws, I. Harrison, E. C. Larkins, and T. M. Benson

Department of Electrical and Electronic Engineering, University of Nottingham,
Nottingham NG7 2RD, England

T. S. Cheng and C. T. Foxon

Department of Physics, University of Nottingham, Nottingham NG7 2RD, England

(Submitted February 11, 1998; accepted for publication February 24, 1998)
Fiz. Tekh. Poluprovodn. **32**, 1175–1180 (October 1998)

A detailed study of the effect of rapid thermal annealing in a N_2 or Ar atmosphere on the properties of thin GaN layers grown by molecular-beam epitaxy on sapphire substrates was performed. After rapid thermal annealing, an enhancement of the crystal quality of such films was observed. Low-temperature photoluminescence measurements revealed a substantial increase in impurity recombination near the fundamental absorption edge after a rapid high-temperature anneal in a nitrogen atmosphere. A significant decrease in the impurity photoluminescence of the GaN films with protective SiO_2 coatings was observed following the anneals. © *1998 American Institute of Physics.* [S1063-7826(98)00610-3]

1. INTRODUCTION

Nitrides of group-III elements, in particular, GaN are of significant scientific and practical interest. This interest has to do, first of all, with the possibility of building lasers and photodiodes based on them, which emit in the blue and ultraviolet regions of the spectrum, and also high-temperature electronic devices.[1]

It is known that the optical and electronic properties of GaN films depend substantially not only on their conditions of growth, but also on their post-growth processing. For example, to obtain *p*-type conductivity, Mg-doped GaN layers are subjected to high-temperature annealing. In this case, annealing breaks the H–Mg bonds, which activates the Mg as an acceptor impurity.[2,3]

The authors of Ref. 4 noted an increase in the intensity of the electroluminescence of Mg-doped diodes after subjecting them to a rapid high-temperature anneal (RHTA) at 1150 °C.

A substantial increase in the intensity of the photoluminescence (PL) and an enhancement of the surface morphology after RHTA in a nitrogen atmosphere (N_2) were observed by the authors of Ref. 5, who examined the effect of RHTA on the physical properties of undoped, relatively thick ($\sim 5\ \mu$m) GaN films grown by metallo-organic chemical vapor deposition (MOCVD).

In addition, the successful application of RHTA in the context of ion implantation of dopant impurities into GaN films has been reported in the literature.[6]

Thus, a study of the effect of RHTA on the properties of GaN films (such as their crystal quality, surface morphology, optical properties, etc.) is necessary both for an understanding of the processes occurring during RHTA and to further advance the post-growth technology of fabricating devices based on such films.

In this paper we report the results of an in-depth study of the effect of RHTA in N_2 and in an argon (Ar) atmosphere on the crystallographic and optical properties (surface morphology, crystal quality, photoluminescence) of GaN thin films.

2. SAMPLES AND MEASUREMENT TECHNIQUES

We investigated GaN films with *n*-type conductivity and electron concentration $n \sim 10^{17}\,\mathrm{cm}^{-3}$ and $1\ \mu$m thickness. Such films were grown on sapphire substrates with orientation [0001] using a Varian Modular Gen II MBE setup with a growth rate of $0.3\ \mu$m/h at 700 °C. As the N_2 source we used an Oxford Applied Research CARS 25 source with an RFC discharger at 13.5 MHz. The design of the experimental setup and characteristics of the nitrogen RFC discharger are described in detail in Ref. 7.

RHTA was performed in a quartz reactor at 100 °C for 30 s in a stream of N_2 or Ar. The samples, placed in a silicon holder, were heated by a quartz lamp. Both uncoated GaN films and GaN films coated with protective layers of SiO_2 were investigated. Such layers were deposited by chemical vapor deposition.

A Kimmon He–Cd laser with a lasing wavelength of 325 nm (photon energy 3.815 eV) and maximum optical power about 5 mW was used to excite photoluminescence. The He–Cd laser beam was focused on the sample in a spot about $100\ \mu$m in diameter and was attenuated with the help of neutral glass light-filters as needed. The photoluminescence of the samples was analyzed with the help of a 0.75 Spex monochromator with gap widths equal to 0.2 mm, which provided spectral resolution on the order of 1 meV in the region of the edge photoluminescence, and was recorded with a ‘‘bi-alkali’’ photomultiplier. Signal gain and detection were performed with a standard lock–in amplifier.

For low-temperature photoluminescence measurements we used a special helium cryostat, which provided temperature (T) stabilization in the range from 10 to 300 K with an accuracy of ± 0.5 K.

In the x-ray measurements we recorded the reflection of the Cu $K\alpha_1$ line from the (0002) plane of the GaN samples. Measurements of the x-ray reflection spectra were carried out using two techniques. The first was standard recording of the rocking curves $\varphi(2\theta)$, where the receiver is rotated through the angle 2θ at the same time as the sample is rotated through an angle θ relative to the incident x-ray beam. In this event, the half-width of the reflection spectrum $\Delta 2\theta_{1/2}$ gives information about the spread in the lattice parameter in the GaN film.

Using the second method we measured the angular spectrum of the x-ray reflection from the sample $\varphi(\Omega)$ without varying the orientation of the receiver. In this case, its half-width $\Delta\Omega_{1/2}$ gives information about the misorientation of the crystallites, of which the GaN film is composed.[8]

The surface morphology was investigated with a profilometer which gave an accuracy of measurement of the surface roughness on the order of 1 nm.

TABLE I.

Samples	Position of reflection maximum 2θ, deg	$\Delta 2\theta_{1/2}$, deg	$\Delta\Omega_{1/2}$, deg
Unannealed GaN	34.574	0.099	0.250
GaN, RHTA in N_2	34.563	0.074	0.234
GaN, RHTA in Ar	34.553	0.073	0.228
GaN, with SiO_2, RHTA in N_2	34.566	0.069	0.272

3. EXPERIMENTAL RESULTS AND DISCUSSION

3.1. Effect of RHTA on the crystal quality and surface morphology of GaN

The results of the x-ray studies of GaN films subjected to RHTA under various conditions are listed in Table I.

It is clear from the table that regardless of the conditions of annealing, RHTA leads to a decrease in $\Delta 2\theta_{1/2}$, which suggests an enhancement of crystal quality of the GaN layers; i.e., the spread in the lattice parameter in the epitaxial layer is reduced. At the same time, the narrowing of the x-ray reflection spectra $\varphi(\Omega)$ of the unprotected layers after RHTA suggests a decrease in the misorientation of the crystallites.

However, in the case of RHTA of protected GaN films the misorientation of the crystallites, in contrast, increases

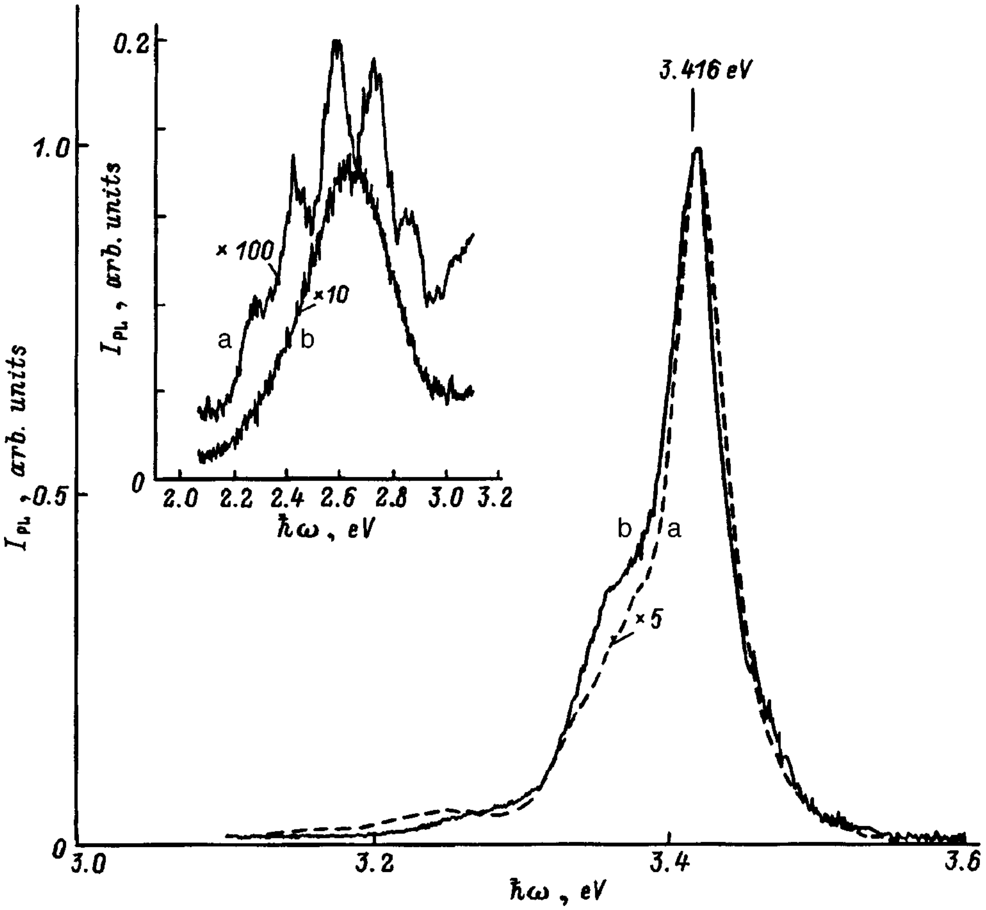

FIG. 1. Photoluminescence spectra of GaN films at room temperature before (a) and after (b) RHTA.

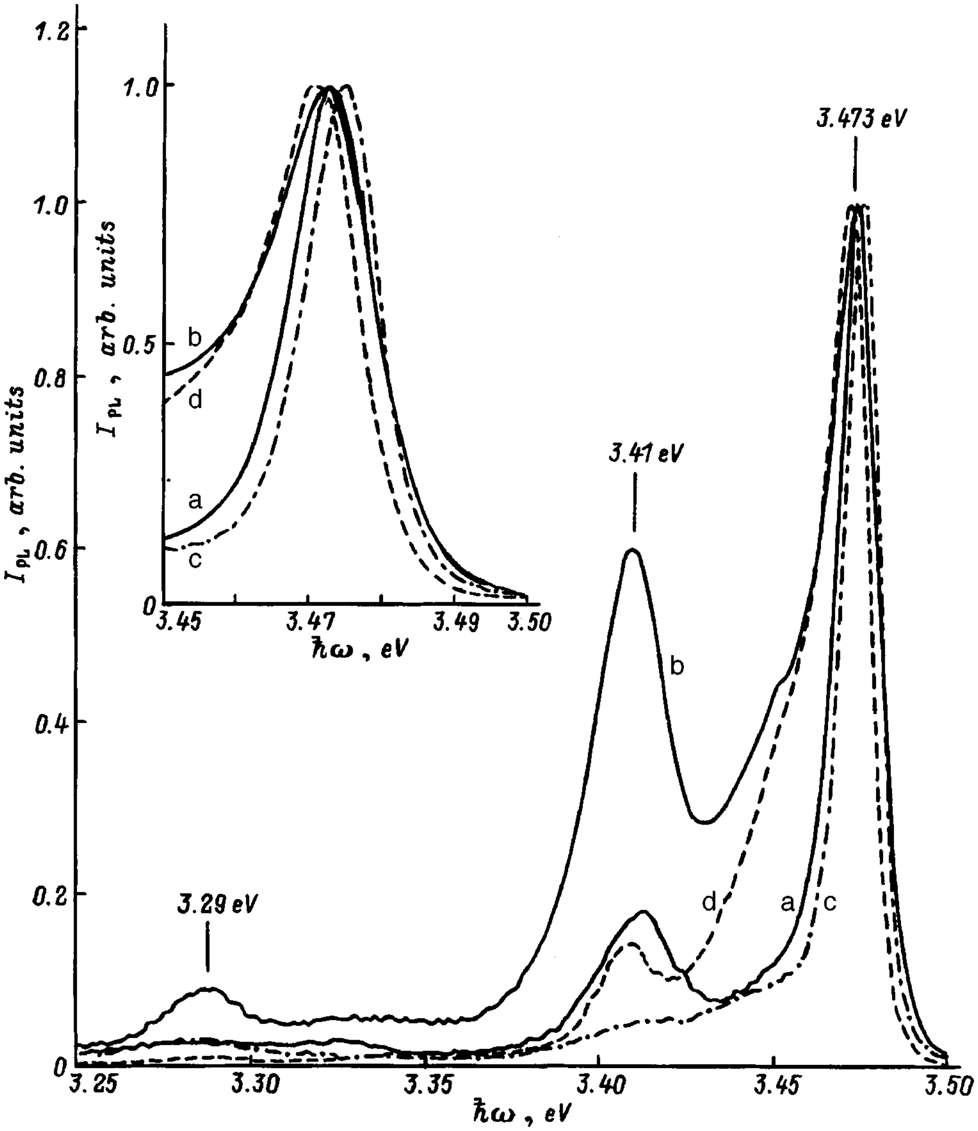

FIG. 2. Low-temperature photoluminescence spectra of the unannealed GaN films (a), of unprotected GaN films after RHTA in a N_2 (b) and in an Ar atmosphere (d), and of GaN films protected by a layer of SiO_2 after RHTA in a N_2 atmosphere (c). $T=10$ K.

($\Delta\Omega_{1/2}$ grows). This is probably due to additional mechanical stresses imposed by the SiO_2 layer.

Photoluminescence studies of unprotected GaN films in N_2 and Ar atmospheres showed that the form of the photoluminescence spectra at room temperature (see Fig. 1) and also the ratio of intensities (I_{PL}) of the edge band and impurity (''yellow'') band change hardly at all (in the investigated GaN films this ratio is $\sim 100{:}1$), but a substantial (more than fivefold) increase in the photoluminescence intensity is observed in the entire spectral range, which is in accord with the data of Ref. 5. The increase in the photoluminescence intensity is accompanied by a disappearance of interference modulation in the ''yellow'' band (see the inset in Fig. 1). Measurements of the surface roughness of the GaN films before and after RHTA showed that RHTA of unprotected samples leads to an increase in surface roughness from 1 to 100 nm.

RHTA of samples protected by a layer of SiO_2 does not lead to an increase in the photoluminescence intensity or to the disappearance of interference modulation of the spectrum in the ''yellow'' band.

It can thus be assumed that the increase in the intensity of the photoluminescence of unprotected GaN films after RHTA is connected with a growth of the external quantum yield due to an increase in the surface roughness.

3.2. Effect of RHTA on low-temperature photoluminescence spectra associated with exciton recombination

At low temperatures ($T=10$ K) the form of the photoluminescence spectrum near the fundamental absorption edge after RHTA is radically altered. The narrow photoluminescence line with energy $\hbar\omega=3.473$ eV and half-width 14 meV (Fig. 2), which is usually attributed to the recombination of excitons localized at a neutral donor (D^0X transitions; Ref. 9) in the case of RHTA of unprotected GaN films in both a N_2 and an Ar atmosphere is substantially broadened (by up to 20 meV) and shifted into the low-energy region of the spectrum by $2-4$ meV (see inset in Fig. 2). In the case of RHTA of unprotected samples, the exciton band is slightly narrowed (to 12 meV) and shifted into the high-energy region of the spectrum by $3-4$ meV.

From an analysis of the photoluminescence and x-ray data it can be assumed that the low-energy shift of the exciton band after RHTA of unprotected samples is due to a decrease in the mechanical stresses in the GaN film associated with misorientation of the crystallites. In contrast, the high-energy shift of the exciton band under RHTA of GaN films with a protective SiO_2 layer is presumably associated with a growth of these mechanical stresses due to an increase in the misorientation of the crystallites.

The change in the width of the D^0X exciton photoluminescence band after RHTA may be connected with the change in the crystal quality of the lattice of the GaN layers after RHTA.[10] However, the width of the D^0X photoluminescence band after RHTA under various external conditions does not correlate with the rocking-curve x-ray data $\varphi(2\theta)$. The explanation for this may lie in the fact that the x-ray measurements contain information about the crystal quality of the entire GaN layer (the x-ray penetration depth in GaN is on the order of 1 μm) while the photoluminescence measurements contain information only about the surface layer [the penetration depth of the exciting radiation and the diffusion length of the nonequilibrium charge carriers in GaN do not exceed 0.25 μm (Ref. 11)].

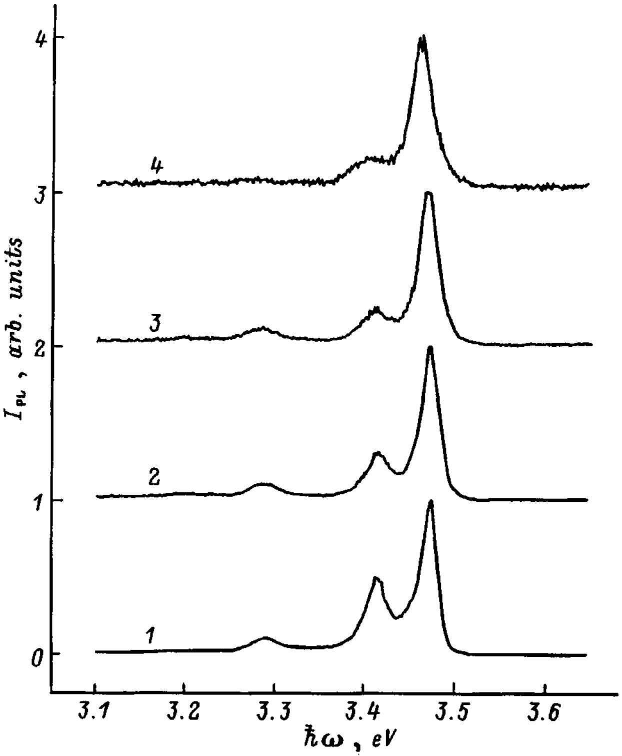

FIG. 3. Temperature dependence of the form of the photoluminescence spectrum of GaN films after RHTA in a N_2 atmosphere. *T*, K: *1* — 10, *2* — 50, *3* — 100, *4* — 150.

3.3. Effect of RHTA on low-temperature photoluminescence in the impurity region of the spectrum near the fundamental absorption edge

RHTA of GaN samples leads to a radical change in the form of the photoluminescence in the impurity region of the spectrum at low temperatures.

In the case of unprotected GaN films, RHTA in N_2 causes an abrupt increase (by more than a factor of 3) of the maximum in the region of 3.41 eV and an additional maximum in the region of 3.29 eV (see Fig. 2, curve *b*). This effect is not observed after RHTA of GaN films with the protective SiO_2 coating (see Fig. 2, curve *c*). In the latter case the maximum in the region of 3.41 eV has almost disappeared and the additional maximum is not seen.

RHTA of unprotected samples in an Ar atmosphere also does not lead to an increase in the maximum in the region of 3.41 eV and the appearance of an additional maximum in the region of 3.29 eV (see Fig. 2, curve *d*).

To elucidate the nature of the photoluminescence bands with maxima at $\hbar\omega=3.41$ and 3.29 eV we carried out an additional study of the dependence of these bands on the temperature (see Fig. 3) and the photoexcitation intensity (see Fig. 4). The abrupt temperature dependence (the bands almost disappear at 150 K), the sublinear character of variation of the photoluminescence intensity, and the shift of the maxima toward higher energies with increase of the photoexcitation intensity indicate that these levels are of the impurity type.

Previously, in the low-temperature spectra of GaN a maximum was observed in the region of 3.42 eV, which has usually been linked with recombination of free holes with electrons localized at donor levels due to the presence of oxygen.[12,13] It can thus be assumed that the abrupt growth of the photoluminescence line in the region of 3.41 eV after RHTA in a N_2 atmosphere is due to the presence of water vapor as the oxygen source. The invariability of the intensity of these lines after RHTA in an Ar atmosphere can then be attributed to a higher purity of Ar. However, the above-expressed supposition cannot explain the disappearance of the photoluminescence line in the region of 3.41 eV after RHTA of GaN films which are protected by a SiO_2 coating. Thus, in our opinion, the nature of this line is still unclear and requires further study.

The low-temperature photoluminescence line in the region of 3.287 eV is usually linked with the second-order phonon echo of the exciton D^0X band (the LO_{x2} transition).[14] However, in this case the behavior of the photoluminescence line with variation of the sample temperature and photoexcitation intensity should correlate with the behavior of the D^0X band itself, which is not confirmed by our experiments.

Apparently, the maximum in the region of 3.29 eV is associated with recombination of nonequilibrium electrons with holes localized at acceptor levels, as was observed by the authors of Ref. 15. Thus, the appearance of a maximum in the region of 3.29 eV after RHTA of unprotected GaN films in a N_2 atmosphere may be caused by an increase in the concentration of acceptor levels. This assumption accords with the results of Ref. 5, whose authors observed a decrease of the free electron concentration as a result of RHTA in a N_2 atmosphere.

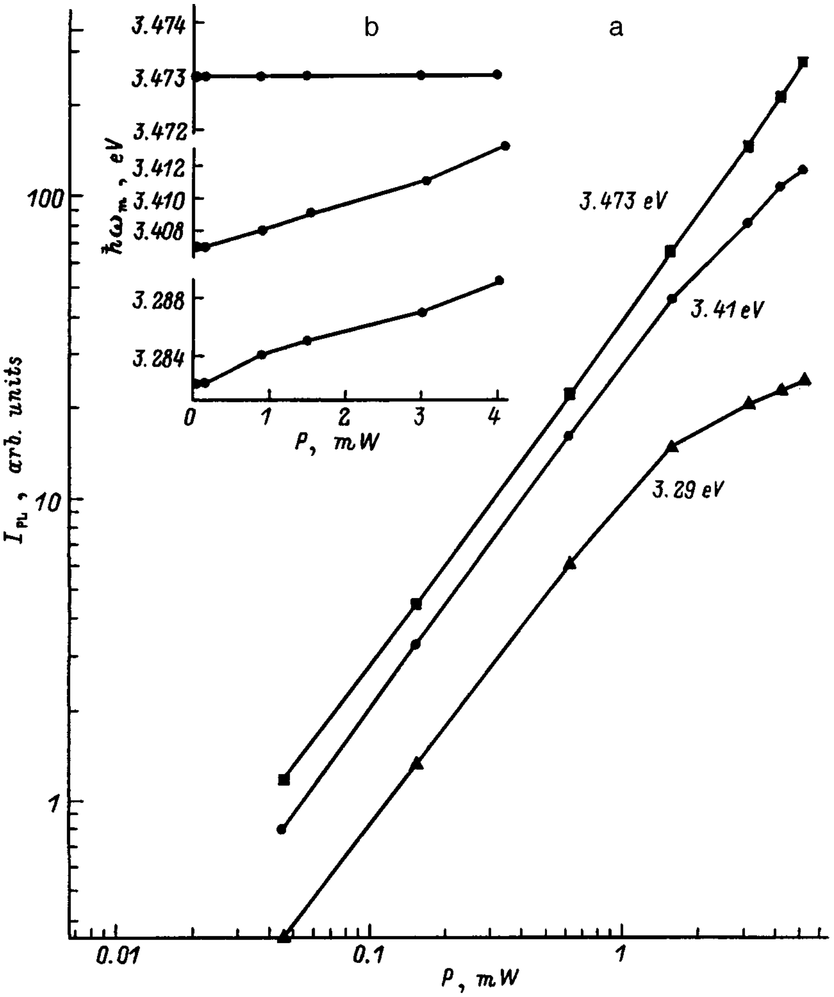

FIG. 4. Dependence of the intensity (I_{PL}) (a) and position ($\hbar\omega_m$) (b) of the photoluminescence lines on the photoexcitation intensity (P).

4. CONCLUSIONS

On the basis of the results of our experimental studies we can thus draw the following conclusions:

1. RHTA of GaN films in both a nitrogen and an argon atmosphere leads to an improvement of their crystal quality (the spread in the lattice constant is decreased).

2. RHTA of unprotected GaN samples leads to a decrease in the misorientation of the crystallites of which the GaN film is composed. In the case of RHTA of GaN films protected by a layer of SiO_2, on the other hand, the misorientation of the crystallites is increased. This increase is probably due to the appearance of additional mechanical stresses.

3. RHTA of unprotected GaN samples leads to an abrupt (by more than a factor of 5) growth of the photoluminescence intensity over the entire spectral range. This is apparently connected with an increase of the external quantum yield caused by a growth of surface roughness of the samples. In the case of a GaN layer with a protective SiO_2 film, the surface roughness does not vary even in the smallest amount, and an increase in the photoluminescence intensity is not observed.

4. The low-temperature photoluminescence spectra near the fundamental absorption edge of GaN samples after RHTA varies considerably:

a) a broadening of the D^0X exciton band is observed, along with a low-energy shift by $2-4$ meV in the case of RHTA of unprotected GaN films, and a moderate narrowing and high-energy shift by $3-4$ eV in the case of GaN films protected by a layer of SiO_2;

b) RHTA of unprotected GaN films in a N_2 atmosphere leads to a substantial increase in the intensity of impurity radiative transitions near the fundamental absorption edge, while RHTA of samples protected by a layer of SiO_2 leads to a significant decrease; no effect of RHTA on the impurity transitions was observed in an Ar atmosphere.

The present work was partly supported by the Royal Society, which provided financial support for a scientific visit of N. I. Katsavets to the University of Nottingham, and by the Russian Fund for Fundamental Research (Grant No. 96-02-17203).

We would like to thank D. M. Demidov and A. V. Andrianov for a helpful discussion of the experimental results.

[1] S. Stripe and H. Mocros, J. Vac. Sci. Technol. B **10**, 1237 (1992).
[2] H. Amano, M. Kito, K. Hiramatsu, and I. Akasaki, Jpn. J. Appl. Phys. **28**, L2112 (1989).
[3] S. Nakamura, T. Mukai, M. Senoh, and N. Iwasa, Jpn. J. Appl. Phys. **31**, L139 (1992).
[4] M. A. Khan, Q. Chen, R. A. Skogman, and J. N. Kuznia, Appl. Phys. Lett. **66**, 2046 (1995).

[5] J. C. Zolper, M. H. Crawford, A. J. Howard, J. Rames, and S. D. Hersee, Appl. Phys. Lett. **68**, 200 (1996).

[6] J. C. Zolper, H. H. Tan, J. S. Williams, J. Zou, D. J. Cockayne, S. J. Pearton, M. H. Crawford, and R. E. Karlicek, Appl. Phys. Lett. **70**, 2729 (1997).

[7] T. S. Cheng, L. C. Jenkins, S. E. Hooper, C. T. Foxon, J. W. Orton, and D. E. Lacklison, Appl. Phys. Lett. **66**, 1509 (1995).

[8] F. A. Ponce, MRS Internet Journal of Nitride Semiconductor Research, **2**, 51 (1997).

[9] J. Mennger, U. Jahn, O. Brandt, H. Yang, and K. Ploog, Phys. Rev. B **53**, 1881 (1996).

[10] E. I. Rashba and M. D. Sturge, *Excitons* (North-Holland, Amsterdam, 1981), p. 865.

[11] S. J. Rosher, E. G. Carr, M. J. Ludwise, G. Girolami, and M. I. Ericson, Appl. Phys. Lett. **70**, 420 (1997).

[12] B. C. Chung and M. Gershenzon, J. Appl. Phys. **72**, 651 (1992).

[13] A. V. Andrianov, D. E. Lacklison, J. W. Orton, D. J. Dewshir, S. E. Hooper, and C. T. Foxon, Semicond. Sci. Technol. **11**, 366 (1996).

[14] R. Dingle, D. D. Sell, S. E. Stokowski, and M. Ilegems, Phys. Rev. B **4**, 1211 (1971).

[15] R. Dingle and M. Ilegems, Solid State Commun. **9**, 175 (1971).

Translated by Paul F. Schippnick

SEMICONDUCTORS VOLUME 32, NUMBER 10 OCTOBER 1998

Nitrogen divacancies — the possible cause of the ''yellow band'' in the luminescence spectra of GaN

A. É. Yunovich*)

M. V. Lomonosov Moscow State University, Department of Physics, 119899 Moscow, Russia

(Submitted March 6, 1998; accepted for publication March 12, 1998)
Fiz. Tekh. Poluprovodn. **32**, 1181–1183 (October 1998)

A strong analogy is demonstrated between the well-known impurity complex NN_1 in GaP consisting of a pair of nearest-neighbor isovalent nitrogen impurity atoms in the nitrogen-doped gallium phosphide lattice (GaP : N), and the divacancy complex of nearest-neighbor vacancies in the nitrogen sublattice of gallium nitride. This divacancy or complexes of this divacancy with impurities may be the cause of the ''yellow band'' in the luminescence spectra of GaN. This work was presented at a session of the Electrochemical Society (Paris, September 1997 by A. E. Yunovich, in *Proceedings of the Second Symposium on III-V Nitride Materials and Processes,* Electrochemical Society (Pennington, New Jersey, 1998), Vol. 98-02, p. 258. © *1998 American Institute of Physics.* [S1063-7826(98)00710-8]

One of the unresolved problems in the luminescence spectra of gallium nitride is the origin of the so-called ''yellow band'' (see Refs. 2 and 3) and the references cited there). This band has a spectral maximum near 2.1−2.2 eV and predominates in the luminescence of imperfect GaN crystals. It is associated with some native defects or their complexes in the GaN lattice. The theory of native point defects in GaN was considered in Ref. 4. The experimental data on structural defects in GaN were analyzed in Ref. 5. The absence of the yellow band or its low intensity relative to the main blue edge band in the spectra is usually taken as a criterion of perfection of GaN crystals and epitaxial films. However, the microscopic nature of this spectral band is not yet understood.

The luminescence spectra of heavily nitrogen-doped gallium phosphide, GaP : N, were investigated in detail in the 1960s and 1970s (see Ref. 6 and the references cited there). The properties of the solid solutions $GaP_{1-x}N_x$ were recently investigated in Ref. 7.

The bright luminescence line with maximum at 2.18 eV and intense phonon echoes is clearly distinguished in the GaP : N spectra at temperatures below $T=77$ K and can be seen up to $T=300$ K (Fig. 1). It has been identified with recombination of the exciton bound in the complex NN_1 of nearest-neighbor isovalent atoms of the N impurity. These atoms replace P atoms at neighboring sites of the anion sublattice of the GaP sphalerite structure.[8] In Ref. 9 it was shown that the external quantum yield in the NN_1 emission band for GaP : N photodiodes reaches 27% at $T=60$ K for currents on the order of 1 μA. Thus, the probability for the recombination of an exciton bound in a NN_1 complex is very high.

We represent the structure of the NN_1 complex as follows (Fig. 2). The central Ga atom has four neighboring atoms at the sites of a deformed tetrahedron—two N atoms and two P atoms. Each of the four atoms has three more tetrahedrally coordinated Ga atoms surrounding it. This entire complex is surrounded by the GaP sphalerite lattice with width of the band gap $E_g(\mathrm{GaP})=2.3$ eV. The presence of N atoms lowers the mass of the complex of 17 atoms relative to the mass of the 17 analogous atoms in an ideal GaP lattice.

Let there be N vacancies (V_N) in the GaN lattice and let complexes of two nearest-neighbor vacancies be possible. We represent the structure of the complex (a divacancy) in the following way (Fig. 2). The central Ga atom has four neighboring atoms at the sites of a deformed tetrahedron, two N atoms and two V_N vacancies (instead of two P atoms). Each of these four sites has three more tetrahedrally coordinated Ga atoms surrounding it. The complex is surrounded by a GaN würzite lattice with $E_g(\mathrm{GaN})=3.4$ eV.

Two of the vacancies are neutral, the same as with the P atoms in the preceding case. The presence of vacancies lowers the mass of the complex relative to the mass of the 17 analogous atoms in an ideal GaN lattice. The analogy between the two complexes is easily visualized. Figure 1 shows spectra of the yellow band of the GaN luminescence,[10,11] together with the luminescence spectrum of the NN_1 lines in GaP : N; the rather wide band is broadened by the electron–phonon interaction.

There are sufficient reasons to assume that the reason for the appearance of the yellow band is recombination of excitons bound in the complex of nitrogen divacancies in GaN. It would be very interesting to validate this model by theoretical calculations and various experiments.

In favor of this model we cite several well-known facts about the formation of nitrogen vacancies and evaporation–escape from the lattice of N_2 molecules during heat treatments of GaN (see the original papers of J. Pankove *et al.*[12] and the more recently published papers (Refs. 13 and 14). Of course, the formation of divacancies is possible at high concentrations of single vacancies. It is possible that their formation is energetically more favorable than formation of isolated vacancies. This assumption is in line with the recently

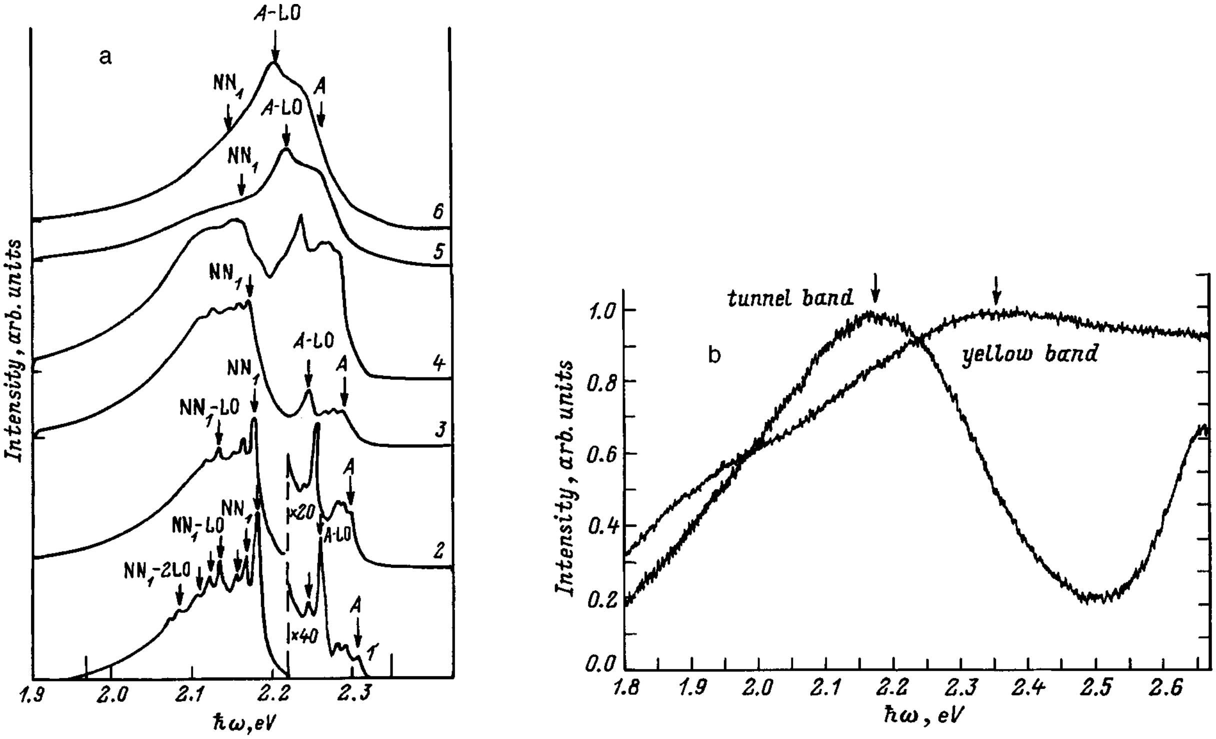

FIG. 1. a — Electroluminescence spectra of GaP : N, in which the NN_1 bands predominate;[6,9] T, K: *1* — 83, *2* — 120, *3* — 160, *4* — 200, *5* — 250, *6* — 293; $I = 10$ mA. b — electroluminescence spectra of GaN manifesting the yellow band for direct currents in the tunnel emission region[10] and under conditions of ionization breakdown.[11]

published calculations of the probability for the formation of pairs of vacancies in GaN (Ref. 15).

In a real crystal divacancies can be filled either by atoms of the main lattice, with formation of Ga_N antisite defects, or by impurities. In particular, they can be filled by neutral donor–acceptor pairs. It is not clear what the charge state of the complexes is under various conditions of doping, compensation, and excitation. In Ref. 16 it was suggested that Ga_N antisite defects and the oxygen impurity participate in the formation of the yellow band. The answers to these questions require detailed study.

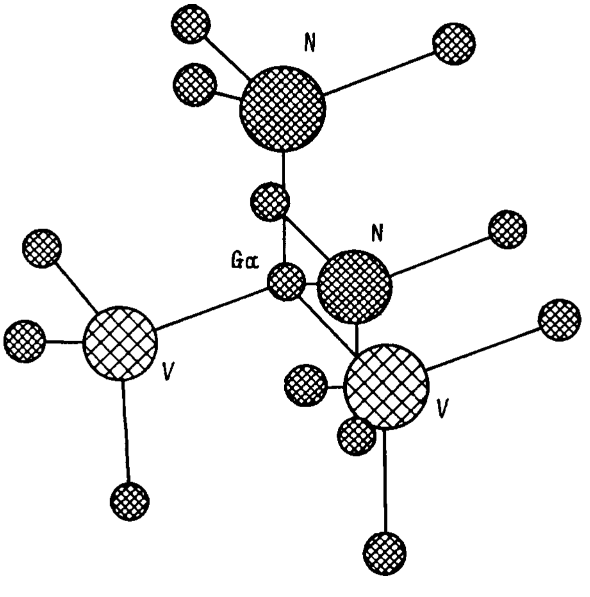

FIG. 2. Model of a cluster of 15 atoms + 2 nitrogen vacancies which forms a complex (divacancy) in the GaN lattice analogous to a cluster of 17 atoms which forms the NN_1 complex in GaP : N.

In summary, the considered analogy between a complex consisting of a pair of nearest-neighbor isovalent nitrogen impurities in GaP : N and a complex of nitrogen divacancies in GaN, and also the luminescence spectra of these materials suggest nitrogen divacancies and/or complexes of nitrogen divacancies with impurities in GaN as a possible reason for the yellow band in the luminescence spectra of GaN. To validate this model, it would be advantageous to perform theoretical calculations of the energy spectrum of complexes of 17 atoms surrounded by a GaP or GaN lattice.

*)E-mail: yunovich@scon175.phys.msu.su

---

[1] A. E. Yunovich, in *Proceedings of the Second Symposium on III–V Nitride Materials and Processes*, Electrochemical Society (Pennington, New Jersey, 1998), Vol. 98-02, p. 258.

[2] D. M. Hoffmann, D. Kovalev, G. Steude, D. Volm, B. K. Meyer, C. Xavier, T. Monteiro, E. Pereira, E. Mokhov, H. Amano, and I. Akasaki, MRS Symp. Proceedings **395**, 619 (1996).

[3] E. R. Glaser, T. A. Kennedy, S. W. Brown, J. A. Freitas, Jr., W. G. Perry, M. D. Bremser, T. W. Weeks, and R. F. Davis, MRS Symp. Proceedings **395**, 667 (1996).

[4] J. Neugebauer and C. G. Van de Walle, Phys. Rev. B **50**, 8067 (1994).

[5] Z. Liliental-Weber, S. Ruvimov, Ch. Kisielovski, Y. Chen, W. Swider, J. Washburn, N. Newman, A. Gassman, X. Liu, I. Schloss, E.R. Weber, I. Grzegory, M. Bockovski, J. Jun, T. Suski, K. Pakula, J. Baranovski, S. Porovski, H. Amano, and T. Akasaki, MRS Symp. Proceedings **395**, 351 (1996).

[6] A. É. Yunovich, in *Radiative Recombination in Semiconductors* (Mir, Moscow, 1972), p. 234.
[7] K. Onabe, MRS Symp. Proceedings **449**, 23 (1997).
[8] J. J. Hopfield, P. J. Dean, and D. G. Thomas, Phys. Rev. **158**, 748 (1967).
[9] É. Yu. Barinova, L. M. Kogan, O. B. Nevskiĭ, N. R. Nurtdinov, O. P. Nurtdinova, I. T. Rassokhin, and A. É. Yunovich, Pis'ma Zh. Tekh. Fiz. **5**, 1381 (1979) [Sov. Tech. Phys. Lett. **5**, 581 (1979)]; A. E. Yunovich, in *Proceedings Conference on Radiative Recombination in* A^3B^5 (Prague, 1979), p. 139.
[10] V. E. Kudryashov, K. G. Zolina, A. N. Kovalev, F. I. Manyakhin, A. N. Turkin, and A. É. Yunovich, Fiz. Tekh. Poluprovodn. **31**, 1304 (1997) [Semiconductors **31**, 1123 (1997)].
[11] A. N. Kovalev, F. I. Manyakhin, A. N. Kovalev, V. E. Kudryashov, A. N. Turkin, and A. É. Yunovich, Fiz. Tekh. Poluprovodn. **32**, 63 (1998) [Semiconductors **32**, 54 (1998)].
[12] J. I. Pankove, E. Miller, and J. E. Berkeyheiser, J. Lumin. **5**, 84, 482 (1972).
[13] C. Vartuli, S. J. Pearton, C. R. Abernathy *et al.*, J. Vac. Sci. Technol. B **14**, 2523 (1996).
[14] J. Leitner, J. Steikal, and P. Vonka, Mater. Lett. **28**, 197 (1996).
[15] D. Boucher and Z. Gal, in *Abstracts of the MRS Fall Meeting 1997* (Boston, 1997), Abstract D15.3.
[16] V. S. Vavilov, I. F. Chetverikova, M. V. Chukichev, in *Proceedings of the International Conference on Deep-Level Centers in Semiconductors* [in Russian] (Ulyanovsk, 1997), p. 114.

Translated by Paul F. Schippnick

SEMICONDUCTORS VOLUME 32, NUMBER 10 OCTOBER 1998

A new recombination center in heavily doped GaAs : Zn grown by liquid-phase epitaxy

K. S. Zhuravlev, T. S. Shamirzaev,*) N. A. Yakusheva, and I. P. Petrenko

Institute of Semiconductor Physics, Siberian Branch of the Russian Academy of Sciences,
630090 Novosibirsk, Russia

(Submitted January 12, 1998; accepted for publication March 17, 1998)
Fiz. Tekh. Poluprovodn. **32**, 1184–1189 (October 1998)

The photoluminescence properties of *p*-GaAs : Zn (100) layers grown by liquid-phase epitaxy from gallium and bismuth melts at various temperatures have been studied. It is shown that a novel radiative recombination center is formed in these layers. The concentration of the centers increases with the doping level in proportion to the concentration of free holes raised to the power 5.35 ± 0.1. The exponent is independent of the growth melt (gallium or bismuth) and the growth temperature. It is found that the center is a neutral complex consisting of an antisite defect of gallium at an arsenic site and two arsenic vacancies. © *1998 American Institute of Physics.* [S1063-7826(98)00810-2]

INTRODUCTION

Epitaxial layers of heavily zinc-doped gallium arsenide are widely used in the fabrication of photocathodes with negative electron affinity and in the base layers of heterobipolar transistors (HBT).[1,2]

To improve the main characteristics of HBT's—the limiting frequency of the combined gain f_T and maximum frequency of generation $f_{\max}$, it is necessary to increase the conductivity of the base layer, which is achieved by raising the doping level of the latter. It is well known, however, that raising the doping level in *p*-GaAs can lead to the formation of defects[3] which, being recombination centers, shorten the lifetime of the nonequilibrium charge carriers. As a result, the transmission coefficient of the HBT is lowered along with the characteristic frequencies f_T and $f_{\max}$.[1]

Our goal was to identify the recombination centers formed in GaAs as a result of heavy zinc doping. Accordingly, we investigated the photoluminescence (PL) of GaAs : Zn layers prepared by liquid-phase epitaxy (LPE) from gallium and bismuth melts.

EXPERIMENTAL PROCEDURE

Layers were grown on substrates of semi-insulating GaAs (100) in two temperature intervals: from 708 to 650 °C and from 800 to 750 °C.1) The thickness of the layers was $10-15\,\mu$m. The hole concentration (p) at room temperature, measured by the van-der-Pauw method (Hall factor was assumed to be unity), varied from $6\times10^{17}\,\text{cm}^{-3}$ to $2\times10^{19}\,\text{cm}^{-3}$ in layers grown from a gallium melt, and from $7\times10^{17}\,\text{cm}^{-3}$ to $7\times10^{19}\,\text{cm}^{-3}$ in layers grown from a bismuth melt. Details of the growth technique and electrical properties of the layers are given in Ref. 4. The dependence of the concentration of zinc atoms in the investigated layers on the doping level was determined by secondary-ion mass spectroscopy (SIMS) on a Riber LAS-3000 setup equipped with a quadrupole mass-spectrometer with resolution $M/\Delta M=2.1M$. The samples were etched using O_2^+ ions with an energy of 10 keV. The concentration of zinc atoms was determined from the ratio of the intensities of the secondary ion fluxes ${}^{64}\text{Zn}^+/{}^{75}\text{As}^+$. The measurements were averaged over a layer with dimensions $\sim0.5\times0.5\,\text{mm}^2$ and thickness ~1000 Å.

Stationary photoluminescence was measured in the wavelength range $0.78-1.0\,\mu$m on a setup assembled from an SDL-1 double monochromator having gratings with 600 rulings/mm. Photoluminescence was recorded by a photomultiplier with an *S*1, photocathode operating in the photon counting regime. To excite photoluminescence, we used an Ar^+ laser with wavelength 5145 Å and power density $30\,\text{w/cm}^2$.

EXPERIMENTAL RESULTS

Figure 1 shows photoluminescence spectra of GaAs : Zn layers with various hole concentrations, grown at $T_G=800\,°\text{C}$ from a gallium melt, measured at 77 K. In all of the spectra the band–acceptor recombination line (B) dominates. A shoulder is observed in the long-wavelength limb of the B line, which becomes more pronounced as the doping level is increased, and in a layer with $p=1.8\times10^{19}\,\text{cm}^{-3}$ transforms into a line with Gaussian shape and maximum at 1.35 eV, denoted in the figure as line C. The energy position of this line is close to that of the line due to transitions through the levels of the deep acceptor associated with copper (e, Cu).[5] The abrupt growth of the intensity of the C line as the doping level is raised from $7.6\times10^{18}\,\text{cm}^{-3}$ to $1.8\times10^{19}\,\text{cm}^{-3}$ and the absence of the phonon echoes characteristic of the (e, Cu) line, however, are surprising.[5]

To identify the C line we measured at various temperatures the photoluminescence spectra of a layer with hole concentration $p=2\times10^{19}\,\text{cm}^{-3}$, in which this line is quite pronounced. The spectra are shown in Fig. 2. It can be seen that as the temperature is raised from 300 to 190 K, the position of the maximum of the C line varies hardly at all, in contrast to the position of the (e, Cu) line, which varies by more than 20 meV in this temperature interval.[5] In addition, the activation energy of quenching of the C line, found from the tem-

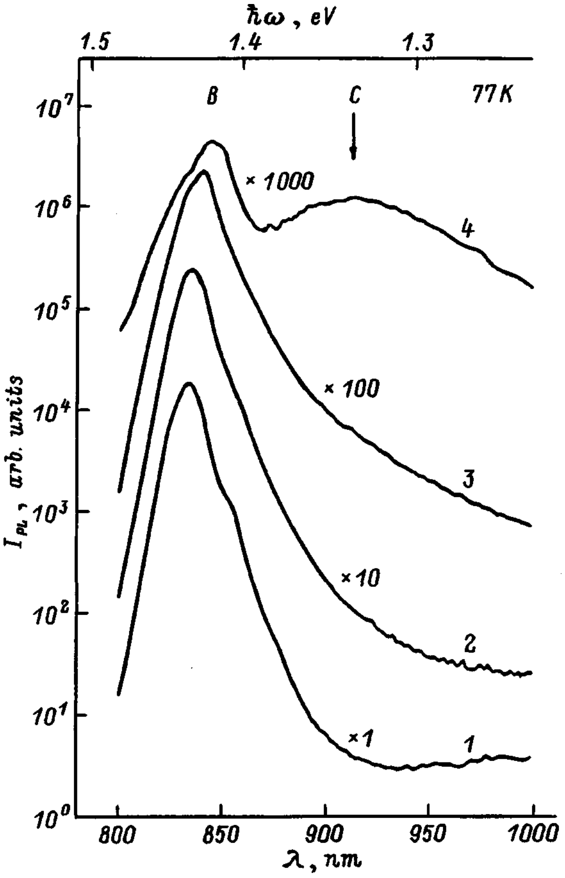

FIG. 1. Photoluminescence spectra of GaAs : Zn layers grown at $T_G = 800\,°\mathrm{C}$ from a gallium melt. Measurement temperature 77 K. Hole concentration in the layers: *1* — $6.0\times10^{17}\,\mathrm{cm}^{-3}$, *2* — $2.2\times10^{18}\,\mathrm{cm}^{-3}$, *3* — $7.6\times10^{18}\,\mathrm{cm}^{-3}$, *4* — $1.8\times10^{19}\,\mathrm{cm}^{-3}$.

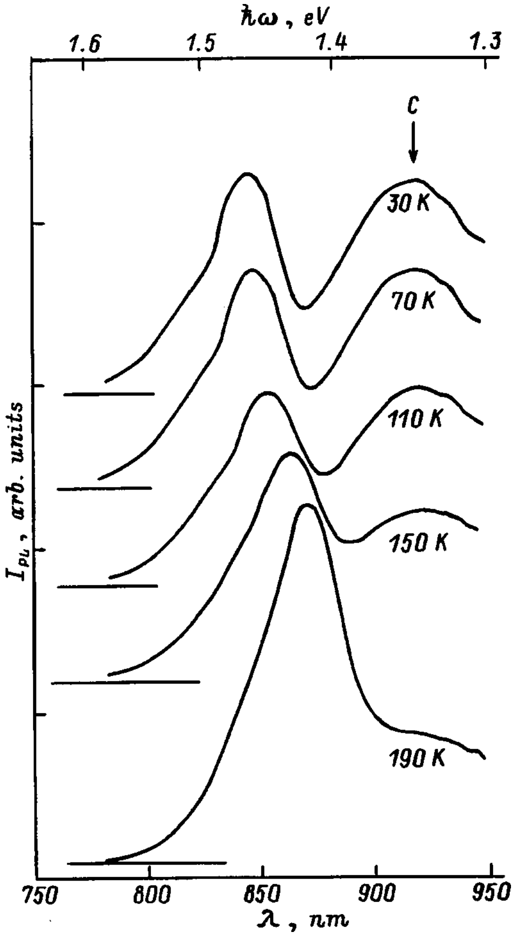

FIG. 2. Photoluminescence spectra of a layer with $p = 2\times10^{19}\,\mathrm{cm}^{-3}$, measured at various temperatures.

perature dependence of the total intensity[2)] which is plotted in Fig. 3, is equal to 41 ± 2 meV, which is much less than the activation energy of quenching of the (e, Cu) line which is equal to 140 meV (Ref. 5).

Thus, the temperature dependence of the position of the *C* line and the activation energy of its temperature quenching indicate that this line is not associated with copper, but is due to recombination through levels of an unknown center formed in GaAs : Zn at high doping levels, which we have denoted as the *R* center.

Figure 4 shows photoluminescence spectra measured at 77 K of layers with nearly the same hole concentration, grown from a gallium melt ($p = 1.8\times10^{19}\,\mathrm{cm}^{-3}$) and a bismuth melt ($p = 2.1\times10^{19}\,\mathrm{cm}^{-3}$) at $T_G = 800\,°\mathrm{C}$. It can be seen that the intensity of the *C* line is higher in the layer grown from the gallium melt. At the same time, lowering the epitaxy temperature from $T_G = 800\,°\mathrm{C}$ to $T_G = 708\,°\mathrm{C}$ does not lead to any changes in the shape of the photoluminescence spectra of layers with the same doping level grown from either the gallium melt or the bismuth melt.

To determine the connection between the intensity of the *C* line and the concentration of the *R* centers, we calculated the ratio of the total intensity of the *C* line (I_C) to the total intensity of the *B* line (I_B) at 77 K, $S = I_C/I_B$, in layers with various doping levels. Since the fraction of nonequilibrium charge carriers that recombine through levels of centers is proportional to their concentration, the ratio *S* is proportional to the ratio of the concentrations of the recombination centers:[7,8]

$$S = a(N_R/N_A). \tag{1}$$

Here N_R and N_A are the concentrations of the *R* centers and shallow acceptors, and a is a factor which cannot be deter-

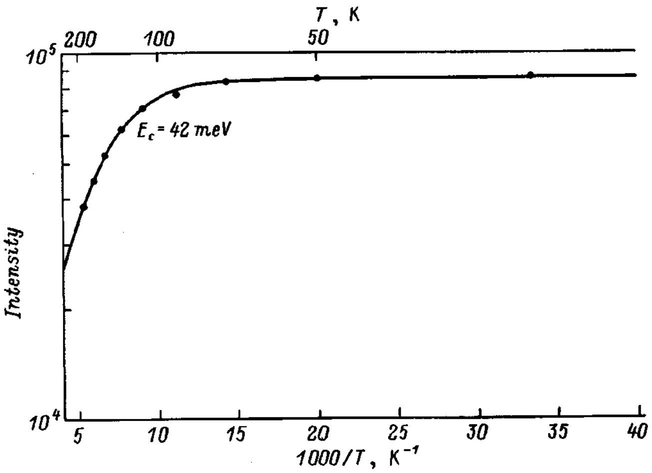

FIG. 3. Temperature dependence of the total intensity of the *C* line in a layer with $p = 2\times10^{19}\,\mathrm{cm}^{-3}$.

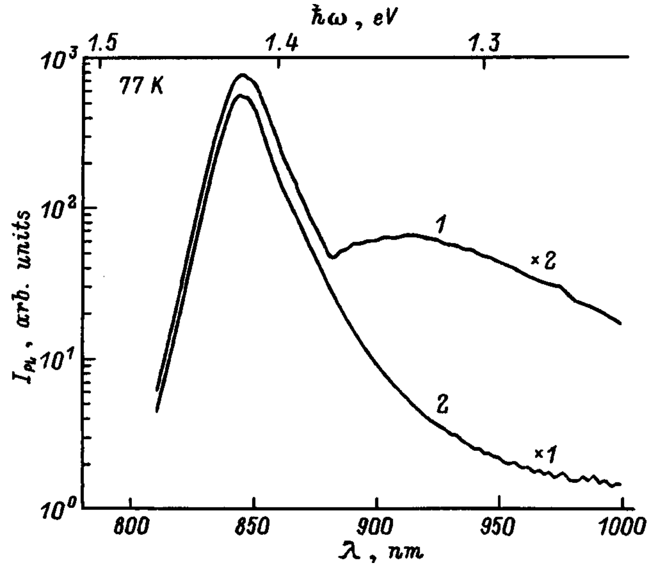

FIG. 4. Photoluminescence spectra of layers grown at $T_G = 800\,°\mathrm{C}$: *1* — from a gallium melt with $p = 1.8\times10^{19}\,\mathrm{cm}^{-3}$, *2* — from a bismuth melt with $p = 2.1\times10^{19}\,\mathrm{cm}^{-3}$.

mined from the available data. We assumed that this factor is independent of the doping level. To ensure that this condition is satisfied, we measured the photoluminescence spectra at a sufficiently low power density of the exciting radiation that the intensity of the photoluminescence lines is proportional to the excitation intensity.

The dependence of *S* on the hole concentration for layers grown from gallium and bismuth melts is plotted in Fig. 5 for two different temperatures. The solid lines are fits to these dependences by functions of the form

$$Y = b\cdot p^{\gamma}. \tag{2}$$

Figure 5 shows that *S* is essentially independent of the hole concentration at low doping levels, and that it increases rapidly with slope $\gamma = 4.45 \pm 0.1$ (of the log–log plot), which does not depend on the growth conditions of the layers, when the hole concentration exceeds a critical value p_{cr} equal to $5\times10^{18}\,\mathrm{cm}^{-3}$ for the layers grown from the gallium melt, and $1\times10^{19}\,\mathrm{cm}^{-3}$ for the layers grown from the bismuth melt.[3)] The value of the coefficient *b* also does not depend on the epitaxy temperature and is equal to $1\times10^{-11}\pm10$ and $8\times10^{-13}\pm10\%$ for layers grown from gallium and bismuth melts, respectively. Consequently, changing the metal–solvent (replacing gallium by bismuth) leads to a decrease in N_R by more than an order of magnitude in the layers with hole concentration exceeding $1\times10^{19}\,\mathrm{cm}^{-3}$.

Using relations (1) and (2), we obtain the functional dependence of the *R*-center concentration on the doping level in layers with $p > p_{cr}$:

$$N_R = (N_A\cdot S)/a \approx (b/a)N_A\cdot p^{\gamma}. \tag{3}$$

Figure 6 plots the ratio of fluxes of ionized zinc and arsenic atoms obtained by SIMS, which is proportional to the concentration of zinc atoms (N_{Zn}),[10] versus doping level for layers grown from a bismuth melt at $T_G = 800\,°\mathrm{C}$. It can be seen that within the limits of accuracy of the determination of N_{Zn} the hole concentration increases linearly with increasing concentration of zinc atoms; consequently, we can assume that

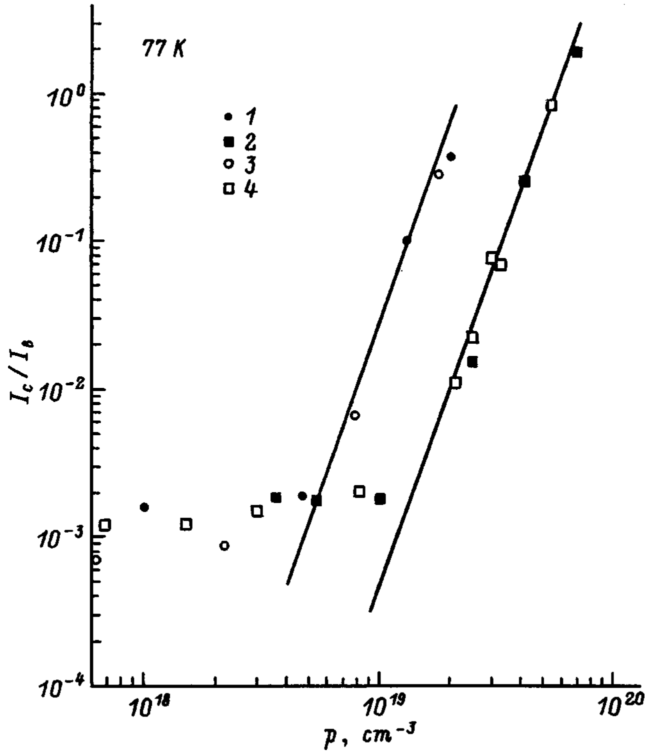

FIG. 5. Dependence of the relative total intensity of the *C* band on the hole concentration for layers grown from a gallium melt (*1, 2*) and a bismuth melt (*3, 4*) at two different temperatures: *1, 3* —$T_G = 708\,°\mathrm{C}$, *2, 4* — $T_G = 800\,°\mathrm{C}$.

$$p \sim N_{\mathrm{Zn}} \sim N_A, \tag{4}$$

and we can write Eq. (3) in the form

$$N_R \sim (b/a)p^{\gamma+1} \sim (b/a)(N_{\mathrm{Zn}})^{\gamma+1}. \tag{5}$$

Using the value of the exponent $\gamma = 4.35$, we find that in layers with $p > p_{cr}$ grown from gallium and bismuth melts the *R*-center concentration for the growth temperatures used by us is proportional to the hole concentration raised to the power 5.35.

DISCUSSION

The power-law dependence of the *R*-center concentration on the doping level indicates that this center has a complicated makeup and is probably a complex consisting of native point defects (PD), whose concentration, as we know, increases with doping level.[11] Such complexes can also include atoms of the dopant impurity;[12] however, in the investigated layers the hole concentration depends linearly on the concentration of zinc atoms over the entire range of doping levels examined, and this fact indicates that the impurity atoms form simple substitution acceptors and do not enter into the composition of the complex responsible for the *R* center.

To determine the possible composition of the *R* center, we analyzed data on the variation of the *R*-center concentration as a function of the growth temperature, doping level,

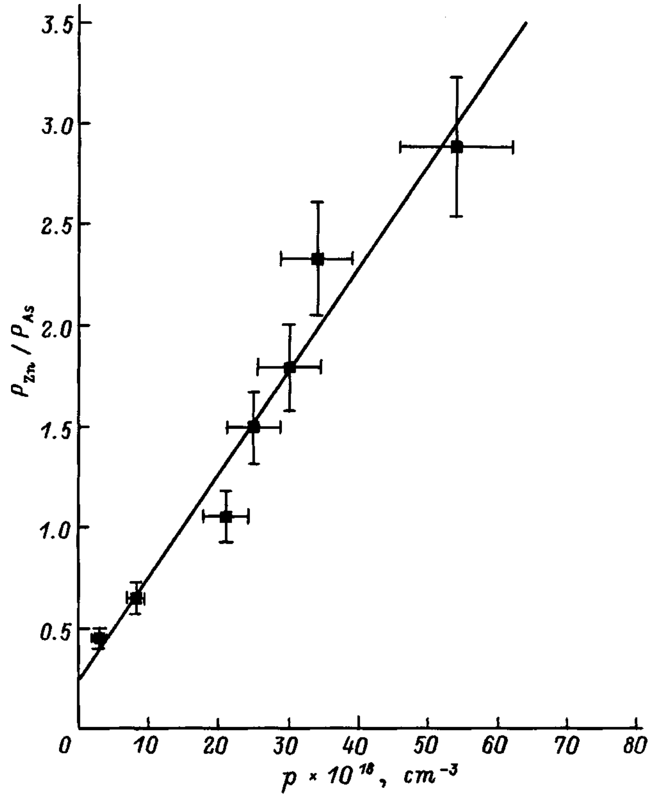

FIG. 6. Ratio of zinc and arsenic ion fluxes in layers with different doping levels at $T_G = 800\,^\circ\mathrm{C}$.

and choice of metal–solvent. We also analyzed the results of electrical measurements in the investigated GaAs : Zn layers reported in Ref. 4.

1) The concentration of R centers is independent of the growth temperature. This means that the concentration of these centers is not proportional to the equilibrium concentrations of point defects at the growth temperatures, which is possible if the centers are formed not during epitaxy, but during cooling.[11]

2) The concentration of R centers is lower in layers grown from a bismuth melt. This suggests that point defects enter into its composition, whose concentration falls when the gallium melt is replaced by a bismuth melt. Such defects can be arsenic vacancies (V_{As}),[13] interstitial gallium (Ga_I), or an antisite defect—gallium at an arsenic site ($\mathrm{Ga}_{\mathrm{As}}$).

3) The degree of compensation of the investigated GaAs : Zn layers, with doping level between $5\times10^{17}\,\mathrm{cm}^{-3}$ and $8\times10^{19}\,\mathrm{cm}^{-3}$, is independent of the melt—gallium or bismuth—from which the sample was grown.[4] At the same time, the concentration of R centers in layers with doping level greater than $1\times10^{19}\,\mathrm{cm}^{-3}$ depends in a substantial way on the metal–solvent used to grow the layer. This fact suggests that the R center is a neutral formation, i.e., both donor point defects and acceptor point defects should enter into its composition. This is extraordinarily surprising since it is customarily assumed that increasing the doping level in p-type layers increases the concentration of donor point defects and lowers the concentration of acceptor point defects.[11]

The following scheme for the formation of an electrically neutral complex explains all of the above experimental data.

During epitaxy zinc is built into GaAs in two forms: as a substitution acceptor $\mathrm{Zn}_{\mathrm{Ga}}^{-1}$ and as an interstitial donor Zn_I^{+1} (Ref. 14). Upon cooling, the zinc atoms located at interstices are built into the gallium sites, pushing the latter out into interstices,4) according to the well-known theory of Zn diffusion in GaAs via the reaction[15,16]

$$\mathrm{Zn}_I^{+1} \leftrightarrows \mathrm{Ga}_I^{+2} + \mathrm{Zn}_{\mathrm{Ga}}^{-1}. \tag{6}$$

It is energetically favorable for the interstitial gallium atoms Ga_I^{+2} formed as a result of this reaction[5] to interact with an arsenic vacancy V_{As}^{+1} with formation of an antisite defect $\mathrm{Ga}_{\mathrm{As}}^{-2}$, which, in turn, by interacting with two arsenic vacancies forms a neutral complex $(\mathrm{Ga}_{\mathrm{As}} - 2V_{\mathrm{As}})^x$:

$$\mathrm{Ga}_I^{+2} + V_{\mathrm{As}}^{+1} \leftrightarrows \mathrm{Ga}_{\mathrm{As}}^{-2} + 5h, \tag{7}$$

$$\mathrm{Ga}_{\mathrm{As}}^{-2} + 2V_{\mathrm{As}}^{+1} \leftrightarrows (\mathrm{Ga}_{\mathrm{As}} - 2V_{\mathrm{As}})^x,$$

where h denotes a hole. The formation of a neutral complex of point defects carrying charges of opposite sign is thermodynamically favorable since the enthalpy of formation of the complex is lower than the sum of enthalpies of formation of the individual charged defects.[11]

According to the law of mass action, starting with reactions (6)–(8) and allowing for the fact that $\mathrm{Ga}_{\mathrm{As}}^x \leftrightarrows \mathrm{Ga}_{\mathrm{As}}^{-2} + 2\cdot h$, and that p is proportional to the concentration of shallow ionized acceptors $\mathrm{Zn}_{\mathrm{Ga}}$, it is possible to obtain an expression which relates the concentration of complexes to the hole concentration:

$$N_R \sim [(N_{\mathrm{Ga}}^x)^3/(N_{\mathrm{Zn}}^2)^2]p^6, \tag{9}$$

where N_{Ga}^x is the concentration of the neutral antisite defects $\mathrm{Ga}_{\mathrm{As}}^x$, which depends only on the temperature,[17] and N_{Zn}^+. It can be seen from Eq. (9) that the concentration of the complexes is proportional to the sixth power of the hole concentration, in good agreement with the value of the exponent ($\gamma + 1 = 5.35$) in expression (5) which relates the concentration of the R centers to the hole concentration. The difference between the power of the hole concentration in expression (9) and the exponent $\gamma + 1$ in expression (5) is due to growth of the concentration of interstitial donors Zn_I^{+1} with increase of the doping level.

CONCLUSION

In summary, we have established that a center of radiative recombination is formed in GaAs : Zn prepared by liquid-phase epitaxy. This center manifests itself in the photoluminescence spectra of layers with doping level $p > 5\times10^{18}\,\mathrm{cm}^{-3}$ and $p > 1\times10^{19}\,\mathrm{cm}^{-3}$ for layers grown from gallium and bismuth melts, respectively. As the doping level is increased, the center concentration grows in proportion to the hole concentration raised to the power 5.35 ± 0.1, where the exponent is independent of the epitaxy temperature in the range $T_G = 800-708\,^\circ\mathrm{C}$. Replacing the gallium melt by a bismuth melt leads to a change in the concentration of the centers by more than an order of magnitude. The experimental data are explained by assuming that the center is electrically neutral complex which consists of an antisite defect of gallium at an arsenic site and two arsenic vacancies.

We wish to thank S. I. Chikichev for fruitful discussions and V. G. Pogadaev for assistance with growing the epitaxial layers.

1) In what follows we will only indicate the epitaxy starting temperature (T_G).

2) To calculate the total intensity of the lines we decomposed the spectra into their component lines with the *C* line described by a Gaussian curve and the shape of the *B* line prescribed in accordance with calculations presented in Ref. 6.

3) The nonmonotonic character of the concentration dependence of *S* is probably due to the presence in the photoluminescence spectra of some line *X*, which strongly overlaps the *C* and *B* lines, whose intensity grows as the doping level is increased. In layers with doping level $p < p_{cr}$ the shoulder in the *B* line is associated with the *X* line, and at higher doping levels the intensity of the *C* line grows abruptly and it begins to dominate in this region of the spectrum. The *X* line can be, for example, the line with maximum at 1.37 eV, which is associated with the $\mathrm{Zn_{Ga}} - V_{\mathrm{As}}$ complex.[9]

4) Interstitial gallium atoms can also form during growth. However, this defect has a high enthalpy of formation ≈6 eV (Ref. 17); therefore the concentration of interstitial gallium atoms formed during growth is much smaller than the concentration of interstitial zinc atoms.

5) In the treatment of reactions involving point defects it was assumed in the estimation of the variation of the Gibbs free energy (ΔG) associated with the reaction that the variation of the entropy can be ignored and it can be assumed that $\Delta G \cong \Delta H$, where ΔH is the variation of the enthalpy.[17] Data on the enthalpy of formation of native point defects were taken from Ref. 17. The difference between the sum of enthalpies of formation of $\mathrm{Ga}_1^{+2} + V_{\mathrm{As}}^{+1}$ (≈6.9 eV) and the enthalpy of formation of $\mathrm{Ga}_{\mathrm{As}}^{-2}$ (≈3.4 eV) gives a gain in energy ≈3.5 eV.

[1] G. Packeiser, H. Tews, and P. Zwicknagl, J. Cryst. Growth **107**, 883 (1991).

[2] Yu. B. Bolkhovityanov, B. V. Morozov, A. G. Paulish, A. S. Suranov, A. S. Terekhov, E. Khaĭri, and S. V. Shevelev, Pis'ma Zh. Tekh. Fiz. **16**, No. 7, 25 (1990) [Tech. Phys. Lett. **16**, 253 (1990)].

[3] E. W. Williams and H. B. Bebb, in *Semiconductors and Semimetals*, edited by R. K. Willardson (Academic Press, New York, 1972), Vol. 8, p. 336.

[4] V. G. Pogadaev and N. A. Yakusheva, Élektron. Tekh. Ser. 6, Materialy, No. 5, 48 (1990).

[5] K. D. Glinchuk and A. V. Prokhorovich, Phys. Status Solidi A **29**, 339 (1975).

[6] A. P. Levanyuk and V. V. Ovipov, Usp. Fiz. Nauk **33**, 427 (1981) [Sov. Phys. Usp. **33**, 105 (1981)].

[7] P. L. Kukk, Izv. Akad. Nauk SSSR, Neorg. Mater. **16**, 1509 (1980).

[8] K. D. Glinchuk, A. V. Prokhorovich, V. E. Radionov, and V. I. Vovnenko, Phys. Status Solidi A **49**, 593 (1978).

[9] C. J. Hwang, Phys. Rev. **180**, 827 (1969).

[10] M. G. Dowsett and E. A. Clark, in *Practical Surface Analysis*, Vol. 2, *Ion and Neutral Spertroscopy*, edited by D. Briggs and M. P. Seah (Wiley, New York, 1992).

[11] F. A. Kröger, *The Chemistry of Imperfect Crystals* (Wiley, New York, 1964; Moscow, 1969).

[12] K. S. Zhuravlev, S. Ch. Chikichev, R. Shtaske, and N. A. Yakusheva, Fiz. Tekh. Poluprovodn. **24**, 1645 (1990) [Sov. Phys. Semicond. **24**, 1027 (1990)].

[13] R. Kh. Akchurin, I. O. Donskaya, S. I. Dulin, and V. B. Ufimtsev, Kristallografiya **33**, 464 (1988) [Sov. Phys. Crystallogr. **33**, 273 (1988)].

[14] T. Kitano, H. Watanabe, and J. Matsui, Appl. Phys. Lett. **54**, 2201 (1989).

[15] T. Y. Tan, S. Yu, and U. Gösele, J. Appl. Phys. **70**, 4823 (1991).

[16] G. Bösker, N. A. Stolwijk, H.-G. Hettwer, A. Rucki, W. Jäger, and U. Södervall, Phys. Rev. B **52**, 11 927 (1995).

[17] J. F. Wager, J. Appl. Phys. **69**, 3022 (1991).

Translated by Paul F. Schippnick

SEMICONDUCTORS VOLUME 32, NUMBER 10 OCTOBER 1998

Effect of In doping on the kinetic coefficients in solid solutions of the system $(Pb_zSn_{1-z})_{0.95}Ge_{0.05}Te$

S. A. Nemov, V. I. Proshin, and S. M. Nakhmanson

St. Petersburg State Technical University, 195251 St. Petersburg, Russia

(Submitted March 23, 1997; accepted for publication March 24, 1998)
Fiz. Tekh. Poluprovodn. **32**, 1190–1193 (October 1998)

In the quaternary solid solutions $(Pb_zSn_{1-z})_{0.95}Ge_{0.05}Te$ ($z=0.35$ and 0.40) the effect of addition of indium (in amounts of $5-20$ at. %) on the temperature dependence of the electrical conductivity σ, Hall coefficient R, Seebeck coefficient S, and Hall mobility u is investigated on samples prepared using powder technology. We found a monotonic dependence of the hole density p on the indium content N_{In} with a tendency toward saturation at a level $p_{\max}\approx 3\times 10^{21}\,\mathrm{cm}^{-3}$, an abrupt drop in the mobility in samples with $p\approx p_{\max}$, and changes in the character of the temperature dependences $R(T)$ and $\sigma(T)$. We show that these peculiarities in the behavior of the kinetic coefficients can be interpreted in terms of quasilocal indium impurity states against the background of the valence band spectrum (with energy $\varepsilon_{\mathrm{In}}\sim 0.3$ eV) and resonance hole scattering into these states. *© 1998 American Institute of Physics.* [S1063-7826(98)00910-7]

Tin telluride and germanium telluride and their mutual solid solutions crystallize with a large deviation from stoichiometry (~ 1 at. % or more) on the side of a chalcogenide excess. The vacancies formed in the metal sublattice are electrically active—they deposit holes in the valence band. The samples have typical hole concentrations $p\sim 10^{20}-10^{21}\,\mathrm{cm}^{-3}$ (Ref. 1). For this reason, doping with impurities is an ineffective means of controlling the electrical properties of these materials. The exception is indium, which combines a huge solubility (~ 10 at. %) in IV–VI compounds with an extraordinarily strong localization of the impurity electron states.[2] In the series of IV–VI compounds, indium creates quasilocal impurity states against the background of the allowed electron spectrum in the crystals. In SnTe and ternary solid solutions based on it, indium forms quasilocal states which are located deep within the valence band.[3–5]

It is of interest to examine the possibility for the existence of such strongly localized indium states in the quaternary solid solutions $(Pb_zSn_{1-z})_{1-y}Ge_yTe$, in particular, in connection with interesting properties of the superconductivity of thin layers of such systems.[6,7]

In the present paper we report the results of an experimental study of the electrical properties of solid solutions with a fixed concentration of lead ($z=0.35$ and 0.40) and germanium ($y=0.05$) and variable concentration of indium N_{In} ($5-20$ at. %). The composition of the samples corresponds to the formula $[(Pb_zSn_{1-z})_{0.95}Ge_{0.05}]_{1-x}In_xTe$. The samples were polycrystals prepared by a powder technique, subjected to a homogenizing anneal. The compositions of the samples and their main electrical characteristics are listed in Table I. We investigated the temperature dependence of their electrical conductivity (σ) and Hall (R) and Seebeck (S) coefficients in the temperature interval $77-400$ K.

Judging from the sign of the thermal voltage and Hall coefficient, all the samples possess a p-type conductivity, and their small values are evidence of high current-carrier concentrations and strong degeneracy of the hole gas. Note that the variation of the Hall coefficient with growth of N_{In} probably reflects a change in the hole concentration in the valence band since it correlates with the variation of the thermal voltage S (see Fig. 1).

Unfortunately, the energy spectrum of the quaternary solid solutions $(Pb_zSn_{1-z})_{1-y}Ge_yTe$, so far as we know, has not been studied. Therefore, for estimates we used data for SnTe.[8,9] According to Refs. 8 and 9 the values of the Hall coefficient at 77 K (R_{77}) give Hall concentrations close to the true hole concentration. Therefore, in the investigated solid solutions we determined the hole concentration from the R_{77} data as $p=(eR_{77})^{-1}$ and the Hall mobility as $u(T)=R_{77}\sigma(T)$. The observed nonmonotonicity in the dependence of the hole concentration p on N_{In} is probably connected with fluctuations in the vacancy concentration in the metal sublattice of the solid solution $(Pb_zSn_{1-z})_{1-y}Ge_yTe$.

Let us consider the data obtained by us. As can be seen from Table I and Figs. 1 and 2, with growth of the indium content in the samples the Hall coefficient decreases, the Hall hole concentration increases with increasing saturation at the level $(2-3)\times 10^{21}\,\mathrm{cm}^{-3}$, the temperature dependence of the Hall coefficient weakens, and the Hall mobility u at 77 K decreases radically (by $1.5-2$ orders of magnitude). In the process, the nature of the temperature dependence of the conductivity changes from a decreasing dependence (sample 1 with the lowest hole concentration; see the inset in Fig. 2) to a monotonically increasing dependence $\sigma(T)$ in the samples with the largest indium content (see the inset in Fig. 2).

The above-noted peculiarities in the behavior of the kinetic coefficients with growth of N_{In} and with penetration of the Fermi level ε_F into the valence band of these quaternary solid solutions are similar to those observed in lead chalcogenides with a thallium impurity,[2,10] and can also be ex-

TABLE I. Composition and electrical parameters of samples of the system of solid solutions $[(Pb_zSn_{1-z})_{0.95}Ge_{0.05}]_{1-x}In_xTe$.

Sample No.	Composition		R, cm^3/C		σ, $\Omega^{-1}\cdot$cm^{-1}		S, μV/K	u, cm^2/(V·s)
	z, at. %	x, at. %	77 K	300 K	77 K	300 K	300 K	77 K
1	0.35	0.05	0.35	0.14	220	220	95	75
2	0.35	0.08	0.09	0.027	230	280	35	21
3	0.35	0.10	0.22	0.099	170	180	100	38
4	0.35	0.16	0.0039	0.0020	310	370	5−6	1.2
5	0.35	0.20	0.0020	0.0010	490	530	4	1.1
6	0.40	0.16	0.0025	0.0025	210	280	7−8	0.9

plained by the existence of a band of quasilocal impurity states against the background of the spectrum of states of the valence band. In this model the nonlinear character of the dependence $p(N_{\mathrm{In}})$ and its saturation are linked with the entrance of the Fermi level into the band of indium states and pinning of the Fermi level by the peak of the density of impurity states.

An estimate of the position of the indium level inferred from the position of the Fermi level in the samples with maximum hole concentration using SnTe band parameters gave $\varepsilon_{\mathrm{In}} \sim 0.3\,\mathrm{eV}$ (on the scale of the hole energies).

The change in the shape of the $R(T)$ curve for the indium-doped samples may be due to a temperature shift of the $\varepsilon_{\mathrm{In}}(T)$ impurity level [if the coefficient $|d\varepsilon_{\mathrm{In}}/dT|$ is small, then In $R(T) \approx \mathrm{const}$ in the above-considered model with a quasilocal indium level].

It is logical to attribute the significant lowering of the mobility in the samples with hole concentrations $p \sim 10^{21}\,\mathrm{cm}^{-3}$ and Fermi level $\varepsilon_F \approx \varepsilon_{\mathrm{In}}$ to the activation of an efficient additional scattering mechanism—resonance scattering of holes into the band of quasilocal indium states. Estimates of the mobility for resonance scattering, based on the expression for the relaxation time[11]

$$\tau_{\mathrm{res}} = \frac{\hbar g_b(\varepsilon_{\mathrm{In}})}{N_{\mathrm{In}}}, \tag{1}$$

where $g_b(\varepsilon_{\mathrm{In}})$ is the density of band states in the region of energies near the resonance level $\varepsilon \approx \varepsilon_{\mathrm{In}}$, give values $u_{\mathrm{res}} \sim 1\,\mathrm{cm}^2/(\mathrm{V}\cdot\mathrm{s})$, which are similar to the experimental values. Thus, resonance scattering can indeed be responsible for the experimentally observed hole mobilities in $[(Pb_zSn_{1-z})_{0.95}Ge_{0.05}]_{1-x}In_xTe$ ($z \approx 0.35-0.40$) with large indium content.

The experimental data obtained by us on the kinetic phenomena in the quaternary solid solutions $(Pb_zSn_{1-z})_{1-y}Ge_yTe:In$ can thus be explained in the framework of a model which assumes the existence of a band of quasilocal indium impurity states against the background of the valence band with energy $\varepsilon_{\mathrm{In}} \sim 0.3\,\mathrm{eV}$ and resonance scattering of holes into these states.

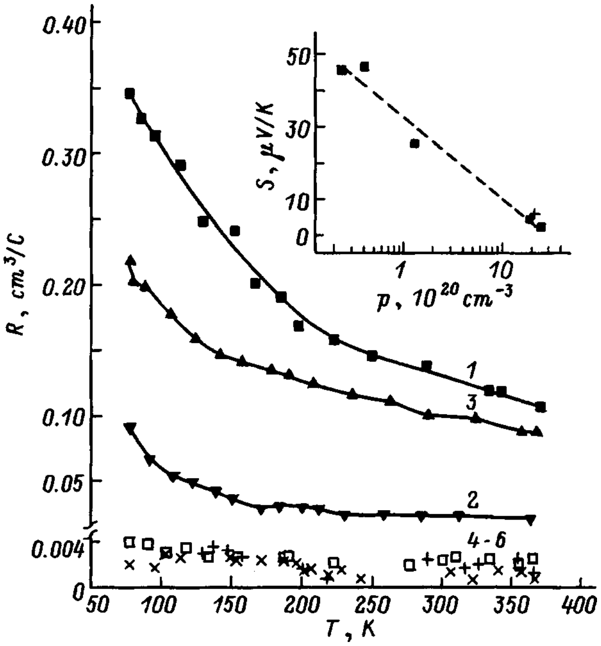

FIG. 1. Temperature dependence of the Hall coefficient $R(T)$ in samples of $[(Pb_zSn_{1-z})_{0.95}Ge_{0.05}]_{1-x}In_xTe$. Points correspond to experiment. The numbers labelling the dependences correspond to the sample numbers in the table. The inset plots the dependence of the Seebeck coefficient S at 120 K on the hole concentration p (points); the dashed line plots the dependence $S \sim p^{-2/3}$, which is valid for a quadratic dispersion relation for strong degeneracy of the gas of current carriers; the cross is the data point for sample 6.

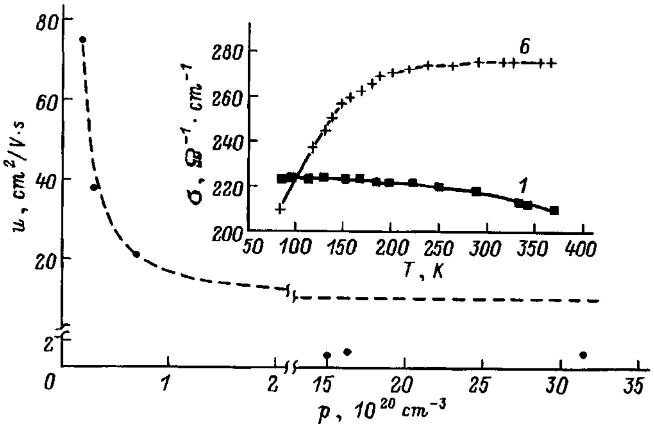

FIG. 2. Dependence of the Hall mobility u on the hole concentration p in samples of $[(Pb_zSn_{1-z})_{0.95}Ge_{0.05}]_{1-x}In_xTe$ at 77 K (points). The dashed line plots the dependence $u \sim p^{-4/3}$, which is valid for the case of a strongly degenerate hole gas and dominant impurity scattering mechanism, where $p \approx N_{\mathrm{imp}}$, where N_{imp} is the impurity concentration. The inset plots the dependence of the conductivity σ on temperature for samples 1 and 6.

[1] N. Kh. Abrikosov and L. E. Shelimova, *IV–VI Based Semiconductor Materials* [in Russian] (Nauka, Moscow, 1975).

[2] V. I. Kaĭdanov and Yu. I. Ravich, Usp. Fiz. Nauk **145**, 51 (1985) [Sov. Phys. Usp. **28**, 31 (1985)].

[3] L. D. Dudkin, N. A. Erasova, V. I. Kaĭdanov, T. N. Kalshnikova, and É. F. Kosolapova, Fiz. Tekh. Poluprovodn. **6**, 2294 (1972) [Sov. Phys. Usp. **6**, 1934 (1972)].

[4] G. S. Bushmarina, I. A. Drabkin, V. V. Kompaniets, R. V. Parfen'ev, D. V. Shamshur, and M. A. Shakhov, Fiz. Tverd. Tela (Leningrad) **28**, 1094 (1986) [Sov. Phys. Solid State **28**, 612 (1986)].

[5] G. S. Bushmarina, I. A. Drabkin, D. V. Mashovets, R. V. Parfeniev, D. V. Shamshur, and M. A. Shachov Physica B **169**, 687 (1991).

[6] S. A. Nemov, S. F. Musikhin, D. I. Popov, V. I. Proshin, and D. V. Shamshur, Fiz. Tverd. Tela (St. Petersburg) **37**, 3366 (1995) [Phys. Solid State **37**, 1850 (1995)].

[7] S. A. Nemov, S. F. Musikhin, R. V. Parfen'ev, V. N. Svetlov, D. I. Popov, V. I. Proshin, and D. V. Shamshur, Fiz. Tverd. Tela **37**, 3523 (1995) [Phys. Solid State **37**, 1936 (1995)].

[8] B. F. Gruzinov, P. P. Konstantinov, B. Ya. Moĭzhes, Yu. I. Ravich, and L. M. Sysoeva, Fiz. Tekh. Poluprovodn. **10**, 497 (1976) [Sov. Phys. Semicond. **10**, 209 (1976)].

[9] B. F. Bushmarina, I. A. Drabkin, M. A. Kvantov, and O. E. Kvyatkovskiĭ, Fiz. Tverd. Tela (Leningrad) **32**, 2869 (1990) [Sov. Phys. Semicond. **32**, 1666 (1990)].

[10] V. I. Kaĭdanov, S. A. Nemov, and Yu. I. Ravich, Fiz. Tekh. Poluprovodn. **26**, 201 (1992) [Sov. Phys. Semicond. **26**, 113 (1992)].

[11] V. I. Kaĭdanov, R. B. Mel'nik, and I. A. Chernik, Fiz. Tekh. Poluprovodn. **7**, 759 (1973) [Sov. Phys. Semicond. **7**, 522 (1973)].

Translated by Paul F. Schippnick

SEMICONDUCTORS VOLUME 32, NUMBER 10 OCTOBER 1998

Differential methods for determination of deep-level parameters from recombination currents of $p-n$ junctions

S. V. Bulyarskiĭ, N. S. Grushko, and A. V. Lakalin

Ulyanovsk State University, 432700 Ulyanovsk, Russia

(Submitted April 6, 1998; accepted for publication April 8, 1998)
Fiz. Tekh. Poluprovodn. **32**, 1193–1196 (October 1998)

Two techniques for determining the activation energies of centers that create deep levels in the space-charge region (SCR) of $p-n$ junctions are developed on the basis of the Shockley–Read–Hall recombination model. The proposed techniques are based on a consideration of recombination currents in the SCR for a low injection level. The first technique involves a differential analysis of the reduced recombination rate $\partial R_{np}(U)/\partial U$ and the second technique involves an analysis of the dependence $R_{np}^2(U)/\exp(qU/2kT)$. These techniques are used to analyze the current–voltage characteristics of gold-doped silicon p^+-n diodes. The gold-related deep center activation energies obtained from the current–voltage characteristics are in good agreement with the available data in the literature. © *1998 American Institute of Physics.* [S1063-7826(98)01010-2]

INTRODUCTION

Generation–recombination processes in the space-charge region (SCR) of a $p-n$ junction were first considered in Ref. 1. Using the statistics of recombination through a simple two-charge Shockley–Read–Hall center, the authors of Ref. 1 obtained a general expression for the recombination current density in the SCR (in the form of an integral over the SCR of the recombination rate). They were able to obtain analytical expressions only for some particular cases for various simplifying assumptions. The entire current–voltage characteristic (CVC) due to recombination currents in the SCR of the $p-n$ junction for a low injection level (LIL) was obtained in Refs. 2–6. Although complete agreement with the results of numerical integration of the recombination rate was not obtained, some estimates may still be considered as satisfactory.[5–7]

The approach developed in Refs. 5 and 6 allows one to determine the activation energy of deep levels, and with additional information it also allows one to determine the ratio of capture coefficients or lifetimes in the quasineutral regions. In comparison with the techniques of transient generation of carriers in the SCR of the $p-n$ junction [thermally stimulated capacitance (TSC),[8] deep-level transient spectroscopy (DLTS)[9]] which require measurements over a wide temperature interval, an analysis of the recombination current can be performed at some fixed temperature (e.g., room temperature). This leads to simpler measurements. On the basis of the method developed in Ref. 8 we developed two additional techniques of processing the recombination current in the SCR for low injection levels. What sets this work apart is the use of the computer at every stage of the process: from performing the measurements to producing the final result. The objects of study were gold-doped silicon p^+-n diodes of commercial manufacture (D-220). About these diodes (D-220) it is known that they are produced by an alloy technology, and the doping levels of the p^+ and n regions are constant (the $p-n$ junction is sharp, as is confirmed by the results of capacitance measurements. This choice was motivated by the fact that gold in silicon has been studied extensively[10] and can be used as a test of the proposed techniques.

RECOMBINATION CURRENTS IN THE SCR AND THE REDUCED RECOMBINATION RATE

Recombination currents in the SCR of a $p-n$ junction through simple two-charge deep centers are described by the expression[6]

$$i_r=\sum_{m=1}^{s}\frac{qSw(U)c_{nm}c_{pm}n_i^2\left(\exp\left(\frac{qU}{kT}\right)-1\right)N_{tm}}{2n_i\sqrt{c_{nm}c_{pm}}\exp\left(\frac{qU}{2kT}\right)+c_{nm}n_{1m}+c_{pm}p_{1m}}\times\frac{2kT}{q(U_{\mathrm{dif}}-U)},\tag{1}$$

where $w(U)$ is the width of the SCR, s is the number of deep levels, S is the area of the $p-n$ junction, $n_{1m}=N_c\exp(-E_{mm}/kT)$, $p_{1m}=N_v\exp(-E_{tpm}/kT)$, c_n and c_p are the electron and hole capture coefficients for capture by the given center averaged over all states, N_t is the concentration of deep levels, and E_t is the position of the deep level in the band gap. $E_{tn}=E_c-E_t$, $E_{tp}=E_t-E_v$. Expression (1) holds provided the following conditions are satisfied: the deep centers are uniformly distributed over the band gap, the levels are discrete, the system is found in thermal equilibrium, illumination is absent, and tunneling transitions and recombination are controlled entirely by thermal processes.[4,5] Expression (1) was derived on the basis of the Shockley–Read–Hall theory of recombination through a simple two-charge center and differs somewhat from the expression derived in Ref. 1. This difference was discussed in detail in Refs. 4 and 7, and the derivation is given in Ref. 6; we will therefore not consider it here. The limits of applicability of expression (1) were also determined in Refs. 4–6. Each term in expression (1) is the recombination current through the corresponding (mth) deep level. Expression (1) can be represented in the form[7]

$$i_r=\frac{2kTw(U)Sn_i}{U_{\rm dif}(u)-U}\sum_{m=1}^{s}\frac{\alpha_m\left(\exp\left(\dfrac{qU}{kT}\right)-1\right)}{2\zeta_m\exp\left(\dfrac{qU}{2kT}\right)+\zeta_m^2+1},\tag{2}$$

where $\alpha_m=(n_{1m})/n_i)c_{nm}N_{tm}$ and $\zeta_m=(n_{1m}/n_i)\sqrt{c_{nm}/c_{pm}}$ (here we have made use of the equality $n_{1m}p_{1m}=n_i^2$). The dependences $U_{\rm dif}(U)$ and $w(U)$ in Eqs. (1) and (2) can be found from the capacitance measurements. Thus, only the parameters α_m and ζ_m, which depend only on the nature of the deep levels, on their concentration $(c_{nm}, c_{pm}, E_{tm}, N_{tm})$, and on the material of the semiconductor (n_j), remain unknown. Earlier it was proposed to analyze the recombination currents with the help of the reduced recombination rate R_{np} (Refs. 4–6), which is defined as

$$R_{np}(U)=\frac{i_r(U)\exp\left(\dfrac{qU}{2kT}\right)}{Sw(U)n_i\left(\exp\left(\dfrac{qU}{kT}\right)-1\right)}\,\frac{U_{\rm dif}(U)-U}{2kT}.\tag{3}$$

From Eqs. (2) and (3) the relation between this quantity and the deep-center parameters is apparent:

$$R_{np}(U)=\sum_{m=1}^{s}R_{npm}(U)=\sum_{m=1}^{s}\frac{\alpha_m\left(\exp\left(\dfrac{qU}{kT}\right)-1\right)}{2\zeta_m\exp\left(\dfrac{qU}{2kt}\right)+\zeta_m^2+1}.\tag{4}$$

If $s=1$ (one deep level), then Eqs. (2) and (4) are described by only two parameters, which can be found by the trial-and-error method. In general, the number of fitting parameters is $2s$. They can be found by the method of successive trial and error in each segment of $R_{npm}(U)$ for every mth deep center and successive subtraction of $R_{npm}(U)$ from the curve $R(U)$. This procedure can be done graphically[5,6] or automated. Having determined ζ_m, we easily find for fixed temperature

$$E_{tnm}=\frac{E_g}{2}-kT\ln\zeta_m+\frac{3}{4}kT\ln\frac{m_n^*}{m_p^*}+\frac{1}{2}kT\ln\frac{c_{nm}}{c_{pm}}.\tag{5}$$

The activation energy of the mth deep level is determined to the last term, which can be found by making measurements at several temperatures. (For many centers c_n/c_p does not exceed 10^2; thus at $T=300$ K $(kT/2)\ln(c_n/c_p)\cong 0.06$ eV.) In addition,

$$\frac{\alpha_m}{\zeta_m}=\left(\frac{1}{c_{nm}N_{tm}}\right)^{1/2}\cdot\left(\frac{1}{c_{pm}N_{tm}}\right)^{1/2}=\sqrt{\tau_{n0m}\cdot\tau_{p0m}}\,.\tag{6}$$

THE DIFFERENTIAL TECHNIQUE $(\partial R_{np}(U)/\partial U)$

From Eq. (4) we find $\partial R_{np}(U)/\partial U$. Differentiation gives

$$\frac{\partial R_{np}(U)}{\partial U}=\frac{q}{2kT}\sum_{m=1}^{s}\frac{\alpha_m\exp\left(\dfrac{qU}{2kT}\right)(\zeta_m^2+1)}{\left(2\zeta_m\exp\left(\dfrac{qU}{2kT}\right)+\zeta_m^2+1\right)^2}.\tag{7}$$

It is easy to see that the function (7) has maxima. To find them we search for extrema:

$$\frac{\partial^2 R_{np}(U)}{\partial U^2}=\left(\frac{q}{2kT}\right)^2\times\sum_{m=1}^{s}\frac{\alpha_m\exp\left(\dfrac{qU}{2kT}\right)(\zeta_m^2+1)\left(\zeta_m^2+1-2\zeta_m\exp\left(\dfrac{qU}{2kT}\right)\right)}{\left(2\zeta_m\exp\left(\dfrac{qU}{2kT}\right)+\zeta_m^2+1\right)^3}=0.\tag{8}$$

Since we have assumed that the recombination processes proceed independently through each center, Eq. (8) is satisfied if each term in the sum is equal to zero (assumption of the technique). Thus

$$\zeta_m^2+1-2\zeta_m\exp\left(\frac{qU_{0m}}{2kT}\right)=0,\tag{9}$$

$m=1,2,\ldots,s$, where U_{0m} is the position of the maximum for the mth term. Solving the quadratic equation for ζ_m, we find

$$\zeta_m=\exp\left(\frac{qU_{0m}}{2kT}\right)+\sqrt{\left(\exp\left(\frac{qU_{0m}}{2kT}\right)\right)^2-1}\tag{10}$$

(we have chosen the root with the ''+'' sign). If $\exp(qU_{0m}/2kT)\gg 1$, then

$$\zeta_m=2\exp\left(\frac{qU_{0m}}{2kT}\right).\tag{11}$$

Using expression (10) or (11) for ζ_m, we find E_{tnm} using formula (5). Substituting ζ_m^2+1 from Eq. (9) in expression (7), we find that the amplitude of the mth maximum, A_m, is

$$A_m=\frac{q}{2kT}\,\frac{\alpha_m}{8\zeta_m}.\tag{12}$$

Knowing ζ_m, it is easy to find α_m or ζ_m/α_m.

Thus, instead of finding α_m and ζ_m, it is possible by expanding R_{np} into its components to construct the dependence $\partial R_{np}(U)/\partial U$ and find ζ_m and ζ_m/α_m from the positions of the maxima (U_{om}) and the value of the function at these points. Next, using Eqs. (5) and (6), we can calculate the required parameters.

The given technique has two important advantages in comparison with the technique proposed in Ref. 5, which analyzes $\partial\gamma(U)/\partial U$ and $\gamma(U)=(2kT/q)\partial(\ln R_{np}(U))/\partial U$: first, it is necessary to construct only the first derivative of $R_{np}(U)$, and not the second, and second, the positions of the maxima in the first derivative are determined more accu-

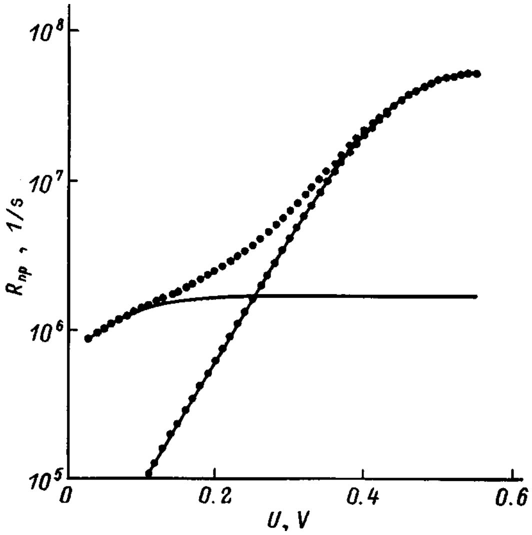

FIG. 1. Separation of the reduced recombination rate into its components ($T=297$ K).

rately than in the second since the numerical ''noise'' in the first derivative is always less than in the second.

THE $(R_{np}^2(U)/\exp(qU/2kT))$ TECHNIQUE

The differential technique described above has one disadvantage: numerical differentiation of the experimental points $\partial R_{np}(U)/\partial U$ leads to an increase in the level of numerical noise in the curve $\partial R_{np}(U)/\partial U$, which complicates the search for U_{0m} substantially. Therefore, we propose another approach. We introduce the function $L(U)$ as follows:

$$L(U)=\frac{R_{np}^2(U)}{\exp\left(\frac{qU}{2kT}\right)}. \tag{13}$$

This function has maxima. To find them, we search for extrema:

$$\frac{\partial L(U)}{\partial U}=\frac{\partial}{\partial U}\left(\frac{R_{np}^2(U)}{\exp\left(\frac{qU}{2kT}\right)}\right)=\frac{2R_{np}\frac{\partial R_{np}}{\partial U}-R_{np}^2\frac{q}{2kT}}{\exp\left(\frac{qU}{2kT}\right)}=0. \tag{14}$$

Using Eq. (7), we obtain

$$2\frac{q}{2kT}\sum_{m=1}^{s}\frac{\alpha_m\exp\left(\frac{qU_{0m}}{2kT}\right)(\zeta_m^2+1)}{\left(2\zeta_m\exp\left(\frac{qU_{0m}}{2kT}\right)+\zeta_m^2+1\right)^2}-\frac{q}{2kT}\sum_{j=1}^{s}\frac{\alpha_j\exp\left(\frac{qU_{0j}}{2kT}\right)}{2\zeta_j\exp\left(\frac{qU_{0j}}{2kT}\right)+\zeta_j^2+1}=0. \tag{15}$$

Keeping track of the summation indices and reducing the left-hand side of Eq. (15) to a common denominator, we obtain

$$\sum_{m=1}^{s}\frac{2\alpha_m\exp\left(\frac{qU_{0m}}{2kT}\right)(\zeta_m^2+1)-\alpha_m\exp\left(\frac{qU_{0m}}{2kT}\right)\left(2\zeta_m\exp\left(\frac{qU_{0m}}{2kT}\right)+\zeta_m^2+1\right)}{\left(2\zeta_m\exp\left(\frac{qU_{0m}}{2kT}\right)+\zeta_m^2+1\right)^2}=0. \tag{16}$$

As above, we assume that Eq. (16) is satisfied if each term is equal to zero. Then

$$\zeta_m^2+1-2\zeta_m\exp\left(\frac{qU_{0m}}{2kT}\right)=0, \tag{17}$$

$m=1,2,\ldots,s$, which exactly coincides with Eq. (9), and the roots of this quadratic equation in ζ_m are given by formula (10) or (11). However, in the analysis of $L(U)$ the parameter α_m cannot be determined from the amplitude of the maximum or in any other way [see Eq. (13)]. Thus, by analyzing $L(U)$ it is possible only to find ζ_m and then determine E_{tnm} using formula (5).

In comparison with the previous technique, the given technique has the advantage that it does not use numerical differentiation; its disadvantage is that it allows one to determine only the parameter ζ_m.

RESULTS OF ANALYSIS OF THE CURRENT-VOLTAGE CHARACTERISTICS OF Si:Au–p^+–n DIODES AND DISCUSSION

Current–voltage characteristics of a gold-doped silicon p^+-n diode (D-220) were measured at $T=297$ K (24 °C). The reduced recombination rate $R_{np}(U)$ was calculated according to formula (3) for each voltage (Fig. 1). $U_{\mathrm{dif}}(U)$ and $w(U)$ were found in the usual way[11] from the results of capacitance measurements plotted in the same figure. According to formula (4), $R_{np}(U)$ was expanded into its components by the method of successive trial and error (numerical search) of the parameters α_m and ζ_m ($m=1,2$) (each ''ledge'' is described by the pair α_m and ζ_m; see Fig. 1). From the parameter values ζ_1 and ζ_2 the activation energy of the deep levels is calculated using formula (5):

$$E_{tn}^{+}=0.33+0.01\cdot\ln\frac{c_n^{+}}{c_p^{0}};\quad E_{tn}^{-}=0.53+0.01\cdot\ln\frac{c_n^{0}}{c_p^{-}}. \tag{18}$$

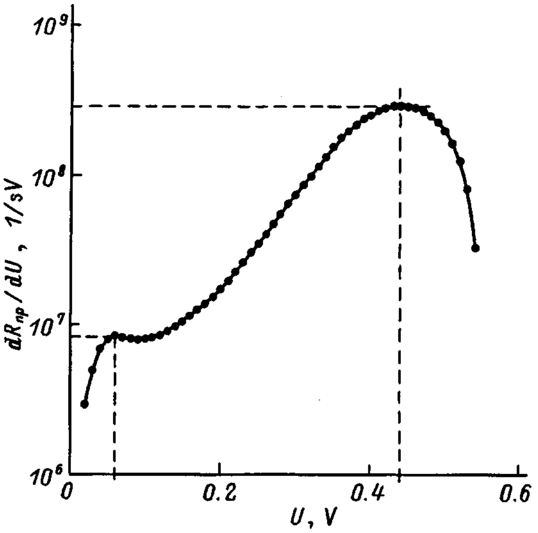

FIG. 2. Derivative of the reduced recombination rate with respect to the voltage ($T = 297$ K). Maxima at 0.06 and 0.44 V.

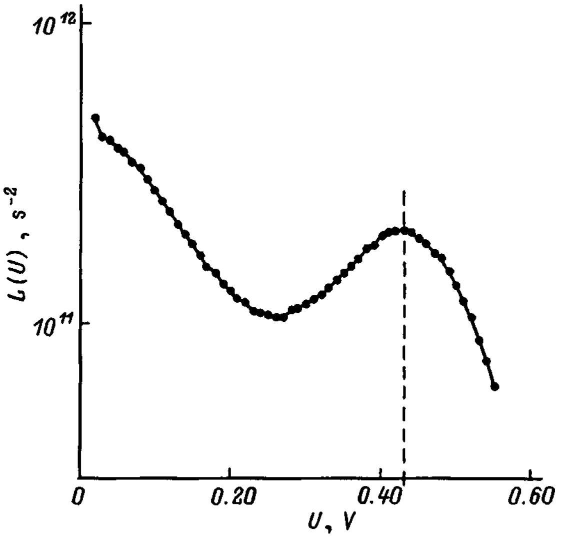

FIG. 3. Reduced recombination rate by the $L(U)$ method. Maximum at 0.43 V.

Since c_n^+, c_p^0, c_n^0, and c_p^- are known [$\ln(c_n^+/c_p^0) \approx 1$, $\ln(c_n^0/c_p^-) \approx 0.4$; Ref. 10], we can determine E_{tn}^+ and E_{tn}^- exactly; however, in general (if the capture coefficients are not known *a priori*) we can only make an approximate estimate. From the expansion of $R_{np}(U)$ into its components we obtain $E_{tn}^+ \approx 0.34$ eV and $E_{tn}^- \approx 0.53$ eV, which are in good agreement with the results of other studies.[10] [As is well known,[10] gold impurity in silicon forms two deep levels in the band gap: 1) an acceptor level $E_t = E_c - 0.55$ eV; for $T = 300$ K $\sigma_n^0 = 1.7 \times 10^{-16}$ cm^2 and $\sigma_p^- = 1.1 \times 10^{-14}$ cm^2; and 2) a donor level $E_t = E_v + 0.35$ eV; for $T = 300$ K $\sigma_n^+ = 6.3 \times 10^{-15}$ cm^2 and $\sigma_p^0 = 2.4 \times 10^{-15}$ cm^2].

Let us now apply the differential expansion technique to $R_{np}(U)$. The derivative $\partial R_{np}(U)/\partial U$ is plotted in Fig. 2. There are two maxima at $U_{01} = 0.06$ V and $U_{02} = 0.44$ V. We find ζ_1 and ζ_2 from formula (10) and calculate the activation energy of the deep levels from formula (5):

$$E_{tn}^+ = 0.33 + 0.01 \ln \frac{c_n^+}{c_p^0}; \quad E_{tn}^- = 0.52 + 0.01 \cdot \ln \frac{c_n^0}{c_p^-}. \qquad (19)$$

The result of processing $R_{np}(U)$ using the second technique [$L(U)$] is plotted in Fig. 3. The first maximum U_{01} does not show up, but we find $U_{02} = 0.43$ V. Using Eqs. (10) and (5), we calculate the activation energy of the deep levels

$$E_{tn}^+ = 0.33 + 0.01 \cdot \ln \frac{c_n^+}{c_p^0}. \qquad (20)$$

It can be seen that results (18), (19), and (20) coincide within 0.01 eV with the results of Ref. 10.

[1] S. T. Sah, R. N. Noyce, and W. Shockley, Proc. IRE **45**, 1228 (1957).

[2] S. V. Bulyarskiĭ and N. S. Grushko, *Physical Principles of the Functional Diagnostics of p–n Transitions with Defects* [in Russian] (Kishinev, Shtiintsa, 1992).

[3] V. I. Starosel'skiĭ, Mikroelektronika **23**, 50 (1994).

[4] S. V. Bulyarskiĭ and N. S. Grushko, *Generation–Recombination Processes in Active Elements* [in Russian] (Moscow State Univ. Press, Moscow, 1995).

[5] S. V. Bulyarskiĭ, N. S. Grushko, and A. V. Lakalin, Zavod. Lab. **63**, 25 (1997).

[6] S. V. Bulyarskiĭ, N. S. Grushko, A. I. Somov, and A. V. Lakalin, Fiz. Tekh. Poluprovodn. **31**, 1146 (1997) [Semiconductors **31**, 983 (1997)].

[7] S. V. Bulyarskiĭ, N. S. Grushko, and A. V. Lakalin, in *Proceedings of the International Conference on Centers with Deep Levels in Semiconductors and Semiconductor Structures* [in Russian] (Ul'yanovsk State Univ. Press, Ul'yanovsk, 1997), p. 65.

[8] M. G. Buehler, Solid-State Electron. **15**, 69 (1972).

[9] D. V. Lang, J. Appl. Phys. **45**, 3014 (1974).

[10] A. G. Milnes, *Deep Impurities in Semiconductors* (Wiley, New York, 1973).

[11] L. S. Berman and A. A. Lebedev, *Capacitance Spectroscopy of Deep Centers in Semiconductors* [in Russian] (Nauka, Leningrad, 1981).

Translated by Paul F. Schippnick

SEMICONDUCTORS VOLUME 32, NUMBER 10 OCTOBER 1998

Experimental corrections for the hot hole distribution function in germanium in crossed electric and magnetic fields

V. N. Tulupenko

Donbass State Mechanical-Engineering Academy, 343913 Kramatorsk, Ukraine

(Submitted December 16, 1997; accepted for publication April 27, 1998)
Fiz. Tekh. Poluprovodn. **32**, 1197–1199 (October 1998)

A procedure for finding corrections for the hot hole distribution functions obtained from absorption measurements on intersubband transitions of hot heavy and light holes in germanium in crossed electric and magnetic fields is proposed. This procedure is based on the multiple-valued dependence of the absorption on the photon energies of transitions from light holes to a subband split off as a result of the spin–orbit interaction. Taking these corrections into account improves the agreement between the gain for direct optical transitions between the light and heavy hole subbands calculated from measurements of the absorption in the near-infrared and direct measurements in the far-infrared. © *1998 American Institute of Physics.* [S1063-7826(98)01110-7]

The problem of determining the hot heavy-hole (HH) and light-hole (LH) distribution functions in germanium has arisen in conjunction with the necessity of experimentally estimating their degree of inverse intersubband redistribution in crossed electric and magnetic fields[1] in the far-infrared.

It is known that the structure of the valence band of germanium (Fig. 1) consists of three subbands: (HH) ε_1, (LH) ε_2, and the subband ε_3 split off as a result of the spin–orbit interaction. The magnitude of the splitting for $k=0$ is 0.29 eV; i.e., the subband ε_3 is almost empty at low temperatures. The fact that the valence band has such a structure allows one to determine the distribution functions of the hot heavy and light holes using the following technique.

As is well known,[2] the absorption occurring as a result of intersubband direct transitions of holes is written as

$$\alpha_{ij}(h\nu)=\frac{2e^2\hbar|\overline{P}_{ij}(k)|^2k[f_i(\varepsilon_i)-f_j(\varepsilon_j)]}{\pi c m_0^2 n h\nu(\partial\varepsilon_i/\partial k^2-\partial\varepsilon_j/\partial k^2)}, \tag{1}$$

where n is the index of refraction, c is the speed of light, $f_\beta(\varepsilon_\beta)$ is the distribution function of holes in the subbands ε_β (β is the number of the subband; $\beta=i,j=1,2,3$), $|\overline{P}_{ij}(k)|^2=(m_0^2k^2/\hbar^2)\overline{W}_{ij}(k)$ is the square of the modulus of the matrix element of the momentum operator averaged over directions of the wave vector $\mathbf{k}$, and $\rho(k)=(k/2\pi)\times(\partial\varepsilon_i/\partial k^2-\partial\varepsilon_j/\partial k^2)$ is the reduced density of states of the ith and jth subbands, which is found from their dispersion relations. According to Ref. 2, for small k (which corresponds to the far-infrared for direct optical transitions between HH and LH subbands) the transition probability $\overline{W}_{ij}(k)$ can be assumed constant and the absorption for the transitions $i\rightarrow 3$ can then be written in the simpler and more convenient form for practical applications

$$\alpha_{i3}=B(\lambda)f_i(\varepsilon). \tag{2}$$

Here λ is the wavelength of the radiation corresponding to the $i\rightarrow 3$ transitions, and $B(\lambda)$ is a coefficient. Comparing the absorption coefficient α_T measured under equilibrium conditions at a temperature T with the absorption coefficient α measured in the presence of electric ($\mathbf{E}$) and magnetic ($\mathbf{B}$) fields, we can then determine the distribution function in the ith subband $f(\varepsilon_i)$ from the relation

$$\frac{\alpha_T}{\alpha}=\frac{f_T(\varepsilon_i)}{f(\varepsilon_i)}, \tag{3}$$

where $f_T(\varepsilon_i)$ is the equilibrium (Boltzmann) distribution function at the temperature T. The experiment measures the modulation of the absorption in crossed electric and magnetic fields $\Delta\alpha(\lambda)$ and, consequently, $\alpha(\lambda)=\alpha_0(\lambda)+\Delta\alpha(\lambda)$, where $\alpha_0(\lambda)$ is the absorption measured under equilibrium conditions ($\mathbf{E}=\mathbf{B}=\mathbf{0}$) at the temperature of the experiment T_0.

An analogous procedure was used earlier to determine the heavy-hole distribution function[3,4] in strong electric fields without a magnetic field. As for the light holes, some comments are in order. First, the reduced density of states of subbands 2 and 3 ($\partial\varepsilon_2/\partial k^2-\partial\varepsilon_3/\partial k^2$) for $\varepsilon_2\approx 0.09$ eV has a singularity—the slopes of subbands 2 and 3 are identical. This leads to a rapid growth of $\alpha_{23}(\lambda)$ with increase of the electric field due to the resulting increase in the number of light holes in the region of the singularity. Second, broadening of the absorption due to intense emission of optical phonons by holes in subband 3 becomes noticeable in comparison with the width of the absorption peak for the $2\rightarrow 3$ transitions. Third, the dependence $h\nu_{23}(\varepsilon_2)$ is not one-to-one (see the inset in Fig. 1), which is especially important when determining the distribution function in strong electric fields. Nevertheless, as was shown by direct calculations in Ref. 5 for the case in which only an electric field is applied to the sample, the light-hole distribution function in the range of energies below the optical phonon energy ε_0 ($\varepsilon_2<\varepsilon_0$), which corresponds to transition wavelengths $\lambda_{23}=4.2-4.5\,\mu$m (the so-called passive region), can be found quite accurately if the mean hole energy is not too large ($\langle\varepsilon_2\rangle\leqslant\varepsilon_0$). In this case, the above-enumerated factors are

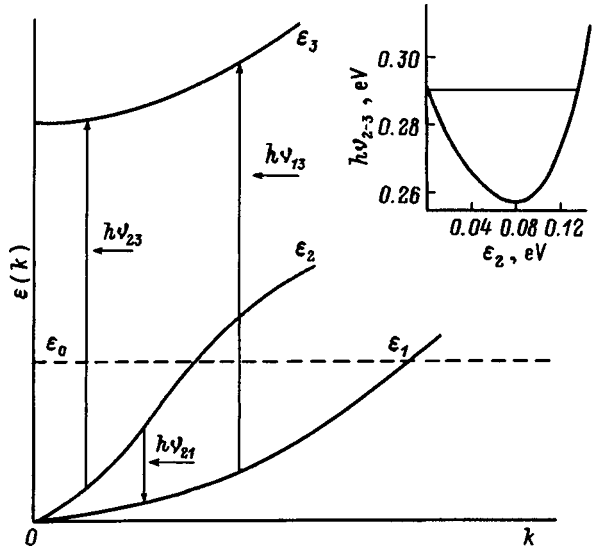

FIG. 1. Structure of the germanium valence band (shown schematically). The inset plots the photon energy for the 2→3 optical transitions as a function of the light-hole energy.

not too important and the proposed scheme for determining the distribution function remains valid for light holes. This condition leads directly to measurements in crossed electric and magnetic fields, where the magnetic field prevents the light holes from acquiring a large energy, and our experiments in electric fields up to 2 kV/cm again confirm the validity of the conclusions drawn in Ref. 5. (For a more detailed treatment of the determination of the light-hole distribution function in crossed fields $\mathbf{E}\perp\mathbf{B}$, see Refs. 6 and 7).

However, in the course of the experiments the necessity arose to determine the light-hole distribution function in the passive region and in stronger electric fields. Here the mean energy of the light holes becomes greater than the optical phonon energy and the absorption coefficient for the 2→3 transitions is a multiple-valued function of the energy of the light holes, including in the passive region. As is shown in the inset in Fig. 1, the absorption measured in the experiment, $\alpha_{2\exp}\equiv\alpha_2$, can be written as a sum of two components

$$\alpha_2|_\lambda=\alpha_2(\varepsilon_2')|_\lambda+\alpha_2(\varepsilon_2'')|_\lambda, \tag{4}$$

where $\alpha(\varepsilon_2')$ is the light-hole absorption on the left side of the dependence $h\nu_{23}(\varepsilon_2)$, and $\alpha(\varepsilon_2'')$ is the light-hole absorption on the right side for the same photon energy $h\nu$ (wavelength λ). Thus, to correctly determine the light-hole distribution function it is necessary to estimate the contribution of high-energy holes with energy $\varepsilon_2\geqslant0.09$ eV to $\alpha_{2\exp}$. Results of our experiments indicate a way in which to do this. The method can be described as follows.

It follows from the form of the dependence $h\nu_{23}(\varepsilon_2)$ that the range of energies ε_2'' which can contribute to the absorption coefficient for the energies ε_2' extends from 0.09 to 0.13 eV. For $\varepsilon_2''>0.13$ eV the energy of the photons absorbed by the light holes corresponds to the spectral range for the 1→3 transitions near $\varepsilon_1=0$. Thus, in strong electric fields the heavy-hole absorption α_1 can also be written as the sum of two terms, by analogy with expression (4),

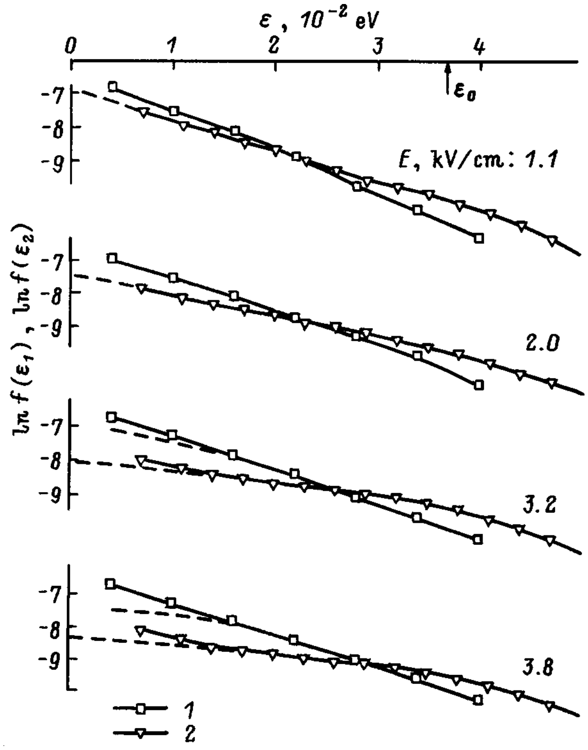

FIG. 2. Distribution functions of the light holes (*1*) and heavy holes (*2*). $T_0=10$ K; $B=2.2$ T; $p=1.6\times10^{15}$ cm^{-3}.

$$\alpha_1|_\lambda=\alpha_1(\varepsilon_1)|_\lambda+\alpha_2(\varepsilon_2'')|_\lambda. \tag{5}$$

Analysis of the heavy-hole distribution function confirms this assumption. Figure 2 plots the logarithms of the light- and heavy-hole distribution functions for different electric field strengths. In fields up to 2 kV/cm $\ln f(\varepsilon_1)$ is rectilinear in the passive region. At the same time, for $E=3.2$ kV/cm and, more visibly, for $E=3.8$ kV/cm, $\ln f(\varepsilon_1)$ exhibits a tendency to increase at lower energies. Since there are no physical reasons explaining this fact if we only consider heavy-hole subbands, it is logical to assume that it is associated with the contribution of high-energy light holes to the measured absorption $\alpha_1|_\lambda$. Thus it is obvious that rectilinear extrapolation of the logarithm of the heavy-hole distribution function into the low-energy region corresponds to its actual values. Next, we use a procedure that is the reverse of reconstructing the distribution function to find the true heavy-hole absorption from the known heavy-hole distribution function $f'(\varepsilon_1)$, i.e., from its values obtained by extrapolation into the low-energy region

$$\alpha_1(\varepsilon_1)=\frac{f'(\varepsilon_1)\alpha_T}{f_T(\varepsilon_1)}. \tag{6}$$

From Eqs. (5) and (6) we find $\alpha_2(\varepsilon_2'')$. Assuming that $f(\varepsilon_2'')$ is the Boltzmann distribution function with temperature T_h,

$$f(\varepsilon_2'')=A\exp\left(-\frac{\varepsilon_2''}{kT_h}\right), \tag{7}$$

and that all the experimental data and the Monte Carlo calculations confirm this assumption,[8] we can reconstruct $f(\varepsilon_2'')$ in explicit form from the two equations (7) (for the two values of the energy ε_2'') for the two unknown values A and T_h. Descending into the energy region $0.09-0.13\,\mathrm{eV}$, we can then find the contribution of the high-energy light holes to the experimentally measured light-hole absorption at a given photon energy. Next, from Eq. (4) we find the ''true'' absorption $\alpha(\varepsilon_2')$ and we find $f_2(\varepsilon_2')$ by the usual technique. The dashed lines in Fig. 2 plot the light-hole distribution function with these corrections taken into account.

Calculations of the light-hole and heavy-hole distribution functions by the Monte Carlo method[8] for the conditions realized in our experiments confirmed the validity of the above-described technique for taking into account the contribution of high-energy light holes to the measured light-hole and heavy-hole absorption. The difference in the gain for $2\rightarrow1$ intersubband transitions in the far-infrared calculated on the basis of the corrected light-hole and heavy-hole distribution functions from its value determined by direct measurements[9] does not exceed 10%. Ignoring these corrections leads to an increase in the divergence from 30 to 60% in the dependence on the applied electric field and the hole concentrations.

We wish to thank L. E. Vorob'ev, D. A. Firsov, and S. N. Danilov for fruitful discussions. This work was carried out with the support of the Ministry of Education (Grant No. 2.4/970 FFD) of the Ukraine and a grant from NATO: HTECH. LG 960931.

[1] A. A. Andronov, V. A. Kozlov, L. S. Mazov, and V. N. Shastin, JETP Lett. **30**, 551 (1979).

[2] E. O. Kane, J. Phys. Chem. Solids **1**, 82 (1956).

[3] W. E. Pinson and R. Bray, Phys. Rev. **136**, 1449 (1964).

[4] L. E. Vorob'ev, Yu. K. Pozhela, A. S. Reklaĭtis, V. I. Stafeev, and A. B. Fedortsov, Fiz. Tekh. Poluprovodn. **12**, 742 (1978) [Sov. Phys. Semicond. **12**, 433 (1978)].

[5] L. E. Vorob'ev, Yu. K. Pozhela, A. S. Reklaĭtis, V. I. Stafeev, and A. B. Fedortsov, Fiz. Tekh. Poluprovodn. **12**, 1585 (1978) [Sov. Phys. Semicond. **12**, 935 (1978)].

[6] L. E. Vorob'ev, F. I. Osokin, V. I. Stafeev, and V. N. Tulupenko, JETP Lett. **34**, 118 (1981).

[7] L. E. Vorob'ev and V. N. Tulupenko, in *Questions of Semiconductor Physics*, Ser. *Current Issues in Semiconductor Physics* [in Russian] (A. F. Ioffe Physicotechnical Institute, Leningrad, 1984), p. 134.

[8] L. E. Vorob'ev, S. N. Danilov, V. I. Stafeev, V. N. Tulupenko, Yu. K. Pozhela, E. V. Starikov, and P. N. Shiktorov, Fiz. Tekh. Poluprovodn. **19**, 1176 (1985) [Sov. Phys. Semicond. **19**, 721 (1985)].

[9] L. E. Vorobjev, S. N. Danilov, V. I. Stafeev, and D. A. Firsov, Laser Phys. **7**, 369 (1997).

Translated by Paul F. Schippnick

Influence of nonuniform spatial distribution of nonequilibrium carriers on the edge emission spectra of direct-gap semiconductors

P. G. Lukashevich

Belorussian State Polytechnical Academy, 220027 Minsk, Belarus

(Submitted February 7, 1997; accepted for publication February 2, 1998)
Fiz. Tekh. Poluprovodn. **32**, 1200–1202 (October 1998)

It is shown that for high single-photon excitation intensities the nonuniform distribution of the nonequilibrium carriers with depth strongly influences the ratio of intensities of different bands and can lead to almost complete suppression of the bands of an electron–hole plasma in the edge emission spectra of crystals. The spreading length of the nonequilibrium electron-hole plasma is estimated. © *1998 American Institute of Physics.* [S1063-7826(98)01210-1]

Calculations (see Refs. 1 and 2) show that a nonuniform distribution of nonequilibrium electron–hole (EH) pairs over a crystal distorts the spectra of the series of recombination emission bands in direct-gap semiconductors. In some cases, one can even expect conversion of one spontaneous emission band into several seemingly independent bands.

A nonuniform distribution of nonequilibrium electron–hole pairs with depth $n(x)$ arises for single-photon excitation of semiconductors.[3] However, there have been no studies of the influence of the profile $n(x)$ on the edge emission spectra of direct-gap compounds under conditions of strong single-photon excitation, when various forms of interactions appear in the ensemble of nonequilibrium carriers and nonlinear recombination mechanism are brought into play.

It is convenient to consider this question in the context of a specific semiconductor material. Figure 1 plots the calculated dependence $n(x)$ for two values of the interband absorption coefficient $k_1=5\times10^4\,\mathrm{cm}^{-1}$ and $k_2=2\times10^4\,\mathrm{cm}^{-1}$ and the case of strong stationary single-photon excitation of a half-infinite sample of zinc telluride. In the approximation of direct interband transitions, the chosen values of the absorption coefficients correspond to excitation of crystals by a nitrogen laser with photon energy $h\nu_{\mathrm{ex}}=3.68\,\mathrm{eV}$ and a dye laser with photon energy $h\nu_{\mathrm{ex}}=2.58\,\mathrm{eV}$. The calculations were based on the technique described in Ref. 3 using the concentration dependence of the lifetime of the electron–hole pairs given in that work. The absorption quantum yield and reflection coefficient of the crystals were taken to be 1 and 0.3, respectively. The diffusion length at low electron–hole concentrations was $L_0=0.5\,\mu\mathrm{m}$, and the temperature $T=5\,\mathrm{K}$.

In the surface region $x<l_1,l_2$, in which the condition of the Mott transition is satisfied and $n>n_{\mathrm{ex}}^M\simeq1.4\times10^{17}\,\mathrm{cm}^{-3}$ (Ref. 4), the electron–hole plasma (EHP) is responsible for the edge emission of zinc telluride; for $x>l_1,l_2$ mainly excitons are responsible for the emission. The volumes of the regions occupied by excitons are greater than the volumes of the regions occupied by electron–hole plasma. Therefore, there are insufficient grounds to expect that the EHP emission band dominates in the edge emission spectra of the samples. However, it follows from Fig. 1 that as the photon energy of the exciting radiation is decreased from 3.68 to 2.58 eV, the volume of the region occupied by the electron-hole plasma will increase by roughly a factor of 2.5. The volume of the region occupied by excitons will increase to a significantly lesser extent. Therefore, it may be expected that when the crystals are excited by radiation with $h\nu=2.58\,\mathrm{eV}$, the relative intensity of the band of the surface electron–hole plasma in the peak-normalized recombination emission spectra will grow.

In the calculations and in what follows we take into account that to obtain the same concentration of electron–hole pairs at the boundaries of the samples, n_0, for different values of $h\nu_{\mathrm{ex}}$ the intensity of the laser radiation should be increased by roughly a factor of 2.5, and the power density P_{ex}, by roughly a factor of 1.8 in the case of dye-laser excitation ($h\nu_{\mathrm{ex}}=2.58\,\mathrm{eV}$).

To test the above hypothesis we studied experimentally the recombination emission of intentionally undoped bulk single crystals of zinc telluride for the indicated photon energies of the exciting radiation. Luminescence was excited by a nitrogen laser ($h\nu_{\mathrm{ex}}=3.68\,\mathrm{eV}$) and a dye laser ($h\nu_{\mathrm{ex}}=2.58\,\mathrm{eV}$) from freshly cleaved samples and studied with the help of a stroboscopic recording system. To reduce the influence of induced emission and to minimize the influence of nonuniformity of the distribution of electron–hole pairs over the excited surfaces on the luminescence spectra, the emission was recorded in a direction approximately normal to the excited surfaces from the center of the excitation spots. The spectral width of the monochromator slit was 0.3 meV, the diameter of the excitation spot was ~0.2 mm, and the temperature was 5 K.

In the recombination emission spectra of crystals excited by photons with energy $h\nu_{\mathrm{ex}}=3.68\,\mathrm{eV}$, a new band with maximum near $h\nu=2.37\,\mathrm{eV}$ appears and develops on the long-wavelength side of the bound-exciton line I_1 (Fig. 2, curves *1* and *2*). It has a complicated contour, which varies with variation of the excitation intensity. For excitation by photons with energy $h\nu_{\mathrm{ex}}=2.58\,\mathrm{eV}$ another band with maximum near $h\nu=2.36\,\mathrm{eV}$ develops on the long-wavelength

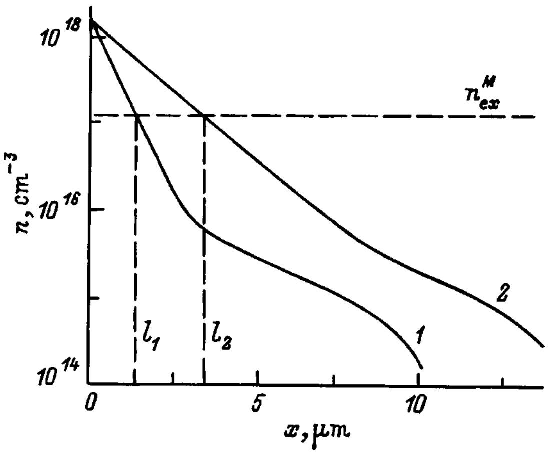

FIG. 1. Calculated dependence of $n(x)$ for $T=5$ K and $L_0=0.5\,\mu$m. *1* — $h\nu_{ex}=3.68$ eV, $P_{ex}=3\,MW/cm^2$; *2* — $h\nu_{ex}=2.58$ eV,$P_{ex}=5.4\,MW/cm^2$.

limb (curves *3* and *4*). In some crystals the intensity (I) of this band can even exceed the intensity of the 2.37-eV band. These results are in good agreement with the known experimental data.[5,6]

Under excitation conditions with $h\nu_{ex}=2.58$ eV and $P_{ex}=2\,MW/cm^2$ lower concentrations of nonequilibrium electron–hole pairs were reached near the excited surfaces than for excitation with $h\nu_{ex}=3.68$ eV and $P_{ex}=3\,MW/cm^2$. Therefore, the luminescence of the 2.36-eV band at $h\nu_{ex}=2.58$ eV cannot be due to the development of a new recombination mechanism characteristic of an ensemble of nonequilibrium carriers with higher density. This is also indicated by the fact that under excitation with $h\nu=3.68$ eV this band is not destroyed even up to the point at which the excited surfaces of the samples are destroyed.

The depth of the region occupied by the ensemble of nonequilibrium electron–hole pairs is small and does not vary substantially as $h\nu_{ex}$ is decreased. For this reason, it is not possible to link the band at 2.36 eV exclusively with induced emission at the frequencies of the 2.37-eV band.

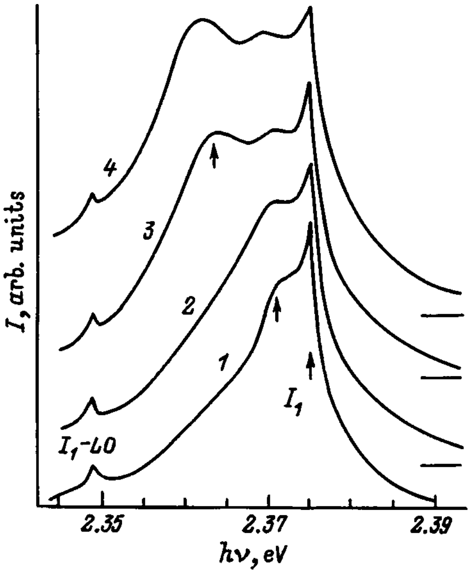

FIG. 2. Emission spectra of ZnTe crystals at $T=5$ K. $h\nu_{ex}$ eV: *1, 2* — 3.68; *3, 4* — 2.58. P_{ex}, MW/cm^2: *1* — 1.5, *2* — 3, *3* — 2.7, *4* — 5.4.

It follows from an earlier analysis (Fig. 1) that the 2.36-eV band is due to recombination of charge carriers in the surface EHP, whose volume increases significantly as $h\nu_{ex}$ drops from 3.68 to 2.58 eV. In the case of excitation by a nitrogen laser, because of its small volume, the EHP participates only in the formation of the long-wavelength limb of the band at 2.37 eV, although substantially greater values of n_0 are reached in this case than for $P_{ex}=1\,MW/cm^2$ and $h\nu_{ex}=2.58$ eV, for which it shows up clearly in the spectra.

In the foregoing discussion, I presented a simplified analysis of the influence of nonuniformity of the nonequilibrium carrier distribution on the edge emission spectra of direct-gap semiconductors under intense laser excitation. I assumed that the EHP can have only one emission band. In reality, the situation is somewhat more complicated. The electron–hole plasma in ZnTe crystals, like free excitons in CdS crystals (see Ref. 7), has two bands under conditions of recombination with creation of mixed plasmon–phonon modes. The band at 2.36 eV is due to recombination of electron–hole pairs with creation of mixed plasmon–phonon modes L_+, and the band near 2.37 eV is due to recombination of electron–hole pairs in the EHP with creation of L_- modes (see Ref. 4). It overlaps the bands due to exciton recombination with creation of L_- modes and inelastic exciton–exciton collisions and is masked by them and is not resolved in the emission spectra of the investigated samples.

Thus, this work shows that at high densities of single-photon excitation the nonuniform distribution of nonequilibrium carriers with depth exerts a strong influence not only on the contours of individual bands, but also on the ratio of the intensities of different bands in the edge emission spectra of direct-gap crystals. When nonequilibrium electrons are excited deep into the conduction band, large values of the interband absorption are reached. This absorption may lead to masking and even to almost complete suppression of the emission bands of the electron–hole plasma.

Let us finally consider an important fact. In Ref. 8 it was found that in crystals of cadmium sulfide entrainment of nonequilibrium excitons by phonons disappears for exciton lifetimes $\tau_{ex}\lesssim 2\times10^{-9}$ s. The calculations of $n(x)$ disregarded spreading of the nonequilibrium electron–hole pairs as a result, e.g., of the phonon wind (see Ref. 9). Clearly, if the spreading length constant of the electron–hole pairs in the surface EHP exceeds $l_0\sim 3k_2^{-1}\sim 1\,\mu$m in the approximation of exponential depth distributions $n(x)$, the edge emission spectra and consequently also the spatial distribution of the electron–hole pairs in the EHP could not depend so strongly on the photon energy of the exciting radiation. Therefore, on the basis of the above-mentioned data,[8] calculations of the depth distributions $n(x)$,[3] and the preceding study we can conclude that at low temperatures the nonequilibrium electron–hole plasma in II–VI compounds with lifetimes of the electron–hole pairs $\sim 10^{-10}$ s has a spreading length constant no greater than 1 μm.

[1] A. A. Klochikhin, D. K. Nel'son, B. S. Razbirin, M. A. Yakobson, G. O. Myuller, and V. D. Egorov, Fiz. Tverd. Tela (Leningrad) **29**, 1123 (1987) [Sov. Phys. Solid State **29**, 641 (1987)].

[2] P. G. Lukashevich, Fiz. Tekh. Poluprovodn. **29**, 2002 (1995) [Semiconductors **29**, 1044 (1995)].

[3] P. G. Lukashevich, Fiz. Tekh. Poluprovodn. **29**, 1253 (1995) [Semiconductors **29**, 648 (1995)].

[4] P. G. Lukashevich, V. N. Pavlovskiĭ, and V. A. Samoĭlyukovich, Fiz. Tekh. Poluprovodn. **23**, 578 (1989) [Sov. Phys. Semicond. **23**, 390 (1989)].

[5] M. Kwietniak, *Zjawiska Luminescencji w ZnTe* [*Luminescence Phenomena in ZnTe*, in Polish] (Wroclaw–Warszawa–Krakow–Gdansk, PAN, 1980).

[6] P. G. Lukashevich and V. A. Ivanov, Zh. Prikl. Spektrosk. **36**, 160 (1980).

[7] N. N. Zinov'ev and I. D. Yaroshetskiĭ, Fiz. Tekh. Poluprovodn. **14**, 464 (1980) [Sov. Phys. Semicond. **14**, 274 (1980)].

[8] N. N. Zinov'ev and I. D. Yaroshetskiĭ, JETP Lett. **33**, 584 (1981).

[9] *Electron–Hole Drops in Semiconductors* [in Russian], edited by C. D. Jeffries and L. V. Keldysh (Nauka, Moscow, 1988).

Translated by Paul F. Schippnick

SEMICONDUCTORS VOLUME 32, NUMBER 10 OCTOBER 1998

SEMICONDUCTOR STRUCTURES, INTERFACES, AND SURFACES

Optoelectronic phenomena in GaAs and GaP layers prepared by nitrogen treatment

V. F. Agekyan

St. Petersburg State University, 198904 St. Petersburg, Russia

V. I. Ivanov-Omskiĭ, V. N. Knyazevskiĭ, and Yu. V. Rud'

A. F. Ioffe Physicotechnical Institute, Russian Academy of Sciences, 194021 St. Petersburg, Russia

V. Yu. Rud'

St. Petersburg State Technical University, 195251 St.Petersburg, Russia

(Submitted February 19, 1998; accepted for publication February 24, 1998)
Fiz. Tekh. Poluprovodn. **32**, 1203–1205 (October 1998)

Plasma processing of single-crystal wafers of gallium arsenide and gallium phosphide is employed to obtain thin wideband layers. The spectral dependence of the photoluminescence of the layers and of the photosensitivity of the corresponding layer/substrate structures is investigated. An analysis of the results of these studies gives us reason to believe that the described process leads to replacement of arsenic and phosphorus atoms by nitrogen and to the formation of wideband layers of solid solutions on the surface of the indicated semiconductors. © *1998 American Institute of Physics.* [S1063-7826(98)01310-6]

INTRODUCTION

It is generally known what importance nitrides of group-III elements have acquired since Nakamura and coworkers demonstrated the efficiency of GaN-based optoelectronic devices.[1] GaAs and GaP are frequently used as the substrates for growing epitaxial GaN layers and heterostructures based on it. An important element of the technology here is the operation of preliminary nitrogen treatment of the substrate surface, performed in a nitrogen plasma discharge. The electronic properties of the arising transitional layer have not been adequately investigated. In the present article we report the results of a study of the photoelectrical properties and photoluminescence of layers formed on the surface of single-crystal GaAs and GaP substrates during treatment in a nitrogen gas discharge plasma.

SAMPLES

Single-crystal wafers of *n*-GaAs and *n*-GaP oriented in the (100) plane with free electron concentration $n = 10^{17}\,\mathrm{cm}^{-3}$ were subjected to nitrogen treatment at $T = 300\,\mathrm{K}$. For this purpose, the wafers were placed in a screened cavity in a metal vacuum chamber with vacuum on the order of 2×10^{-6} Torr. In the first stage of the process, hydrogen was admitted to the chamber at pressures up to those permitting a stable constant-current gas discharge, after which the GaAs or GaP wafer was processed in a hydrogen plasma at temperatures of about 50 °C for 5 min. Immediately after this procedure, the chamber was flushed with nitrogen and at pressures about 8×10^{-2} Torr an rf discharge at a frequency of 13.6 MHz was ignited. The temperature of the wafers was raised to 500 °C and they were processed for 20 min with the current through the plasma equal to $30-40$ mA.

PHOTOELECTRIC PROPERTIES OF LAYER/SUBSTRATE STRUCTURES

Immediately after creation of the layers we measured the photoelectric properties of the structures. Toward this end, samples were cleaved from the structures having mean dimensions of $2\times2\times0.3$ mm. After ohmic contacts of pure indium were created on the layers and on the substrates, the substrates were mounted in the housings of mass-produced diodes.

Illumination of such structures by unfiltered or monochromatic focused radiation (with a diameter of 0.1 mm) from the side of the layers and from the side of the substrates resulted in the appearance of a photovoltaic effect. In all of the investigated structures the sign of the photovoltage was independent of the spectral composition of the light and the energy of the incident photons and also the location of the light probe on the surface of the structures. This suggests that separation of photogenerated pairs takes place in a single active region that arises as a result of the formation of the layer on substrates of the two different semiconductor compounds. The photosensitivity of such structures is maximal when they are illuminated from the side of the layers and for the better structures reaches 10^4 V/W at $T = 300$ K.

Typical spectral curves of the relative quantum efficiency of photoconversion, defined as the ratio of the short-circuit photocurrent to the number of incident photons, are plotted in Fig. 1 (curves *1* and *2*). The long-wavelength

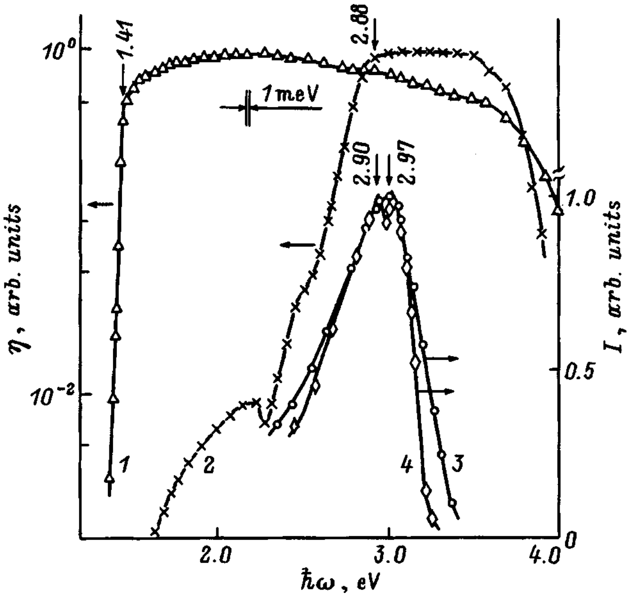

FIG. 1. Spectral dependence of the relative quantum efficiency η of GaAs/layer (*1*) and GaP/layer (*2*) heterocontacts at 300 K and photoluminescence of the layers in GaAs (*3*) and GaP (*4*) at 80 K. Spectra *1* and *2* were obtained for illumination from the layer side.

boundary of the photosensitivity of the structures is determined by the substrate material. In the case of layer/GaAs structures, the long-wavelength growth of the quantum efficiency is exponential with semilog slope equal to $s = 40 - 50\,\mathrm{eV}^{-1}$. The spectral position of the long-wavelength edge of the photosensitivity of these structures may be due to direct interband transitions in gallium arsenide. With growth of the photon energy over the wide spectral range $1.7 - 2.7$ eV, the photosensitivity remains nearly constant, which indicates a low level of optical absorption of the layer in the indicated spectral range, on the one hand, and a high efficiency of separation of photogenerated pairs in the electric field of the layer/GaAs heterojunction, on the other. The full width of the photosensitivity spectra of such structures at half-maximum (FWHM) $\delta_{1/2}$ reaches 2.2 eV. The wideband character of the photoconversion taking place in these structures indicates that the layer is a wideband layer relative to the substrate material (GaAs), and that the interface region of these structures is of high quality. Note that when these structures are illuminated from the side of the 0.3-mm-thick substrates, the photosensitivity spectrum transforms into a narrow selective spectrum ($\delta_{1/2} = 25 - 35$ meV) due to abrupt growth of the optical absorption as the photon energy approaches the width of the GaAs band gap.

Layer/GaP structures (see Fig. 1, curve *2*) also manifest wideband photosensitivity when illuminated from the layer side. The lower value of $\delta_{1/2} = 0.9$ eV is due to the larger band gap of GaP relative to GaAs, which also causes a sizable shift of the long-wavelength edge of the photosensitivity of the layer/GaP heterojunctions toward higher photon energies. The spectral contour of the long-wavelength edge of the photosensitivity of these structures is governed by absorption in GaP and is characteristic for gallium-phosphide photoconverters.[2,3] The main peculiarity of these photosensitive structures based on two different binary compounds with widely different band gaps is the fact that the onset of the short-wavelength falloff is localized about a common photon energy $\hbar\omega$ above 3.4 eV. This circumstance may be due to the effect of absorption in thin wideband layers, for which the width of the band gap is similar for different structures and exceeds the width of the band gap of the substrate materials. Growth of the width of the band gap in the layers relative to the initial substrates, with allowance for the special features of the growth process developed by us, may be a consequence of replacement of As or P atoms in the substrates by nitrogen atoms.

PHOTOLUMINESCENCE OF THE LAYERS

Typical spectral curves of the photoluminescence (PL) of the layers formed during the implemented production process on the surface of GaAs and GaP single crystals are plotted in Fig. 1 (curves *3* and *4*). Photoluminescence was excited by a pulsed nitrogen laser ($\hbar\omega = 3.68$ eV) with a pulse duration of 2 ns and pulse repetition rate equal to 100 Hz. The spectral curves of the photoluminescence plotted in the figure were measured in the stroboscopic regime with a delay time relative to the exciting pulse $\tau = 0$ s for a time constant of 100 ns.

Visually, the photoluminescence at 80 K in the localization region of the exciting light probe on the surface of the layers formed on the GaAs and GaP substrates has the form of a blue band, within the limits of which in a number of samples it is possible to distinguish points whose brightness exceeds that of the blue band. As can be seen from the figure, for layers on substrates of GaAs and GaP the recombination radiation has the form of a wide, structureless, asymmetrical band, whose maximum is centered in the vicinity of 3 eV, which is substantially higher than the width of the band gap of either GaAs or GaP and is in qualitative agreement with the data presented above on the photosensitivity of the layer/substrate structures. The full width at half-maximum $w_{1/2}$ of the photoluminescence bands for the layers on GaAs is equal to 630 meV, where the long-wavelength width $w_l = 380$ meV exceeds the short-wavelength width $w_s = 250$ meV. In the case of the layers on GaP we have $w_{1/2} = 550$ meV ($w_l = 410$ meV, $w_s = 180$ meV) at $T = 80$ K. For the layers on GaP, a doublet structure of the photoluminescence maximum was also detected (curve *4*). The large values of the photoluminescence bandwidths indicate that the bands responsible for the observed radiation are of a non-elementary nature and their identification will require further study.

The main result of our photoluminescence studies is that the developed production process results in an increase in the width of the band gap of the GaAs or GaP substrate, which may be a result of replacement of As or P by nitrogen.

[1] S. Nakamura, M. Senoh, N. Iwasa, S. Nagahama, T. Yamada, and T. Mukai, Jpn. J. Appl. Phys. **30**, 1998 (1991).
[2] Yoshida, J. Cryst. Growth **136**, 37 (1994).
[3] S. G. Konnikov, V. Yu. Rud', Yu. V. Rud', D. Melebaev, A. Berkeliev, M. Serginov, and S. Televov, Jpn. J. Appl. Phys. **32S**, 515 (1993).

Translated by Paul F. Schippnick

SEMICONDUCTORS VOLUME 32, NUMBER 10 OCTOBER 1998

Photoelectric properties of GaN/GaP heterostructures

V. M. Botnaryuk and S. D. Raevskiĭ

State University of Moldova, MD2009 Kishinev, Moldova

V. V. Bel'kov, Yu. V. Zhilyaev, Yu. V. Rud', and L. M. Fedorov

A. F. Ioffe Physicotechnical Institute, Russian Academy of Sciences, 194021 St. Petersburg, Russia

V. Yu. Rud'

St. Petersburg State Technical University, 195251 St. Petersburg, Russia
(Submitted April 1, 1998; accepted for publication April 3, 1998)
Fiz. Tekh. Poluprovodn. **32**, 1206–1210 (October 1998)

Thin interference layers of *n*-GaN were grown on *n*- and *p*-type GaP substrates with (100) and (111) orientations by vapor phase epitaxy in an open chloride system. Photosensitivity spectra of isotypic and anisotypic heterojunctions under linear polarized light from the side of the wideband component (GaN) at oblique incidence were investigated. Induced polarized photosensitivity was observed, and peculiarities of this photosensitivity caused by interference in the GaN layers are discussed. © *1998 American Institute of Physics.* [S1063-7826(98)01410-0]

The creation of epitaxial layers of gallium nitride and heterostructures based on them is of great interest in short-wavelength semiconductor optoelectronics because of the favorable combination of fundamental parameters of this material.[1–4] Note that the photoelectric properties of GaN and device structures based on it have not been adequately investigated, and the studies that exist were performed only with unpolarized light. In the present paper we report the results of the first studies of photoelectric phenomena in heterojunctions created by deposition of GaN layers on single-crystal wafers of *n*- and *p*-type gallium phosphide.

1. p^+-GaP/n^+-GaN and n^+-GaP/n^+-GaN heterojunctions were prepared in the following way. Single-crystal wafers of *n*- and *p*-type gallium phosphide with free-charge-carrier concentration in the range $(5-10)\times10^{17}\,\mathrm{cm}^{-3}$ at $T=300\,\mathrm{K}$, with 0.4 mm thickness and (100) and (111) orientations, were etched in a saturated aqueous solution of HCl $+\mathrm{K_2Cr_2O_3}+\mathrm{H_2O}$ for 10 min. They were then washed in deionized water, dried in isopropanol vapor, and placed in a reactor for growing gallium-nitride layers. Growth took place in an open Ga–HCl–$\mathrm{NH_3}$–$\mathrm{H_2}$ gas-transport system. The temperature in the deposition zone was 900 °C. Under these conditions thin ($\approx0.5\,\mu$m), uniformly colored layers of gallium nitride were formed on the GaP substrates, which varied in color from red to a dark lilac, depending on the growth conditions. The layers exhibit high adhesion to the substrate and have a free electron concentration of $10^{19}-10^{20}\,\mathrm{cm}^{-3}$ at $T=300\,\mathrm{K}$. Note also that the described growth method leads to the formation of mirror-smooth GaN layers, regardless of the orientation of the substrates. The created GaP/GaN heterojunctions had average dimensions of 10×10 mm and were mounted on a Fedorov stage to perform the polarized photosensitivity measurements. This made it possible to vary the angular coordinates of the receiving plane with an accuracy of 30′ or better. Monochromatic, linearly polarized light (LPL) was produced with the help of an SPM-2 monochromator with a $\mathrm{SiO_2}$ prism and a set of polarization filters.

2. As follows from measurements of the steady-state current–voltage characteristics (CVC), all of the isotypic and anisotypic heterojunctions fabricated by the indicated technique reveal a sharp rectification. A typical CVC of one of the heterojunctions is shown in Fig. 1. Forward bias in the overwhelming majority of the heterojunctions corresponds to positive polarity of the external bias on the *n*-GaN layer. For forward biases $U>U_0$ the current in the investigated heterojunctions grows with the voltage according to the linear law

$$I=\frac{1}{R_0}(U-U_0),$$

where R_0 is the residual resistance. For the investigated heterojunctions, R_0 varied over wide limits (from 10^3 to $10^7\,\Omega$), and the cutoff voltage varied in the interval $0.7-2.0$ V (it increased with increasing R_0). In the region of small forward currents the CVC's of the investigated heterojunctions are consistent with the standard diode equation

$$I=I_s(e^{\frac{eU}{nkT}}-1),$$

and the ideality factor takes a high value $n=4-5$, which is probably due to the influence of the high series resistance. For the better heterojunctions the reverse current at room temperature is 2×10^{-9} A for a reverse bias $U_{\mathrm{rev}}=2$ V. Note also that the orientation of the GaP substrates has hardly any effect on the observed regularities in the CVC's of the investigated structures.

3. Exposure of the heterojunctions to unpolarized light gives rise to a photovoltaic effect which is attributable to separation of the nonequilibrium charge carriers of the common active region that forms at the GaP–GaN contact. This conclusion is based on the fact that the photovoltage does not change sign, regardless of the magnitude of the change in the

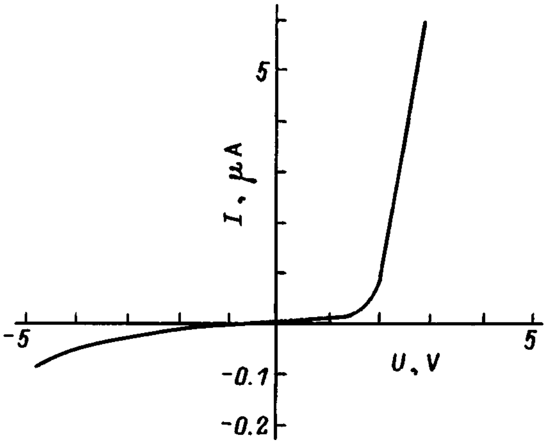

FIG. 1. Stationary current–voltage characteristic of GaN/n-GaP heterojunctions at $T=300$ K. (The pass-through direction corresponds to positive polarity of the external bias on the GaN layer, sample 107-3n.)

localization of the light probe or in the wavelength of the exciting light. The the sign of the photovoltage and the sign of the pass-through voltage of the hypothetical band diagram of the heterocontact agreed for all of the investigated heterojunctions. The maximum voltage photosensitivity in the heterojunctions is observed when they are illuminated from the side of the wideband (GaN) layer and for better samples reaches 10^3 V/W at $T=300$ K. Figure 2 plots typical spectral curves of the relative quantum efficiency of photoconversion η, calculated as the ratio of the short-circuit photocurrent i to the number of incident photons of natural light. It can be seen from Fig. 2 that when the heterojunctions are illuminated from the side of the GaN layer η was found to vary over six or seven orders of magnitude in the spectral range $0.8-3.5$ eV. Comparison of the spectral dependence of η for the investigated heterojunctions (Fig. 2) with the analogous dependence for GaP-based surface-barrier structures[5–7] allows us to link the long-wavelength part of these curves (for photon energies $\hbar\omega<3$ eV) with photoactive absorption in the narrowband component of the heterojunction. The photosensitivity in the region of the band $\hbar\omega<2.2$ eV, as can be seen from Fig. 2, varies widely from sample to sample. This may be due to differences in the concentrations and types of defects in the substrate material. These differences may be due to the particular features of the initial substrate parameters and due to the influence of the growth conditions of the GaN layers. The growth of η starting at $\hbar\omega>2.25$ eV and the inflection points at 2.70 and 2.80 eV are well reproduced in the photosensitivity spectra of all the investigated heterojunctions and are due to indirect and direct interband optical transitions in the energy spectrum of the narrow-band component.[6]

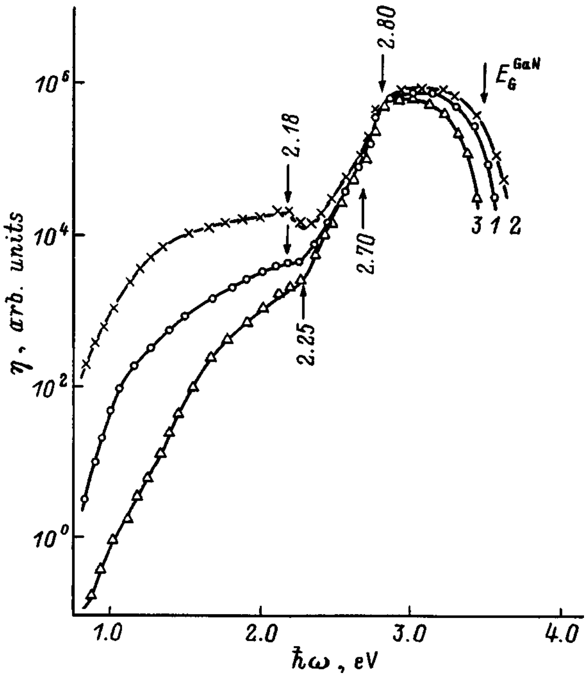

FIG. 2. Spectral dependence of the relative quantum efficiency of photoconversion η of GaN/GaP heterojunctions in unpolarized light at $T=300$ K. (*1* — GaN/n-GaP, sample 107-3n; *2* — GaN/p-GaP, sample 106-1p;*3* — GaN/p-GaP, sample 107-1p, illumination from the side of the GaN layer normal to the layer surface).

The maximum photosensitivity of the investigated heterojunctions, as can be seen from Fig. 2, is observed in the interval between the widths of the band gaps of the contacting semiconductors GaN and GaP. If surface recombination in the GaP-based surface-barrier structures is efficiently suppressed, and if the short-wavelength falloff of η is essentially eliminated,[6] then for all of the heterojunctions investigated in this study the falloff of the photosensitivity starts to be discernible at photon energies $\hbar\omega>3-3.2$ eV for different samples and becomes precipitous near the width of the GaN band gap, $E_g\approx3.5$ eV. This has to do, first of all, with the onset of strong absorption by the wideband layer and recombination of carriers in the active region of such heterojunctions, as is indicated by the magnitude of their ideality factor $n>2$. The wideband character of the photosensitivity of these heterojunctions relative to the light intensity is characterized by a half-width at half-maximum of the η spectra in the region $\delta_{1/2}=0.5-0.7$ eV for different samples.

4. Studies in linearly polarized light have shown that when the angle of incidence of the linearly polarized light $\Theta=0°$, no sensitivity of the photocurrent to changes in the orientation of the electric field vector **E** relative to the principal crystallographic axes of the substrate is observed in the entire photosensitivity region for all the heterojunctions. This circumstance allows us to conclude that the given direction of propagation of linearly polarized light in the investigated heterojunctions is photoisotropic and, consequently, the natural photopleochroism is equal to zero.[8] When the angle of incidence is different from zero, a difference begins to show up between the photocurrents for the case where **E** lies in the plane of incidence of the incident light (i^p) and when it is perpendicular to it (i^s). This inequality takes the form $i^p>i^s$ in the entire photosensitivity region of the heterojunction. An example of the angular dependences $i^p(\Theta)$ and $i^s(\Theta)$ is given in Fig. 3 for illumination with photon energies near E_g^{GaN}. Similar angular dependences of the photocurrents turned out to be characteristic of the entire photosensitivity region. It can be seen that in contrast to the surface-barrier structures and GaP/Si heterojunctions,[5–7,9–12] for both polar-

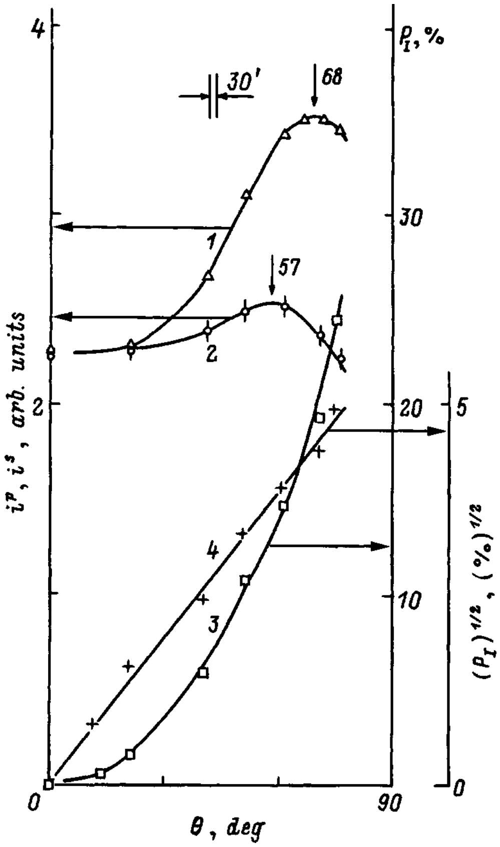

FIG. 3. Dependence of the short-circuit photocurrent (*1* — i^p,*2* — i^s) and induced photopleochromism (*3, 4*) of a GaN/*p*-GaP heterojunction on the angle of incidence of linearly polarized light onto the GaN plane at $T = 300$ K. (Sample 106-1*p*, $\lambda = 0.355\,\mu$m.)

izations the photocurrent at first increases with Θ, then passes through a maximum, and then starts to fall. This trend seems to indicate that for both polarizations an increase in Θ is accompanied by a reduction of reflection losses. Taking the results of Refs. 13 and 14 into account, this trend can be linked with interference effects in the wideband GaN layer. Obviously, the clearing effect is maximized if the photocurrents approach each other $i^s \rightarrow i^p$. As a result, the induced photopleochroism coefficient P_1 tends to zero. As can be seen from Fig. 3, increasing the angle of incidence (curves *3* and *4*) is accompanied by an increase in $P_1 \sim \Theta^2$ as in the absence of interference.[5–7]

Figure 4 plots the spectral dependence of P_1 for two different heterojunctions for $\Theta = \text{const}$. It can be seen that for the investigated heterojunctions the induced photopleochroism experiences oscillations which are due to interference. It is characteristic that the energy positions of the minima and maxima of the two different heterojunctions are different. This is due to differences in the parameters of the GaN layers, which causes the corresponding differences in the $P_1(\hbar\omega)$ spectra. An estimate of the layer thickness based on the spectral position of neighboring maxima of P_1 (Fig. 4, curve *1*) and the index of refraction of GaN (Ref. 15) gives $d_c \approx 0.3\,\mu$m, which agrees with the measured value of the thickness of the GaN layer.

The presence of oscillations in P_1 thus characterizes the GaN layers as being of high quality and uniform. On the other hand, the observed oscillations allow us to conclude that fabrication of heterojunctions with thin interference layers can find application in the production of tunable selective photoanalyzers of linearly polarized light.

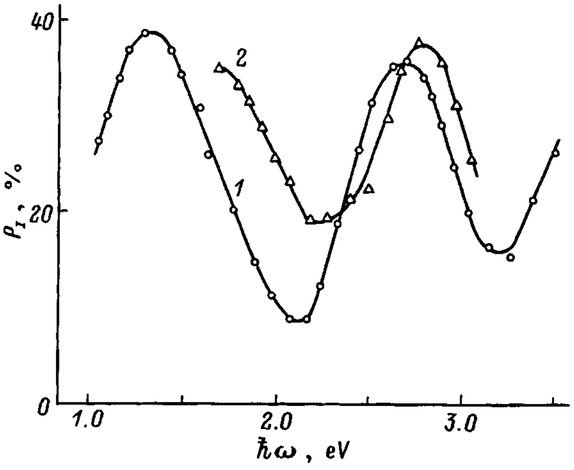

FIG. 4. Spectral dependence of the induced photopleochromism of a GaN/GaP heterojunction at $T = 300$ K. (*1* — sample 106-1*p*, *2* — sample 107-2*n*, $\Theta = 75°$).

[1] S. Nakamura, M. Sench, N. Iwasa, S. Nagahawa, T. Yamada, and T. Mukai, Jpn. J. Appl. Phys. Pt. 2, **34**, L1332 (1995).

[2] S. Nakamura, M. Sench, Y. Nagahawa, N. Iwasa, T. Yamada, T. Matsushita, H. Kiyoko, and Y. Sugimoto, Appl. Phys. Lett. **68**, 3269 (1996).

[3] Y. C. Yeo, T. C. Chong, and M. F. Li, J. Appl. Phys. **83**, 1429 (1998).

[4] J. C. Carrano, T. Li, P. A. Grudowski, C. J. Eiting, R. D. Dupuis, and J. C. Campbell, Appl. Phys. Lett. **72**, 542 (1998).

[5] S. G. Konnikov, D. Melebaev, V. Yu. Rud', M. Serginov, S. Tilevov, and Zh. Khanov, Pis'ma Zh. Tekh. Fiz. **18**, No. 24, 11 (1992) [Sov. Tech. Phys. Lett. **18**, 798 (1992)].

[6] S. G. Konnikov, D. Melebaev, V. Yu. Rud', A. Berkeliev, M. G. Durdymuradova, and O. V. Kornyakova, Pis'ma Zh. Tekh. Fiz. **19**, 57 (1993) [Tech. Phys. Lett. **19**, 23 (1993)].

[7] S. G. Konnikov, V. Yu. Rud', Yu. V. Rud', D. Melebaev, A. Berkeliev, M. Serginov, and S. Tilevov, Jpn. J. Appl. Phys. **32**, Suppl. 32–3, 545 (1993).

[8] F. P. Kesamanli, V. Yu. Rud', and Yu. V. Rud', Fiz. Tekh. Poluprovodn. **30**, 1921 (1996) [Semiconductors **30**, 1001 (1996)].

[9] V. Yu. Rud', M. Serginov, and S. Tilevov, Pis'ma Zh. Tekh. Fiz. **18**, 50 (1992) [Sov. Tech. Phys. Lett. **18**, 44 (1992)].

[10] S. G. Konnikov, D. Malebaev, V. Yu. Rud', and L. M. Fedorov, Pis'ma Zh. Tekh. Fiz. **18**, 11 (1992) [Sov. Tech. Phys. Lett. **18**, 8 (1992)].

[11] Yu. V. Zhilyaev, N. Nazarov, V. Yu. Rud', Yu. V. Rud', and L. M. Fedorov, Fiz. Tekh. Poluprovodn. **27**, 1611 (1993) [Semiconductors **27**, 1540 (1993)].

[12] A. Berkeliev, Yu. V. Zhilyaev, N. Nazarov, V. Yu. Rud', and Yu. V. Rud', Fiz. Tekh. Poluprovodn. **28**, 14 (1994) [Semiconductors **28**, 8 (1994)].

[13] T. Val'ter, V. Yu. Rud', Yu. V. Rud', and G. V. Shok, Fiz. Tekh. Poluprovodn. **31**, 806 (1997) [Semiconductors **31**, 681 (1997)].

[14] V. M. Botnaryuk, A. V. Koval', A. V. Simashkevich, D. A. Shcherban, V. Yu. Rud', and Yu. V. Rud', Fiz. Tekh. Poluprovodn. **31**, 800 (1997) [Semiconductors **31**, 677 (1997)].

[15] *Selected Topics in Electronics and Systems*, Vol. 4, *Compound Semiconductor Electronics: The Age of Maturity*, edited by M. Shur (World Scientific, 1996).

Translated by Paul F. Schippnick

SEMICONDUCTORS VOLUME 32, NUMBER 10 OCTOBER 1998

Photoluminescence of the space charge region of metal–zinc selenide contacts

V. P. Makhniĭ and M. M. Sletov

Yu. Fed'kovich Chernovtsy State University, 274012 Chernovtsy, Ukraine

(Submitted December 16, 1997; accepted for publication April 8, 1998)
Fiz. Tekh. Poluprovodn. **32**, 1210–1212 (October 1998)

The results of a study of photoluminescence excited by a nitrogen laser in the space charge region of Ni–ZnSe contacts are presented. It is found that the photoluminescence intensity is modulated not only in the presence of an external voltage but also in its absence, and that it depends on the diode switching regime: no load or short circuit. A physical interpretation of the results is given. © *1998 American Institute of Physics.* [S1063-7826(98)01510-5]

The presence of a strong electric field in a semiconductor crystal has a substantial effect on radiative recombination of the nonequilibrium charge carriers.[1] Conditions for studying such processes can be easily realized in structures with a rectifying barrier—heterojunctions[2,3] or Schottky diodes.[1] In such structures, one observes, in particular, modulation of the photoluminescence intensity by the barrier electric field. In this paper we report the results of a study of such phenomenon in Ni–ZnSe contacts.

As the starting substrates we used low-resistance *n*-ZnSe crystals that contain isovalent tellurium impurity. A characteristic feature of these samples is the presence of an efficient ($\sim 20\%$ at 300 K) orange γ-luminescence band that possesses a high thermal and radiation hardness.[4] The technology of fabricating the diode structures is described in Ref. 5. The choice of Ni as the rectifying contact is dictated by the fact that it forms a high potential barrier with *n*-ZnSe (Ref. 6), and thin nickel films possess good transparency in the spectral range $0.2-1\ \mu$m (Ref. 7). Photoluminescence was excited by a nitrogen laser with $\lambda_m = 0.34\ \mu$m, and the spectra were measured using an MDR-23 monochromator and a lock-in detector system with automated recording. Since the ionized donor concentration in the diode substrates varies in the range $10^{16}-10^{17}\ \mathrm{cm}^{-3}$, the width of the space charge region (SCR) at zero bias varies in the range $(5-15) \times 10^{-5}$ cm. On the other hand, the absorption α of ZnSe at λ_m is not less than $5 \times 10^4\ \mathrm{cm}^{-1}$ (Ref. 8) and, accordingly, the absorption length $\alpha^{-1} \leqslant 2 \times 10^{-5}$ cm. We can conclude, therefroe, that at zero bias the laser radiation is almost completely absorbed in the space charge region of the diode.

The photoluminescence spectrum of the Ni–ZnSe contact at zero bias consists of a wide band with its peak at about $0.64\ \mu$m (Fig. 1). Emission is due to transitions of free electrons to a deep acceptor level, which is attributable to the complex group,[4] which consists of doubly charged Frenkel' pairs of the cation sublattice and a neutral atom of the isovalent tellurium impurity. The magnitude and sign of the external voltage do not alter the position of the peak of the emission band; however, they affect its intensity and shape. Photoluminescence spectra are shown in Fig. 1, of which spectra *1–3* are peak-normalized. Increasing the reverse bias V_r leads to a smooth deformation of the the long-wavelength limb of the photoluminescence band (see Fig. 1), which may be due to the Franz–Keldysh effect. The forward bias voltage V_s compensates for the contact barrier, and the shape of the spectrum in this case approaches that of the neutral crystal.[4]

The intensity I_{PL} of photoluminescence depends substantially on the magnitude and sign of the voltage applied to the diode with V_r having a stronger effect than V_s (Fig. 2). The decrease of I_{PL} with increasing V_r is due to an increase in the fraction of electron–hole pairs separated by the barrier electric field that do not participate in radiative recombination. Note that a steeper dependence of $I_{PL}(V)$ is observed for structures with higher concentration of ionized donors in the diode substrate. This is explained by an increase in the electric field strength (for the same value of V) with growth of the doping level. The same figure plots the dependence of the photocurrent I_p on V for the same two diodes (with different doping levels). For a specific value of the reverse bias voltage the following empirical relationship roughly holds for each sample:[2,3]

$$I_{PL} + I_P = \mathrm{const.} \tag{1}$$

The increase in I_{PL} for forward bias is the result of a decrease in the fraction of carriers separated by the barrier electric field. The latter decreases with increasing V_s, and the probability for the radiative recombination increases.

The photoluminescence intensity I_{PL} of the investigated samples was also found to depend on the switching regime of the structure in the absence of an external voltage. However, in contrast to the results reported in Ref. 3, the photoluminescence intensity of the Ni–ZnSe diodes for open contacts I_{PL}^{∞} was lower than for shorted contacts I_{PL}^{0} (Fig. 1). The shape of the spectrum in this case remains unchanged, but the ratio $K_m = I_{PL}^{0}/I_{PL}^{\infty}$ increases with decreasing excitation level. (Note that $K_m = 1.65$ for curve *4* in Fig. 1.) The above-noted experimental results can be explained as follows.

According to Ref. 6, the height of the potential barrier V_c of metal–ZnSe contacts depends not only on the work function of the metal but also on the surface levels at the interface. They are distributed quasicontinuously in a wide energy interval, and their density is about $5 \times 10^{12}\ \mathrm{cm}^{-2}$. In the no-load (open circuit) regime the photocarriers are separated by the barrier electric field. The electrons migrate into

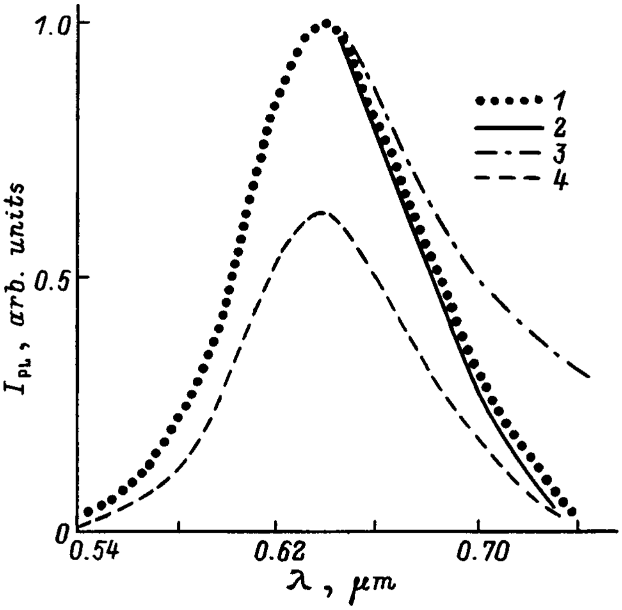

FIG. 1. Photoluminescence spectra in different switching regimes of the Ni–ZnSe contact: *1* — The short-circuit regime, *2* — $V=1$ V, *3* — $V=-6$ V, *4* — the no-load regime. $T=300$ K.

the quasineutral region of the crystal and the holes migrate to the metal–semiconductor interface. Here the holes can be captured by the surface levels at which the electrons are found. Thus, some of the nonequilibrium holes are excluded from the process of radiative recombination, which accounts for the decrease in I_{PL}. The concentration of holes at the surface levels increases with increasing excitation level. The excess positive charge limits the hole flux to the surface, causing the photoluminescence intensity to increase. In particular, a 50-fold increase in the excitation level (in comparison with the power at which curves *1* and *4* in Fig. 1 were measured) leads to a decrease of K_m from 1.65 to 1.05. In the short-circuit regime, accumulation of holes at the surface levels does not occur because of their outflow into the external circuit.

In conclusion, we note that the proposed model does not in principle rule out the possibility of obtaining $K_m<1$. It is first necessary, therefore, to create conditions under which the no-load voltage will be close to the height of the potential barrier. Such a situation is realized in the *ITO*–CdTe heterojunctions considered in Ref. 3, for which $V_{oc}\approx V_c$. For the Ni–ZnSe contacts investigated here, however, even under conditions of maximum excitation $V_{oc}/V_c\leqslant 0.5$, for which K_m is always greater than unity.

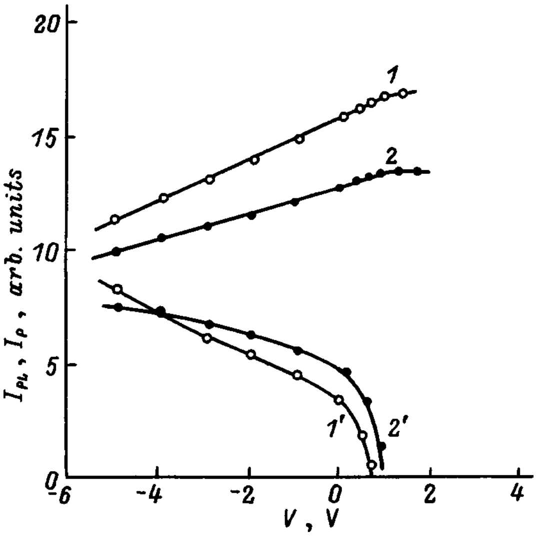

FIG. 2. Dependence of I_{PL} (*1, 2*) and (*1′,2′*) on the voltage across the Ni–ZnSe contact at 300 K. The concentration of uncompensated donors in the diode substrate: 10^{16} (*1*) and 10^{17} (*2*) cm^{-3}.

It thus follows from the above discussion that metal–ZnSe contacts can be used to modulate the intensity of photoluminescence not only by varying the external voltage but also in the absence of an external voltage by closing and opening the contacts of the diode at a fixed frequency.

[1] G. P. Peka, *Physical Phenomena on Semiconductor Surfaces* [in Russian] (Vyshcha Shkola, Kiev, 1984).
[2] Zh. I. Alferov, D. Z. Garbuzov, and E. P. Morozov, Fiz. Tekh. Poluprovodn. **1**, 465 (1967) [Sov. Phys. Semicond. **1**, 389 (1967)].
[3] N. Adib, A. V. Koval', O. S. Koshchuch, A. V. Simashkevich, and D. A. Shcherban, Fiz. Tekh. Poluprovodn. **19**, 2102 (1985) [Sov. Phys. Semicond. **19**, 1297 (1985)].
[4] V. D. Ryzhikov, *Scintillation Crystals of II–VI Semiconductor Compounds* [in Russian] (NIITEKhIM, Moscow, 1989).
[5] V. P. Makhniĭ and V. V. Mel'nik, Fiz. Tekh. Poluprovodn. **29**, 1468 (1995) [Semiconductors **29**, 764 (1995)].
[6] V. P. Makhniĭ, Poverkhnost' **5**, 83 (1995).
[7] K. Gopra and S. Das, *Thin-Film Solar Cells* (Mir, Moscow, 1986).
[8] *Physics and Chemistry of II–VI Compounds* (Mir, Moscow, 1970).

Translated by Paul F. Schippnick

SEMICONDUCTORS VOLUME 32, NUMBER 10 OCTOBER 1998

The nature of the deep levels responsible for photoelectric memory in GaAs/AlGaAs multilayer quantum-well structures

V. N. Ovsyuk

Technological Institute of Applied Microelectronics, Siberian Branch of Russian Academy of Sciences, 630090 Novosibirsk, Russia

M. A. Dem'yanenko, V. V. Shashkin, and A. I. Toropov

Institute of Semiconductor Physics, Siberian Branch of Russian Academy of Sciences, 630090 Novosibirsk, Russia

(Submitted December 24, 1997; accepted for publication February 10, 1998)
Fiz. Tekh. Poluprovodn. **32**, 1213–1218 (October 1998)

The electron capture parameters and photoionization cross section of the unintentional deep levels, which are responsible for photoelectrical memory in GaAs/AlGaAs multilayer quantum-well structures, have been found from an analysis of the kinetics of the excess current during and after optical illumination of these structures. The dependence of the photoionization cross section on the photon energy, the capture cross section, and the energy barrier for capture of an electron from the bottom of the conduction band indicate that the unintentional deep levels are *DX* centers formed by the silicon impurity. These *DX* centers probably appear during growth of the structures as a result of silicon diffusion from the quantum wells along as-grown defects. Fax: (383-2) 35-08-58 © *1998 American Institute of Physics.* [S1063-7826(98)01610-X]

1. INTRODUCTION

A number of studies have shown (see Refs. 1–6) that the dark current and photocurrent in GaAs/Al$_x$Ga$_{1-x}$As multilayer quantum-well (MLQW) structures grown by molecular-beam epitaxy possess an asymmetry in their dependence on the polarity of the applied bias voltage and correspond, on the whole, to the AlGaAs rectangular potential barrier model. The excess dark current in a GaAs/Al$_x$Ga$_{1-x}$ As MLQW structure with composition $x<0.3$ due to the presence of defects in the barrier is usually small and has been observed only at temperatures $T<77$ K (Ref. 7). In MLQW structures with $x>0.3$ a significant excess current has been observed for $T>77$ K, which increases by two or three orders of magnitude after exposure to light with wavelength $\lambda<1.3\ \mu$m. This current persists for an extended time at lower temperatures and then decreases to the initial value after the sample is heated above 170 K (Ref. 7). The indicated photoelectrical memory is explained by the model of the AlGaAs barrier with a sagging conduction band, which facilitates electron tunneling. The magnitude of the sag and the current increase as the incident radiation ionizes the local clusters of unintentional deep levels (DL) present in the barrier and then decrease as the conduction-band electrons are captured at these levels.[8]

On the basis of an analysis of the kinetics of the excess current in a GaAs/AlGaAs MLQW structure observed during exposssure to light and after it we have identified the dependence of the photoionization cross section of the deep levels on the photon energy of the optical radiation, the capture cross section, and the height of the energy barrier for capture of electrons from the bottom of the conduction band to the unintentional deep levels. The data indicate that the unintentional deep levels responsible for photoelectrical memory are *DX* centers formed by the silicon impurity.

2. EXPERIMENT AND RESULTS

We investigated GaAs/Al$_x$Ga$_{1-x}$As MLQW structures with $x=0.335$ and 0.385, grown by molecular-beam epitaxy on Riber 32P and Katun'-S setups. These structures had the following parameters: width of the quantum wells $L_w=43(48)$ Å, barrier thickness $L_b=400(500)$ Å, number of periods $N=25(50)$, and sheet concentration of the silicon impurity $\Gamma_{\mathrm{Si}}=10^{12}(2\times10^{12})$ cm^{-2} (delta doping at the well center) for $x=0.385(0.335)$. The mesa-structures had a square shape with side length 300 μm. (For more details, see Ref. 8).

In order to (1) confirm the hypothesis of the prevalence of one type of recharging deep level and determine the absolute value of their photoionization cross section, (2) identify the dependence of the photoionization cross section of the deep levels on the wavelength of the optical radiation, and (3) determine the parameters of capture of electrons by the deep levels, we have investigated the following processes.

1. The kinetics of growth of the dark current of GaAs/AlGaAs MLQW structures at $T=75$ K during illumination of the structures by optical radiation from a THR 1000 monochromator at the fixed wavelength $\lambda=1\ \mu$m up to saturation of the current. The intensity of the incident radiation $P(1)$ was measured by means of the photocurrent of a calibrated silicon photodiode and was found to be equal to 8.2×10^{15} photons/(cm$^2\cdot$s). For this intensity of radiation with

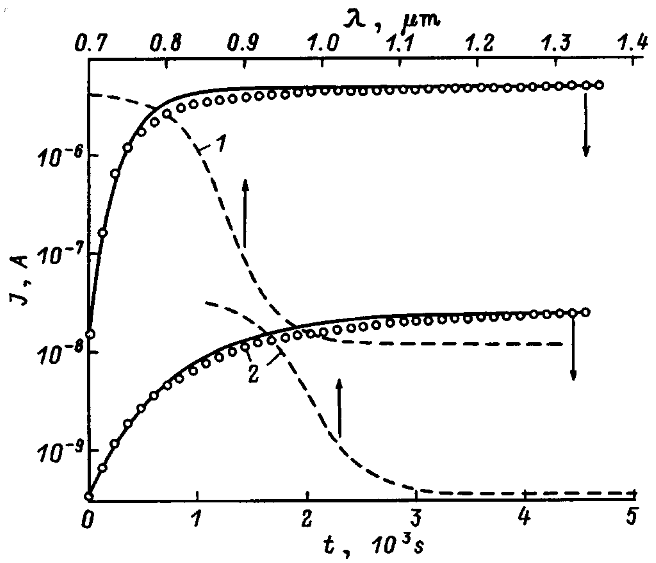

FIG. 1. Dependence of the dark current J on the exposure time t ($\lambda = 1.0$ μm) and on the wavelength λ for GaAs/Al$_x$Ga$_{1-x}$As multilayer quantum-well structures (MLQW) with $x = 0.335$ (*1*) and $x = 0.385$ (*2*). $T = 75$ K, $V_b = 0.2$ V.

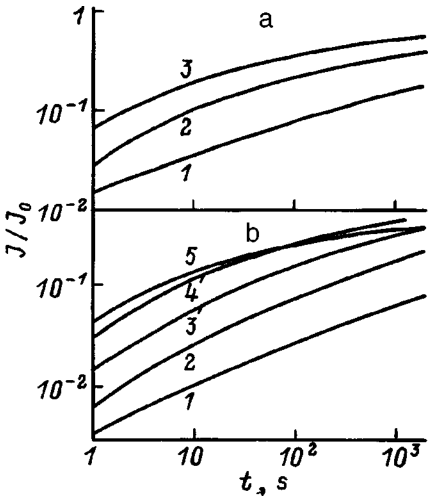

FIG. 2. Dependence of the normalized dark current J on the time t after illumination of GaAs/Al$_x$Ga$_{1-x}$As MLQW structures at various temperatures T. J_0 is the dark current at the moment the illumination is switched on ($t = 0$); $V_b = 0.2$ V. The AlAs fraction in the solid solution x is equal to 0.335 (a) and 0.385 (b). The temperatures in graph a (T, K) are equal to 78 (*1*), 100 (*2*), 130 (*3*). In graph b they are equal to 80 (*1*), 90 (*2*), 101 (*3*), 115 (*4*), and 130 (*5*).

$\lambda \approx 1$ μm the photocurrent in a MLQW structure is negligible and the dark current varies as a result of charge exchange of the deep levels in the AlGaAs barrier layers.[8]

2. The kinetics of growth of the dark current of the structures at $T = 75$ K during illumination by optical radiation from a THR 1000 monochromator, whose wavelength was varied from 1.4 to 0.7 μm at the rate 2×10^{-4} μm/s. The relative intensity of the radiation $P(\lambda)$ was measured with the help of a RTN-30S thermocouple, after which absolute values were determined from the already known value of the intensity $P(1) = 8.2 \times 10^{15}$ photons/(cm$^2 \cdot$ s).

3. Relaxation of the dark current at various temperatures T after illumination of GaAs-photodiode structures (emission maximum at $\lambda \approx 0.95$ μm) for 10–20s, which leads to an increase in the dark current by two or three orders of magnitude at $T = 77$ K (Ref. 8).

Before recording the variation of the dark current during illumination, the samples were brought back to their initial state, which is characterized by minimal dark current. This state is prepared by heating the sample to $T > 170$ K with subsequent cooling in darkness to the measurement temperature.[8] The structures were illuminated from the side of the *i*-GaAs substrate. The measurements were performed for the bias $V_b = 0.2$ V.

Figure 1 plots the dependence of the dark current for the above-indicated MLQW structures as a function of exposure time at the fixed wavelength $\lambda = 1.0$ μm and as a function of the wavelength which varies from a larger value to a smaller value at the rate 2×10^{-4} μm/s. The choice of this direction of variation of the wavelength was dictated by the fact that in this case a significantly greater relative variation of the current takes place at larger wavelengths, at which the photoionization cross section is very small. In both cases the current J grows from its minimum value $J_{\min}$, which corresponds to the initial state of the sample, to values exceeding $J_{\min}$ by two or three orders of magnitude. For the optical radiation intensities and wavelength scanning rate used by us, it was possible in all cases to reach a state close to current saturation.

Figure 2 plots the dependence of the dark current J on the time t after switching off illumination of the structures. The curves are normalized to the current J_0 at $t = 0$. It can be seen that relaxation of the dark current slows down as the temperature is lowered and as the time is increased. At at $T = 80$ K the current has decreased by roughly 10% after a time on the order of 10^3 s.

3. ANALYSIS OF EXPERIMENTAL RESULTS

According to the model proposed in Ref. 8, there are local regions in MLQW structures that penetrate through the entire structure, within the limits of which the barrier layers contain unintentional donor levels, in general, both shallow and deep. The latter are characterized by a relatively high energy barrier for capture of free electrons from the bottom of the conduction band. Under equilibrium conditions (before illumination) at least the shallow donors are ionized. This leads to the appearance of an internal electric field and sagging of the conduction band (Fig. 3). As a result, thermally assisted tunneling of electrons from quantum wells into the conduction band of the barrier layers through the relatively narrow potential barriers leads to an increase in the dark current. Ionization of deep levels (DL) when the sample is illuminated increases the degree of sagging of the conduction band, which leads to further increase of the dark current. The presence of a high energy barrier for capture of electrons at the deep levels ensures remembering of the new state after the illumination is switched off at low temperatures. With subsequent heating of the sample to temperatures $T > 170$ K the electrons, by surmounting the energy barrier, return to the deep levels located below the Fermi level and neutralize

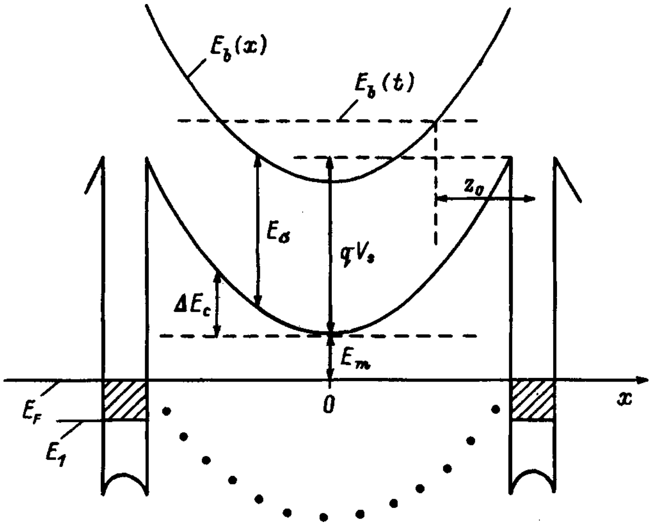

FIG. 3. Energy diagram of the potential barrier in a GaAs/Al$_x$Ga$_{1-x}$As MLQW structure with a sagging conduction band. Deep levels are shown by filled circles. E_1 is the first quantum level, E_F is the Fermi level, $E_b(x)$ is the total energy barrier for electron capture to the deep levels. The rest of the notation is explained in the text.

their positive charge. The sag of the conduction band is decreased and the dark current returns to its original value.

Following Ref. 8, for simplicity, we assume that the shallow and deep levels are uniformly distributed over local regions whose dimensions exceed the thickness of the barrier, so that the potential can be assumed to be one-dimensional and the same for all local regions.

3.1. Photoionization cross section of unintentional deep levels

Since ionization of deep levels as a result of exposure to light occurs uniformly in the local regions (we ignore capture of electrons at the deep levels at $T=75$ K), the degree of sag of the conduction band V_s (see Fig. 3) is related to the number of ionized donor levels N^+ by the equation

$$V_s = qN^+L_b^2/8\varepsilon_b. \tag{1}$$

Here $N^+=N_d+(N_t-n_t)$, and N_d and N_t are respectively the concentration of shallow and deep donors, n_t is the concentration of occupied deep levels, q is the electron charge, and ε_b is the dielectric constant of the barriers. The variation of n_t obeys the following differential equation:

$$dn_t/dt = -2(1-R)\sigma_n^o(\lambda)P(\lambda)n_t, \tag{2}$$

where $\sigma_n^o(\lambda)$ is the optical ionization cross section of the deep levels, and $P(\lambda)$ is the photon flux of the optical radiation incident on the sample, $R=0.28$ is the reflection coefficient of optical radiation from an *i*-GaAs substrate. The factor 2 on the right-hand side of Eq. (2) takes into account the optical radiation flux reflected from the metallized upper contact of the mesa structure. For $P(\alpha)$, which does not depend on time [for the case of measuring the dependence $J(t)$ for $\lambda=1\ \mu$m], and for complete filling of the deep levels before startup of illumination of the structure

$$n_t = N_t\exp(-t/\tau),$$

where

$$\tau^{-1} = 2(1-R)\sigma_n^o(\lambda)P(\lambda), \tag{3}$$

and the variation of V_s with time is given by

$$V_s - V_{s0} = \Delta V_{sm}\left[1-\exp\left(-\frac{t}{\tau}\right)\right]. \tag{4}$$

Here V_{s0} is the value of V_s at $t=0$,which corresponds to minimal sag of the conduction band, and $\Delta V_{sm} = qN_tL_b^2/8\varepsilon_b$.

According to the results of Ref. 8, in the GaAs/Al$_x$Ga$_{1-x}$As MLQW structure with $x=0.385$ at temperatures near $T=77$ K the main current is the one flowing along the local regions with a sagging conduction band, and its value J can be accurately related to the degree of sagging of the conduction band V_s by the formula

$$\log(J/J_{\min}) = \beta(T)(V_s - V_{s0}),$$

(see Fig. 1 and the calculated values of V_s in Ref. 8). Similar calculations of $J(T)$ for GaAs/Al$_x$Ga$_{1-x}$As MLQW structures with $x=0.335$ have demonstrated the applicability of the above formula to this sample as well. Using Eq. (4), we obtain the dependence of the current J on the exposure time (t) for fixed λ

$$\log\left[\frac{J(t)}{J_{\min}}\right] = \beta(T)\Delta V_{sm}\left[1-\exp\left(-\frac{t}{\tau}\right)\right]. \tag{5}$$

Dependences calculated from Eq. (5) for $\tau=260$ s for a GaAs/Al$_x$Ga$_{1-x}$As MLQW structure with $x=0.335$ and $\tau=750$ s for $x=0.385$ are plotted in Fig. 1. The good agreement between calculation and experiment indicates that the deep levels present in both samples are characterized by one charge-exchange time τ and, correspondingly, one optical ionization cross section. Consequently, we can assume that in each sample one type of deep level predominates. From the found values of τ, from the known photon flux $P(1)$, and from relation (3) we find the optical ionization cross sections for $\lambda=1\ \mu$m: $\sigma_n^o(1)=4.3\times10^{-19}$ cm^2 for the GaAs/Al$_x$Ga$_{1-x}$As MLQW structure with $x=0.335$ and $\sigma_n^o(1)=1.1\times10^{-19}$ cm^2 for the MLQW structure with $x=0.385$.

The spectral dependence $\sigma_n^o(\lambda)$ can be determined from the dependences $J(t)$ and $J(\lambda)$ in Fig. 1. Using Eqs. (1) and (2), we find

$$\sigma_n^o(\lambda) = \sigma_n^o(1)\frac{(dV_s/dt)_\lambda P(1)}{(dV_s/dt)_t P(\lambda)}, \tag{6}$$

where the subscripts λ and t on the derivatives indicate that they are to be calculated respectively from the experimental dependences $J(\lambda)$ and $J(t)$. Here the derivative in the denominator is calculated for the same value of V_s (or J) as the derivative in the numerator. The dependences $\sigma_n^o(\lambda)$ so obtained are plotted in Fig. 4. Comparison with the data in the literature,[9,10] plotted in the same figure, shows that the spectral dependence of the photoionization cross section of the unintentional deep levels corresponds to *DX* centers in Si-doped AlGaAs.

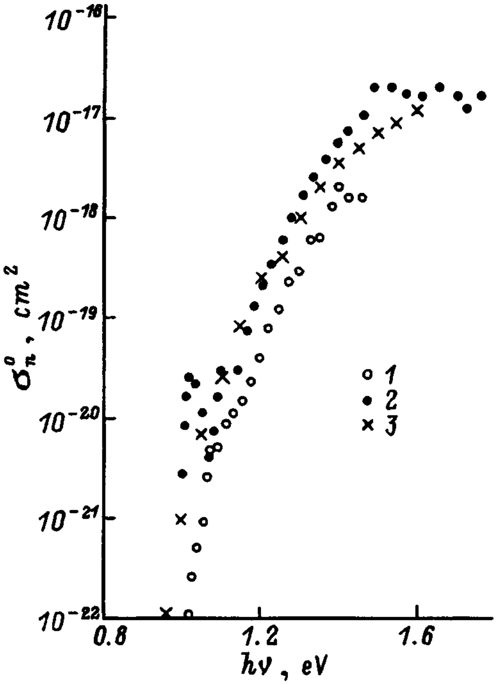

FIG. 4. Spectral dependence of the photoionization cross section of the uncompensated deep levels in a GaAs/Al$_x$Ga$_{1-x}$As MLQW with $x=0.385$ (*1*) and 0.335 (*2*) at $T=75$ K and of the *DX* centers in Si-doped AlGaAs (*3*) at $T=80$ K (Refs. 9 and 10).

3.2. Parameters of the capture of electrons at unintentional deep levels

According to Ref. 8, the charge exchange of ionized deep levels, whose energy levels are found below the Fermi level, proceeds by capture of electrons from the conduction band:

$$\frac{dn_t}{dt}=(N_t-n_t)\nu(T)\exp\left[-\frac{E_b+\Delta E_b(x,t)-\Delta E_F}{kT}\right]. \quad (7)$$

Here E_b is the total energy barrier for capture of electrons at deep levels at $t=0$ (for brevity, the energy barrier); $\Delta E_b(x,t)$ and ΔE_F are the increment in the barrier height E_b due to decrease in the degree of sagging of the conduction band, and the change in the Fermi level relative to the bottom of the quantum well during relaxation, respectively; $\nu(T)=\sigma_c^\infty V_e N_{cb}$; σ_c^∞ is the capture cross section for $1/T=0$; V_e is the thermal velocity of the electrons; and N_{cb} is the effective density of states in the conduction band of the barrier. According to the model proposed in Ref. 8,

$$E_b=E_\sigma+E_m+\Delta E_c(x)$$

(see Fig. 3). Here E_σ is the height of the energy barrier (activation energy of the capture cross section) for capture of electrons at a deep level from the bottom of the conduction band; E_m is the minimum energy of the conduction band in the region of its local sagging, measured from the Fermi level at $t=0$; $\Delta E_c(x)$ is the energy of the bottom of the conduction band at $t=0$, measured from its minimum energy E_m (see Fig. 3).

Note that in the investigated MLQW structures the Γ valley of the conduction band is the lower one. According to Eq. (7), the charge exchange of the deep levels located at $x=0$, which have the lowest barrier height E_b and, correspondingly, the shortest charge-exchange time, occurs at the onset of relaxation. This is followed by the charge exchange of the deep levels at $|x|>0$, whose charge-exchange time increases in accordance with $\exp\{[\Delta E_c(x)+\Delta E_b(x,t)-\Delta E_F]/kT\}$. It can be assumed, for simplicity, that at a given time t the charge exchange of the deep levels occurs in a narrow range of energy barriers: charge exchange has already occured for the deep levels with barrier heights less than some value E_b, while the charge exchange is negligible for those with higher values. In this case the charge exchange for the deep levels, whose energy barrier is less than E_b, occurs at the time

$$t=\frac{1}{\nu(t)}\exp\left[\frac{E_b+\Delta E_b(x,t)-\Delta E_F}{kT}\right]. \quad (8)$$

It follows from Eqs. (7) and (8) that the relaxation process is determined to a significant degree by the capture cross section σ_c^∞ and the distribution of the deel-level sheet concentration (integrated over the barrier thickness) over the total energy barrier $\Gamma_t(E_b)$. To determine these quantities, we employ an approach proposed in Ref. 11 for the case of electron emission from the surface states in a metal–insulator–semiconductor structure.

Noting that the barrier increment $\Delta E_b(x,t)\leqslant q\Delta V_s$, we assume that ΔE_b is significantly less than E_b and, consequently, can be considered as a correction, which we expand to first order: $\Delta E_b\approx\alpha(x,t)q\Delta V_s$. Here $\Delta V_s=V_{sm}-V_s$, where V_{sm} and V_s are the initial (maximum) and current degree of sagging of the conduction band. The coefficient α has a complicated dependence on the coordinate x and the time t, taking the value $\alpha=1$ at $x=0$ and values $\alpha<1$ for $|x|>0$. For simplification, we assume it to be constant for all charge-exchange deep levels and indendent of time. It follows from Eq. (8) that at the time t the deep levels undergo charge exchange with the energy barrier

$$E_b(t)=kT\ln[\nu(T)t]-\alpha q\Delta V_s+\Delta E_F. \quad (9)$$

The rate of variation of the degree of sagging of the conduction band V_s is

$$\frac{dV_s}{dt}=-\frac{qz_0\Gamma_t(E_b)}{2\varepsilon_b}\frac{dE_b}{dt}, \quad (10)$$

where z_0 is the effective distance from the charge-exchange deep levels to the quantum well. Differentiating expression (9), we find

$$\frac{dE_b}{dt}=\frac{kT}{t}+\alpha q\frac{dV_s}{dt}-\left(\frac{\Gamma_t}{N_{2D}}\right)\frac{dE_b}{dt}.$$

Here N_{2D} is the two-dimensional density of states in the quantum well, and we have taken into account that $\Delta E_F=\Delta\Gamma_n/N_{2D}$ and, by virtue of electrical neutrality, $d\Gamma_n/dt=-\Gamma_t dE_b/dt$. Finally, after transforming Eq. (10) we find

$$\frac{\Gamma_t(E_b)}{1+\Gamma_t/N_{2D}}=\frac{2\varepsilon_b}{q^2z_0}\frac{B}{(1-\alpha B)}, \quad (11)$$

where $B=-t(q/kT)dV_s/dt$.

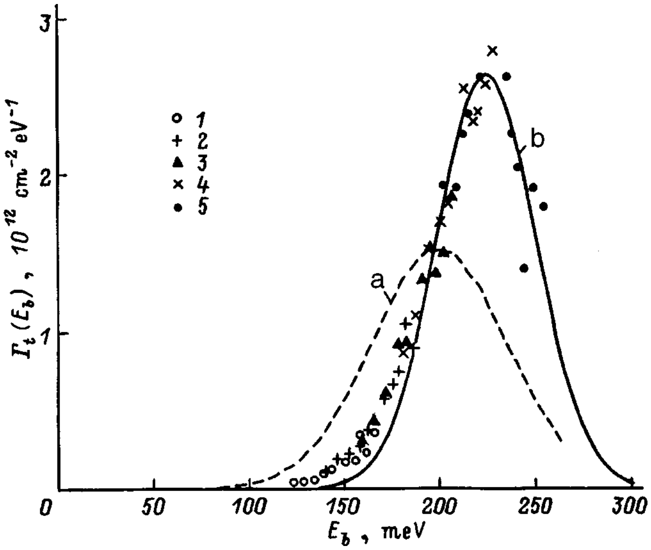

FIG. 5. Distributions of the local sheet concentration of unintentional deep levels Γ_t on the height of the energy barrier for electron capture E_b in the barriers of the GaAs/Al$_x$Ga$_{1-x}$As MLQW structure, found from the relaxational dependences plotted in Fig. 2 for structures with x equal to 0.335 (a) and 0.385 (b). The points are experimental values, the curves are a Gaussian fit to the experimental values. The dependences are numbered the same as in Fig. 2b.

Relations (9) and (11) allow us, if $V_s(t)$ is known, to determine the distributions $\Gamma_t(E_b)$. In this case, by combining the distributions $\Gamma_t(E_b)$ found from the relaxation dependences $V_s(t)$ measured at various temperatures, we can determine the capture cross sections σ_c^∞ entering into $\nu(T)$ (Ref. 11). The dependences $V_s(t)$ can be constructed from the measured relaxation dependences of the dark current $J(t)$ (see Fig. 2) making use of the relation between J and V_s established by calculating the family of dependences $J(T)$ (Ref. 8). Figure 5 plots the distributions $\Gamma_t(E_b)$ for the investigated structures, obtained for $z_0=L_b/2$ and $\alpha=1$. Good agreement between the distributions $\Gamma_t(E_b)$ for the structure with $x=0.385$ is observed for $\sigma_c^\infty=10^{-17}$ cm^2. The solid curve plots a Gaussian distribution with mean value $\langle E_b\rangle=225$ meV and variance 25 meV, in approximate agreement with the experimental data. For the structure with $x=0.335$ only the Gaussian distribution with mean value $\langle E_b\rangle=200$ meV and variance 35 meV fitted to the data is plotted. For this structure, good agreement between the distributions $\Gamma_t(E_b)$ is observed for $\sigma_c^\infty=10^{-18}$cm^2.

On the basis of the considered model the deep-level concentration N_t does not depend on x or $\Gamma_t(E_b)=2N_t(dx/dE_b)$. Since $E_b=E_\sigma+E_m+\Delta E_c(x)$ and $\Delta E_c(x)=4qV_s(x/L_b)^2$, we find

$$\Gamma_t(E_b)=\left(\frac{N_tL_b}{2}\right)\sqrt{qV_s(E_b-E_\sigma-E_m)}.$$

Fluctuations in the values of E_σ and E_m with allowance for the finite width of the region E_b (of order kT), in which electrons are captured to the deep level at the given time, require us to replace the distribution with an asymptotic gap at the point

$$\langle E_b\rangle=E_\sigma+E_m \tag{12}$$

by a distribution with the maximum roughly at this point.

If we know the values of $\langle E_b\rangle$ and E_m, we can use relation (12) to determine the energy barrier (the activation energy of the capture cross section) for electron capture from the bottom of the conduction band to the deep level E_σ, which for the samples with $x=0.335$ and 0.385 turns out to be equal to ≈170 and 224 mV. Here we have used values of E_m, which were obtained from a calculation of families of temperature dependences of the dark current in the investigated MLQW structures (see Ref. 8) and which are on the order of 30 mV in the structure with $x=0.335$ and 1 mV in the structure with $x=0.385$. Note that the obtained data on the parameters of capture to unintentional deep levels (capture cross section and their activation energy) correspond to the data for the *DX* centers in Si-doped AlGaAs (Ref. 9). We explain the somewhat depressed values of σ_c^∞, in comparison with the values given in Ref. 9, by the fact that besides direct capture of electrons to deep levels, which we have considered, another capture process is possible. This process involves preliminary tunneling of the electron into the band gap of the AlGaAs barrier from the lowest point of the conduction band in the region of its sagging. In this case, the measured capture cross section is equal to $\sigma_c^\infty D$, where D is the probability that the electron tunnels to some effective depth. In this case, the energy barrier for capture of an electron can decrease so that the process of capture with tunneling becomes more probable. We will not dwell on this point in more detail since the indicated process of electron capture at *DX* centers requires separate detailed study.

4. CONCLUSIONS

The data obtained on the spectral dependence of the photoionization cross section, on the electron capture cross section, and on the magnitude of the energy barrier for capture of an electron from the bottom of the conduction band indicate that unintentional deep levels responsible for photoelectric memory in GaAs/AlGaAs multilayer quantum-well structures are *DX* centers formed by the silicon impurity. These *DX* centers probably appear during growth of the structures as a result of silicon diffusion from the quantum wells along as-grown defects.

We are grateful to A. F. Kravchenko for fruitful discussions.

[1] B. F. Levine, J. Appl. Phys. **74**, R1 (1993).
[2] K. K. Choi, B. F. Levine, C. G. Bethea, J. Walker, and R. J. Malik, Appl. Phys. Lett. **50**, 1814 (1987).
[3] B. F. Levine, C. G. Bethea, G. Hasnain, V. O. Shen, E. Pelvé, R. R. Abbott, and S. J. Hsieh, Appl. Phys. Lett. **56**, 851 (1990).
[4] E. Pelvé, F. Beltram, C. G. Bethea, B. F. Levine, V. O. Shen, and S. J. Hsieh, J. Appl. Phys. **66**, 5656 (1989).
[5] B. F. Levine, A. Zussman, J. M. Kuo, and J. de Jong, J. Appl. Phys. **71**, 5130 (1992).
[6] A. Zussman, B. F. Levine, J. M. Kuo, and J. de Jong, J. Appl. Phys. **70**, 5101 (1991).
[7] G. M. Williams, R. E. DeWames, C. W. Farley, and R. J. Anderson, Appl. Phys. Lett. **60**, 1324 (1992).
[8] V. N. Ovsyuk, M. A. Dem'yanenko, V. V. Shashkin, and A. I. Toropov, Fiz. Tekh. Poluprovodn. **32**, 209 (1998) [Semiconductors **32**, 189 (1998)].
[9] P. M. Mooney, J. Appl. Phys. **67**, R1 (1990).
[10] P. M. Mooney, G. A. Northrop, T. N. Morgan, and H. G. Grimmeiss, Phys. Rev. B **37**, 8298 (1988).
[11] J. C. Simmons and L. S. Wei, Solid-State Electron. **17**, 117 (1974).

Translated by Paul F. Schippnick

SEMICONDUCTORS VOLUME 32, NUMBER 10 OCTOBER 1998

LOW-DIMENSIONAL SYSTEMS

Weak localization in *p*-type quantum wells

N. S. Averkiev, L. E. Golub, and G. E. Pikus

A. F. Ioffe Physicotechnical Institute, Russian Academy of Sciences, 194021 St. Petersburg, Russia

(Submitted February 16, 1998; accepted for publication February 18, 1998)
Fiz. Tekh. Poluprovodn. **32**, 1219–1228 (October 1998)

A weak-localization theory is derived for quantum heterostructures with strong spin-orbit interaction that predicts anomalous magnetoresistance. This theory treats real quantum wells with a few occupied quantum-well subbands. It is shown that in the presence of intense elastic transitions between these subbands the parameters that define the conductivity in classically weak magnetic fields are averaged efficiently. In the opposite limiting case, all the subbands give independent contributions to the anomalous magnetoresistance. Relevant characteristic magnetic fields are calculated for arbitrary ratios between the times for phase breaking and intersubband transitions. © *1998 American Institute of Physics.* [S1063-7826(98)01710-4]

1. INTRODUCTION

The phenomenon of weak localization arises from quantum interference between waves propagating along the same path in opposite directions. One of the most striking consequences of this phenomenon is an anomalous change in resistance in classically weak magnetic fields. This happens because electron waves traveling along a path in two opposite directions in an external magnetic field pick up an additional phase difference proportional to the field. This phase difference disrupts the initial interference, which decreases the anomalous contribution to the conductivity (i.e., the negative magnetoresistance).

The interference is disrupted not only by the magnetic field but also by inelastic processes, and also as a result of spin relaxation. The theory developed in Refs. 1 and 2 takes into account these circumstances and explains the anomalous magnetoresistance in metals and metal films, while Refs. 2–5 treat the same problem for two- dimensional carriers in semiconductor heterostructures. In these papers it is assumed that the spin relaxation time can be comparable to the time for breaking of the wave-function phase, but both of these times are assumed to be much longer than the momentum relaxation time. In this case the spin-orbit interaction that leads to spin relaxation is treated as a perturbation. However, current experimental and theoretical studies of heterostructures based on III–V semiconductors, whose valence bands form under the influence of a strong spin-orbit interaction, indicate that the spin and momentum relaxation times are the same order of magnitude in these systems. Consequently, the method used to calculate the magnetoresistance in Refs. 1–5 is inapplicable for these systems. Moreover, in real structures more than one quantum-well level may be occupied. Transitions between these levels can also lead to relaxation of wave- function phases, and can change the anomalous contribution for the conductivity. The specific form of the magnetoresistance curve depends on the ratio of phase- breaking rates within each subband in the presence of interband transitions, as it does in the presence of a magnetic field. In a previous paper,[6] we studied *p*-type quantum wells with a single occupied quantum-well subband.

Our goal in this paper is to formulate a theory of weak localization in III–V semiconductor *p*-type quantum wells with several occupied quantum-well subbands that predicts anomalous magnetoresistance, and cast the results of this theory in a form that allows direct comparison with experimental data. By making a detailed comparison of this data with the theory, we can determine a number of parameters of the structure that determine the spin-relaxation rate. In order to simplify the theoretical model, we do not include terms in the energy spectrum of electrons that are odd with respect to the wave vector. Preliminary results of our study were presented in Ref. 7.

2. ANOMALOUS MAGNETORESISTANCE

One of the most striking consequences of weak localization is the way it modifies the effect of a classically weak magnetic field on the static conductivity. The expression for the latter can be written in the form of the three diagrams shown in Fig. 1:

$$\Delta\sigma_{ij}=\Delta\sigma_{ij}^{(I)}+\Delta\sigma_{ij}^{(II)}+\Delta\sigma_{ij}^{(III)}, \tag{1}$$

$$\Delta\sigma_{ij}^{(I)}=\frac{e^2\hbar}{2\pi}\sum_{\alpha\beta\gamma\delta}\int\frac{d^2k}{(2\pi)^2}\int\frac{d^2q}{(2\pi)^2}\tilde{v}_i^{\alpha\gamma}(-\mathbf{k})\tilde{v}_j^{(\beta\delta)}(\mathbf{k})$$
$$\times G_\gamma^A(-\mathbf{k})G_\alpha^R(-\mathbf{k})G_\beta^A(\mathbf{k})G_\delta^R(\mathbf{k})C_{\delta\alpha}^{\gamma\beta}(\mathbf{k},-\mathbf{k},\mathbf{q}), \tag{2}$$

$$\Delta\sigma_{ij}^{(II)}=\frac{e^2\hbar}{2\pi}\sum_{\alpha\beta\gamma\delta\mu\nu}\int\frac{d^2k}{(2\pi)^2}\int\frac{d^2k'}{(2\pi)^2}\int\frac{d^2q}{(2\pi)^2}$$
$$\times\tilde{v}_i^{(\alpha\mu)}(-\mathbf{k})\tilde{v}_j^{(\beta\nu)}(\mathbf{k}')G_\mu^A(-\mathbf{k})G_\alpha^R(-\mathbf{k})$$
$$\times G_\beta^A(\mathbf{k}')G_\nu^R(\mathbf{k}')\langle V_{\mu\gamma}(-\mathbf{k},-\mathbf{k}')V_{\delta\beta}(\mathbf{k},\mathbf{k}')\rangle$$
$$\times G_\gamma^A(-\mathbf{k}')G_\delta^A(\mathbf{k})C_{\nu\alpha}^{\gamma\delta}(\mathbf{k}',-\mathbf{k},\mathbf{q}), \tag{3}$$

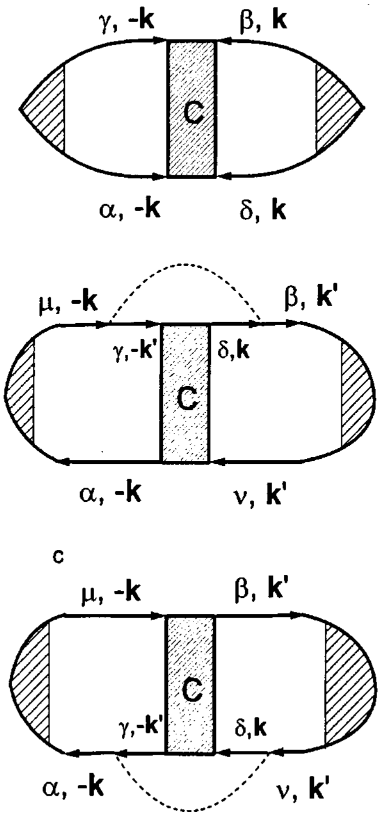

FIG. 1. Diagrammatic representation of the contributions to the conductivity: a —$\Delta\sigma^{(I)}$, b — $\Delta\sigma^{(II)}$, c —$\Delta\sigma^{(III)}$.

$$\Delta\sigma_{ij}^{(III)}=\frac{e^2\hbar}{2\pi}\sum_{\alpha\beta\gamma\delta\mu\nu}\int\frac{d^2k}{(2\pi)^2}\int\frac{d^2k'}{(2\pi)^2}\int\frac{d^2q}{(2\pi)^2}\times\tilde{v}_i^{(\alpha\mu)}(-\mathbf{k})\tilde{v}_j^{(\beta\nu)}(\mathbf{k}')G_\mu^A(-\mathbf{k})\times G_\alpha^R(-\mathbf{k})G_\beta^A(\mathbf{k}')G_\nu^R(\mathbf{k}')\langle V_{\gamma\alpha}(-\mathbf{k}',-\mathbf{k})V_{\nu\delta}(\mathbf{k}',\mathbf{k})\rangle G_\delta^R(\mathbf{k})G_\gamma^R(-\mathbf{k}')C_{\nu\alpha}^{\gamma\delta}(\mathbf{k},-\mathbf{k}',\mathbf{q}). \quad (4)$$

Here i and j label directions in the plane of the quantum well, and Greek letters denote states with a given wave vector $\mathbf{k}$ and various subband labels and momentum projections. Thus, $\tilde{\mathbf{v}}^{(\alpha\beta)}(\mathbf{k})$ is the matrix element of the velocity operator, and $V_{\alpha\beta}(\mathbf{k},\mathbf{k}')$ is the matrix element for scattering of a particle of type α with wave vector $\mathbf{k}$ into a state $|\beta\mathbf{k}'\rangle$, including dependence on the concentration of scatterers. The angle brackets denote averaging over the positions of the scatterers:

$$\langle V_{\alpha\beta}(\mathbf{k},\mathbf{k}')V_{\gamma\delta}(\mathbf{g},\mathbf{g}')\rangle=\sum_{\bar{z}}\int d\mathbf{r}\hat{\Psi}^\dagger_{\alpha\mathbf{k}}(\mathbf{r})V(\boldsymbol{\rho},z-\bar{z})\hat{\boldsymbol{\Psi}}_{\beta\mathbf{k}'}(\mathbf{r})\times\int d\mathbf{r}'\hat{\boldsymbol{\Psi}}^\dagger_{\gamma\mathbf{g}}(\mathbf{r}')V(\boldsymbol{\rho}',z'-\bar{z})\hat{\boldsymbol{\Psi}}_{\delta\mathbf{g}'}(\mathbf{r}'), \quad (5)$$

where $\boldsymbol{\rho}$ and z are coordinates that characterize motion in the plane of the quantum well and along the growth axis, $\bar{z}$ is the coordinate of the scatterer, and $\hat{\Psi}_{\alpha\mathbf{k}}(\mathbf{r})$ is the wave function of state $|\alpha\mathbf{k}\rangle$. $G_\alpha^{A,R}(\mathbf{k})$ are the advanced and retarded Green's functions:

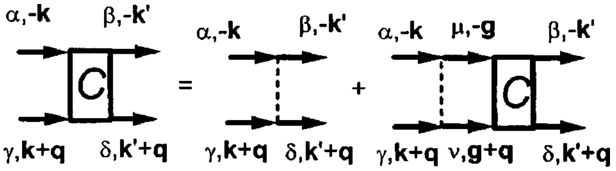

FIG. 2. Diagrammatic representation of the cooperon integral equation.

$$G_\alpha^{A,R}(\mathbf{k})=\frac{1}{E_F-E_\alpha(\mathbf{k})\pm\dfrac{i\hbar}{2\tau_\alpha(\mathbf{k})}\pm\dfrac{i\hbar}{2\tau_\varphi^{(\alpha)}(\mathbf{k})}}, \quad (6)$$

where E_F is the Fermi energy, and $\tau_\alpha(\mathbf{k})$ is the total residence time of particles in the state $|\alpha\mathbf{k}\rangle$:

$$\frac{1}{\tau_\alpha(\mathbf{k})}=\frac{2\pi}{\hbar}\sum_\nu\int\frac{d^2k'}{(2\pi)^2}\langle|V_{\alpha\nu}(\mathbf{k},\mathbf{k}')|^2\rangle\delta[E_F-E_\nu(\mathbf{k}')]. \quad (7)$$

Here $\tau_\varphi^{(\alpha)}(\mathbf{k})$ is the relaxation time of the wave-function phase, and $E_\alpha(\mathbf{k})$ is the dispersion law for the corresponding quantum-well subband.

In studying the contribution of weak localization to the conductivity, we will use $C_{\gamma\delta}^{\alpha\beta}(\mathbf{k},\mathbf{k}',\mathbf{q})$ to denote the sum of ladder diagrams at low total momentum $\mathbf{q}$ (i.e., the cooperon; see Fig. 2).

The corresponding integral equation for the cooperon averaged over the distribution of impurities has the form

$$C_{\gamma\delta}^{\alpha\beta}(\mathbf{k},\mathbf{k}',\mathbf{q})=\langle V_{\alpha\beta}(-\mathbf{k},-\mathbf{k}')V_{\gamma\delta}(\mathbf{k}+\mathbf{q},\mathbf{k}'+\mathbf{q})\rangle+\sum_{\mu\nu}\int\frac{d^2g}{(2\pi)^2}\times\langle V_{\alpha\mu}(-\mathbf{k},-\mathbf{g})V_{\gamma\nu}(\mathbf{k}+\mathbf{q},\mathbf{g}+\mathbf{q})\rangle\times C_{\nu\delta}^{\mu\beta}(\mathbf{g},\mathbf{k}',\mathbf{q})G_\nu^R(\mathbf{g}+\mathbf{q})G_\mu^A(-\mathbf{g}). \quad (8)$$

The matrix element of the velocity operator, denoted by the crosshatched vertex, satisfies the equations

$$\tilde{\mathbf{v}}^{(\alpha\beta)}(\mathbf{k})=\mathbf{v}^{(\alpha)}(\mathbf{k})\delta_{\alpha\beta}+\sum_{\mu\nu}\int\frac{d^2g}{(2\pi)^2}\times\langle V_{\alpha\mu}(\mathbf{k},\mathbf{g})V_{\nu\beta}(\mathbf{g},\mathbf{k})\rangle\tilde{\mathbf{v}}^{(\mu\nu)}(\mathbf{g})G_\nu^R(\mathbf{g})G_\mu^A(\mathbf{g}), \quad (9)$$

$$\mathbf{v}^{(\alpha)}(\mathbf{k})=\frac{1}{\hbar}\frac{\partial E_\alpha(\mathbf{k})}{\partial\mathbf{k}}. \quad (10)$$

In a classically weak magnetic field, as a particle moves around a closed trajectory its wave function acquires a phase equal to $\pi\Phi/\Phi_0$, where Φ is the value of the magnetic flux passing through the trajectory, and $\Phi_0=\pi\hbar c/e$ is the magnetic flux quantum. Therefore, when two waves propagate along the same trajectory in opposite directions, they acquire an additional phase difference equal to $2\pi\Phi/\Phi_0$, which disrupts their interference. This is equivalent to the additional phase acquired in the magnetic field by particles with charge $2e$. The magnetic field begins to affects weak localization starting at the value at which

$$l_H^2 \sim D\tau_\varphi,$$

where l_H is the magnetic length of a particle with charge $2e$, and D is the diffusion coefficient. This condition can be rewritten in the form

$$\omega_c \tau E_F \tau_\varphi/\hbar \simeq 1,$$

where $E_F\tau_\varphi\hbar \gg 1$. Here ω_c is the cyclotron frequency.

Let us consider the case of a rectangular symmetric quantum well with infinitely high barriers. In order to describe the valence-band states, we will use the spherical approximation. The spectrum and wave functions of valence-band carriers have been investigated in many papers using these approximations. We will use the form of the wave functions given in Ref. 8. If Bloch functions for **k** at the top of the valence band are used, there is a basis corresponding to projections of angular momentum 3/2, 1/2, $-1/2$, $-3/2$, and the wave functions form four- component column vectors in this basis. In the spherical approximation each energy level is doubly degenerate, and the corresponding wave functions can be written in the form

$$\hat{\Psi}_{\alpha\mathbf{k}} = e^{i\mathbf{k}\boldsymbol{\rho}}\hat{F}_\alpha(\mathbf{k},z), \tag{11}$$

$$\hat{F}_1 = \begin{bmatrix} -v_0C(z) \\ iv_1S(z)e^{i\varphi_\mathbf{k}} \\ -v_2C(z)e^{2i\varphi_\mathbf{k}} \\ iv_2S(z)e^{3i\varphi_\mathbf{k}} \end{bmatrix}, \quad \hat{F}_2 = \begin{bmatrix} iv_3S(z)e^{-3i\varphi_\mathbf{k}} \\ v_2C(z)e^{-2i\varphi_\mathbf{k}} \\ iv_1S(z)e^{-i\varphi_\mathbf{k}} \\ v_0C(z) \end{bmatrix}. \tag{12}$$

Here $\varphi_\mathbf{k}$ is the azimuthal angle of the vector **k**, and $C(z)$ and $S(z)$ are symmetric and antisymmetric functions of the coordinate z. The dispersion relation for the energies of these states $E(k)$, as well as the expressions for $C(z)$, $S(z)$ and the real coefficients v_i (i = 0 to 3), which are independent of $\varphi_\mathbf{k}$, are given in Ref. 8; all of these quantities depend on the subband level. Note that the choice of wave function phases made in Eq. (12) implies that $|V_{\alpha\beta}|$ depends only on the phase difference $\varphi_\mathbf{k} - \varphi_{\mathbf{k}'}$, and hence the residence times τ_α do not depend on **k**.

It is well known that Eq. (8) is singular in the limit $\mathbf{q} \to 0$. In order to obtain the contribution associated with this singularity, we must retain **q** only in $G_\nu^R(\mathbf{g}+\mathbf{q})$. Expanding $E_\nu(\mathbf{g}+\mathbf{q})$ to second order in **q** and then integrating with respect to $E_\nu(\mathbf{g})$, we obtain the equation

$$\begin{aligned} C_{\gamma\delta}^{\alpha\beta}(\mathbf{k},\mathbf{k}',q) &= \langle V_{\alpha\beta}(-\mathbf{k},-\mathbf{k}')V_{\gamma\delta}(\mathbf{k},\mathbf{k}')\rangle \\ &\quad + \sum_{\mu\nu} \zeta(\mu,\nu)\frac{2\pi\tau_\nu N_\nu}{\hbar}\int\frac{d\varphi_g}{2\pi} \\ &\quad \times\langle V_{\alpha\mu}(-\mathbf{k},-\mathbf{q})V_{\gamma\nu}(\mathbf{k},\mathbf{g})\rangle \\ &\quad \times C_{\nu\delta}^{\mu\beta}(\mathbf{g},\mathbf{k}',\mathbf{q})[1-T_\nu(\mathbf{g},\mathbf{q})], \end{aligned} \tag{13}$$

$$T_\nu(\mathbf{g},\mathbf{q}) = i\mathbf{v}^{(\nu)}(\mathbf{g})\mathbf{q}\tau_\nu + [\mathbf{v}^{(\nu)}(\mathbf{g})\mathbf{q}\tau_\nu]^2 + \frac{\tau_\nu}{\tau_\varphi^{(\nu)}(\mathbf{g})}. \tag{14}$$

Here N_ν is the density of states for subband ν at the Fermi level, which is given in terms of the velocity $v_F^{(\nu)}$ and quasimomentum $k_F^{(\nu)}$ of the particles as follows:

$$N_\nu = \frac{k_F^{(\nu)}}{2\pi\hbar v_F^{(\nu)}}. \tag{15}$$

The factor $\zeta(\mu,\nu)$, which equals unity if states μ and ν belong to the same subband, and zero otherwise, takes into account the fact that states from different subbands do not interfere since their wave vectors at the Fermi surface differ in magnitude by a quantity of order k_F.

Expression (13) represents a complicated system of equations, since the cooperon depends not only on the spin indices and subband labels but also on **k**, **k**′, and **q**. In Ref. 6 we outlined a general method for solving this system of equations, but in this paper we will explicitly solve it for the two most interesting cases, in which one and two quantum-well subbands are occupied.

3. A QUANTUM WELL WITH A SINGLE LEVEL

In Ref. 6 we showed that the solution to Eq. (13) depends on the ratio of E_F to Δ, where Δ is the minimum energy difference between the two lowest subbands. If $E_F \leqslant \Delta$, the spin relaxation time is the same order as the momentum relaxation time, and only states with zero total angular momentum contribute to weak localization. Consequently, the cooperon can be represented in the form

$$C_{\gamma\delta}^{\alpha\beta}(\mathbf{k},\mathbf{k}',\mathbf{q}) = s(\mathbf{k},\mathbf{k}'\mathbf{q})S_\gamma^\alpha S_\delta^\beta. \tag{16}$$

Here

$$S_1^1 = S_2^2 = 0, \quad S_2^1 = -S_1^2 = 1/\sqrt{2}. \tag{17}$$

This structure of S_γ^α implies that the cooperon acquires a diffusive contribution due to interference of waves with oppositely directed spins. The function $s(\mathbf{k},\mathbf{k}'\mathbf{q})$ satisfies the equation

$$\begin{aligned} s(\mathbf{k},\mathbf{k}',\mathbf{q}) &= \langle|V_{11}(\varphi_\mathbf{k}-\varphi_{\mathbf{k}'})|^2 + |V_{12}(\varphi_k-\varphi_{k'})|^2\rangle \\ &\quad + \frac{2\pi\tau N}{\hbar}\int\frac{d\varphi_g}{2\pi}\langle|V_{11}(\varphi_k-\varphi_g)|^2 \\ &\quad + |V_{12}(\varphi_\mathbf{k}-\varphi_\mathbf{g})|^2\rangle s(\mathbf{g},\mathbf{k}',\mathbf{q})[1-T(\mathbf{g},\mathbf{q})]. \end{aligned} \tag{18}$$

Here the residence is calculated by using Eq. (7):

$$\tau^{-1} = \frac{2\pi N}{\hbar}\int\frac{d\varphi}{2\pi}\langle|V_{11}(\varphi)|^2 + |V_{12}(\varphi)|^2\rangle. \tag{19}$$

In deriving Eq. (18) we took into account that the quantities $|V_{\alpha\beta}|$ depend on the phase difference $\varphi_\mathbf{k}-\varphi_\mathbf{g}$, and assumed that τ_φ, like τ, does not depend on **g**.

We solve Eq. (18) by expanding $s(\mathbf{k},\mathbf{k}',\mathbf{q})$ in a Fourier series:

$$s(\mathbf{k},\mathbf{k}',\mathbf{q}) = \sum_{n=-\infty}^{\infty} s_n(\mathbf{k}',\mathbf{q})e^{in\varphi_\mathbf{k}}. \tag{20}$$

The coefficients of the expansion satisfy the equation:

$$(1-W_n)s_n=\frac{\hbar}{2\pi N\tau}W_n\exp(in\varphi_{\mathbf{k}'})-\sum_{m=-\infty}^{\infty}T_{nm}(q)s_m, \tag{21}$$

where

$$W_n=\frac{2\pi N\tau}{\hbar}\int\frac{d\varphi}{2\pi}\langle|V_{11}(\varphi)|^2+|V_{12}(\varphi)|^2\rangle e^{-in\varphi}, \tag{22}$$

$$T_{nm}(q)=W_n\biggl[-i\frac{v_Fq\tau}{2}\delta_{|n-m|,1}+\frac{(v_Fq\tau)^2}{2}\times\left(\delta_{nm}+\frac{1}{2}\delta_{|n-m|,2}\right)+\frac{\tau}{\tau_\varphi}\delta_{nm}\biggr]. \tag{23}$$

Since according to (19) we have $W_0=1$ and $|T_{nm}|\ll 1$, the coefficients s_n have different orders of magnitude. It is clear from Eq. (21) that $s_0\sim q^{-2}$, while $s_\pm\sim q^{-1}$. For the remaining n quantities we have $|s_n|\ll|s_1|$. Equation (21) specifies a coupling between s_0 and $s_{\pm 1}$ for $n=\pm 1$:

$$s_1=s_{-1}=i\frac{v_Fq\tau}{2}\frac{W_1}{1-W_1}s_0. \tag{24}$$

It is clear, therefore, that s_1 does not depend on $\mathbf{k}'$. Substituting Eq. (24) into Eq. (21), we finally obtain an expression for $s(\mathbf{k},\mathbf{k}',\mathbf{q})$:

$$s(\mathbf{k},\mathbf{k}',\mathbf{q})\approx s_0=\frac{\hbar}{2\pi N\tau}\frac{1}{Dq^2\tau+\tau/\tau_\varphi}, \tag{25}$$

where the diffusion coefficient is

$$D=\frac{1}{2}v_F^2\tau_{tr}, \tag{26}$$

and τ_{tr} is the transport time:

$$\tau_{tr}^{-1}=\frac{2\pi N}{\hbar}\int\frac{d\varphi}{2\pi}\langle|V_{11}(\varphi)|^2+|V_{12}(\varphi)|^2\rangle(1-\cos\varphi). \tag{27}$$

When $E_F\ll\Delta$, the spin-orbit interaction is suppressed, and the spin relaxation time turns out to be longer than the momentum relaxation time. Hence, all four two- particle spin states contribute to the weak localization. In Ref. 6 we showed that in this limit the cooperon can be written in the form

$$\begin{aligned}C_{\gamma\delta}^{\alpha\beta}(\mathbf{k},\mathbf{k}',\mathbf{q})&=s(\mathbf{k},\mathbf{k}',\mathbf{q})S_\gamma^\alpha S_\delta^\beta\\&+p_1(\mathbf{k},\mathbf{k}',\mathbf{q})(P_{+\gamma}^\alpha P_{+\delta}^\beta+P_{-\gamma}^\alpha P_{-\delta}^\beta)\\&+p_0(\mathbf{k},\mathbf{k}',\mathbf{q})P_{0\gamma}^\alpha P_{0\delta}^\beta,\end{aligned} \tag{28}$$

where the nonzero components of P_{ij}^α are

$$P_{+1}^1=P_{-2}^2=1,\quad P_{02}^1=P_{01}^2=1/\sqrt{2}. \tag{29}$$

The equation for $s(\mathbf{k},\mathbf{k}',\mathbf{q})$ coincides with Eq. (18), while the function $p_{0,1}(\mathbf{k},\mathbf{k}',\mathbf{q})$ satisfies the equation

$$\begin{aligned}p_0(\mathbf{k},\mathbf{k}',\mathbf{q})&=\langle|V_{11}(\varphi_{\mathbf{k}}-\varphi_{\mathbf{k}'})|^2-|V_{12}(\varphi_{\mathbf{k}}-\varphi_{\mathbf{k}'})|^2\rangle+\frac{2\pi\tau N}{\hbar}\\&\times\int\frac{d\varphi_g}{2\pi}\langle|V_{11}(\varphi_{\mathbf{k}}-\varphi_{\mathbf{g}})|^2-|V_{12}(\varphi_{\mathbf{k}}-\varphi_{\mathbf{g}})|^2\rangle\\&\times p_0(\mathbf{q},\mathbf{k}',\mathbf{q})[1-T(\mathbf{g},\mathbf{q})],\end{aligned} \tag{30}$$

$$\begin{aligned}p_1(\mathbf{k},\mathbf{k}',\mathbf{q})&=\langle V_{11}^2(\varphi_{\mathbf{k}}-\varphi_{\mathbf{k}'})\rangle+\frac{2\pi\tau N}{\hbar}\\&\times\int\frac{d\varphi_g}{2\pi}\langle V_{11}^2(\varphi_{\mathbf{k}}-\varphi_{\mathbf{g}})\rangle p_1(\mathbf{g},\mathbf{k}',\mathbf{q})\\&\times[1-T(\mathbf{g},\mathbf{q})].\end{aligned} \tag{31}$$

For $E_F\ll\Delta$, mixing of the hole states at the Fermi surface is small, there is no spin relaxation, and the following equations hold:

$$V_{12}=0,\quad V_{11}=|V_{11}|. \tag{32}$$

In this case Eqs. (18), (30), and (31) coincide, and $p_0=p_1=s$.

If we include mixing of the hole states, then Eq. (32) does not hold and Eqs. (30) and (31) will differ from Eq. (18) by small terms, which can be included in the same way as the terms containing q and τ/τ_φ. We can therefore find p_0 and p_1 by the same procedure as s:

$$s(\mathbf{k},\mathbf{k}',\mathbf{q})=\frac{\hbar}{2\pi N_0\tau_0}\frac{1}{D_0q^2\tau_0+\tau_0/\tau_\varphi}, \tag{33}$$

$$p_1(\mathbf{k},\mathbf{k}',\mathbf{q})=\frac{\hbar}{2\pi N_0\tau_0}\frac{1}{D_0q^2\tau_0+\tau_0/\tau_\varphi+\tau_0/\tau_\parallel}, \tag{34}$$

$$p_0(\mathbf{k},\mathbf{k}',\mathbf{q})=\frac{\hbar}{2\pi N_0\tau_0}\frac{1}{D_0q^2\tau_0+\tau_0/\tau_\varphi+\tau_0/\tau_\perp}. \tag{35}$$

Here the label ''0'' indicates that the corresponding quantities should be calculated without allowance for mixing of the hole subbands. The small terms are

$$\frac{\tau_0}{\tau_\perp}=\frac{2\pi}{\hbar}\int\frac{d\varphi}{2\pi}\{N_0\tau_0\langle[V_{11}^{(0)}(\varphi)]^2\rangle-N\tau\langle[V_{11}(\varphi)]^2\rangle\}, \tag{36}$$

$$\frac{\tau_0}{\tau_\perp}=\frac{4\pi}{\hbar}N_0\tau_0\int\frac{d\varphi}{2\pi}\langle|V_{12}(\varphi)|^2\rangle. \tag{37}$$

The quantities $\tau_{\parallel,\perp}$ have the sense of longitudinal and transverse spin relaxation times, where the role of a preferred axis is played by the normal to the plane of the quantum well.

Equations (33)–(35) are applicable when $\tau_0\ll\tau_\varphi$, $\tau_\parallel$, $\tau_\perp$. As $\tau_\parallel$ and $\tau_\perp$ decrease, the quantities p_1 and p_0 become smaller than s by a factor of $(D_0q^2\tau_0+\tau_0/\tau_\varphi)^{-1}$, and the expression for the cooperon takes a form analogous to Eqs. (16) and (25). Therefore, we can say that weak-localization effects are contained in Eqs. (33)–(35) for arbitrary E_F/Δ via modifications of D, τ_φ, $\tau_{\parallel,\perp}$, and τ.

The expressions for the diffusion coefficient and relaxation time are valid for arbitrary scattering potentials. As an example, we calculate these quantities for the case where the potential is short-range:

$$V(r)=V_0\delta(r). \tag{38}$$

A peculiarity of the complicated band structure is the fact that the scattering cross section depends on the initial and final hole quasimomenta even for this potential. Calculations show that the expression for the spin relaxation time has the form

$$\frac{\tau_0}{\tau_\parallel}=\frac{4}{3}av_1^4\int_0^{a/2}dzS^4(z), \tag{39}$$

$$\frac{\tau_0}{\tau_\perp}=\frac{16}{3}[a(v_1v_2)^2+2v_3^2]\int_0^{a/2}dz\cos^2\left(\frac{\pi z}{a}\right)S^2(z), \tag{40}$$

where a is the width of the quantum well, and v_1, v_2, and v_3 should be calculated to first nonvanishing order in E_F/Δ. Expressions (39) and (40) are valid for

$$\frac{m_h}{m_l}\left(\frac{k_Fa}{\pi}\right)^2\ll 1,$$

where m_h and m_l are the heavy- and light-hole masses.

3.1. Calculation of the anomalous contribution to the conductivity

Equation (9) for the matrix element $\tilde{\mathbf{v}}$ is similar to the equation for the cooperon (13), and its kernel depends on the difference $\varphi_{\mathbf{k}}-\varphi_{\mathbf{g}}$. This allows us to express $\tilde{\mathbf{v}}^{(\alpha\beta)}(\mathbf{k})$ in terms of the residence time (τ) and the transport time (τ_{tr}) as follows:

$$\tilde{\mathbf{v}}^{(\alpha\beta)}(\mathbf{k})=\mathbf{v}^{(\alpha)}(\mathbf{k})\frac{\tau_{tr}}{\tau}\delta_{\alpha\beta}. \tag{41}$$

Substituting this expression into Eqs. (2)–(4), we obtain

$$\Delta\sigma^{(I)}=-\frac{e^2}{\pi\hbar}D\frac{2\pi N\tau\tau_{tr}}{\hbar}\int\frac{d^2q}{(2\pi)^2}\sum_{\alpha\beta}C^{\alpha\beta}_{\beta\alpha}(q),$$

$$\Delta\sigma^{(II)}=\Delta\sigma^{(III)}=\frac{1}{2}\frac{\tau-\tau_{tr}}{\tau_{tr}}\Delta\sigma^{(I)}. \tag{42}$$

Using Eqs. (25) and (33)–(35) for the cooperon, we obtain an expression for the contribution to the conductivity. For $E_F\ll\Delta$,

$$\Delta\sigma=-\frac{e^2}{\pi\hbar}\int\frac{d^2q}{(2\pi)^2}\left[\frac{2}{q^2+(D_0\tau_\varphi)_{-1}+(D_0\tau_\parallel)^{-1}}\right.$$
$$\left.+\frac{1}{q^2+(D_0\tau_\varphi)^{-1}+(D_0\tau_\perp)^{-1}}-\frac{1}{q^2+(D_0\tau_\varphi)^{-1}}\right], \tag{43}$$

while for $E_F\simeq\Delta$

$$\Delta\sigma=\frac{e^2}{\pi\hbar}\int\frac{d^2q}{(2\pi)^2}\frac{1}{q^2+(D\tau_\varphi)^{-1}}. \tag{44}$$

In order to calculate the magnetoresistance, we follow Refs. 1 and 2 and replace the integrals in Eqs. (42) according to the rule

$$\int\frac{d^2q}{(2\pi)^2}\to\frac{eH}{4\pi^2\hbar c}\sum_n, \quad q^2\to\frac{eH}{\pi\hbar c}(n+1/2), \tag{45}$$

where H is the projection of the magnetic field onto the normal to the quantum well.

Usually, experiments determine the difference between the conductivity in a magnetic field and the zero-field conductivity:

$$\delta\sigma(H)=\Delta\sigma(H)-\Delta\sigma(0).$$

When $E_F\simeq\Delta$, this quantity is

$$\delta\sigma(H)=-\frac{e^2}{4\pi^2\hbar}f_2\left(\frac{H}{H_\varphi}\right), \tag{46}$$

where

$$H_\varphi=\frac{\hbar c}{4eD\tau_\varphi}. \tag{47}$$

When $E_F\ll\Delta$, the magnetoresistance is

$$\delta\sigma(H)=\frac{e^2}{4\pi^2\hbar}\left[2f_2\left(\frac{H}{H_\parallel}\right)+f_2\left(\frac{H}{H_\perp}\right)-f_2\left(\frac{H}{H_\varphi}\right)\right]. \tag{48}$$

Here

$$H_\parallel=\frac{\hbar c}{4eD_0}\left(\frac{1}{\tau_\varphi}+\frac{1}{\tau_\parallel}\right), \quad H_\perp=\frac{\hbar c}{4eD_0}\left(\frac{1}{\tau_\varphi}+\frac{1}{\tau_\perp}\right), \tag{49}$$

while

$$f_2(x)=\ln x+\psi(1/2+1/x), \tag{50}$$

where $\psi(y)$ is the digamma function.

A peculiarity of the function $\delta\sigma(H)$ is its change in sign as the doping level increases. The concentration dependences of the times $\tau_{\parallel,\perp}$ are different:

$$\tau_0/\tau_\parallel\sim(E_F/\Delta)^2, \quad \tau_0/\tau_\perp\sim(E_F/\Delta)^3,$$

due to the different k-dependences of matrix elements V_{11} and V_{12} [see Eqs. (36) and (37)]. As an illustration, Fig. 3 shows magnetoconductivity curves for various values of the parameter k_Fa. In these calculations we assumed that the ratio $\tau_\varphi/\tau=5$, and that it does not depend on k_F, while $m_l/m_h=0.16$. These curves demonstrate the transition from the case where the spin relaxation is slow to the case where it is faster than the phase breaking of the wave function.

4. QUANTUM WELL WITH TWO LEVELS

In the previous sections we considered the case where only one quantum-well subband was occupied. However, in real structures two or more subbands can be occupied. In this section we consider a situation where two subbands are occupied.

The specific form of the contribution to the magnetoconductivity depends on the ratios of the intersubband transition times to the spin and phase relaxation times. For carriers in the lower subband the spin relaxation time is of the same order of magnitude as the momentum relaxation time. This implies that weak localization in the lower subband is determined by the states with zero total angular momentum, so

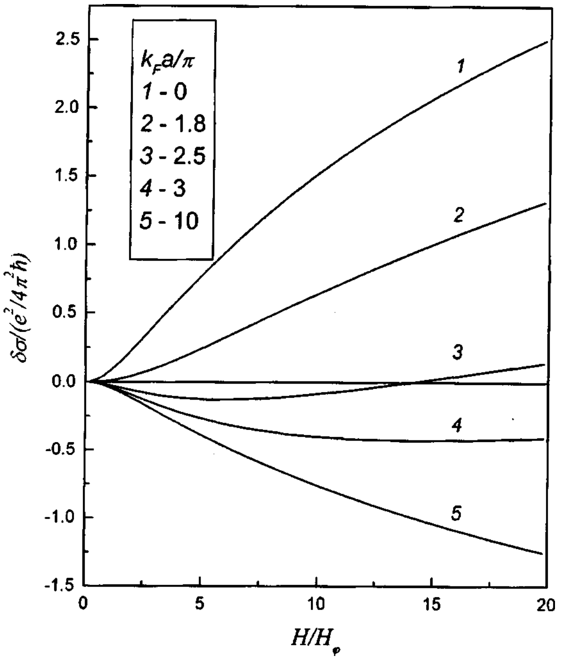

FIG. 3. Magnetoresistance curves for various hole concentrations in the quantum well.

that $\tau_0/\tau_\parallel$ and $\tau_0/\tau_\perp \simeq 1$ in Eqs. (34) and (35). In the upper subband, the ratio of the spin relaxation and momentum relaxation times depends on the subband occupation: If $(E_F - \Delta)/\Delta \simeq 1$, the times are the same order of magnitude, and the contribution also comes from states that have zero total angular momentum, whereas when $(E_F - \Delta)/\Delta \ll 1$, all four two-particle states contribute.

For $(E_F - \Delta)/\Delta \simeq 1$, we have

$$\begin{aligned} C^{\alpha\beta}_{\gamma\delta}(\mathbf{k},\mathbf{k}',\mathbf{q}) = {} & s_l(\mathbf{k},\mathbf{k}',\mathbf{q}) S^\alpha_{l\gamma} S^\beta_{l\delta} + s_u(\mathbf{k},\mathbf{k}',\mathbf{q}) S^\alpha_{u\gamma} S^\beta_{u\delta} \\ & + s_{lu}(\mathbf{k},\mathbf{k}',\mathbf{q}) S^\alpha_{l\gamma} S^\beta_{u\delta} \\ & + s_{ul}(\mathbf{k},\mathbf{k}',\mathbf{q}) S^\alpha_{u\gamma} S^\beta_{l\delta}, \end{aligned} \tag{51}$$

where the Greek labels enumerate the upper subband (u) and the lower subband (l) and their associated spin states (1, 2): $\alpha = u1$, $u2$, $l1$, and $l2$. The nonzero components of $S^\alpha_{i\gamma}$ is

$$S^{l1}_{ll1} = -S^{l2}_{ll1} = S^{u1}_{uu2} = -S^{u2}_{uu1} = 1/\sqrt{2}. \tag{52}$$

Substituting (51) into Eq. (13), summing over the spin labels, and integrating over $\mathbf{k}$ and $\mathbf{k}'$, we obtain equations for the coefficients s_i:

$$\begin{aligned} s_l(\mathbf{k},\mathbf{k}',\mathbf{q}) = {} & \langle |V_{l1,l1}(\varphi_\mathbf{k} - \varphi_{\mathbf{k}'})|^2 + |V_{l1,l2}(\varphi_\mathbf{k} - \varphi_{\mathbf{k}'})|^2 \rangle \\ & + \frac{2\pi\tau_l N_l}{\hbar} \int \frac{d\varphi_\mathbf{g}}{2\pi} \langle |V_{l1,l1}(\varphi_\mathbf{k} - \varphi_\mathbf{g})|^2 \\ & + |V_{l1,l2}(\varphi_\mathbf{k} - \varphi_\mathbf{g})|^2 \rangle s_l(\mathbf{g},\mathbf{k}',\mathbf{q})[1 - T_l(\mathbf{g},\mathbf{q})] \\ & + \frac{2\pi\tau_u N_u}{\hbar} \int \frac{d\varphi_\mathbf{g}}{2\pi} \langle |V_{l1,u1}(\varphi_\mathbf{k} - \varphi_\mathbf{g})|^2 \\ & + |V_{l1,u2}(\varphi_\mathbf{k} - \varphi_\mathbf{g})|^2 \rangle \\ & \times s_{ul}(\mathbf{g},\mathbf{k}',\mathbf{q})[1 - T_u(\mathbf{g},\mathbf{q})], \end{aligned} \tag{53}$$

$$\begin{aligned} s_{ul}(\mathbf{k},\mathbf{k}',\mathbf{q}) = {} & \langle |V_{u1,l1}(\varphi_\mathbf{k} - \varphi_{\mathbf{k}'})|^2 + |V_{u1,l2}(\varphi_\mathbf{k} - \varphi_{\mathbf{k}'})|^2 \rangle \\ & + \frac{2\pi\tau_l N_l}{\hbar} \int \frac{d\varphi_\mathbf{g}}{2\pi} \langle |V_{u1,l1}(\varphi_\mathbf{k} - \varphi_\mathbf{g})|^2 \\ & + |V_{u1,l2}(\varphi_\mathbf{k} - \varphi_\mathbf{g})|^2 \rangle s_l(\mathbf{g},\mathbf{k}',\mathbf{q})[1 - T_l(\mathbf{g},\mathbf{q})] \\ & + \frac{2\pi\tau_u N_u}{\hbar} \int \frac{d\varphi_\mathbf{g}}{2\pi} \langle |V_{u1,u1}(\varphi_\mathbf{k} - \varphi_\mathbf{g})|^2 \\ & + |V_{u1,u2}(\varphi_\mathbf{k} - \varphi_\mathbf{g})|^2 \rangle \\ & \times s_{ul}(\mathbf{g},\mathbf{k}',\mathbf{q})[1 - T_u(\mathbf{g},\mathbf{q})], \end{aligned} \tag{54}$$

$$\begin{aligned} s_u(\mathbf{k},\mathbf{k}',\mathbf{q}) = {} & \langle |V_{u1,u1}(\varphi_\mathbf{k} - \varphi_{\mathbf{k}'})|^2 + |V_{u1,u2}(\varphi_\mathbf{k} - \varphi_{\mathbf{k}'})|^2 \rangle \\ & + \frac{2\pi\tau_u N_u}{\hbar} \int \frac{d\varphi_\mathbf{g}}{2\pi} \langle |V_{u1,u1}(\varphi_\mathbf{k} - \varphi_\mathbf{g})|^2 \\ & + |V_{u1,u2}(\varphi_\mathbf{k} - \varphi_\mathbf{g})|^2 \rangle \, s_u(\mathbf{g},\mathbf{k}',\mathbf{q})[1 - T_u(\mathbf{g},\mathbf{q})] \\ & + \frac{2\pi\tau_l N_l}{\hbar} \int \frac{d\varphi_\mathbf{g}}{2\pi} \langle |V_{u1,l1}(\varphi_\mathbf{k} - \varphi_\mathbf{g})|^2 \\ & + |V_{u1,l2}(\varphi_\mathbf{k} - \varphi_\mathbf{g})|^2 \rangle \\ & \times s_{lu}(\mathbf{g},\mathbf{k}',\mathbf{q})[1 - T_l(\mathbf{g},\mathbf{q})], \end{aligned} \tag{55}$$

$$\begin{aligned} s_{lu}(\mathbf{k},\mathbf{k}',\mathbf{q}) = {} & \langle |V_{l1,u1}(\varphi_\mathbf{k} - \varphi_{\mathbf{k}'})|^2 + |V_{l1,u2}(\varphi_\mathbf{k} - \varphi_{\mathbf{k}'})|^2 \rangle \\ & + \frac{2\pi\tau_u N_u}{\hbar} \int \frac{d\varphi_\mathbf{g}}{2\pi} \langle |V_{l1,u1}(\varphi_\mathbf{k} - \varphi_\mathbf{g})|^2 \\ & + |V_{l1,u2}(\varphi_\mathbf{k} - \varphi_\mathbf{g})|^2 \rangle s_u(\mathbf{g},\mathbf{k}',\mathbf{q})[1 - T_u(\mathbf{g},\mathbf{q})] \\ & + \frac{2\pi\tau_l N_l}{\hbar} \int \frac{d\varphi_\mathbf{g}}{2\pi} \langle |V_{l1,l1}(\varphi_\mathbf{k} - \varphi_\mathbf{g})|^2 \\ & + |V_{l1,l2}(\varphi_\mathbf{k} - \varphi_\mathbf{g})|^2 \rangle \\ & \times s_{lu}(\mathbf{g},\mathbf{k}',\mathbf{q})[1 - T_l(\mathbf{g},\mathbf{q})]. \end{aligned} \tag{56}$$

Solutions of Eqs. (53)–(56) depend on the ratio of momentum relaxation times in each subband τ_l, τ_u, and the ratios of interband transition times τ_{lu} and τ_{ul}, which are determined by the equations

$$\tau_{lu}^{-1} = \frac{2\pi N_u}{\hbar} \int \frac{d\varphi}{2\pi} \langle |V_{l1,u1}(\varphi)|^2 + |V_{l1,u2}(\varphi)|^2 \rangle, \tag{57}$$

$$\tau_{ul}^{-1} = \frac{2\pi N_l}{\hbar} \int \frac{d\varphi}{2\pi} \langle |V_{u1,l1}(\varphi)|^2 + |V_{u1,u2}(\varphi)|^2 \rangle. \tag{58}$$

Since elastic scattering from one subband to another is accompanied by a large change in quasimomentum, this ratio depends in turn on the form of the scattering potential. If the potential is smooth, then interband transitions are suppressed:

$$\tau_{ul} \gg \tau_u, \quad \tau_{lu} \gg \tau_l.$$

If the potential is short-range, then

$$\tau_{ul} \simeq \tau_u, \quad \tau_{lu} \simeq \tau_l.$$

Let us consider these two cases separately.

For a smooth potential we find that $\langle|V_{l1,u1}|^2+|V_{l1,u2}|^2\rangle\ll\langle|V_{u1,u1}|^2\rangle$ in Eqs. (53)–(56), and terms like $\langle|V_{l1},u1|^2+|V_{l1,u2}|^2\rangle T_\alpha\ll\langle|V_{u1,u1}|^2\rangle T_\alpha$ need not be included. As in the single-level case, we must expand these quantities in Fourier series in order to determine s_i. After integrating and solving the resulting system of algebraic equations, we find the expressions

$$s_l=\frac{\hbar}{2\pi N_l D_l^{(0)}(\tau_l^{(0)})^2}\,\frac{q^2/2+A_u}{q^2+A_l+A_u}\times\left[\frac{1}{q^2+A_l+A_u-F}+\frac{1}{q^2+A_l+A_u+F}\right], \tag{59}$$

$$s_{ul}=\frac{\hbar}{2\pi N_l D_l^{(0)}(\tau_l^{(0)})^2}\,\frac{[2D_u^{(0)}\tau_{ul}]^{-1}}{q^2+A_l+A_u}\times\left[\frac{1}{q^2+A_l+A_u-F}+\frac{1}{q^2+A_l+A_u+F}\right], \tag{60}$$

$$s_u=\frac{\hbar}{2\pi N_u D_u^{(0)}(\tau_u^{(0)})^2}\,\frac{q^2/2+A_l}{q^2+A_l+A_u}\times\left[\frac{1}{q^2+A_l+A_u-F}+\frac{1}{q^2+A_l+A_u+F}\right], \tag{61}$$

$$s_{lu}=\frac{\hbar}{2\pi N_u D_u^{(0)}(\tau_u^{(0)})^2}\,\frac{[2D_l^{(0)}\tau_{lu}]^{-1}}{q^2+A_l+A_u}\times\left[\frac{1}{q^2+A_l+A_u-F}+\frac{1}{q^2+A_l+A_u+F}\right], \tag{62}$$

where

$$A_l=\frac{1}{2D_l^{(0)}}\left[\frac{1}{\tau_\varphi^{(l)}}+\frac{1}{\tau_{lu}}\right],\quad A_u=\frac{1}{2D_u^{(0)}}\left[\frac{1}{\tau_\varphi^{(u)}}+\frac{1}{\tau_{ul}}\right], \tag{63}$$

$$F=\left[(A_l-A_u)^2+\frac{1}{D_l^{(0)}\tau_{lu}D_u^{(0)}\tau_{ul}}\right]^{1/2}. \tag{64}$$

The label (0) implies that the corresponding quantities are calculated without including interband transitions.

For a short-range potential there are no simplifications due to smallness of the interband matrix elements. When expanded in Fourier series, the equations contain both zero and first harmonics of the potentials, as in the single-level case [see Eq. (24)]:

$$L_n=\frac{2\pi}{\hbar}\int\frac{d\varphi}{2\pi}\langle|V_{l1,l1}(\varphi)|^2+|V_{l1,l2}(\varphi)|^2\rangle e^{-in\varphi}, \tag{65}$$

$$U_n=\frac{2\pi}{\hbar}\int\frac{d\varphi}{2\pi}\langle|V_{u1,u1}(\varphi)|^2+|V_{u1,u2}(\varphi)|^2\rangle e^{-in\varphi}, \tag{66}$$

$$W_n=\frac{2\pi}{\hbar}\int\frac{d\varphi}{2\pi}\langle|V_{l1,u1}(\varphi)|^2+|V_{l1,u2}(\varphi)|^2\rangle e^{-in\varphi}. \tag{67}$$

Since interband transitions are efficient, we cannot reduce the diffusion process to diffusion of particles in separate bands. Therefore, the expression for the cooperon now contains generalized diffusion coefficients and phase breaking times, which come from averaging over both bands:

$$s_{l,u}=\frac{\hbar}{2\pi(N_l+N_u)\tau_{l,u}^2}\,\frac{1}{Dq^2+\tau_\varphi^{-1}}, \tag{68}$$

$$s_{lu}=s_{ul}=\frac{\hbar}{2\pi(N_l+N_u)\tau_l\tau_u}\,\frac{1}{Dq^2+\tau_\varphi^{-1}}, \tag{69}$$

$$D=\frac{N_l}{N_l+N_u}\,\frac{(v_F^{(l)})^2\tau_l}{2}\,\frac{1-N_u\tau_uU_1}{Z}+\frac{N_u}{N_l+N_u}\,\frac{(v_F^{(u)})^2\tau_u}{2}\,\frac{1-N_l\tau_lL_1}{Z}+\frac{N-[l]N_u}{N_l+N_u}v_F^{(l)}v_F^{(u)}\tau_l\tau_u\frac{W_1}{Z}, \tag{70}$$

$$Z=(1-N_l\tau_lL_1)(1-N_u\tau_uU_1)-N_lN_u\tau_l\tau_uW_1^2,$$

$$\tau_\varphi^{-1}=\frac{N_l/\tau_\varphi^{(l)}+N_u/\tau_\varphi^{(u)}}{N_l+N_u}. \tag{71}$$

The methods of averaging over subbands in the expressions for D and τ_φ are different because our phenomenological introduction of a phase relaxation implies that these quantities do not depend on angles.

In order to find the velocity operator, we must solve Eq. (9) while including the two subbands. This also can be done by Fourier expansion:

$$\tilde{\mathbf{v}}^{(\alpha\beta)}=\tilde{\mathbf{v}}^{(\alpha\alpha)}\delta_{\alpha\beta},$$

$$\tilde{\mathbf{v}}^{(l1,l1)}=\tilde{\mathbf{v}}^{(l2,l2)}=\frac{1-N_uU_1\tau_u}{Z}\mathbf{v}^{(l)}+\frac{N_uW_1\tau_u}{Z}\mathbf{v}^{(u)},$$

$$\tilde{\mathbf{v}}^{(u1,u1)}=\tilde{\mathbf{v}}^{(u2,u2)}=\frac{1-N_lL_1\tau_l}{Z}\mathbf{v}^{(u)}+\frac{N_lW_1\tau_l}{Z}\mathbf{v}^{(l)}. \tag{72}$$

For a smooth potential we have $|W_1|\ll|L_1|,|U_1|$, and the velocity operator is determined by scattering within a single subband:

$$\tilde{\mathbf{v}}^{(l1,l1)}=\mathbf{v}^{(l)}\frac{\tau_{tr}^{(l)}}{\tau_l},$$

$$\tilde{\mathbf{v}}^{(u1,u1)}=\mathbf{v}^{(u)}\frac{\tau_{tr}^{(u)}}{\tau_u}. \tag{73}$$

In order to calculate the anomalous contribution to the conductivity we must substitute the coperon expressions and the velocity operator into Eqs. (2)–(4). For a smooth potential

$$\Delta\sigma^{(I)}=\frac{2e^2}{\hbar^2}\int\frac{d^2q}{(2\pi)^2}[N_lD_l^{(0)}\tau_l^{(0)}\tau_{tr}^{(l)}s_l(q)+N_uD_u^{(0)}\tau_u^{(0)}\tau_{tr}^{(u)}s_u(q)], \tag{74}$$

$$\Delta\sigma^{(II)}=\Delta\sigma^{(III)}=\frac{e^2}{\hbar^2}\int\frac{d^2q}{(2\pi)^2}[N_lD_l^{(0)}\tau_l^{(0)}(\tau_l^{(0)}\tau_{tr}^{(l)})s_l(q)$$
$$+N_uD_u^{(0)}\tau_u^{(0)}(\tau_u^{(0)}-\tau_{tr}^{(u)})s_u(q)]. \tag{75}$$

For scattering by a short-range potential,

$$\Delta\sigma^{(I)}=\frac{e^2}{\hbar^2}\int\frac{d^2q}{(2\pi)^2}\{[\tilde{v}^{(l1,l1)}]^2N_l\tau_l^3s_l(q)$$
$$+[\tilde{v}^{(u1,u1)}]^2N_u\tau_u^3s_u(q)\}, \tag{76}$$

$$\Delta\sigma^{(II)}=\Delta\sigma^{(III)}=-\frac{e^2}{2\hbar^2}\int\frac{d^2q}{(2\pi)^2}\{[\tilde{v}^{(l1,l1)}N_l\tau_l^2]^2L_1s_l(q)$$
$$+[\tilde{v}^{(u1,u1)}N_u\tau_u^2]^2U_1s_u(q)+\tilde{v}^{(l1,l1)}\tilde{v}^{(u1,u1)}$$
$$\times N_lN_u\tau_l^2\tau_u^2W_1[s_{lu}(q)+s_{ul}(q)]\}. \tag{77}$$

It thus follows from Eqs. (59)–(62), (68), and (69) that when interband transitions are taken into account, the expressions for cooperons can be represented in the form of diffusive poles for a smooth potential and for a short-range potential. Therefore, the expression for $\delta\sigma(H)$ is obtained by substituting into Eq. (45).

For scattering by a short-range potential

$$\delta\sigma(H)=-\frac{e^2}{4\pi^2\hbar}f_2\left(\frac{4eD\tau_\varphi H}{\hbar c}\right), \tag{78}$$

where D and τ_φ are defined in Eqs. (70) and (71).

For scattering by a smooth potential,

$$\delta\sigma(H)=-\frac{e^2}{4\pi^2\hbar}\left[f_2\left(\frac{H}{H_+}\right)+f_2\left(\frac{H}{H_-}\right)\right], \tag{79}$$

where

$$H_\pm=\frac{\hbar c}{4e}(A_l+A_u\pm F). \tag{80}$$

This expression for the conductivity is valid for arbitrary ratios of the interband transition and phase breaking times for wave functions. In limiting cases, the expressions for $H_\pm$ simplify. For $\tau_{lu}\gg\tau_\varphi^{(l)}$ and $\tau_{ul}\gg\tau_\varphi^{(u)}$ we have

$$H_-=\frac{\hbar c}{4eD_l^{(0)}\tau_\varphi^{(l)}},\quad H_+=\frac{\hbar c}{4eD_u^{(0)}\tau_\varphi^{(u)}}, \tag{81}$$

while for $\tau_{lu}\ll\tau_\varphi^{(l)}$ and $\tau_{ul}\ll\tau_\varphi^{(u)}$

$$H_-=\frac{\hbar c}{4eD_0\tau_\varphi},\quad H_+=\frac{\hbar c}{4e}\left(\frac{1}{D_l^{(0)}\tau_{lu}}+\frac{1}{D_u^{(0)}\tau_{ul}}\right),$$
$$H_+\gg H_-, \tag{82}$$

where τ_φ coincides with Eq. (71), and D_0 is obtained from Eq. (70) for $|W_1|\ll|L_1|,|U_1|$:

$$D_0=\frac{N_lD_l^{(0)}+N_uD_u^{(0)}}{N_l+N_u}.$$

The physical meaning of these expressions is transparent. If the phase breaking time is shorter than the time for interband transitions, both subbands give independent contributions to the conductivity. If, however, a carrier can execute many transitions between subbands within the phase breaking time, then the conductivity has the standard form Eq. (78), where D_0 and τ_φ enter in as averages over the two subbands.

Expression (79) implies that the magnetoresistance curve has two structural features, one at $H=H_-$ and one at $H=H_+$. When $H_+\gg H_-$ ($\tau_{l,u}\ll\tau_{lu,ul}\ll\tau_\varphi^{(l,u)}$), the second feature can appear for fields $H\gg H_+$, since the frequency for phase breaking by the magnetic field becomes higher than the intersubband transition frequency. For this ratio between times, both features can be observed experimentally. The lack of a second feature in Eq. (78) is explained by the fact that for scattering by a short-range potential we have

$$H_+\simeq\frac{\hbar c}{4eD\tau},$$

and this is the limiting field for diffusion theory.

When the mixing of states at the Fermi level in the upper subband is small, as we stated above, the contribution to weak localization comes from all the two-particle states within it. This situation is realized for $(E_F-\Delta)/\Delta\ll 1$. However, in the spherical approximation contributions to the cooperon from states with angular momentum 1 and 0 are separated. In this case, the mixing of states in the lower subband is strong, and only states with zero total angular momentum enter into it significantly. Therefore, the cooperon has the form

$$C_{\gamma\delta}^{\alpha\beta}(q)=s_1(q)S_{l\gamma}^\alpha+s_u(q)S_{u\gamma}^\alpha S_{u\delta}^\beta$$
$$+s_{lu}(q)(S_{l\gamma}^\alpha S_{u\delta}^\beta+S_{u\gamma}^\alpha S_{l\delta}^\beta)$$
$$+p_{ul}(q)(P_{u+\gamma}^\alpha P_{u+\delta}^\beta+P_{u-\gamma}^\alpha P_{u-\delta}^\beta)$$
$$+p_{u0}(q)P_{u0\gamma}^\alpha P_{u0\delta}^\beta. \tag{83}$$

Here $S_{l\gamma}^\alpha$ and $S_{u\gamma}^\alpha$ are defined in Eq. (52), while the nonzero components of $P_{i\gamma}^\alpha$ are

$$(P_{u+})_{u1}^{u1}=(P_{u-})_{u2}^{u2}=1,\quad (P_{u0})_{u2}^{u1}=(P_{u0})_{u1}^{u2}=1/\sqrt{2}. \tag{84}$$

The expressions for the coefficients s_i and p_i depend on the ratio of times for interband transitions and momentum relaxation in the upper subband. For $\tau_{ul}\simeq\tau_u$ the coefficients p_{ul} and p_{u0} do not have the form of diffusion poles and do not contribute to the weak localization effect, and the expressions for s_i coincide with Eqs. (68) and (69). Accordingly, the function $\delta\sigma(H)$ is determined by Eq. (78).

In the opposite case, when $\tau_{ul}\gg\tau_u$, the equations for p_{u0} and p_{u1} are similar in form to Eqs. (30) and (31), in which we had to take into account occasional transitions to the lower subbands. Therefore, the final expression for these quantites has the form

$$p_{u1}(q)=\frac{\hbar}{2\pi N_u\tau_u^{(0)}}$$
$$\times\frac{1}{D_u^{(0)}q^2\tau_u^{(0)}+\tau_u^{(0)}/\tau_\varphi+\tau_u^{(0)}/\tau_\parallel^{(u)}+\tau_u^{(0)}/\tau_{ul}}, \tag{85}$$

$$p_{u0}(q)=\frac{\hbar}{2\pi N_u\tau_u^{(0)}}\times\frac{1}{D_u^{(0)}q^2\tau_u^{(0)}+\tau_u^{(0)}/\tau_\varphi+\tau_u^{(0)}/\tau_\perp^{(u)}+\tau_u^{(0)}/\tau_{ul}}. \quad (86)$$

The expressions for s_i are completely analogous to Eqs. (59)–(62).

The times $\tau_{\|,\perp}^{(u)}$ describe spin relaxation in the upper subbands. We determined them for scattering by a short-range potential. More general expressions for these times depend on the type of subband excited, i.e., heavy-hole or light-hole. If at $k=0$ the upper subband is the second quantum well level for heavy holes, then

$$\frac{\tau_0}{\tau_\|^{(u)}}=\frac{4}{3}av_2^4\int_0^{a/2}dzC^4(z), \quad (87)$$

$$\frac{\tau_0}{\tau_\perp^{(u)}}=\frac{16}{3}[a(v_1v_2)^2+2v_0^2]\int_0^{a/2}dz\sin^2\left(\frac{2\pi z}{a}\right)C^2(z), \quad (88)$$

If, however, it corresponds to the first light-hole level, then

$$\frac{\tau_0}{\tau_\|^{(u)}}=\frac{4}{3}av_3^4\int_0^{a/2}dzS^4(z), \quad (89)$$

$$\frac{\tau_0}{\tau_\perp^{(u)}}=\frac{16}{3}[a(v_0v_3)^2+2v_1^2]\int_0^{a/2}dz\cos^2\left(\frac{\pi z}{a}\right)S^2(z). \quad (90)$$

We note here that because we have used the spherical approximation with infinitely high barriers, the nature of the upper subband is determined by the ratio m_l/m_h. For $m_l/m_h<1/4$ the upper subband is made up of heavy holes, while for $m_l/m_h>1/4$ it is a light-hole state. However, in real structures the type of subband depends on more than just the mass ratio, so that in comparing theory with experimental data we should use expressions (87) and (88) or expressions (89) and (90) for the spin relaxation time, depending on the type of excited subband.

The expression for $\delta\sigma(H)$ has the form

$$\delta\sigma(H)=\frac{e^2}{4\pi^2\hbar}\left[2f_2\left(\frac{H}{H_\|^{(u)}}\right)+f_2\left(\frac{H}{H_\perp^{(u)}}\right)-f_2\left(\frac{H}{H_-}\right)-f_2\left(\frac{H}{H_+}\right)\right], \quad (91)$$

where

$$H_\|^{(u)}=\frac{\hbar c}{4eD_u^{(0)}}\left(\frac{1}{\tau_\varphi^{(u)}}+\frac{1}{\tau_\|^{(u)}}+\frac{1}{\tau_{ul}}\right), \quad (92)$$

$$H_\perp^{(u)}=\frac{\hbar c}{4eD_u^{(0)}}\left(\frac{1}{\tau_\varphi^{(u)}}+\frac{1}{\tau_\perp^{(u)}}+\frac{1}{\tau_{ul}}\right), \quad (93)$$

while the quantities $H_\pm$ are defined by Eq. (80).

For $H_\pm<H_{\|,\perp}^{(u)}$ the function $\delta\sigma(H)$ changes sign, while for $H_\pm>H_{\|,\perp}^{(u)}$ it is positive in the entire range in which the diffusion theory is applicable.

As the carrier concentration in the upper subband increases, its spin relaxation times $\tau_\|^{(u)}$ and $\tau_\perp^{(u)}$ decrease, and the first two terms in Eq. (91) disappear. In this case Eq. (91) becomes Eq. (79).

5. CONCLUSIONS

We have derived a theory of weak localization for quantum wells with strong spin-orbit interaction, taking into account the possibility of several quantum well subbands being filled. We have obtained expressions for the magnetoresistance for various ratios of the spin relaxation, momentum relaxation, phase relaxation, and intersubband transition times. We calculated values of the characteristic magnetic fields where features in the magnetoresistance can arise, taking into account the real band structure of a quantum well system.

This paper was supported in part by the Russian Fund for Fundamental Research (Grants Nos. 96-02-16959a and 96-15-96955), the program ''Physics of Solid-State Nanostructures,'' and the Volkswagon Foundation.

[1] S. Hikami, A. Larkin, and Y. Nagaoka, Prog. Theor. Phys. **63**, 707 (1980).
[2] B. L. A'tshuler, A. G. Aronov, A. I. Larkin, and D. E. Khmel'nitskiĭ, Zh. Éksp. Teor. Fiz. **81**, 768 (1981) [Sov. Phys. JETP **54**, 411 (1981)].
[3] S. V. Iordanskiĭ, Yu. B. Lyanda-Geller, and G. E. Pikus, JETP Lett. **60**, 206 (1994).
[4] F. G. Pikus and G. E. Pikus, Phys. Rev. B **51**, 16 928 (1995).
[5] W. Knap, C. Skierbiszewski, A. Zduniak, E. Litvin-Staszevska, D. Bertho, F. Kobbi, J. L. Robert, G. E. Pikus, F. G. Pikus, S. V. Iordanskii, V. Moser, K. Zekenes, and Yu. B. Lyanda-Geller, Phys. Rev. B **53**, 3912 (1996).
[6] N. S. Averkiev, L. E. Golub, and G. E. Pikus, Zh. Éksp. Teor. Fiz. **113**, 1429 (1998) [JETP **79**, 1103 (1998)].
[7] N. S. Averkiev, L. E. Golub, and G. E. Pikus, Solid State Commun. **107** (1998) (in press).
[8] I. A. Merkulov, V. I. Perel', and M. E. Portnoĭ, Zh. Éksp. Teor. Fiz. **99**, 1202 (1991) [JETP **72**, 669 (1991)].

Translated by Frank J. Crowne

SEMICONDUCTORS VOLUME 32, NUMBER 10 OCTOBER 1998

Capacitance-voltage profiling of Au/*n*-GaAs Schottky barrier structures containing a layer of self-organized InAs quantum dots

P. N. Brunkov, A. A. Suvorova, N. A. Bert, A. R. Kovsh, A. E. Zhukov, A. Yu. Egorov,
V. M. Ustinov, A. F. Tsatsul'nikov, N. N. Ledentsov, P. S. Kop'ev,
and S. G. Konnikov

A. F. Ioffe Physicotechnical Institute, Russian Academy of Sciences, 194021 St. Petersburg, Russia

L. Eaves and P. S. Main

Department of Physics, University of Nottingham, NG7 2RD Nottingham, United Kingdom

(Submitted February 24, 1998; accepted for publication February 26, 1998)
Fiz. Tekh. Poluprovodn. **32**, 1229–1234 (October 1998)

Capacitance-voltage measurements are used to obtain profiles of the free carrier distribution in Schottky barriers grown on uniformly doped *n*-GaAs hosts containing layers of self-organized InAs quantum dots. It is found that electrons accumulate at a depth of 0.54 μm, which corresponds to the depth of the quantum-dot layer. As the temperature drops below 90 K, a second peak appears in the concentration profile at 0.61 μm, which becomes dominant as the temperature continues to decrease. It is shown that the appearance of the second peak in the concentration profile is not due to electron density redistribution over the structure, but rather is observed when the rate of thermal emission of electrons from the quantum dots is slower than the angular frequency of the capacitance measurement signal. © *1998 American Institute of Physics.* [S1063-7826(98)01810-9]

Considerable interest has recently been focused on device-related semiconductor heterostructures containing self-organized quantum dots, in which the motion of quasiparticles is quantized along all three coordinates and the spectrum of the density of states is represented by a set of δ functions.[1] In Refs. 2 and 3 the authors reported high-efficiency injection lasers with active regions containing quantum dots. Very recently the creation of optical memory elements was shown to be possible in principle,[4] along with optical bistability[5] and resonant-tunneling structures[6,7] based on quantum dots. In order to develop a new generation of devices for micro- and optoelectronics, it is necessary to investigate the influence of quantum dots on the electrical properties of these semiconductor structures. Capacitance spectroscopy is recommended as a highly efficient method for studying the properties of structures with quantum dots.[8–12] In this paper we present the results of capacitance-voltage ($C-V$) studies of the free carrier distribution profile in a uniformly doped *n*-GaAs host containing a layer of self-organized InAs quantum dots.

SAMPLES AND METHODS OF STUDY

The structures under study were grown by molecular-beam epitaxy in a Riber 32P MBE device with a solid-state source of arsenic on a n^+-GaAs (100) substrate. The assembly of InAs quantum dots consists of three layers located at a distance 50 Å from one another, each of which formed *in situ* as a result of the conversion of an elastically strained InAs layer with effective thickness 5 Å into a collection of islands. The transformation of the InAs distribution at the GaAs surface from two-dimensional to three-dimensional was monitored by changes in the reflection high-energy electron diffraction (RHEED) pattern.[13] Due to the small thickness of GaAs between the InAs quantum dot layers, each previous quantum dot layer acts as a source of elastic scattering for the next quantum dot layer as it grows.[14,15] As a result, the quantum dots are ordered in the growth direction. The assembly of quantum dots was located at the center of an undoped 200-Å-thick layer of GaAs grown on a 1-μm-thick buffer layer of Si-doped GaAs ($n\sim 2\times 10^{16}\,\mathrm{cm}^{-3}$). The last step in growing the structure was to deposit a 0.5-μm-thick capping layer of GaAs ($n\sim 2\times 10^{16}\ \mathrm{cm}^{-3}$).

$C-V$ characteristics were measured in the frequency range from 10 kHz to 1 MHz using a HP4274A capacitance bridge at temperatures from $T=4.7$ to 300 K. The amplitude of the measurement signal was 10 mV. The helium cryostat had a built-in superconducting magnet, allowing us to make measurements in magnetic fields from 0 to 12 T.

The structures of the samples were investigated by transmission electron microscopy (TEM), using a Philips EM 420 electron microscope with an accelerating voltage of 100 kV.

Photoluminescence (PL) spectra were measured at $T=77$ K using a cw helium-neon laser with a wavelength of 632.8 nm, a monochromator, and a cooled photomultiplier operated in the photon counting regime. The excitation power density was about 1 W/cm^2.

EXPERIMENTAL DATA AND DISCUSSION OF RESULTS

Figure 1a shows the $C-V$ characteristics of a structure with InAs/GaAs quantum dots measured at a frequency of 1 MHz at various temperatures. Using the depletion approxi-

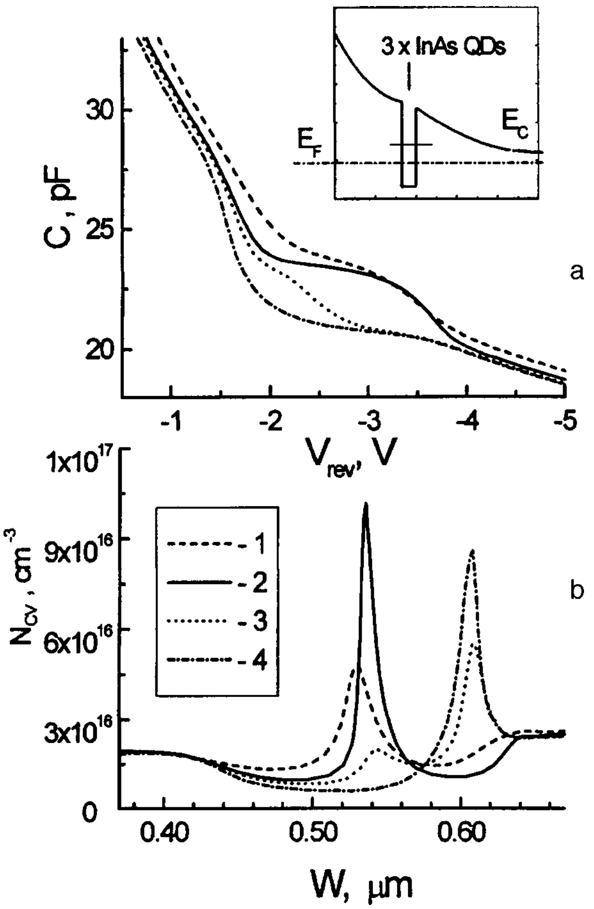

FIG. 1. $C-V$- (a) and $N_{CV}-W$- (b) characteristics of a structure with InAs/GaAs quantum dots, measured at $f=$ 1 MHz. T, K: *1* — 200, *2* — 77, *3* — 30, *4* — 15.

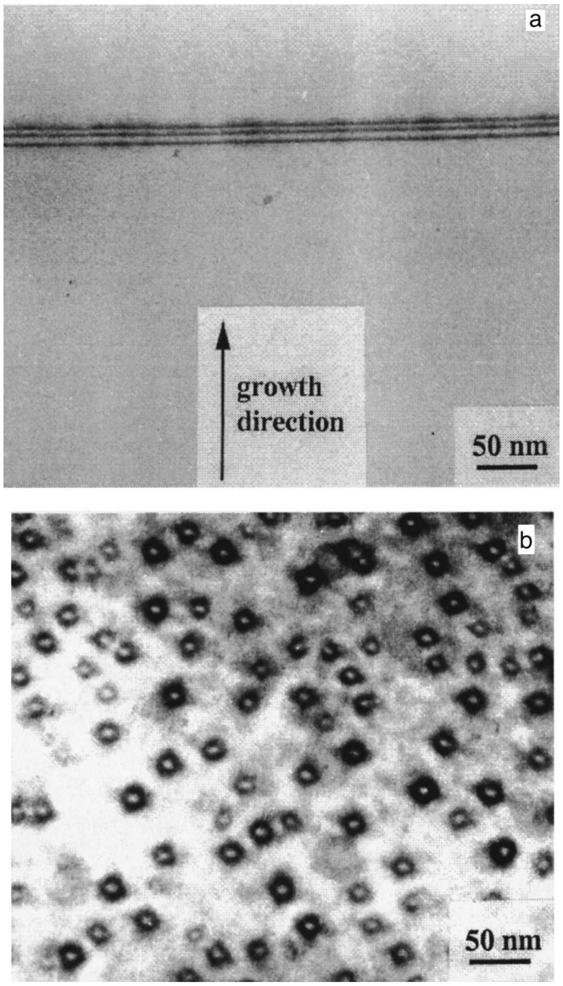

FIG. 2. Bright-field TEM images: cross section ($g=200$) (a) and in planar geometry (b) of a structure with InAs/GaAs quantum dots

mation, we can use the $C-V$ characteristics to calculate the profile of the free carrier distribution ($N_{CV}-W$; see Fig. 1b):

$$N_{CV}(W)=\frac{C^3}{q\varepsilon\varepsilon_0\left(\dfrac{dC}{dV}\right)}, \quad W=A\frac{\varepsilon\varepsilon_0}{C}, \tag{1}$$

where ε_0 is the free-space dielectric constant, ε is the semiconductor dielectric constant, W is the width of the space-charge region, and A is the area of the Schottky barrier.

Accumulation of carriers in the assembly of quantum dots leads to the appearance of a characteristic step in the $C-V$ function (Fig. 1a) and a peak in the profile of the free-carrier distribution $N_{CV}-W$ at a depth of 0.54 μm (Fig. 1b). This position corresponds to the depth at which the assembly of quantum dots was created, as inferred from TEM measurements. Upon decreasing the temperature from 200 to 77 K, we observed an increase in the width of the step in the $C-V$ characteristic (Fig. 1a) and an increase in the amplitude of the peak in the $N_{CV}-W$ profile (Fig. 1b), which corresponds to an increase in the concentration of electrons localized in the assembly of quantum dots. We showed previously that this process is caused by an increase in the Fermi level in the GaAs host.[10,11] However, further decreasing the temperature to 15 K causes this step in the $C-V$ characteristic first to decrease and then to disappear completely (Fig. 1a). In this case, the peak at $W=0.54$ μm in the $N_{CV}-W$ profile is suppressed, and a second peak appears at a depth of $W=0.61$ μm (Fig. 1b). It should be noted that the samples we studied contained no structural nonuniformity of any kind at this depth (Fig. 2a).

According to our model, which is based on solving the one-dimensional Poisson equation,[10–12] at a given temperature the width of the peak in the $C-V$ characteristic depends on the electron concentration in the quantum-dot layer Q_{qd}, which in turn is determined by the concentration of quantum dots N_{qd} and the Fermi–Dirac function, which depends on the position of the electron level (E_{qd}) in the quantum dot with respect to the Fermi level (E_F) in the GaAs host. The two-dimensional concentration of quantum dots N_{qd} was measured by TEM and came to 5×10^{10} cm^{-2} (Fig. 2b). The density of states in the quantum-dot layer could be described by a Gaussian function, reflecting the nonuniformity distribution in the sizes of the quantum dots. The magnitude of the dispersion ΔE of the quantum-dot density of states function, which was determined by analyzing PL (Fig. 3) related to electron-hole recombination in the quantum dots,[1] is 60 meV. The electron concentration in the quantum-dot layer can then be written as[12]

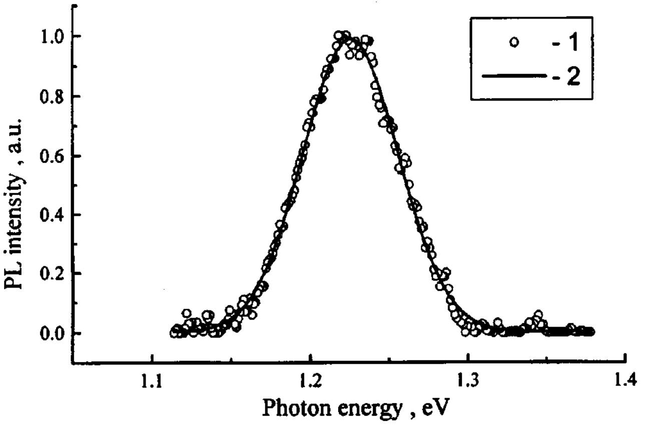

FIG. 3. PL spectrum of a structure with InAs/GaAs quantum dots (1) at $T=77$ K. The solid curve (2) is an approximation of the experimental data by a Gaussian function with $\Delta E=60$ meV and a value of 1.22 eV at its maximum.

$$Q_{qd}=\int \frac{2N_{qd}}{\sqrt{\frac{\pi}{2}}\Delta E}\,\frac{\exp(-2(E-E_{qd})^2/(\Delta E)^2)}{1+\exp((E-E_F)/kT)}\,dE, \tag{2}$$

where k is the Boltzmann constant.

This model describes the $C-V$ characteristics rather well for $T>77$ K (Figs. 4a and 4b) for the following parameter values: $N_{qd}=5\times10^{10}$ cm^{-2}, $E_{qd}=70$ meV, $\Delta E_{qd}=70$ meV, and $d_{\text{cap}}=0.52$ μm. Note that the concentration of quantum dots N_{qd} and thickness of the capping layer d_{cap} determined from analyzing the $C-V$ characteristics are in rather good agreement with the TEM data (Fig. 2b). However, below $T=77$ K we observed considerable discrepancies between the experimental and theoretical $C-V$ and $N_{CV}-W$- characteristics: the step in the $C-V$ characteristic is suppressed and a second peak appears in the $N_{CV}-W$ profile at $W=0.61$ μm (Figs. 4c and 4d). We suggest that this is not associated with a redistribution of electron density across the structure, but rather arises from the fact that in our model the capacitance of the structure is calculated in the quasistatic approximation:

$$C=\Delta Q/\Delta V, \tag{3}$$

i.e., we disregard the time-dependent part of the change ΔQ in charge caused by a change in voltage ΔV. However, these changes in the capacitance can be measured by superimposing a small ac signal (dV_{osc}) with frequency f on the dc reverse bias (V_{rev}). The measurement signal dV_{osc} modulates the charge at the edge of the space-charge region (dQ_{3D}) formed by the Schottky barrier, and also the charge in the quantum-dot layer (dQ_{qd}) where the Fermi level intersects the electronic level in the quantum dot. Therefore, the capacitance of the structure with quantum dots consists of two parts:[12]

$$C=C_{3D}+C_{qd}=\frac{dQ_{3D}}{dV}+\frac{dQ_{qd}(E_{qd}-E_F)}{dV}, \tag{4}$$

where C_{3D} is the bulk capacitance, and C_{qd} is that part of the capacitance associated with the quantum-dot layer.

Calculations of the $C-V$ characteristics of a structure with quantum dots show that the region of quasi-constant capacitance from -2 to -3.5 (Fig. 5a) is associated with a linear decrease in the concentration of electrons in the plane of the quantum dots with increasing reverse bias (Fig. 5b). In this case, the change dW in the width of the space-charge

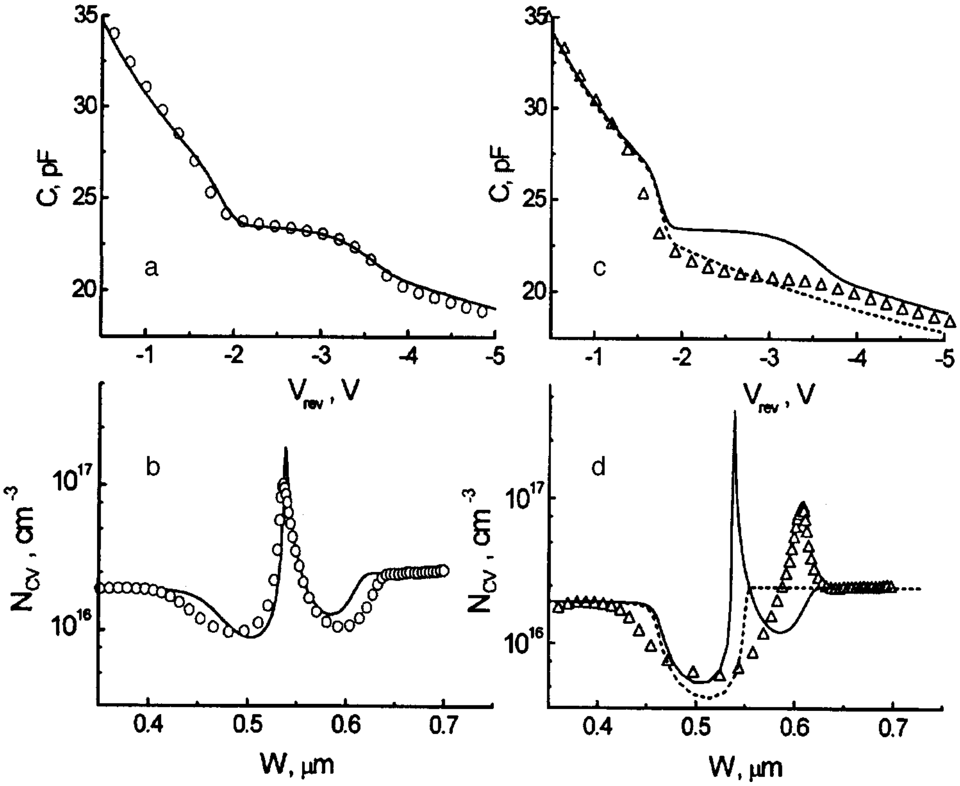

FIG. 4. $C-V$- (a) and $N_{CV}-W$- (b) characteristics of a structure with InAs/GaAs quantum dots, measured at $T=77$ K (a and b) and at $T=15$ K (c and d): experimental data (light symbols) and model calculations (solid curves) are for $N_{qd}=5\times10^{10}$ cm^{-2}, $E_{qd}=70$ meV, and $\Delta E_{qd}=80$ meV. The dotted curves (c and d) show model calculations at $T=15$ K with an electron concentration n_{qd} in the quantum dots which is fixed and which is independent of the reverse bias voltage V_{rev}.

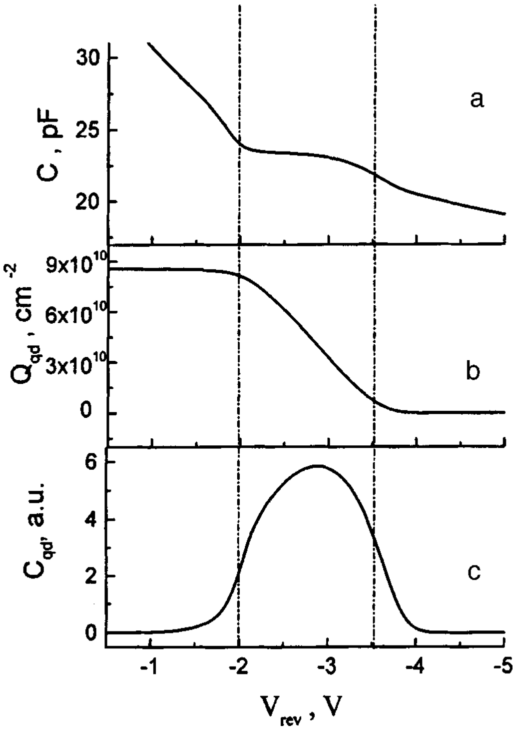

FIG. 5. $C-V$- (a), $Q_{qd}-V$- (b), and $C_{qd}-V$- (c) characteristics of a structure with InAs/GaAs quantum dots obtained at $T=77$ K for $N_{qd}=5\times10^{10}$ cm^{-2}, $E_{qd}=70$ meV, and $\Delta E_{qd}=70$ meV.

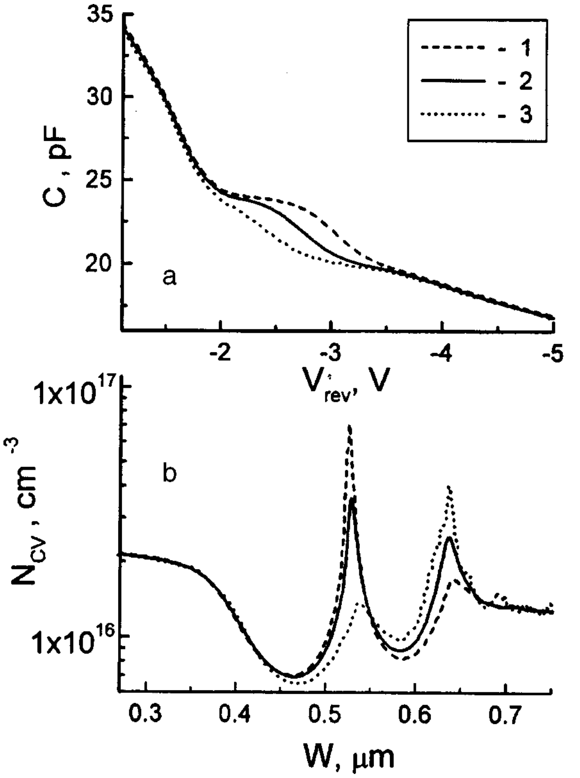

FIG. 6. $C-V$- (a) and $C_{qd}-V$- (b) characteristics of a structure with InAs/GaAs quantum dots computed at $T=29$ K for various measurement signal frequencies. f, kHz: *1* — 10, *2* — 100, *3* — 1000.

region caused by a change dV in the bias voltage becomes so small that dQ_{qd} is considerably larger than dQ_{3D}; i.e., C_{qd} will overwhelm C_{3D} in the voltage range from -2 to -3.5 V (Fig. 5c).

Measurements show (Fig. 1a) that when the temperature is decreased below 70 K, the capacitance C_{qd} is suppressed, and at $T = 15$ K it disappears entirely, whereas the calculations imply that occupancy of the quantum-dot layer by electrons saturates in this temperature region .[10,11] This disagreement arises from the fact that the model assumes that the position of the Fermi level in the assembly of quantum dots coincides with the Fermi level in the GaAs host. Whether this condition is satisfied or not depends on the rate of exchange of electrons between the quantum dots and the bulk GaAs. It is well known that self-organized quantum dots are characterized by a very high rate of charge-carrier capture.[1] Therefore, the ratio of Fermi levels in the quantum dot and the bulk material will, to a considerable degree, be determined by carrier emission from the quantum dot. In this case, suppression of the capacitance C_{qd} at low temperatures could be associated with the fact that the rate of thermionic emission of electrons from the quantum dot (e_n) is considerably smaller than the angular frequency of the measurement signal $2\pi f$; i.e., a ‘‘freeze-out’’ of electrons in the quantum dot levels takes place. This effect is a manifestation of the zero-dimensional nature of states in the quantum dot, and is not observed in structures with quantum wells.[16] To model this situation we calculated $C-V$ and $N_{CV}-W$- characteristics at $T=15$ K under the condition that the concentration of electrons in the quantum dot does not depend on the reverse bias. In this case we observe rather good agreement between the experimental and calculated $C-V$ characteristics (Fig. 4c).

In order to remove electrons from the quantum-dot layer at $T = 15$ K it is necessary to apply a higher electric field, so that the electrons can tunnel from the quantum dots to the GaAs through a narrow triangular barrier (see the inset in Fig. 1a). This process leads to the appearance of the second peak in the $N_{CV}-W$-profile at $W=0.61$ μm, which corresponds to the second plateau in the $C-V$ characteristic in the bias range -3 to -3.5 V (Figs. 4c and 4d). However, the theoretical $N_{CV}-W$ profile (Fig. 4d) shows no peak at $W=0.61$ μm. This is because the calculations were based on the quasistatic approximation, which disregards the tunneling effect.

Let us assume that the rate of thermionic emission of electrons from the quantum dots depends exponentially on temperature and on the energy of the quantum state in the quantum dot. The assembly of quantum dots is characterized by a Gaussian density of states; therefore, at a given temperature and frequency of the measurement signal, one group of quantum dots is characterized by a high rate of thermionic emission, when $(e_n \gg 2\pi f)$, while the rest have a low rate of thermionic emission $(e_n \ll 2\pi f)$. Decreasing the measurement-signal frequency from 1 MHz to 10 kHz at $T=28$ K leads to an increase in the number of quantum dots that satisfy the condition $e_n \gg 2\pi f$; in this case, the step in the $C-V$ characteristic broadens (Fig. 6a) and the peak in the $N_{CV}-W$ profile at $W=0.54$ μm increases in height even as the peak at $W=0.61$ μm is suppressed (Fig. 6b).

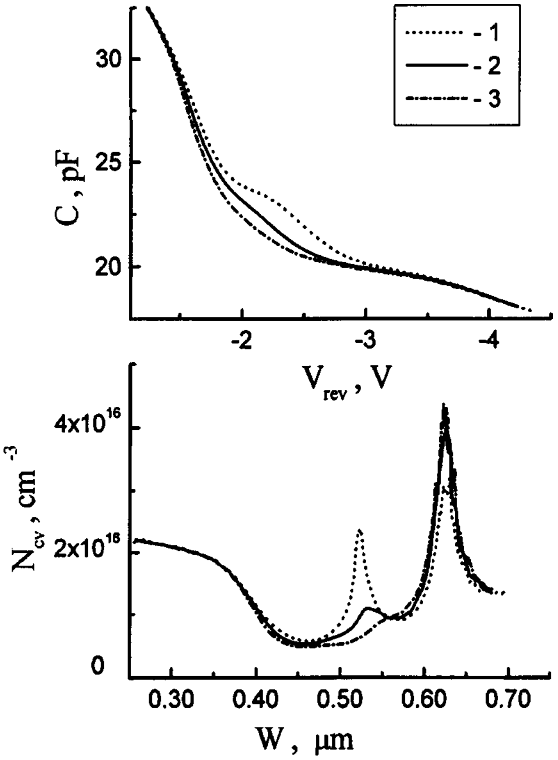

FIG. 7. $C-V$ - (a) and $N_{CV}-W$ - (b) characteristics of a structure with InAs/GaAs quantum dots obtained at $T=17$ K and $f=10$ kHz for various magnetic field values. B, T: *1* — 0, *2* — 8.1, *3* — 12. The magnetic field intensity vector B is perpendicular to the sample surface.

Even magnetic fields as large as 12 T turn out to have little effect on the electron level in the quantum dot.[17] However, they lead to the formation of Landau levels in the GaAs conduction band, and consequently raise the lowest possible state in the GaAs conduction band by $\Delta E_c = \hbar\omega_c/2 \approx 10$ meV, where $\hbar\omega_c$ is the cyclotron energy. This leads to an effective deepening of the electronic level in the quantum dot[17,18] which is manifested as a decrease in the width of the step in the $C-V$ characteristic (Fig. 7a) and an increase in the peak amplitude at $W=0.61$ μm in the $N_{CV}-W$ profile (Fig. 7b). It should be noted that this effect does not depend on the orientation of the magnetic field, which is connected with the zero-dimensional nature of the quantum states in the quantum dot. The magnetic field has no effect at $T>70$ K, when $kT \geqslant \Delta E_c$.

CONCLUSIONS

In this paper we have described studies of the $C-V$ profiles of a uniformly doped *n*-GaAs host with a Schottky barrier at its surface that contains a layer of self-organized InAs quantum dots. We have established that electron accumulation can be observed at a depth of 0.54 μm, which coincides with the geometric position of the quantum-dot layer. As the measurement temperature is decreased below 90 K, a second peak appears in the profile at a depth of 0.61 μm, which upon further lowering of the temperature becomes dominant. We have established that the appearance of this second peak in the free-carrier distribution profile is not connected with redistribution of the electronic density throughout the depth of the structure, but rather appears when the rate of thermal emission of electrons from the quantum dots to the GaAs conduction band becomes considerably smaller than the angular frequency of the signal used to measure the capacitance. We have shown that applying a magnetic field leads to a decrease in the rate of thermionic emission from the quantum well due to effective deepening of the electronic level in the quantum well caused by the formation of ladders of Landau levels in the GaAs conduction band.

This work was supported by the INTAS-RFFI 95-IN-Ru-618 program and the program ‘‘Physics of Solid-State Nanostructures’’ from the Science Ministry of the Russian Federation.

[1] N. N. Ledentsov, M. Grundmann, N. Kirstaedter, O. Schmidt, R. Heitz, J. Bö hrer, D. Bimberg, V. M. Ustinov, V. A. Shchukin, P. S. Kop’ev, Zh. I. Alferov, S. S. Ruvimov, A. O. Kosogov, P. Werner, U. Richter, U. Goesele, and J. Heydenreich, Solid-State Electron. **40**, 785 (1996).

[2] N. Kristaedter, N. N. Ledentsov, M. Grundmann, D. Bimberg, V. M. Ustinov, M. V. Maximov, P. S. Kop’ev, Zh. I. Alferov, U. Richter, P. Werner, U. Goesele, and J. Heyndenreich, Electron. Lett. **30**, 1416 (1994).

[3] Zh. I. Alferov, N. A. Bert, Yu. A. Egorov, P. S. Kop’ev, A. O. Kosogov, I. L. Krestnikov, N. N. Ledentsov, A. V. Lunev, A. V. Sakharov, V. M. Ustinov, A. F. Tsatsul’nikov, Yu. M. Shernyakov, and D. Bimberg, Fiz. Tekh. Poluprovodn. **30**, 351 (1996) [Semiconductors **30**, 194 (1996)].

[4] K. Imamura, Y. Sugiyama, Y. Nakata, S. Muto, and N. Yokoyama, Jpn. J. Appl. Phys. **34**, L1445 (1995).

[5] G. Yusa and H. Sakaki, Appl. Phys. Lett. **70**, 345 (1997).

[6] I. E. Itskevich, T. Ihn, A. Tornton, M. Henini, T. J. Foster, P. Moriarty, A. Nogaret, P. H. Beton, L. Eaves, and P. C. Main, Phys. Rev. B **54**, 16 401 (1996).

[7] M. Narihiro, G. Yusa, Y. Nakamura, T. Noda, and H. Sakaki, Appl. Phys. Lett. **70**, 105 (1997).

[8] G. Medeiros-Ribeiro, D. Leonard, and P. M. Petroff, Appl. Phys. Lett. **66**, 1767 (1995).

[9] S. Anand, N. Carlsson, M-E. Pistol, L. Samuelson, and W. Seifert, Appl. Phys. Lett. **67**, 3016 (1995).

[10] P. N. Brunkov, S. G. Konnikov, V. M. Ustinov, A. E. Zhukov, A. Yu. Egorov, V. M. Maximov, N. N. Ledentsov, and P. S. Kop’ev, Fiz. Tekh. Poluprovodn. **30**, 924 (1996) [Semiconductors **30**, 492 (1996)].

[11] P. N. Brounkov, N. N. Faleev, Yu. G. Misikhin, A. A. Suvorova, A. F. Tsatsul’nikov, V. M. Maximov, A. E. Zhukov, A. Yu. Egorov, V. M. Ustinov, P. S. Kop’ev, and S. G. Konnikov, in *The Physics of Semiconductors* (World Scientific, Singapore, 1996), p. 1361.

[12] P. N. Brounkov, N. N. Faleev, Yu. G. Musikhin, A. A. Suvorova, A. F. Tsatsul’nikov, V. M. Maximov, A. Yu. Egorov, A. E. Zhukov, V. M. Ustinov, N. N. Ledentsov, P. S. Kop’ev, and S. G. Konnikov, Inst. Phys. Conf. Ser. 155 (IOP, Bristol, 1997), p. 841.

[13] F. Yu. Egorov, A. E. Zhukov, P. S. Kop’ev, N. N. Ledentsov, V. M. Maximov, and V. M. Ustinov, Fiz. Tekh. Poluprovodn. **28**, 1439 (1994) [Semiconductors **28**, 809 (1994)].

[14] G. S. Solomon, J. A. Trezza, A. F. Marshall, and J. S. Harris, Jr., Phys. Rev. Lett. **76**, 952 (1996).

[15] A. Yu. Egorov, A. E. Zhukov, P. S. Kop’ev, N. N. Ledentsov, V. M. Maximov, V. M. Ustinov, A. F. Tsatsul’nikov, N. A. Bert, A. O. Kosogov, Zh. I. Alferov, and D. Bimberg, Fiz. Tekh. Poluprovodn. **30**, 1682 (1996) [Semiconductors **30**, 879 (1996)].

[16] P. N. Brounkov, T. Benyattou, and G. Guillot, J. Appl. Phys. **80**, 864 (1996).

[17] I. E. Itskevich, M. Henini, H. A. Carmona, L. Eaves, P. C. Main, D. K. Maude, and J. C. Portal, Appl. Phys. Lett. **70**, 505 (1997).

[18] P. N. Brounkov, A. A. Suvorova, M. V. Maximov, A. F. Tsatsul’nikov, A. E. Zhukov, A. Yu. Egorov, A. R. Kovsh, S. G. Konnikov, T. Ihn, S. T. Stoddart, L. Eaves, and P. C. Main, Physica B (1998) (to be published).

Translated by Frank J. Crowne

SEMICONDUCTORS VOLUME 32, NUMBER 10 OCTOBER 1998

Electron-hole Coulomb interaction in InGaN quantum dots

V. E. Bugrov and O. V. Konstantinov

A. F. Ioffe Physicotechnical Institute, Russian Academy of Sciences, 194021 St. Petersburg, Russia

(Submitted March 2, 1998; accepted for publication March 16, 1998)
Fiz. Tekh. Poluprovodn. **32**, 1235–1239 (October 1998)

In contrast to group-III arsenide-based quantum dots, group-III nitride-based quantum dots are much smaller in size and have less conduction band offset. For this reason, it is important to take into account the electron-hole Coulomb interaction in which the spherical quantum dot is substituted for the cube-shaped quantrum dot, which in this paper is treated within the Hartree approximation. In addition to making the electron binding energy several times larger, this strong Coulomb interaction between carriers in quantum dots makes conventional distribution functions invalid, requiring their recalculation. Such calculations reveal that while the one-particle distribution functions are donor-like, the electron-hole function is quite different from its predecessors. © *1998 American Institute of Physics.* [S1063-7826(98)01910-3]

1. INTRODUCTION

At this time there is great interest in heterojunction lasers based on solid solutions in the InGaN system, which emit in the blue and violet regions of the spectrum. The first such lasers were made at the end of 1995 and the beginning of 1996.[1] Their active region was a sequence of 30 to 50-Å-thick $In_{0.2}Ga_{0.8}N$ quantum wells, each enclosed by 60 to 100-Å-thick $In_{0.05}Ga_{0.95}N$ barrier layers. Recent studies of these structures[2,3] show that the layers that form the quantum wells are broken up into regions that are enriched with indium surrounded by regions with a InN content close to that of the barrier layers. Thus, the active region of these structures can be treated as an assembly of cube-shaped quantum dots.

The theory of the quantum-dot laser was developed previously[4–6] and applied to systems based on arsenides. However, structures based on group-III nitrides differ significantly from arsenide-based structures. First of all, the value of the conduction band offset is small, since the ratio $\Delta E_c : \Delta E_v = 30:70$.[7] Secondly, and more importantly, quantum dots in the nitride systems are much smaller than those based on arsenides. Typical dimensions of the latter are only 100 Å. Because of the small sizes of the dots and the small value of ΔE_c, bound states of an electron in an InGaN dot are either entirely absent or at best have ionization energies close to thermal energy. Therefore, a quantum dot occupied by an electron-hole pair can easily lose the electron and cease to be a source of laser radiation. Under these conditions, the Coulomb attraction between the electron and hole becomes extremely important. As we show in this paper, this interaction strongly suppresses the thermal ionization of electron-hole pairs in a quantum dot. Its inclusion in theoretical calculations, which was not done in Refs. 4–6 mentioned above, has even more important consequances with regard to electron and hole statistics in the quantum dot. In the absence of this interaction, the way that electrons and holes occupy their respective levels in the quantum dot is described by the usual Fermi functions f_c and f_v, which have been used before. However, when the interaction is included, the occupation statistics change significantly. Their derivation will constitute the second part of this paper.

2. WAVE EQUATIONS AND ENERGY

If the quantum dot is occupied by only one particle (an electron or hole), then the wave equation of the particle has the standard form

$$-\frac{\hbar^2}{2m_{c,v}}\nabla^2\Psi_{c,v}^{(0)}(\mathbf{r})+U_{c,v}(\mathbf{r})\Psi_{c,v}^{(0)}(\mathbf{r})=-\varepsilon_{c,v}^{(0)}\Psi_{c,v}^{(0)}(\mathbf{r}). \qquad (1)$$

Here $\varepsilon_{c,v}^{(0)}>0$ are the ionization energies of a particle (electron or hole) in the singly occupied quantum dot. $U_{c,v}(\mathbf{r})$ is the step-like potential created by the heterostructure, which we set equal to zero in the host surrounding the quantum dot. Within the dot this potential is

$$U_{c,v}(\mathbf{r})=-\Delta E_{c,v} \qquad (2)$$

for electrons or holes. For the case of interest to us, the dot has the shape of a cube with size a. Following previous papers, we replace the cubic well by a spherical well for simplicity, choosing the radius of the sphere R to be

$$R=\frac{a}{\sqrt{3}}. \qquad (3)$$

This choice is made so that the ground state energy of a cube-shaped well with infinitely high walls coincides with that of the spherical well. Equation (1) has a well-known sinusoidal solution, and the energy is found from the usual transcendental equation.

If the quantum dot is occupied by an electron and a hole, then their wave functions $\Psi_c(r)$ and $\Psi_v(r)$, and also their single-particle energy parameters $\varepsilon_c>0$ and $\varepsilon_v>0$, can be found from the system of Hartree equations

$$\begin{cases} -\dfrac{\hbar^2}{2m_c}\nabla^2\Psi_c(r)+U_c(r)\Psi_c(r) \\ \quad -V_{vv}(r)\Psi_c(r)=-\varepsilon_c\Psi_c(r), & (4a) \\ -\dfrac{\hbar^2}{2m_v}\nabla^2\Psi_v(r)+U_v(r)\Psi_v(r) \\ \quad -V_{cc}(r)\Psi_v(r)=-\varepsilon_v\Psi_v(r), & (4b) \end{cases}$$

where the potentials due to the Coulomb interaction within the Hartree approximation are

$$V_{vv}(\mathbf{r})\equiv\frac{e^2}{\varepsilon}\int d^3\mathbf{r}'\frac{|\Psi_v(\mathbf{r}')|^2}{|\mathbf{r}-\mathbf{r}'|},$$

$$V_{cc}(\mathbf{r})\equiv\frac{e^2}{\varepsilon}\int d^3\mathbf{r}'\frac{|\Psi_c(\mathbf{r}')|^2}{|\mathbf{r}-\mathbf{r}'|}. \qquad (5)$$

Here ε is the dielectric constant, which we assume is the same inside and outside the well since its discontinuity at the heterojunction is only a few percent. We ignore the difference in effective masses for electrons and holes across the heterojunction. The total energy of an electron-hole pair located in the quantum dot is

$$E=E_g-\varepsilon_c-\varepsilon_v+V_{cc}^{vv}, \qquad (6)$$

where the matrix element for the Coulomb interaction is

$$V_{cc}^{vv}=\int V_{cc}(\mathbf{r})|\Psi_v(\mathbf{r})|^2d^3\mathbf{r}=\int V_{vv}(\mathbf{r})|\Psi_c(\mathbf{r})|^2d^3\mathbf{r}. \qquad (7)$$

In Eq. (6) we have subtracted the average value of the Coulomb interaction of the electron and hole on the right side, as is done in helium-atom calculations,[8] since it has already been included twice: once in Eq. (4a), and again in Eq. (4b).

Using the variational method which is described, for example, in the monograph of Ref. 9, we can successively derive Eqs. (4a), (4b), and (6) by assuming that the system wave function has the form of a product, i.e., $\Psi(\mathbf{r}_e,\mathbf{r}_h)=\Psi_c(\mathbf{r}_e)\Psi_v(\mathbf{r}_h)$, where $\mathbf{r}_e$ and $\mathbf{r}_h$ are the electron and hole coordinates. We will consider only the ground state of the electron and hole. The Hartree potential determined by Eq. (5) simplifies for spherically symmetric ground-state functions:

$$V(r)=\frac{e^2}{\varepsilon}\left[\frac{1}{r}\int_0^r\varphi^2(r')dr'+\int_r^\infty\frac{\varphi^2(r')}{r'}dr'\right], \qquad (8)$$

where $\varphi(r)$ is determined from the expression

$$\Psi(r)=\frac{1}{\sqrt{4\pi}}\frac{\varphi(r)}{r}; \qquad \int_0^\infty\varphi^2(r)dr=1.$$

In Fig. 1, the original step-like quantum well is shown schematically by the solid curve, while the dashed curve shows how the well is distorted by the Coulomb interaction between the electron and hole. In our quantum-dot calculations we assumed that $E_g=3.325$ eV, $\Delta E_c=67.5$ meV, $\Delta E_v=157.5$ meV, $\varepsilon=9$, $m_c=0.2m_0$, and $m_v=m_0$, where m_0 is the mass of a free electron. Figure 2 shows the dependence of the binding energy of an electron and hole on the size of the quantum dot. The dashed curves show the size dependences of the single-particle energy parameters ε_c and ε_v, which are eigenvalues of Eqs. (4a) and (4b). For comparison, the solutions $\varepsilon_c^{(0)}$, $\varepsilon_v^{(0)}$ of Eq. (1) with the step-like potentials alone, which give the binding energies of an electron and hole in the quantum well without allowance for the Coulomb interaction, are shown by the dashed curves. It is clear that for a step potential there is no longer a bound state for the electron when $a<50$Å.

As we have already said, one possible decay mode of a bound exciton is thermal ejection of an electron or hole from the quantum well into the semiconductor bulk. In this case, the ionization energy of an electron $I_c>0$ or hole $I_v>0$ will be the quantity $I_{c,v}=E_2-E_1$, where $E_1=E$ is the energy of the initial state determined by Eq. (6), and $E_2=E_g-\varepsilon_{v,c}^{(0)}$ is the energy of a bound hole (electron) when its partner is absent:

$$I_c=\varepsilon_c+\varepsilon_v-V_{cc}^{vv}-\varepsilon_v^{(0)}, \quad I_v=\varepsilon_c+\varepsilon_v-V_{cc}^{vv}-\varepsilon_c^{(0)}. \quad (9)$$

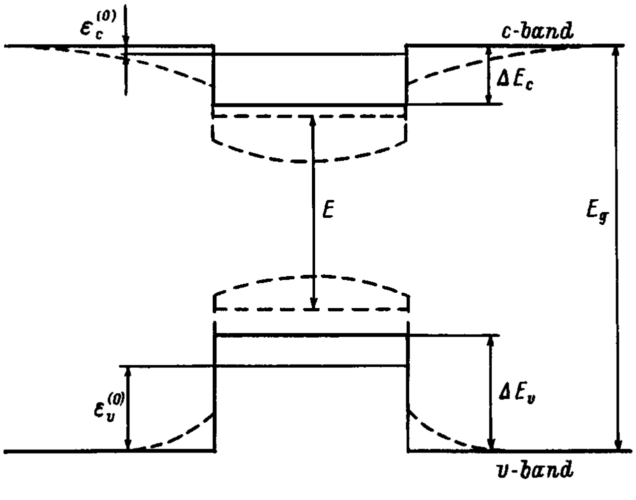

FIG. 1. Schematic illustration of the shape of the energy bands in a quantum dot without including (solid curve) and including (dashed curve) the Coulomb interaction between the electron and hole.

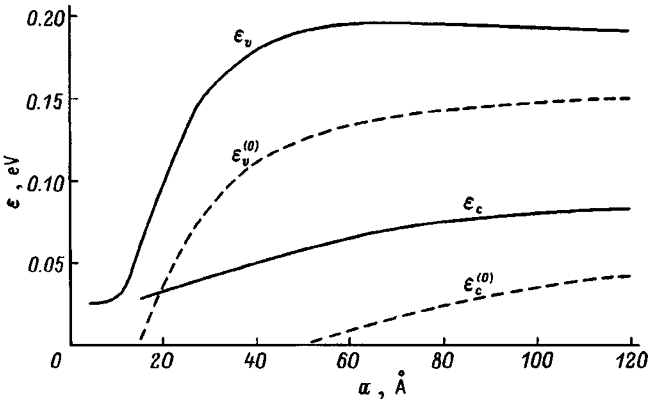

FIG. 2. Dependence of the binding energy of an electron and hole on the size of the quantum dot a obtained by solving the system of equations; the solid curves are for the Hartree Eqs. (4a), (4b), while the dashed curves include only the step potential Eq. (1).

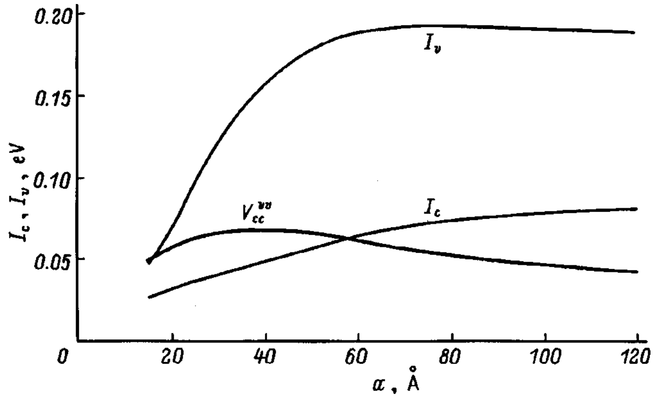

FIG. 3. Dependence of the Coulomb potential V_{cc}^{vv} and ionization energy for an electron (I_c) and a hole (I_v) on the size of the quantum dot.

Figure 3 shows the dependence of the ionization energy of an electron and hole on the size of the quantum dot. Note that the ionization energy of the electron I_c as a function of the size of the quantum dot a virtually coincides with the single-particle energy parameter $\varepsilon_c(a)$. According to the Koopmans theorem,[9] this is a characteristic sign of the successful choice of a variational electron wave function. The hole ionization energy $I_v(a)$ is also in fairly good agreement with the single-particle energy parameter $\varepsilon_v(a)$. In this case, however, the agreement is somewhat worse for $a<50$ Å. Figure 3 also shows the dependence of the Coulomb matrix element V_{cc}^{vv} on the size of the quantum dot. This function has a maximum at $a \simeq 40$ Å. For smaller quantum dots the wave functions are found to be weakly localized within the dots, and the average Coulomb interaction energy decreases. For larger dots the wave functions are almost completely localized, and the average energy of the Coulomb interaction turns out to be inversely proportional to the size of the dot.

In Fig. 4 we show the dependence of the total energy of an electron-hole pair on the size of the quantum dot. In the range of values $a=15$—50 Å, the energy of an emitted photon decreases rapidly as a increases by 170 meV. This is sufficient to significantly lower the absorption of light in the host material. For this reason, the interval of optimum quantum-dot size is somewhere in the range 40–60 Å, since further increasing the size of the quantum dot leads to the appearance of new energy levels.

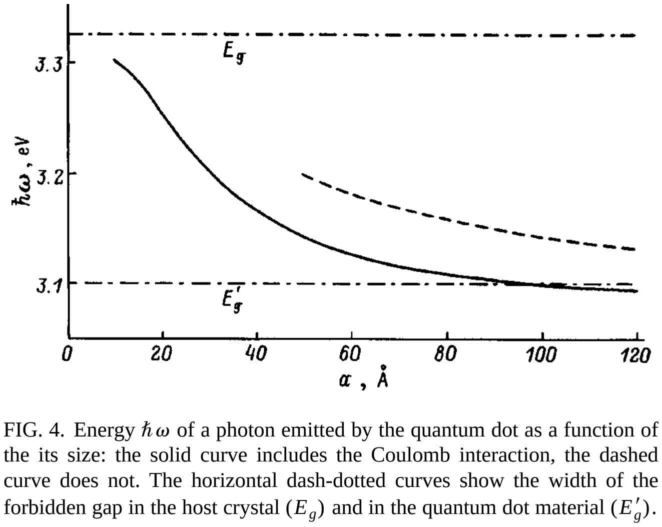

FIG. 4. Energy $\hbar\omega$ of a photon emitted by the quantum dot as a function of the its size: the solid curve includes the Coulomb interaction, the dashed curve does not. The horizontal dash-dotted curves show the width of the forbidden gap in the host crystal (E_g) and in the quantum dot material (E_g').

3. STATISTICS OF ELECTRONS AND HOLES IN A QUANTUM DOT

Our studies of the Coulomb interaction between an electron and hole require that we replace the usual single-particle functions for occupation of states f_c and f_v by a certain generalized function f_{ex} that characterizes the degree of occupation of the dot by electron-hole pairs, i.e., excitons. The fact is that we no longer can separately determine energy levels for an electron and hole. We know only the total energy of an exciton E given by Eq. (6). Furthermore, only singlet excitons, for which the spins of the electron and hole are antiparallel, are capable of radiative recombination. This fact is disregarded in computations of the probability for the absorption and emission of a photon based on the distribution functions f_c and f_v.

As usual, we assume that all the electronic states adjacent to the edge of the conduction band are in quasithermal equilibrium, with a quasi-Fermi level ξ_c, whereas all the states located near the edge of the valence band are likewise in equilibrium with a quasi-Fermi level ξ_v. The usual condition for this approach to be correct is smallness of the momentum relaxation time compared to the recombination time. In constructing the distribution function f it is necessary to use the grand canonical distribution, according to which the probability F_{nm} of creating a system of n and m holes is

$$F_{nm}=Cg_{nm}\exp\left(-\frac{E-n\xi_c-m\xi_v}{k_BT}\right), \tag{10}$$

where C is a normalizing constant determined from the condition $\Sigma_{nm}F_{nm}=1$; $g_{nm}=2s_{nm}+1$ is a degeneracy factor determined by the total spin of the quasiparticle s_{nm}; and E is the total energy of the system measured from the same level as the quasi-Fermi levels of the electrons and holes.

Let us consider the distribution function for various types of occupation of the quantum dot.

1. **Absence of particles in the quantum dot:** $g_{00}=1$; in this case $F_{00}=C$.

2. **Only electrons or only holes in the quantum dot**. We note at the outset that the case of two identical particles in the quantum dot with different spins can be excluded, due to the strong Coulomb repulsion of identical particles. This case, which is completely analogous to that of electron statistics in shallow donors,[10] obviously requires that $s_{10}=s_{01}=1/2$, $g_{10}=g_{01}=2$. The distribution functions is

$$f_{1c}=\sum_n nF_{nm}\Big|_{m=0}=2C\exp\zeta_c, \quad \zeta_c\equiv\frac{\varepsilon_c^{(0)}-\mu_n}{k_BT}, \tag{12}$$

$$f_{1v}=\sum_m mF_{nm}\Big|_{n=0}=2C\exp\zeta_v, \quad \zeta_v\equiv\frac{\varepsilon_v^{(0)}-\mu_p}{k_BT}, \tag{13}$$

where μ_n and μ_p, i.e., the quasi-Fermi levels of electrons and holes measured from the bottom of the conduction band

and the top of the valence band in the host, respectively, are positive for nondegenerate electrons and holes in the host.

3. **An electron and hole in the quantum dot simultaneously**. If the spins of the electron and hole are antiparallel, the electron and hole can radiatively recombine. Here the possible particle numbers are both $n=m=1$ and $n=m=2$. However, it should be kept in mind that two excitons in one quantum dot constitutes an extremely short-lived state, which very easily decomposes via Auger recombination. Therefore, we will ignore such states, and assume $n=m=1$. For this same reason, in what follows we will ignore states for which not only an exciton but also additional holes and electrons are contained in the quantum dot. Since the total spin of a singlet exciton equals zero, we have $g_{11}=1$. We thus easily find that

$$f_{\text{ex}}=F_{11}=C\ \exp\zeta_{\text{ex}},\quad \zeta_{\text{ex}}\equiv-\frac{E-\mu_{\text{ex}}}{k_BT},\tag{14}$$

where E is the energy of an electron-hole pair given by (6), and $\mu_{\text{ex}}=E_g-\mu_n-\mu_p$ is the quasi-Fermi level of the exciton determined by the distance between the quasi-Fermi levels of an electron in the conduction band and one in the valence band. If the spins of the electron and hole are parallel, i.e., the exciton is a triplet, then the total spin of the exciton equals 1 and $g_{11}=3$. Then

$$f_{\text{ex}}^{(t)}=3C\ \exp\zeta_{\text{ex}}=3f_{\text{ex}}.\tag{15}$$

The constant C is given by the normalization condition

$$C=\frac{1}{1+2\exp\,\zeta_c+2\exp\,\zeta_v+4\exp\,\zeta_{\text{ex}}}.\tag{16}$$

4. QUASI-FERMI LEVELS OF ELECTRONS AND HOLES

The probability of stimulated emission equals

$$w_{st}=w_{vc}f_{\text{ex}},\tag{17}$$

where w_{vc} is the probability for an optical transition, and the radiated energy of the photon is $\hbar\omega=E_g-\varepsilon_c-\varepsilon_v+V_{cc}^{vv}$ according to Eq. (6). The probability of absorbing a photon at the same energy $\hbar\omega$ is

$$w_a=w_{vc}F_{00}.\tag{18}$$

According to Eqs. (17) and (18), the magnitude of the optical gain in the active region is

$$g=A(f_{\text{ex}}-F_{00})=\frac{A(\exp\,\zeta_{\text{ex}}-1)}{1+2\exp\,\zeta_c+2\exp\,\zeta_v+4\exp\,\zeta_{\text{ex}}},\tag{19}$$

where A is an energy-dependent coefficient of proportionality. From (19) it is easy to find where the dividing line is between absorption and amplification of electromagnetic radiation with frequency ω by the quantum dot. This condition for replacing absorption by amplification has the usual form:

$$\mu_{\text{ex}}=E.\tag{20}$$

It is convenient to represent the quantity μ_{ex} in terms of the chemical potentials of electrons and holes injected into the host. Then the critical condition for the appearance of gain, according to Eq. (20), has the form

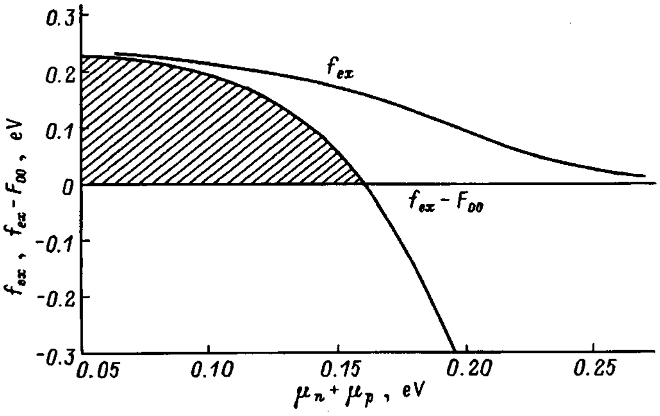

FIG. 5. Dependence of the distribution functions f_{ex} and $(f_{\text{ex}}-F_{00})$ on the sum of chemical potentials of electrons and holes $\mu_n+\mu_p$.

$$\mu_n+\mu_p=E_g-E.\tag{21}$$

For a prespecified value of required gain in the active region, (19) allows us to determine the ratio of quasi-Fermi levels for electrons and holes. However, the problem is that we need to determine not only their ratio but each of these quantities individually. For this we use the condition of electrical neutrality. Let N_{QD} be the concentration of quantum dots. Then the total electron concentration n_{tot} equals

$$n_{\text{tot}}=n+n_e+n_{\text{ex}},\tag{22}$$

where $n=N_c\exp(-\mu_n/k_BT)$ is the concentration of free electrons in the host; $n_e=N_{QD}f_{1c}$ is the concentration of quantum dots filled by a single electron; and n_{ex} is the concentration of quantum dots filled by excitons. Analogous expressions can be written for the total concentration of holes p_{tot} as well, by replacing μ_n by μ_p and f_{1c} by f_{1v}. The condition of electrical neutrality takes the form

$$n_{\text{tot}}=p_{\text{tot}}.\tag{23}$$

For simplicity of discussion we assume the active region and the region occupied by the wide-gap host are undoped. Substituting the expression for the total concentration of electrons and holes into (23), we obtain the equation that relates the quantities μ_n and μ_p:

$$N_c\ \exp\left(-\frac{\mu_n}{k_BT}\right)+2N_{QD}C\ \exp\,\zeta_c$$
$$=N_v\ \exp\left(-\frac{\mu_p}{k_{BN}T}\right)+2N_{QD}C\ \exp\,\zeta_v,\tag{24}$$

where C is determined from Eq. (16).

Figure 5 shows the dependence of the functions f_{ex} and $(f_{\text{ex}}-F_{00})$ on the parameter $\mu_n+\mu_p$. The function $f_{\text{ex}}-F_{00}$, according to Eq. (19), is proportional to the gain coefficient in the active region. In these calculations we assumed that the size of the quantum dot was 40 Å, the distance between dots in the plane of a single layer was also 40 Å, and the distance between layers was 80 Å, so that $N_{QD}\approx1.3\times10^{18}\ \text{cm}^{-3}$. Note that in this kind of quantum dot we have $f_{1c}=0$. In the dashed region, the optical gain coefficient is positive.

[1] S. Nakamura, M. Senoh, S. Hagahama, N. Isawa, T. Yamada, T. Matsushita, H. Kiyoku, and Y. Sugimoto, J. Appl. Phys. **35** , L74 (1996).
[2] S. Chichibu, T. Azuhata, T. Sota, and S. Nakamura, Appl. Phys. Lett. **69**, 4188 (1996).
[3] Y. Narukawa, Y. Kawakami, M. Funato, S. Fujita, and S. Nakamura, Appl. Phys. Lett. **70**, 981 (1997).
[4] M. Asada, Y. Miyamoto, and Y. Suematsu, IEEE J. Quantum Electron. **QE-22**, 1915 (1986).
[5] K.J. Vahala, IEEE J. Quantum Electron. **QE- 24**, 523 (1988).
[6] L.V. Asryan, and R.A. Suris, Semicond. Sci. Technol. **11**, 554 (1996).
[7] G. Martin, A. Botchkarev, A. Rockett, and H. Morkoc, Appl. Phys. Lett. **68**, 2541 (1996).
[8] H. A. Bethe, *Quantum Mechanics of the Simplest Systems* (ONTI, Leningrad, Moscow, 1935).
[9] L. Zülike, *Quantum Chemistry* [Mir, Moscow, 1976].
[10] R. A. Smith, *Semiconductors* (Cambridge Univ. Press, Cambridge, 1959; Mir, Moscow, 1982).

Translated by Frank J. Crowne

Shallow acceptors in strained multiquantum-well Ge/Ge$_{1-x}$Si$_x$ heterostructures

V. Ya. Aleshkin, V. I. Gavrilenko, I. V. Erofeeva, D. V. Kozlov,
and M. D. Moldavskaya

Institute for Physics of Microstructures, Russian Academy of Sciences, 603600 N. Novgorod, Russia

O. A. Kuznetsov

Physicotechnical Research Institute, N. I. Lobachevsky State University at Nizhnii Novgorod, 603600 Nizhnii Novgorod, Russia

(Submitted March 16, 1998; accepted for publication March 26, 1998)
Fiz. Tekh. Poluprovodn. **32**, 1240–1245 (October 1998)

Far infrared photoconductivity spectra due to excitation of shallow acceptors in strained multi-quantum well Ge/Ge$_{1-x}$Si$_x$ ($x\approx 0.1$) heterostuctures are investigated. It is shown that these spectra are shifted toward longer wavelengths in the far infrared region compared with those of bulk *p*-Ge, owing to ″built-in″ strain and size quantization, which lead to splitting of the light- and heavy-hole subbands in the Ge layers. Shallow acceptor spectra are calculated variationally for bulk germanium under uniaxial tension, which is ″equivalent″ to the strained Ge layers in the heterostructures. Although this method is only appropriate for wide quantum wells ($d_{\mathrm{Ge}}\approx 800$ Å), the calculations are shown to qualitatively account for photoconductivity spectra obtained from narrower wells ($d_{\mathrm{Ge}}\approx 200$ Å) as well. © *1998 American Institute of Physics.* [S1063-7826(98)02010-9]

Strain is one of the techniques for controlling the energy spectrum of both free and bound charge carriers. By lowering the crystal symmetry, uniaxial strain in semiconductors with degenerate valence bands at $\mathbf{k}=0$ (e.g., in Ge and Si) causes splitting of the heavy- and light-hole subbands and reconstruction of the shallow acceptor spectrum. The influence of $\mathbf{P}\|[001]$ and $\mathbf{P}\|[111]$ uniaxial strains on the spectrum of shallow acceptors in bulk germanium and silicon has been investigated previously, both theoretically[1–3] and experimentally.[4–6] In these papers it was shown that uniaxial strain causes splitting of the ground and excited fourfold-degenerate states into two twofold-degenerate states. Since the distance between light- and heavy-hole subbands increases linearly with pressure,[1] as the strain increases the spectrum of acceptor bound states is determined primarily by the subband that forms the top of the valence band. It is known[1] that for $P\neq 0$ the dispersion relation for holes becomes anisotropic in both subbands. The problem of motion of a particle near the top of a simple anisotropic band in a Coulomb potential was investigated in Refs. 2 and 7, where the dependences of the ground and excited state energies of an impurity center on the anisotropy parameter of the effective mass was calculated. In Ref. 3 the authors calculated the spectrum of a shallow acceptor in uniaxially strained germanium for arbitrary values of the strain.

In this paper we will investigate shallow acceptors in wide strained Ge/Ge$_{1-x}$Si$_x$ heterostructure quantum wells grown on a (111) germanium substrate. By ‘‘wide’’ quantum wells we mean wells whose width exceeds the characteristic size of the wave function in the acceptor ground state. In such quantum wells, the spectrum of shallow acceptors is primarily determined by the strain of the quantum well material, i.e., essentially the magnitude of the splitting of the heavy- and light- hole subbands. Therefore, in calculating bound-state energies quantum-well effects can to first approximation be included through their influence on the magnitude of the subband splitting of the light and heavy holes.

It is well known that the germanium layers in strained Ge/Ge$_{1-x}$Si$_x$ heterostructures are potential wells for holes.[8] If the total thickness of the heterostructure exceeds a critical value, then the germanium layers undergo compression in the growth plane of the heterostructure. This strain may be considered as hydrostatic compression plus uniaxial tension along the [111] axis. The hydrostatic compression, which does not decrease the crystal symmetry, leads to an insignificant change the hole mass and therefore has only a slight effect on the binding energy of acceptors. Thus, the spectrum of shallow acceptors in wide germanium layers in the strained Ge/Ge$_{1-x}$Si$_x$ heterostructures can be approximately treated as the spectrum of shallow acceptors in bulk germanium under uniaxial tension. The results of Ref. 3 cannot be used to analyze the impurity spectra in such heterostructures, because these calculations were made for material under compression. In this paper we calculate the spectrum of shallow acceptors in germanium under uniaxial tension in the direction [111] for an arbitrary value of the strain using the variational method discussed in Ref. 9 for calculating acceptor levels in unstrained germanium.

METHOD OF CALCULATION AND RESULTS OBTAINED

The Luttinger Hamiltonian,[10]which describes light and heavy holes in a Cartesian system of coordinates $\hat{x}[110]$, $\hat{y}[112]$, $\hat{z}[111]$, has the form:

$$H_L=\frac{\hbar^2}{2m_0}\begin{pmatrix} F & H & I & 0\\ H^* & G & 0 & I\\ I^* & 0 & G & -H\\ 0 & I^* & -H^* & F\end{pmatrix},$$

$$F=\ A(k_x^2+k_y^2+k_z^2)+\frac{D}{2\sqrt{3}}(k_x^2+k_y^2-2k_z^2)$$

$$+\left\{a\varepsilon+\frac{d}{2\sqrt{3}}(\varepsilon_{xx}+\varepsilon_{yy}-2\varepsilon_{zz})\right\}\frac{2m_0}{\hbar^2},$$

$$G=\ A(k_x^2+k_y^2+k_z^2)-\frac{D}{2\sqrt{3}}(k_x^2+k_y^2-2k_z^2)$$

$$+\left\{a\varepsilon-\frac{d}{2\sqrt{3}}(\varepsilon_{xx}+\varepsilon_{yy}-2\varepsilon_{zz})\right\}\frac{2m_0}{\hbar^2},$$

$$H=\frac{i}{\sqrt{3}}\left(B-\frac{D}{\sqrt{3}}\right)k_+^2-\frac{2i}{\sqrt{3}}\left(B+\frac{D}{2\sqrt{3}}\right)k_zk_-\,,$$

$$I=\frac{1}{2\sqrt{3}}\left(B+\frac{2D}{\sqrt{3}}\right)k_-^2-\sqrt{\frac{2}{3}}\left(B-\frac{D}{\sqrt{3}}\right)k_zk_+\,,$$

where *A*, *B*, and *D* are constants that determine the hole dispersion relations, m_0 is the free electron mass, *a* and *d* are constants that determine the change in the hole spectrum under strain (see Ref. 1), $k_\pm=k_x\pm ik_y$; ε_{ij} are components of the strain tensor, and $\varepsilon=\varepsilon_{xx}+\varepsilon_{yy}+\varepsilon_{zz}$. All the nonzero components of the strain tensor can be expressed in terms of ε_{xx}:

$$\varepsilon_{xx}=\varepsilon_{yy}\,,$$

$$\varepsilon_{zz}=-\frac{2(C_{11}+2C_{12}-2C_{44})}{C_{11}+2C_{12}+4C_{44}}\varepsilon_{xx}=-0.369\varepsilon_{xx}\,,$$

where C_{ij} are elements of the elastic stiffness tensor.[11] The quantity ε_{xx} is linearly related to the tensile stress (pressure)

$$P=-\frac{6C_{44}(C_{11}+2C_{12})}{C_{11}+2C_{12}4C_{44}}\varepsilon_{xx}=183.3\varepsilon_{xx}\text{GPa}.$$

In germanium uniaxially strained along the direction [111], the center of the Brillouin zone corresponds to the symmetry point group D_{3d}. In unstrained germanium, the *L*-point possesses this symmetry group. Therefore, wave functions of acceptors in the strained material will transform according to a complementary representation of the double group at the *L* point. There exist six such irreducible representations of the group D_{3d}: $L_4^\pm$, $L_5^\pm$, and $L_6^\pm$ (Ref. 12). The wave function of the acceptor ground state transforms according to an irreducible representation corresponding to the top of the valence band. In unstrained germanium the top of the valence band corresponds to the four-dimensional representation Γ_8^+ (Ref. 12). This representation decomposes into irreducible representations under the group D_{3d} as follows:

$$\Gamma_8^+=L_4^++L_5^++L_6^+\,.$$

Representations L_4^+ and L_5^+ are one- dimensional and complex conjugates of one another; they should therefore be treated as the single, two-dimensional, irreducible representation $L_{4,5}^+$ for transforming the wave functions.[13] Representation L_6^+ is two-dimensional. As we already noted, uniaxial strain lifts the degeneracy of the light- and heavy-hole subbands at the point $\mathbf{k}=0$. In this case, wave functions corresponding to states with projections ±3/2 of total angular momentum on the strain axis (heavy holes) transform according to the representation $L_{4,5}^+$. Wave functions of states with the projections ±1/2 of total angular momentum on the strain axis (light holes) transform according to the representation L_6^+. Note that for those holes determined to be ''heavy'' the mass in the direction [111] is larger than that of the light holes (by a factor of almost 10). In general, this assertion is incorrect for other directions. In uniaxial strained germanium, the top of the valence band is made up of heavy holes, while under uniaxial compression it is made up of light holes.

In this paper we use a variational method to calculate the spectra of shallow acceptor states. Starting from the symmetry of the problem and using group theory analogous to Ref. 9, we can minimize the number of variational parameters and choose the following trial wave functions for the split ground state that transform according to representations $L_{4,5}^+$ and L_6^+:

$$\Psi_h=c_1\begin{pmatrix}1\\0\\0\\i\end{pmatrix}\exp\left(\frac{-\sqrt{\rho^2+(qz)^2}}{f}\right)$$

$$+\left\{c_2[\rho^2-2(qz)^2]\begin{pmatrix}1\\0\\0\\i\end{pmatrix}+c_3\rho^2\begin{pmatrix}0\\ie^{-2i\varphi}\\e^{2i\varphi}\\0\end{pmatrix}\right.$$

$$\left.+c_4\rho z\begin{pmatrix}0\\-ie^{i\varphi}\\e^{-i\varphi}\\0\end{pmatrix}\right\}\exp\left(\frac{-\sqrt{\rho^2+(qz)^2}}{b}\right),\tag{1}$$

$$\Psi_l=c_1\begin{pmatrix}0\\1\\0\\0\end{pmatrix}\exp\left(\frac{-\sqrt{\rho^2+(qz)^2}}{f}\right)$$

$$+\left\{c_2[\rho^2-(qz)^2]\begin{pmatrix}0\\1\\0\\0\end{pmatrix}+i\rho z\begin{pmatrix}c_3e^{i\varphi}+c_4e^{-i\varphi}\\0\\0\\0\end{pmatrix}\right.$$

$$\left.+i\rho^2\begin{pmatrix}c_5e^{2i\varphi}+c_6e^{-2i\varphi}\\0\\0\\0\end{pmatrix}\right\}\exp\left(\frac{-\sqrt{\rho^2+(qz)^2}}{b}\right).\tag{2}$$

Here Ψ_h and Ψ_l transform according to the representations $L_{4,5}^+$ and L_6^+, respectively; $\rho^2=x^2+y^2$, φ is the angle of the radius vector in the plane *xy*, and c_i, *q*, *f*, and *b* are variational parameters.

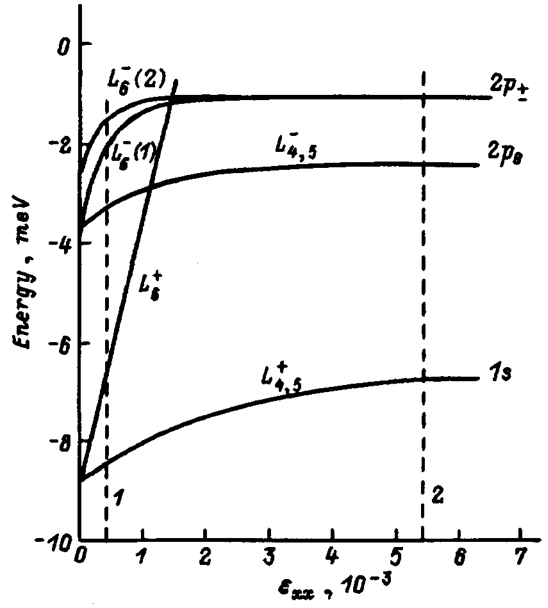

FIG. 1. Dependence of the binding energy of the ground and lowest excited states of an acceptor in germanium under uniaxial tensile strain along the (111) direction on the magnitude of the strain. The vertical lines indicate values of the effective strain corresponding to the splitting of the light- and heavy-hole subbands in Ge/Ge$_{1-x}$Si$_x$ heterostructures 309 (*1*) and 306 (*2*) including size quantization.

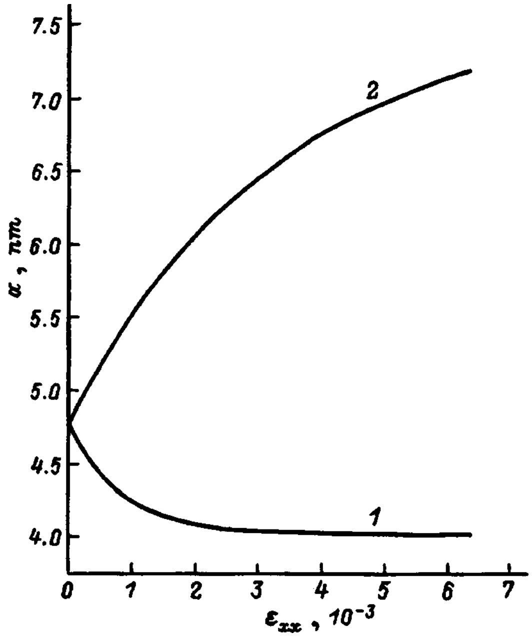

FIG. 2. Dependence of the longitudinal (along the tension axis *1*) and transverse (*2*) localization scales *a* for the wave function of the acceptor ground state in germanium under tensile uniaxial strain along (111) on the magnitude of the strain.

In Fig. 1 we plot the calculated energies of the components of the split acceptor ground state, i.e., $L_{4,5}^+$ [with wave function (*1*)] and L_6^+ [with wave function (*2*)], versus the strain ε_{xx}. The energy origin corresponds to the edge of the heavy-hole subband. The ionization energy obtained in this paper for the acceptor ground state when $P=0$ equals 8.87 meV, which is in good agreement with the value 8.83 meV obtained in Ref. 9. At large strains ($\varepsilon_{xx}>15\times10^{-3}$) the ionization of the ground state approaches an asymptotic value of 5.57 meV, which is in good agreement with calculations using the single-band model with an anisotropic mass.[14]

Figure 2 shows how the scales of localization of the ground-state wave function along the strain axis and in the perpendicular direction depend on the magnitude of the strain. It is easy to see that the localization radius (or ''Bohr'' radius) along the direction of tension decreases with increasing strain down to 4.0 nm, while in the perpendicular direction it increases. This behavior is explained by the change in mass in the corresponding directions.[1]

Let us now consider *p*-type excited states. The wave functions of these states are odd under inversion, and therefore they correspond to irreducible representations $L_{4,5}^-$ or L_6^-. Note that dipole transitions from the ground state are allowed in odd states and forbidden in even states.

In accordance with the symmetry of the problem (see Ref. 9) trial wave functions that transform according to representations $L_{4,5}^-$ and L_6^- can be written in the following form. For $L_{4,5}^-$:

$$\begin{aligned}\Psi_{4,5}=&c_1z\begin{pmatrix}1\\0\\0\\i\end{pmatrix}\exp\left[-\frac{\sqrt{\rho^2+(qz)^2}}{f}\right]+ic_2\rho\begin{pmatrix}0\\e^{i\varphi}\\ie^{-i\varphi}\\0\end{pmatrix}\\&\times\exp\left[-\frac{\sqrt{\rho^2+(qz)^2}}{f}\right]+c_3z\left(z^2-\frac{1}{5}r^2\right)\begin{pmatrix}1\\0\\0\\i\end{pmatrix}\\&\times\exp\left[-\frac{\sqrt{\rho^2+(qz)^2}}{b}\right]+ic_4\rho\left(z^2-\frac{3}{5}r^2\right)\begin{pmatrix}0\\e^{i\varphi}\\ie^{-i\varphi}\\0\end{pmatrix}\\&\times\exp\left[-\frac{\sqrt{\rho^2+(qz)^2}}{b}\right]+ic_5\rho^2z\begin{pmatrix}0\\e^{-2i\varphi}\\ie^{2i\varphi}\\0\end{pmatrix}\\&\times\exp\left[-\frac{\sqrt{\rho^2+(qz)^2}}{b}\right]+c_6\rho^3\begin{pmatrix}e^{3i\varphi}\\0\\0\\ie^{-3i\varphi}\end{pmatrix}\\&\times\exp\left[-\frac{\sqrt{\rho^2+(qz)^2}}{b}\right]+c_7\rho^3\begin{pmatrix}e^{-3i\varphi}\\0\\0\\ie^{3i\varphi}\end{pmatrix}\end{aligned}$$

$$\times\exp\left[-\frac{\sqrt{\rho^2+(qz)^2}}{b}\right]. \tag{3}$$

For L_6^-:

$$\Psi_6=c_1 z\begin{pmatrix}0\\1\\0\\0\end{pmatrix}\exp\left[-\frac{\sqrt{\rho^2+(qz)^2}}{f}\right]+\rho\begin{pmatrix}i(c_2 e^{i\varphi}+c_3 e^{-i\varphi})\\c_4 e^{-i\varphi}\\0\\0\end{pmatrix}$$

$$\times\exp\left[-\frac{\sqrt{\rho^2+(qz)^2}}{f}\right]+c_5 z\left(z^2-\frac{1}{5}r^2\right)\begin{pmatrix}0\\1\\0\\0\end{pmatrix}$$

$$\times\exp\left[-\frac{\sqrt{\rho^2+(qz)^2}}{b}\right]+\rho\left(z^2-\frac{3}{5}r^2\right)$$

$$\times\begin{pmatrix}i(c_6 e^{i\varphi}+c_7 e^{-i\varphi})\\c_8 e^{-i\varphi}\\0\\0\end{pmatrix}$$

$$\times\exp\left[-\frac{\sqrt{\rho^2+(qz)^2}}{b}\right]+i\rho^2 z\begin{pmatrix}c_9 e^{2i\varphi}+c_{10}e^{-2i\varphi}\\0\\0\\0\end{pmatrix}$$

$$\times\exp\left[-\frac{\sqrt{\rho^2+(qz)^2}}{b}\right]+\rho^3\begin{pmatrix}c_{11}e^{3i\varphi}+c_{12}e^{-3i\varphi}\\0\\0\\0\end{pmatrix}$$

$$\times\exp\left[-\frac{\sqrt{\rho^2+(qz)^2}}{b}\right]. \tag{4}$$

In this paper we find two excited states with wave function (4), which we denote by L_6^- (1) and L_6^- (2). In finding the second state we impose an additional condition on the variational parameters: the requirement that the upper state (4) be orthogonal to the lower state. For states of type (3) we find only the lower excited state, since the second rapidly departs into the continuum with increasing strain. Figure 1 also shows the dependences of the calculated excited acceptor state energies on the strain ε_{xx}. On the right we indicate the corresponding acceptor states in the limit of large strain for a simple anisotropic band ($1s$, $2p_0$, $2p_\pm$). It is clear that the energy of the excited levels approaches its asymptotic value more rapidly than the ground- state energy, which is obviously associated with the lower binding energy of the excited states.

EXPERIMENTAL RESULTS AND COMPARISON WITH CALCULATIONS

The strained multilayer heterostructures Ge/Ge$_{1-x}$Si$_x$ under study (with $x\approx 0.1$, germanium layer thickness $d_{\mathrm{Ge}}\approx$ 200–800 Å, and solid solution layer thickness $d_{\mathrm{GeSi}}\approx 200$ Å) were grown by the gas-phase hydride method on (111) Ge substrates. The number of periods was chosen to be rather large ($n=80\div 160$) so that the total thickness of the heterostructure would exceed its critical value. In this case, a relaxation of the elastic stresses takes place at the heterostructure-substrate boundary, and the period of the lattice in the heterostructure growth plane no longer coincides with the period of the substrate lattice (it is determined primarily by the average content of silicon in the heterostructure), leaving the germanium layers in the heterostructure under biaxial compression. Thus, we can control the strain in the germanium layers by varying the fraction of silicon x in the Ge$_{1-x}$Si$_x$ alloy or the layer thickness. In this paper we studied heterostructures of two types, with different quantum-well widths. The first type ($x=0.07$, $d_{\mathrm{GeSi}}=200$ Å, $n=83$), an example of which is sample 309, had thick germanium layers ($d_{\mathrm{Ge}}=800$ Å) that consequently were weakly strained ($\varepsilon_{xx}=0.46\times 10^{-3}$). The second series consisted of several samples ($x=0.11-0.15$, $d_{\mathrm{GeSi}}\approx 200$ Å, $n=80-160$) with thinner germanium layers ($d_{\mathrm{Ge}}\approx 200$ Å), causing them to be under larger strains ($\varepsilon_{xx}=(0.9-2.1)\times 10^{-3}$). Spectra of these samples were measured previously.[14] We measured submillimeter photoconductivity spectra of these heterostructures using a ''BOMEM DA3.36'' Fourier spectrometer at a temperature T = 4.2 K.

The impurity photoconductivity spectrum of a sample with thick germanium layers is shown in Fig. 3a. This spectrum is shifted as a whole towards longer wavelengths compared to the spectrum of bulk p-Ge (the maximum energy $\hbar\omega_{\max}\approx$ 12 meV; see, e.g., Ref. 15) and consists of a line at $\hbar\omega\approx$ 5.3 meV and a broad band at $\hbar\omega=$ 7.4–10 meV. In this sample the quantum-well effects are unimportant, and the photoconductivity spectrum is in good agreement with the theoretical model described above (Fig. 1); the strain corresponding to sample 309 is indicated by the vertical line *1*). The line at $\hbar\omega\approx$ 5.3 meV corresponds to a transition from the $L_{4,5}^+$ ground state to the first excited $L_{4,5}^-$ state. The spacing (1) between levels $L_{4,5}^+$ and L_6^- amounts to 7.1 meV, which is in good agreement with the start of the short-wavelength band in the spectrum shown in Fig. 3a. The photoconductivity at higher frequencies can in this case be associated with transitions to higher-lying excited states and to the continuum, and also to the split-off light-hole subband (the splitting of the subbands in this sample is $\Delta=$ 3 meV).

Spectra for the Ge/Ge$_{1-x}$Si$_x$ heterostructures with thinner germanium layers are shown in Figs. 3b and 3c. It is clear that these spectra are shifted even farther into the region of lower frequencies; features these spectra have in common are a line at $\hbar\omega\approx$ 6.9 meV and an intense band at $\hbar\omega=$ 3–5 meV. It is obvious that in heterostructures with narrow germanium layers the quantum-well effects are more important. As we have already noted, in these structures strain causes the masses of light and heavy holes along the [111] axis, i.e., the growth direction of the structure, to differ by an order of magnitude. This leads to additional splitting of the light- and heavy-hole subbands due to size quantization. In this paper this effect is included by introducing an effective strain $\varepsilon_{\mathrm{eff}}$ corresponding to the total splitting of the sub-

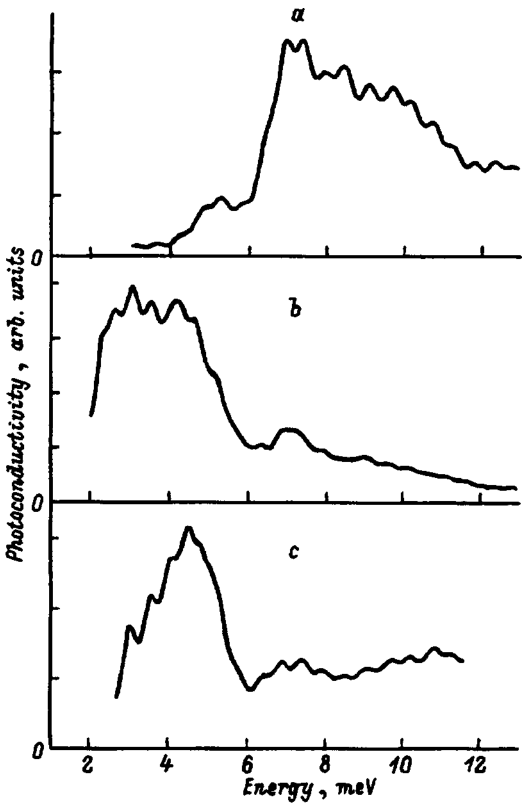

FIG. 3. Photoconductivity spectra for Ge/Ge$_{1-x}$Si$_x$ heterostructures at T = 4.2 K. *a*— heterostructure 309, undoped, $x=0.07$, $d_{\mathrm{Ge}}=800$ Å, $d_{\mathrm{GeSi}}\approx 200$ Å, $n=83$, $\varepsilon_{xx}=0.46\times 10^{-3}$; *b*—heterostructure 306, undoped, $x=0.12$, $d_{\mathrm{Ge}}=200$ Å, $d_{\mathrm{GeSi}}=\approx 200$ Å, $n=162$, $\varepsilon_{xx}=2.1\times 10^{-3}$; *c*—heterostructure 379, central quantum well doped with boron, $x=0.15$, $d_{\mathrm{Ge}}=200$ Å, $d_{\mathrm{GeSi}}\approx 200$ Å, $n=81$, $\varepsilon_{xx}=0.9\times 10^{-3}$.

bands calculated for given ε_{xx} and d_{Ge} (Ref. 16) (in Fig. 1 the vertical line *2* indicates the value of $\varepsilon_{\mathrm{eff}}$ for sample 306). From a comparison of Figs. 1, 3b, and 3c we see that the line at $\hbar\omega\approx$ 6.9 meV is in good agreement with transitions from the ground state to the continuum. The most intense band in the spectrum probably should correspond to transitions from the ground state to states L_6^- (1) and L_6^- (2), i.e., transitions of type $1s\rightarrow 2p_{\pm}$ (since for large subband splittings the spectrum becomes similar to the spectrum of a donor, for which the transition to the lower-lying state $L_{4,5}^-$ $(2p_0)$ is forbidden for light at normal incidence). From Fig. 1 it is clear that this transition should correspond to the line at $\hbar\omega\approx$ 5.5 meV, whereas in the experimental spectra the short-wavelength edge of the intense photoconductivity band corresponds to a photon energy of $\hbar\omega\approx$ 50 meV. This discrepancy indicates the need for a more accurate inclusion of the quantum-well effect in structures with thin germanium layers. The long-wavelength tail of the band $\hbar\omega=$ 3–5 meV can be explained by the dependence of the binding energy of an acceptor on its position in the well: At the well center the energy is a maximum and it decreases as the acceptor moves towards the barrier.[17] The additional structure in the region 1.8 to 3 meV observed in sample 306 can be related to photoexcitation of A^+ centers, which form when an additional hole is captured by a neutral acceptor in the quantum well.[18]

This work was carried out with the financial support of RFFI (Grant 97-02-16326), the Russian Science Ministry programs ''Physics of Solid-State Nanostructures'' (project 97-1069) and ''Microwave Physics'' (Project 4.5), the GNTP ''Physics of Quantum and Wave Processes'' (subprogram ''Fundamental Spectroscopy,'' project 7.8), the ''Leading Scientific Schools'' program (Grant 96-15-96719) and FTsP ''Integration'' program (Projects 540, 541).

[1] G. L. Bir and G. E. Pikus, *Symmetry and Strain-Induced Effects in Semiconductors* (Wiley, New York, 1975; Nauka, Moscow, 1972).

[2] J. Broeckx, P. Clauws, and J. Vennik, J. Phys. C: Sol. St. Phys. **19**, 511 (1986).

[3] J. Broeckx and J. Vennik, Phys. Rev. B **35**, 6165 (1987).

[4] D. H. Dickey and J. O. Dimmock, J. Phys. Chem. Solids **28**, 529 (1967).

[5] A. G. Kazanskii, P. L. Richards, and E. E. Haller, Solid State Commun. **24**, 603 (1977).

[6] A. D. Martin, P. Fisher, C. A. Freeth, E. H. Salib, and P. E. Simmonds, Phys. Rev. Lett. **99A**, 391 (1983).

[7] R. A. Foulkner, Phys. Rev. **184**, 713 (1969).

[8] L. K. Orlov, O. A. Kuznetsov, R. A. Rubtsova, A. L. Chernov, V. I. Gavrilenko, O. A. Mironov, V. V. Nikonorov, I. Yu. Skrylev, and S. V. Chistyakov, Zh. Éksp. Teor. Fiz. **98**, 1028 (1990) [Sov. Phys. JETP **71**, 573 (1990)].

[9] D. Schechter, J. Phys. Chem. Solids **23**, 237 (1962).

[10] J. M. Luttinger, Phys. Rev. **102**, 1030 (1955).

[11] A. L. Polyakova, *Strain in Semiconductors and Semiconductor Devices* (Energiya, Moscow, 1979).

[12] F. Bassani and G. Pastori-Parravicini, *Electronic States and Optical Transitions in Solids* (Nauka, Moscow, 1982).

[13] L. D. Landau and E. M. Lifshitz, *Quantum Mechanics: Non-Relativistic Theory*, 3rd ed. (Pergamon Press, Oxford, 1977; Nauka, Moscow, 1987).

[14] V. I. Gavrilenko, I. V. Erofeeva, A. L. Korotkov, Z. F. Krasil'nik, O. A. Kuznetsov, M. D. Moldavskaya, V. V. Nikonorov, and L. V. Paramonov, JETP Lett. **65**, 209 (1997).

[15] R. L. Jones and P. Fisher, Phys. Rev. B **QQ** 2016 (1970).

[16] V. Ya. Aleshkin, N. A. Bekin, I. V. Erofeeva, V. I. Gavrilinko, Z. F. Krasil'nik, O. A. Kuznetsov, M. D. Moldavskaya, V. V. Nikonorov, and V. M. Tsvetkov, Lithuanian J. Phys. **35**, 368 (1995) [in Lithuanian].

[17] A. A. Reeder, J.-M. Mercy, and B. D. McCombe, IEEE J. Quantum Electron. **24** 1690 (1988).

[18] S. Holms, J.-P. Cheng, B. D. McCombe, and W. Schaff, Phys. Rev. Lett. **69**, 2571 (1992).

Translated by Frank J. Crown

SEMICONDUCTORS VOLUME 32, NUMBER 10 OCTOBER 1998

Potential difference and photovoltaic effect arising from distortion of the electron wave function in a GaAs quantum well with a thin AlGaAs barrier

Yu. Pozhela and K. Pozhela

Semiconductor Physics Institute, 2600 Vilnius, Lithuania

(Submitted March 23, 1998; accepted for publication March 28, 1998)
Fiz. Tekh. Poluprovodn. **32**, 1246–1250 (October 1998)

This paper discusses changes in the spectrum and distortion of the electron wave function of a GaAs quantum well when a thin AlGaAs barrier is introduced into it. The potential difference generated across the quantum well by distortion of the electron wave function is calculated, along with its dependence on the position of the barrier in the quantum well. The photovoltaic response of the structure to optical intersubband excitations is also calculated, along with the role of wave function and electronic spectrum distortion as well as intersubband nonradiative transitions in generating this response. The suitability of a GaAs quantum well with a thin barrier for use as an infrared detector is considered. © *1998 American Institute of Physics.* [S1063-7826(98)02110-3]

1. INTRODUCTION

There is great interest in studying the properties of a two- dimensional electron gas in coupled quantum wells, since it may be possible to controllably regulate the energy spectrum and scattering rate of electrons in such a structure, as well as its optical parameters, by changing the shape of the quantum wells and coupling between them. Coupled quantum wells have become the basis of many semiconductor electronic and optoelectronic devices. These structures have been used to make lasers in the infrared region,[1–3] infrared detectors,[4,5] nonlinear optics elements,[6] and high-speed transistors.[7]

In this article we discuss new phenomena caused by distortion of the electronic wave functions in quantum wells separated by a barrier so thin that the energy levels and wave functions of the electron are common to both quantum wells. We discuss the asymmetry of the polarization electron charge in the quantum well when the thin barrier is placed into it and the appearance in the quantum well of a potential difference and photovoltaic effect connected with this barrier.

A photovoltaic effect is observed in coupled quantum well structures when their electronic states form in quantum wells separated by a thick potential barrier. A thick barrier between the quantum wells prevents photoexcited electrons that are spatially separated with respect to the neutral position from returning by tunneling through the barrier, which ensures a high value of the photovoltaic response of the structure and the feasibility of its use for detecting infrared radiation.[4,8,9] In a structure with a thin barrier a photovoltaic response is possible if an alternative can be found to the thick barrier as a means of ensuring a finite relaxation time of the photoexcited electrons in the equilibrium state. In this article, we propose such an alternative: we argue that by introducing a thin barrier into the quantum well we can radically decrease the rate of intersubband nonradiative transitions .

We calculate the potential difference across the quantum well and the photovoltaic response arising from distortion of the wave function for the example of a quantum well with structure $Al_{0.3}Ga_{0.7}As/GaAs/Al_{0.3}Ga_{0.7}As$ and a thin AlGaAs barrier (one to two monolayers).

2. VOLTAGE ARISING FROM DISTORTION OF THE ELECTRON WAVE FUNCTION IN A GaAs QUANTUM WELL WITH A THIN AlGaAs BARRIER

By introducing a thin barrier into a two-dimensional quantum well that separates it into two unequal parts we change the energy spectrum of electrons in the quantum well and distort the electron wave functions, leading to breaking of the symmetry of the charge distribution in the quantum well.

Let us consider this phenomenon for the example of a specific $Al_{0.3}Ga_{0.7}As/GaAs/Al_{0.3}Ga_{0.7}As$ heterostructure with a GaAs quantum-well width $L=20$ nm, in which we place a thin $Al_{0.3}Ga_{0.7}As$ barrier with thickness $d=1$ nm in the plane $z=l_b$. This structure is shown schematically in Fig. 1. Wave functions and electron energies are calculated by numerically solving the Schrödinger equation. It is assumed that the height of the heterojunction barrier is $U_0=0.3$ eV and the effective masses of the electrons are $m^*=0.067$ in the GaAs layer and $m^*=0.27$ in the AlGaAs layer.

The computed spectrum of electron energies (E) in such a quantum well is shown in Fig. 2, where the first three levels are plotted. The energy levels plotted in Fig. 2 as a function of the coordinates of the barrier in the quantum well are defined by the position of the bottom of various subbands in the coupled quantum wells. The introduction of a barrier into the quantum wells produces a radical change in the character of the electronic spectrum. Energy E_1 of the first (lowest) level corresponds to the energy of the bottom of the lowest electron subband in the wide portion of the divided quantum well. The second energy level E_2 in the quantum well is determined by the energy of the bottom of the second

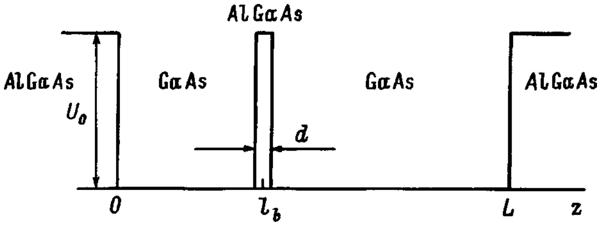

FIG. 1. Potential of the bottom of the conduction band of a AlGaAs/GaAs/AlGaAs quantum well of width L and a thin AlGaAs barrier of thickness d, located in the plane l_b ; U_0 is the height of the heterojunction barrier; z is the coordinate in the growth direction of the heterostructure.

subband of electrons in the wide portion of the quantum well only in the range $l_b<5.0$ nm. For $l_b>5.0$ nm the second energy level corresponds to the energy of the bottom of the first (lowest) subband in the narrow portion of the quantum well, which turns out to be lower than the energy of the bottom of the second subband in the wide portion of the quantum well. As a result, the second energy level E_2 approaches the first level E_1 as the barrier coordinate l_b increases. Analogously, for $l_b<5.0$ nm the third level E_3 corresponds to the bottom of the first subband in the narrow portion of the quantum well, while for $l_b>5.0$ nm it corresponds to the bottom of the second subband of the wide portion of the quantum well.

The wave functions of electrons for levels E_1, E_2, E_3 correspond to wave functions in subbands responsible for the generation of the appropriate level. Figure 3 shows squared wave function amplitudes $|\varphi_{ei}|^2$ for energy levels E_i at three characteristic locations for the barrier in the quantum well: l_b= 2.5, 5.0, and 7.5 nm. For l_b= 2.5 nm electrons in the lower two levels are in subbands of the wide portion of the quantum well and the region of electron charge shifts to this portion of the quantum well. For l_b= 5.0 nm only electrons of the first level E_1 remain in the lowest subband of the wide portion of the quantum well. Electrons for the second level E_2 are found to be partially in the lower subband of the narrow part of the quantum well, while electrons in level E_3, which for l_b=5.0 nm is very close to level E_2, turn out to be primarily at the lowest subband level of the narrow portion of the quantum well.

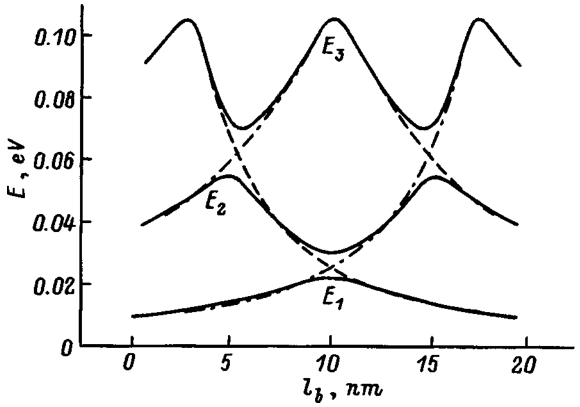

FIG. 2. Dependence of the first three energy levels E_1, E_2, and E_3 of a GaAs quantum well of width L=20 nm with a AlGaAs barrier versus the position l_b of that barrier (solid curves), and the energy of the first and second subbands in wide (right) (dotted-dashed) and narrow (left) (dashed) portions of the quantum well. For $l_b\approx$ 4 nm the types of subbands at levels E_2 and E_3 change.

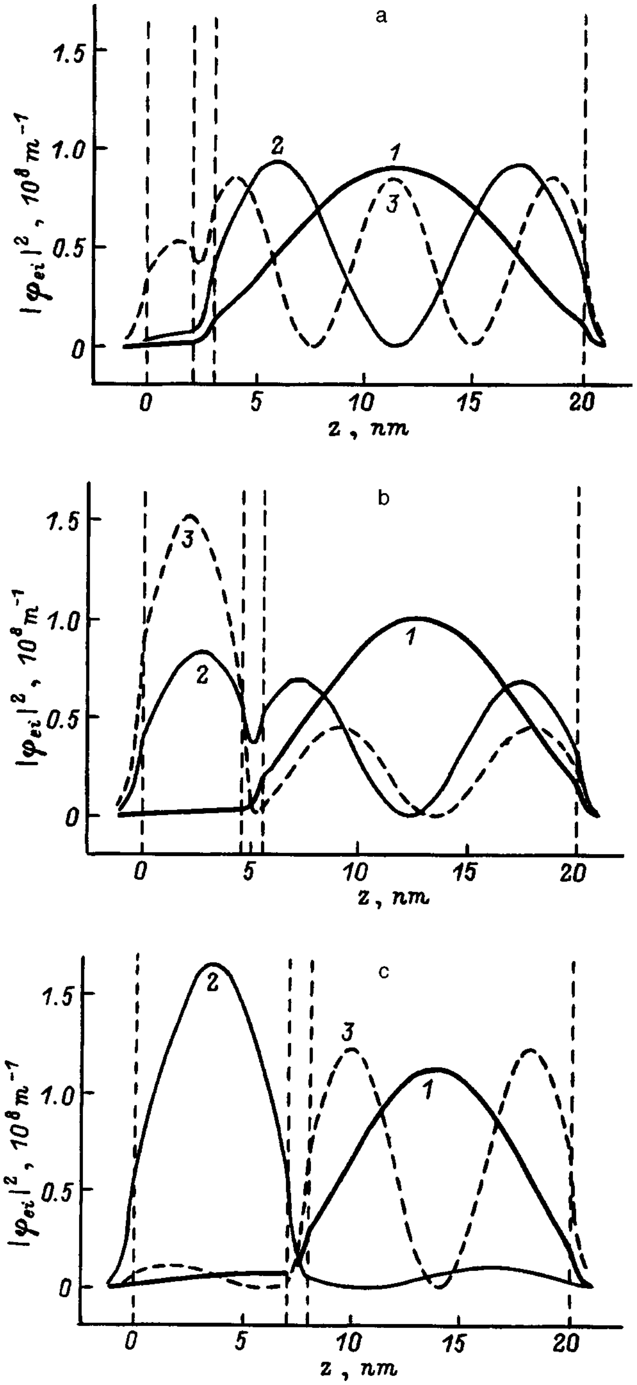

FIG. 3. Squares of the electron wave function amplitudes $|\varphi_{ei}|^2$ plotted versus coordinate z for the first (lowest) (*1*), second (*2*), and third (*3*) energy levels in a GaAs quantum well (L=20 nm) for the following positions of the AlGaAs barrier: l_b=2.5 (a), 5.0 (b) and 7.5 nm (c).

Finally, for l_b=7.5 nm electrons of the first (E_1) and third (E_3) energy levels are found in the first and second subbands of the wide portion of the quantum well, respectively, while all the electrons of the second level (E_2) shift to the first subband of the narrow portion of the quantum well. We see that by moving the thin barrier in the quantum well we cause a significant asymmetry in the electron charge dis-

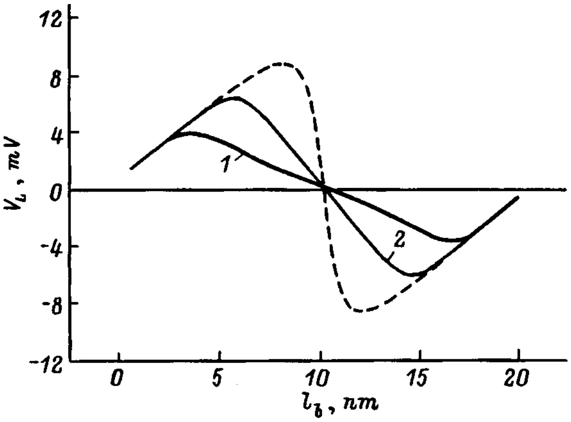

FIG. 4. Dependence of the potential difference V_L caused by distortion of the electron wave function in a GaAs quantum well on the position of the barrier l_b for $T=293$ K (*1*) and 77 K (*2*). The dashed curve is the value of V_L assuming occupation by electrons of only the lowest energy level E_1, i.e., $n_{02}=n_{03}=0$.

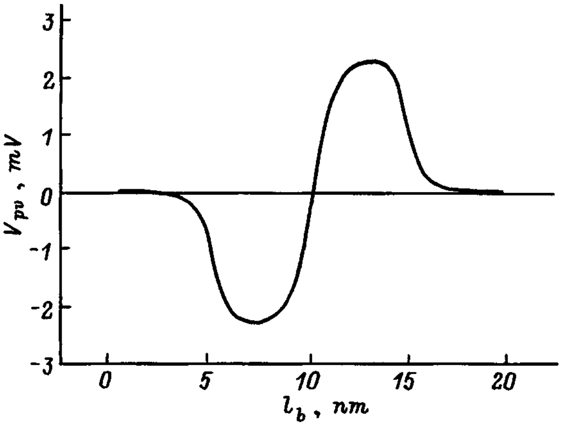

FIG. 5. Photovoltaic response V_{pv} to transfer of $\Delta n=8\times 10^{14}\,\mathrm{m}^{-2}$ electrons from level E_1 to level E_2 as a function of the position of the AlGaAs barrier l_b.

tribution of the quantum-well levels, which leads to the generation of potential differences in the quantum well.

Let us assume that the structure is uniformly doped with donors. These ionized donors define a distribution of positive charge that is uniform over the quantum-well cross section. Solution of the Schrödinger equation gives the following expression for the voltage that appears across the quantum well due to distortion of the electronic wave function for the three quantum-well levels:

$$V_L=\frac{|e|}{\varepsilon_1}N_d(L_2-L_1)\left[\frac{L_2-L_1}{2}-\sum_{i=1}^{3}\frac{n_{0i}}{N_d}\int_{L_1}^{L_2}F_i(z)dz\right], \tag{1}$$

where

$$F_i(z)=\int_{L_1}^{z}|\varphi_{ei}(z')|^2dz'. \tag{2}$$

Here e is the electron charge, ε_1 is the dielectric constant of GaAs, N_d is the concentration of ionized donors, n_{0i} is the equilibrium concentration of electrons in level E_i, and L_1 and L_2 are the coordinates of the edges of the quantum well, which also include regions where the electrons penetrate into the AlGaAs layers.

Figure 4 shows the dependence of V_L on l_b for these heterostructures when $N_d(L_2-L_1)=8\times 10^{15}\,\mathrm{m}^{-2}$. As we see, the voltage V_L is a consequence of distortion of the charge distributions within the quantum well when the barrier is introduced into it. The electron charge in the first two subbands that are occupied at 77 K shifts towards the wide portion of the quantum well as long as $l_b\leqslant 5.0$ nm. For $l_b\geqslant 5.0$ nm electrons from the second level (n_{02}) return to the narrow portion of the quantum well (Fig. 3). As a result, V_L decreases as the barrier moves further towards the quantum-well center, reaching zero when the barrier is located at the center. The dependence of V_L on l_b for a barrier on the right side of the quantum well repeats the picture for the left side with reversed sign. At $T=293$ K occupation of the third level is important, and the maximum of V_L decreases and shifts towards the region of smaller l_b when $l_b<5$ nm.

V_L reaches its maximum value for that position of l_b where the lowest subband of the narrow portion of the quantum well begins to be occupied by electrons from the second level. If the second and third energy levels are not occupied ($n_{02}=n_{03}=0$), then V_L increases as long as l_b does not approach the center of the quantum well (see Fig. 4). Note that the voltage V_L increases with increasing doping N_d and quantum-well width. It is impossible to observe the potential V_L in steady state due to the relaxation of charge induced in the quantum well with time: $V_L\sim\exp(-t/RC)$, where R and C are the leakage resistance and capacitance associated with the quantum well. Therefore, V_L manifests itself only in dynamic perturbations of the electron gas in the quantum well. Such perturbations can be caused by external electromagnetic fields via optical intersubband transfer of electrons. Measurements of the perturbation V_L can be used as an indicator of the degree of occupation of subbands by electrons in strongly coupled quantum wells.

3. PHOTOVOLTAIC EFFECT IN A GaAs QUANTUM WELL WITH AN AlGaAs BARRIER

Let us assume that optical excitation is used to transfer Δn electrons from the first energy level E_1 (either directly or via a third level) to the second level E_2. A photovoltaic signal V_{pv} will then appear at the heterostructure, equal to the difference in the voltages V_L in Eq. (1) in the absence and in the presence of the Δn transferred electrons:

$$V_{pv}=\frac{|e|}{\varepsilon_1}\Delta n\int_{L_1}^{L_2}\left\{\int_{L_1}^{z}[|\varphi_{e1}(z')|^2-|\varphi_{e2}(z')|^2]dz'\right\}dz. \tag{3}$$

Note that the voltage V_{pv} is directly proportional to Δn and does not depend on temperature or doping level N_d. Figure 5 shows the dependence of V_{pv} on the barrier position in the quantum well for $\Delta n=8\times 10^{14}\,\mathrm{m}^{-2}$. The dependence of V_{pv} on l_b reflects the character of the distortion of the electron wave function. V_{pv} appears at $l_b\approx 5.0$ nm, when electrons of the second energy level begin to make transitions from the wide to the narrow portion of the quantum well, and reaches its maximum value at $l_b \approx 7.5$ nm, when the electrons of the first and second levels accumulate in different portions of the quantum well (see Fig. 3) and maximum polarization of the electron gas occurs in the quantum well.

Let us consider conditions for optical transfer of electrons from level E_1 to level E_2 and the possibility of using such structures as photovoltaic detectors of optical radiation. Consider a structure with a barrier in the plane $l_b = 7.5$ nm, where the photovoltage is a maximum. In this structure optical transitions between levels E_1 and E_2 are forbidden, since the overlap integral for electron wave functions $|\int_0^L \varphi_{e1}\varphi_{e2} dz|^2$ equals zero. Therefore, optical transfer of electrons from level E_1 to level E_2 takes place via the third level E_3. For $l_b = 7.5$ nm we have $E_3 - E_1 = 65$ meV. This implies that the structure can be a detector of infrared radiation in the wavelength range 5–19 μm.

After transfer to level E_3 the electrons make nonradiative transitions to the second and first levels. Denoting by W_{ij} the frequency of nonradiative transitions between levels i and j, from the balance equation for transitions in a three-level system we obtain the following expression for the number of transferred electrons from the first to the second quantum-well level:

$$\Delta n = \frac{W_{32}}{W_{21}(W_{31} + W_{32})} \, \frac{P}{h\nu_{13}}, \tag{4}$$

where P is the optical power absorbed in the quantum well, and $h\nu_{13}$ is the transition photon energy between levels E_1 and E_3. Substituting Eq. (4) into Eq. (3), we obtain the following expression for the magnitude of the photovoltaic response of the radiation detector:

$$\frac{V_{pv}}{P} = \frac{|e|}{\varepsilon_1} \, \frac{W_{32}}{W_{21}(W_{31} + W_{32}) h\nu_{13}} \int_{L_1}^{L_2} \left\{ \int_{L_1}^{z} [|\varphi_{e1}(z')|^2 - |\varphi_{e2}(z')|^2] dz' \right\} dz. \tag{5}$$

In order to increase the magnitude of the photovoltaic response we must increase W_{32} (which also increases the speed of the detector response), but primarily we must decrease W_{21}. The quantity W_{21}^{-1} is the lifetime of electrons transferred to the second level. In infrared detectors based on intersubband transitions in coupled (asymmetric) quantum wells, increasing the lifetime of electrons in the second level is achieved by increasing the thickness of the barrier between quantum wells, thereby decreasing the rate of electron tunneling through the barrier from the second to the first level.[4] In structures with a thick barrier the first and second levels corresponding to the three-level model are in different quantum wells.

In the structure with a thin separating barrier which we are discussung, the first and second levels are common to both quantum wells and the frequency W_{21} is determined by the frequency of nonradiative transitions between these levels.

Calculations of the rate of intersubband transitions in a GaAs quantum well show that the dominant mechanism responsible for these transitions is scattering of electrons by emission (absorption) of polar optical phonons.[10,11] Calculations of the relaxation rate in a GaAs quantum well with a thin AlGaAs barrier within the approximation of a dielectric continuum, with allowance for the interaction of electrons with trapped and surface polar optical phonons at $T = 77$ K, show that when the position of the AlGaAs barrier in the structure lies in the range $5 < l_b < 15$ nm if $E_k + E_2 - E_1 < \hbar\omega_0$, while $E_k + E_3 - E_2 > \hbar\omega_0$ (where $E_k = 6.6$ meV is the kinetic energy of an electron at 77 K and $\hbar\omega_0 = 36.2$ meV is the energy of an optical phonon in GaAs) the transition frequencies are: $W_{21} = 3 \times 10^9\ \mathrm{s}^{-1}$, $W_{31} = 1 \times 10^{12}\ \mathrm{s}^{-1}$ and $W_{32} = 3 \times 10^{12}\ \mathrm{s}^{-1}$. If the transition energies $E_2 - E_1 > \hbar\omega_0$, then $W_{21} > 10^{12}\ \mathrm{s}^{-1}$. The decrease of frequency W_{21} by almost three orders of magnitude when the barrier is introduced at the central region of the quantum well is due to the energetically forbidden nature of electron transitions with emission of optical phonons.

Thus, introducing a barrier into a quantum well preserves the high value of scattering frequency W_{32} and markedly decreases the scattering frequency W_{21}. This allows us to increase the lifetime of electrons in the transferred state to 0.2 ps, which is comparable to lifetimes in structures with a thick barrier between quantum wells.

When we substitute these values of W_{32}, W_{31}, and W_{21} into Eq. (5), we obtain a photovoltaic response of $V_{pv}/P = 8.8$ V/W for the power absorbed in a quantum well with a thin barrier when $l_b = 7.5$ nm. This is somewhat lower than in detectors with a thick barrier.

Note that a structure with a thin barrier admits reverse optical transfer from level E_2 to level E_1 via level E_3. Although the overlap integral of the wave functions $|\int_{L_1}^{L_2} (\varphi_2 \varphi_3) dz|^2$ goes to zero for $l_b > 7$ nm, the magnitude of the photovoltaic response in a structure where the barrier is located in the plane $l_b \approx 6$ nm turns out to be larger than the case discussed previously with a direct optical transition.

The results we have obtained for a specific GaAs quantum well structure with width $L = 20.0$ nm have a more general character. We can assert that if we increase the width of the quantum well L with proper allowance for scaling, a photovoltaic response will occur for barrier positions in the quantum well $l_b > 0.25L$, and will have a maximum at $l_b = 0.33L$. These scaled structures allow us to specify the transition energy $E_1 \to E_3$ and thus choose the energy of the detected signal.

Note that in structures with $L < 10.0$ nm the photovoltaic response is zero due to the abrupt increase in the transition frequency W_{21} when $E_2 - E_1 > \hbar\omega_0$.

4. CONCLUSIONS

Our calculations of the distortion of the spectrum and electron wave functions in AlGaAs/GaAs/AlGaAs quantum wells with width $L = 20.0$ nm and a thin ($d = 1$ nm) AlGaAs barrier in the plane l_b have shown that introducing such a barrier into the quantum well in the region $0 < l_b < 5$ nm shifts the electron charge toward the wide portion of the quantum well, and for uniform impurity doping leads to the appearance of a potential difference V_L across the quantum well.

For $l_b>5$ nm the energy of the bottom of the first subband in the narrow portion of the crystal turns out to be below the bottom of the second subband in the wide portion of the crystal, and electrons of the second level in the quantum well are shifted back into the narrow portion of the quantum well, which compensates for the potential difference V_L. The strong polarization of electron charge of the second level relative to the first for $l_b>5$ nm creates conditions for a photovoltaic response to optical excitation of electrons between these levels. The maximum photovoltaic response occurs at $l_b=7$ nm.

Calculations of the rates of intersubband transitions in these structures show that the lifetime of photoexcited electrons at the second level for $l_b>5$ nm can be increased to 0.3 ns. This increase in the lifetime ensures a large value of the photovoltaic response and makes the use of GaAs quantum-well structures with a thin AlGaAs barrier suitable as detectors of optical radiation in the infrared region.

[1] F. H. Julien, A. Sa'ar, J. Wang, and J. P. Leburton, Electron. Lett. **31**, 838 (1995).
[2] J. Faist, F. Capasso, D. Sivco, C. Sirtori, A. L. Hutchinson, S. N. G. Chu, and A. Y. Cho, Science **264**, 553 (1994).
[3] P. Boucaud, F. H. Julien, D. D. Yang, J. M. Lourtioz, E. Rosencher, P. Bois, and J. Nagle, Appl. Phys. Lett. **57**, 3 (1990).
[4] B. F. Levine, J. Appl. Phys. **74**(8), R1 (1993).
[5] H. Schneider, C. Schonbein, and G. Bihlmann, Appl. Phys. Lett. **70**, 1602 (1997).
[6] E. Rosencher and Ph. Bois, Phys. Rev. B **44**, 11 315 (1991).
[7] J. Pož ela, *Physics of High-Speed Transistors* (Plenum, N.Y., 1994).
[8] H. Schneider, J. Appl. Phys. **74**, 4789 (1993).
[9] C. Schonbein, H. Schneider, G. Bihlmann, K. Schwarz, and P. Koidl, Appl. Phys. Lett. **68**, 973 (1996).
[10] J. Požela, V. Jucienė, and K. Požela, Semiconductors **10**(12), 1555 (1995).
[11] J. Požela, V. Jucienė, A. Namajūnas, K. Požela, V. G. Mokerov, Yu. V. Fedorov, V. E. Kaminskii, and A. V. Hook, J. Appl. Phys. **82**, 5564 (1997).

Translated by Frank J. Crowne

Effect of partial ordering of a two-dimensional system of scatterers on the anisotropy of its kinetic coefficients

N. S. Averkiev, A. M. Monakhov, and A. Yu. Shik

A. F. Ioffe Physicotechnical Institute, Russian Academy of Sciences, 194021 St. Petersburg, Russia

P. M. Koenraad

COBRA Interuniversity Research Institute, Eindhoven University of Technology, the Netherlands

(Submitted March 3, 1998; accepted for publication April 3, 1998)
Fiz. Tekh. Poluprovodn. **32**, 1251–1253 (October 1998)

The effect of partial ordering of impurities (correlated along one direction and uncorrelated along the other) on the kinetic coefficients is considered. It is shown that the geometry of the spatial impurity distribution by itself has no effect on the diffusion coefficient or conductivity for scattering by a spherically symmetric potential, and these coefficients remain the same as for an uncorrelated system of impurities.
[S1063-7826(98)02210-8]

The way that scattering by randomly located impurities and impurities that randomly occupy sites in a periodic lattice affect conductivity is now well understood. However, the δ-doped layers that can now be grown on vicinal surfaces of semiconductors constitute a class of structures that differ from those considered previously, since they exhibit partial ordering of the scattering centers.[1] At the surface there is a periodic structure of monoatomic steps, and during doping impurities are deposited primarily on these steps, forming a system of parallel chains. Along such a chain the positions of impurities may be treated as completely uncorrelated. In this case, the chains themselves form a periodic lattice, whose period depends on the angle of misorientation of the surface relative to the principal crystal plane. In its geometry this system differs from any studied previously. Experimental studies show[2] that such layers have anisotropic electronic properties. In this paper we discuss how the geometry of the system of scatterers affects the anisotropy of the kinetic coefficients.

Consider the scattering of an electron localized in a δ-layer and freely moving only in the plane of the layer. In this case, we can write the collision integral in the Boltzmann equation, which determines the correction f_1 to the equilibrium distribution function f_0, in the form

$$I_{st}(\mathbf{k})=\int\frac{d^2\mathbf{k}'}{2\pi}W(\mathbf{k},\mathbf{k}')[f_1(\mathbf{k}')-f_1(\mathbf{k})]\delta(\varepsilon_k-\varepsilon_{k'}),\tag{1}$$

where $W(\mathbf{k},\mathbf{k}')\delta(\varepsilon_k-\varepsilon_{k'})$ is the probability for the electron to make a transition from state $\mathbf{k}$ to state $\mathbf{k}'$ as a result of elastic scattering. We are interested only in changes in the distribution function associated with spatial correlations in the impurity positions, and ignore the electron density near an impurity, which, in general, is needed to calculate kinetic coefficients. If we assume that the electron wave function in the plane of the layer is a plane wave, the probability $W(\mathbf{k},\mathbf{k}')$ can be written in the form

$$W(\mathbf{q})=\frac{2\pi}{\hbar}\left|\int dxdydz\, e^{iq_xx}e^{iq_yy}V(\mathbf{r})\varphi^2(z)\right|^2,\quad \mathbf{q}=\mathbf{k}-\mathbf{k}',$$

where $\varphi(z)$ is the quantum-well wave function along the direction z, and

$$V(\mathbf{r})=\sum_j^N v(\mathbf{r}-\mathbf{R}_j)$$

is the impurity potential (where $\mathbf{R}_j$ is the coordinate of the jth impurity). It is easy to show[3] that

$$W(\mathbf{q})=\frac{2\pi}{\hbar}|v(\mathbf{q})|^2S(\mathbf{q}),$$

where $v(\mathbf{q})$ is the Fourier transform of the effective two-dimensional impurity potential, which for a Coulomb potential is

$$v(q)=\frac{2\pi e^2}{\varepsilon q}\int\exp(-q|z|)\varphi^2(z)dz,$$

while $S(\mathbf{q})$, the so-called structure factor

$$S(\mathbf{q})=\left|\sum_j^N e^{i\mathbf{q}\mathbf{R}_j}\right|^2,\tag{2}$$

which contains all the information about the system geometry. Assuming that the positions of the impurities are entirely uncorrelated along a chain (the x direction), and that the chains themselves are positioned on a periodic lattice (the y direction), we obtain for the structure factor averaged over impurity positions

$$\langle S(\mathbf{q})\rangle=N\left[1+\frac{(2\pi)^2}{a}\nu\delta(q_x)\sum_n\delta\left(q_y-\frac{2\pi}{a}n\right)\right],\tag{3}$$

where N is the total number of impurities in the entire plane, and ν is the average number of impurities per unit length of chain. The quantity $\langle S(\mathbf{q})\rangle$ differs from the structure factor for completely uncorrelated impurities only at $q_x=0$. Qualitatively, this behavior of $S(\mathbf{q})$ is connected with the fact that for $q_x\neq 0$ the average number of impurities at the plane-wave front is constant, and only for $q_x\neq 0$ will oscillations begin in the averaged number of impurities at this front.

Equation (3) has a symbolic meaning to a certain extent, since when we substitute it into Eq. (1), we obtain the product of three δ-functions, which after integration formally gives the indeterminate expression $\delta(0)$. In order to assign a meaning to such an expression, we must recall that it was obtained from the sum (2), in which the total number of impurities N is assumed to be a large but finite number. Then

$$2\pi\nu\delta(0)=\overline{N_x^2}-\overline{N_x}, \tag{4}$$

where $\overline{N_x}$ is the average number of impurities on one chain.

Substituting expression (3) into Eq. (1), we obtain

$$\begin{aligned}I_{st}=N\int\frac{d^2k'}{2\pi}|v(\mathbf{k}-\mathbf{k}')|^2(f_1(\mathbf{k}')-f_1(\mathbf{k}))\delta(k-k')\frac{m}{k'}\\+\frac{2\pi\nu}{a}\delta(k_x-k_x')\sum_{n=-\infty}^{\infty}\delta\left(k_y-k_y'-\frac{2\pi}{a}n\right)|v(\mathbf{k}-\mathbf{k}')|^2\\\times(f_1(\mathbf{k}')-f_1(\mathbf{k}))\delta(k-k')\frac{m}{k'}.\end{aligned} \tag{5}$$

The first term on the right side of Eq. (5) corresponds to the collision integral for uncorrelated impurities, and the entire contribution from spatial correlations is contained in the second (singular) term.

Next, we will discuss scattering by a potential with circular symmetry, i.e., $v(\mathbf{k})=v(k)$. Then the correction to the distribution function is conveniently cast in the form of a sum:

$$f_1(k,\varphi)=f_1^+(k,\varphi)+f_1^-(k,\varphi),$$

where

$$f_1^+(k,\varphi)=f_1^+(k,-\varphi),$$

and

$$f_1^-(k,\varphi)=-f_1^-(k,-\varphi).$$

After substituting the quantities f_1^+ and f_1^- into Eq. (5) and integrating, the expression for the collision integral takes the form

$$\begin{aligned}I_{st}=N\int\frac{d\varphi'}{2\pi}|v(k,\varphi-\varphi')|^2(f_1^+(k,\varphi')+f_1^-(k,\varphi')\\-f_1^+(k,\varphi)-f_1^-(k,\varphi))+\frac{|v(2k|\sin\varphi|)|^2}{k|\sin\varphi|}\\\times 2f_1^-(k,\varphi)\sum_{n=1}^{\infty}\delta\left(2k|\sin\varphi|-\frac{2\pi}{a}n\right).\end{aligned} \tag{6}$$

If the field-dependent part of the Boltzmann equation is an even function of angle (for example, proportional to $\cos\varphi$, as happens when we calculate the conductivity in a uniform electric field), then the equations for f_1^+ and f_1^- separate. This can be seen, e.g., if we replace φ by $-\varphi$ in the Boltzmann equation, and then add and subtract the resulting equations. As a result, we find that the function f_1^+ satisfies the Boltzmann equation without the singular term in the collision integral, and that f_1^- satisfies the homogeneous equation:

$$\begin{aligned}\int\frac{d\varphi'}{2\pi}|v(k,\varphi-\varphi')|^2(f_1^-(k',\varphi')-f_1^-(k,\varphi))\\+\frac{|v(2k|\sin\varphi|)|^2}{k|\sin\varphi|}2f_1^-(k,\varphi)\sum_{n=1}^{\infty}\delta\left(2k|\sin\varphi|-\frac{2\pi}{a}n\right)=0.\end{aligned} \tag{7}$$

We emphasize that this separation of the equations for f_1^+ and f_1^- is directly related to the fact that the equation $v(k,\varphi)=v(k,-\varphi)$ is valid for the potential. Since f_1 is the correction for the distribution function caused by external perturbation, while Eq. (7) does not contain the perturbation, we must assume that $f_1^-\equiv 0$.

Thus, in calculating the conductivity or diffusion coefficient for any spherically symmetric potential, the contribution from the singular part of the collision integral equals zero and correlated positions of impurities in itself has no effect on these coefficients.

From these considerations, it does not follow, of course, that the kinetic coefficients in this system are the same as coefficients in the uncorrelated system. For an exact calculation, let us say, of the conductivity, it is necessary to take into account the nonuniform distribution density of the electrons, which immediately leads to anisotropy of the kinetic coefficients.

We note that the probability of scattering, as we should expect, contains the singular part. If we calculate the residence time for elastic scattering in this system of impurities

$$\tau^{-1}(\mathbf{k})=\frac{2\pi}{\hbar}\int\frac{d^3\mathbf{q}}{(2\pi)^3}|V(\mathbf{q})|^2\delta[E(\mathbf{k})-E(\mathbf{k}-\mathbf{q})],$$

as was done in Ref. 4 for a three-dimensional periodic lattice with randomly occupied sites, then according to Eq. (3) we obtain

$$\frac{1}{\tau(\mathbf{k})}=\frac{1}{\tau_r(\mathbf{k})}+\frac{1}{\tau_c(\mathbf{k})}.$$

The quantity τ_r is determined by scattering by randomly located impurities, while τ_c is determined by scattering at ‘‘Bragg’’ angles by the correlated chains:

$$\frac{1}{\tau_c}=\frac{N}{a\hbar}\sum_{n\neq 0,\frac{2\pi}{a}n\in[k_y-|k|,k_y+|k|]}\frac{m}{|k_x|}v\left(0,\frac{2\pi}{a}n\right)2\pi\nu\delta(0). \tag{8}$$

Expression (8) implies that for $k_y=(2\pi/a)n$ there is additional scattering that is enhanced by a factor of $(\overline{N_x^2}-\overline{N_x})/N_x$ compared to the incoherent scattering. In this sense, the situation is analogous to scattering by a crystal lattice: although an external beam (plane wave) gives rise to Bragg peaks [an analog to Eq. (8)], for an electron in the crystal with momentum much smaller than the size of the Brillouin zone the scattering by the lattice is not important at all, since the electronic states at the boundary of the Brillouin zone from which the scattering takes place are unoccupied due to the relatively small concentration of carriers in these states.

Thus, the geometry of impurity positions on δ-doped vicinal surfaces in itself has no effect on kinetic coefficients. Partial ordering in such a system can manifest itself in scattering of an external beam of particles (for example, in surface electron holography).

This work was supported in part by the RFFI Projects No. 96-15-96955, STNSQ No. 97-1039, and the Nederlandse Organisatie voor Wetenschappelijk Onderzoek (NWO).

[1] R. Nötzel, L. Däweritz, and K. Ploog, Phys. Rev. B **46**, 4736 (1992).

[2] A. D. Visser, V. I. Kadushkin, V. A. Kul'bachinskiĭ, V. G. Kitin, A. P. Senichkin, and E. L. Shangina, JETP Lett. **59**, 339 (1994).

[3] D. Ziman, *Principles of the Theory of Solids*, 2nd ed. (Cambridge Univ. Press, 1969; Mir, Moscow, 1974).

[4] A. F. J Levi, S. L. McCall, and P. M. Platzman, Appl. Phys. Lett. **54**, 940 (1989).

Translated by Frank J. Crowne

Polarization of in-plane photoluminescence from InAs/Ga(In)As quantum-well layers grown by metallorganic vapor-phase epitaxy

V. Ya. Aleshkin

Institute for Physics of Microstructures, Russian Academy of Sciences, 603600 Nizhniĭ Novgorod, Russia

B. N. Zvonkov, I. G. Malkina, Yu. N. Saf'yanov, and A. L. Chernov

Physicotechnical Research Institute, N. I. Lobachevsky State University at Nizhniĭ Novgorod, 603600 Nizhniĭ Novgorod, Russia

D. O. Filatov

Regional Center for Scanning Microscopy, Physicotechnical Research Institute at N. I. Lobachevskiĭ State University at Nizhniĭ Novgorod, 603600 Nizhniĭ Novgorod, Russia

(Submitted January 27, 1998; accepted for publication April 14, 1998)
Fiz. Tekh. Poluprovodn. **32**, 1254–1259 (October 1998)

This paper investigates the linear polarization of photoluminescence emitted along the plane of an InAs / Ga(In)As wafer. The polarization was observed to depend on the asymmetry of the quantum-well shape, quantum-dot formation, and the presence of inclusions in the bulk alloy. © *1998 American Institute of Physics.* [S1063-7826(98)02310-2]

Contemporary methods for investigating surfaces such as atomic-force and tunneling microscopy have strongly motivated the study of the complex growth mechanisms and structures of quantum-well layers. However, many features of quantum-well layers that are a consequence of the processes that occur during epitaxy have not been studied by these methods. Processes such as impurity segregation, which leads to changes in the potential profile of the quantum-well layers, or stratification of the solid solution, develop in the bulk of the structure while the next set of layers is being grown. Thus, since the evolution of the structure is not over until its capping layer is grown, it is important to develop methods of investigation that allow us to study the structure of quantum-well layers buried under thicknesses of other epitaxial layers. In this situation the method of optical anisotropy, which is very sensitive to the crystal structure can be one of the most important analysis tools. Among the many publications that touch on optical anisotropy of III-V structures with quantum-well layers, the number of papers devoted to the polarization of edge photoluminescence (PL), i.e., PL emitted from quantum wells[1–5] and quantum dots[5] in the plane of the epitaxial structure layers, is comparatively small. However, the effect of quantum confinement and mechanical stress in the quantum layer on the optical anisotropy should be strongest in this direction, which is perpendicular to the optic axis.

It is known that quantum wells made of tetragonally distorted InGaAs layers on substrates of GaAs or InP contain only heavy-hole levels[6,7] and hence the direction of the electric field vector **E** for PL emission from the quantum well should lie in the plane of the quantum well. In this case, if there were an axis of symmetry of lower than third order normal to the layers of the structure, then states of heavy and light holes would not be mixed, and the edge PL would be 100% linearly polarized.[8,9] Because of the presence of the heterojunction, the III–V heterolayers have a lower symmetry, and directions [110] and [−110] are not equivalent. Furthermore, additional lowering of the symmetry of atomic bonds at the heterostructure is possible due to the appearance of various morphological peculiarities at the time of epitaxial growth. Therefore, mixing of heavy- and light-hole states is possible at the heterojunction.[10] In this case, it also follows from group theory that we should observe 100% polarization of light from a quantum well with a symmetric potential profile (if the mixing parameter[10] is not too large). However, deviations of the quantum-well potential profile from rectangular shape should influence the degree of polarization.

In this paper we investigate the anisotropy of PL from structures with quantum-well layers grown by MOCVD- hydride epitaxy (i.e., gas-phase epitaxy using metallorganic compounds) at atmospheric pressure. We observe a connection between the structure of the quantum-well layers and linear polarization of the PL from cleaved facets of In(Ga)As / GaAs and InAs / GaInAs / InP structures with strained quantum wells and quantum dots. As far as we know, edge PL from quantum-well layers of In(Ga)As on GaAs substrates or InAs / InGaAs heterolayers on InP substrates have never been investigated before.

EXPERIMENTAL METHOD

Our structures were grown in an atmosphere of hydrogen, starting with trimethyl gallium (TMG) and trimethyl indium (TMI) as sources of the group-III elements and an excess of the group-V source, i.e., arsenic or phosphorous.

The quantum-well layers of InAs (InGaAs) were grown on (001) GaAs substrates. The samples either contained a single quantum-well layer capped with GaAs or were multilayer periodic structures. These multilayer periodic structures consisted of 10–20 quantum-well layers separated

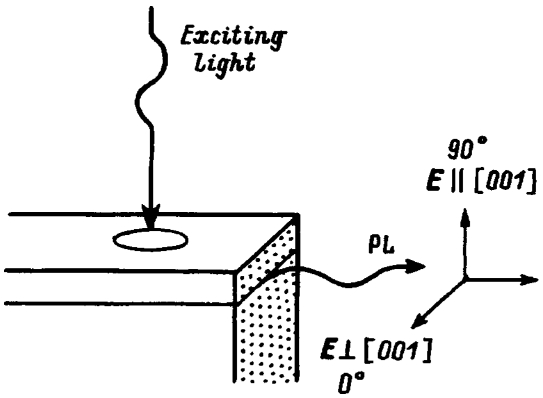

FIG. 1. Sketch of setup for measuring PL along the layers of the structure.

by 0.1-μm-thick GaAs barriers. The quantum wells were grown at 650 °C, with more than 20% InAs and thicknesses below the critical thickness for spontaneous formation of quantum dots.[11] The quantum dots were grown according to the Stransky–Kastanov mechanism at 630 °C with subsequent stopping of the growth. The growth and properties of these quantum dots were described in detail in Refs. 12 and 13. The quantum dots contained from 2 to 5 monolayers of InAs. Studies in a TMX2100 atomic-force microscope of the surfaces of control samples of InAs / GaAs (grown without the GaAs capping layer) reveal the presence of mounds with characteristic dimensions 10–20 nm and density $\sim 10^{11}\,\mathrm{cm}^{-2}$.[14]

Multilayer periodic structures with $\mathrm{In}_{0.5}\mathrm{Ga}_{0.5}\mathrm{As}$ / InP quantum wells were grown on (001) InP substrates at 600 °C. The composition of the solid solution was determined by *x*-ray diffraction. Lattice parameters of the $\mathrm{In}_{0.5}\mathrm{Ga}_{0.5}\mathrm{As}$ layers were close to that of the substrate (the mismatch of lattice parameters was less than $\pm 5\times 10^{-3}$). A strained layer of InAs was located in the middle of the $\mathrm{In}_{0.5}\mathrm{Ga}_{0.5}\mathrm{As}$ layer at the same distance from the InP with a nominal thickness of 2.5–7.5 monolayers (0.8–2.4 nm).

Figure 1 clarifies the system for making the measurements. A beam of PL excitation light from a He–Ne laser (with wavelength 633 nm) was focused onto the surface of the structure near the cleave down to a spot of diameter 0.1 mm. Emission from the sample (its PL) was focused by a collecting lens onto the slit of a monochromator and recorded using an automated system. A polarizer was placed in front of the monochromator slit and was rotated around the direction of observation. The direction of the electric field vector of PL from the sample (the vector **E**) that was perpendicular to the normal to the plane of the structure layers (i.e., along the layers), was assigned the angle 0°. When this vector was directed along the normal to the layer, its direction corresponded to an angle of 90° in our notation.

The degree of polarization was estimated from the expression $P = 100\% \cdot (I_0 - I_{90})/(I_0 + I_{90})$ (where I_0 and I_{90} are intensities corresponding to 0° and 90°). The error in determining this quantity was approximately ±10%.

RESULTS AND DISCUSSION

The photoluminescence from all the samples we studied, which was observed in the direction normal to the surface, was not noticeably polarized: *P* was less than 10%. The edge PL of calibration samples, which consisted of uniform epitaxial homoepitaxial layers of GaAs or InP, or GaAs structures with periodically located δ-layers of acceptor carbon, also showed no significant polarization.

Also weak is the dependence of the polarization on the geometric parameters of the sample: the distance between the excitation spot and the cleave, the thickness of the substrate, and the quality of the sample surface. Nevertheless, in order to decrease the possibility of errors due to these factors, only the results of measurements made under the same conditions were compared among themselves .

Edge PL from all the heterostructures we studied was linearly polarized, and the directions of maximum and minimum PL intensity relative to the structure layers were always either 0° or 90°.

1. Isolated quantum-well layers

An isolated In(Ga)As size-quantized layer on a substrate of GaAs or InP is distinguished by its weak waveguiding effect compared to multilayer structures, which confine most of the propagating light to their bulk. If the thickness of the capping layer becomes smaller than the wavelength of the PL in the material (in our case, $\sim 0.3\ \mu$m), a large fraction of the emission along the quantum-well layers propagates in the capping layer. Near the surface there is a surface-state electric field, which, on the one hand, can lead to rotation of the plane of polarization due to the electrooptic effect and, on the other, can disrupt the polarization selection rules by causing the quantum-well potential profile to deviate from its rectangular shape.

In fact, it was observed experimentally that the thickness of the capping layer is the most important factor, and should be taken into account in determining the magnitude of the linear polarization of edge PL from an isolated quantum-well layer. The dependence of the linear polarization on thickness of the capping quantum-well layer was measured on small-angle cross sections of GaAs / In(Ga)As / GaAs and InP / InAs / InP structures prepared by chemical etching. The excitation beam was shifted along the wedge of the cross section parallel to the emitting edge.

Figure 2 shows the dependence of the intensity (I_{PL}) of edge PL of a GaAs / In(Ga)As / GaAs structure ($n = 10^{16}\,\mathrm{cm}^{-3}$) on the thickness of the GaAs capping layer. If the quantum-well layer is in the quasi-neutral region (i.e., outside the space-charge region of surface states, whose thickness at this doping level was 0.3 μm; see Ref. 15), then maximum PL intensity from the quantum-well layers is observed for optical-wave electric-fields **E** parallel to the plane of the layer (0°), and the minimum is observed in the perpendicular direction (90°). In the range of 0–0.2 μm the thickness of the capping layer strongly affects the polarization of the edge PL. As this thickness decreases, the degree of polarization decreases and even changes sign, reaching a

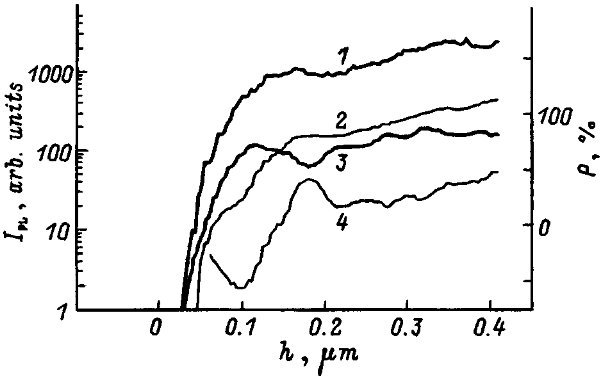

FIG. 2. Dependence of the intensity of edge PL I_{PL} (*1–3*) and degree of polarization P (*4*) of an isolated InGaAs quantum-well layer on the thickness of the GaAs capping layer h. *1*—Total intensity, *2*—intensity of PL polarized in the plane of the SQL (0°); *3*—intensity of PL polarized normal to the plane of the SQL (90°).

value of $P=-60\%$, which is characteristic of transitions with the participation of light-hole states.

For a InP/InAs/InP structure with the same level of doping we observed the same regularities, but for capping layer thicknesses 30–60 nm smaller, which is in agreement with the characteristically smaller height of the surface barrier for this material.

The electrooptic effect should lead to a smooth change in the direction of polarization as we vary the distance between the radiating edge and the translation path of the excitation laser beam spot. However, since this is not observed, the most likely reason for the change in polarization should be disruption of the symmetry of the quantum-well potential profile by the barrier electric field.

Deviations of the potential profile from rectangular can arise not only from the electric field but also from a nonuniform distribution of indium concentration in the quantum well along the growth direction. In order to study how such a nonuniformity affects the polarization, we grew $In_xGa_{1-x}As/GaAs$ structures with highly asymmetric indium distributions relative to the center of the quantum well.

The control samples were ''symmetric quantum wells,'' containing a $In_xGa_{1-x}As$ layer during whose growth time (9 seconds) the trimethyl indium flux was either held constant or increased at the center for 3 seconds. During the growth of nonsymmetric quantum wells, the trimethyl indium flux was increased for 2 seconds at the beginning or at the end of the growth. The thickness of the capping (and buffer) layer was 0.4 μm, much larger than the thickness of the space charge region, which for this series of samples came to 50 nm (samples 2246–2249, doping level $n=2.5\times10^{17}\,\mathrm{cm}^{-3}$). The thickness of the quantum well was 5 nm. These results are presented in Table I, where we also list the compositions used to grow the quantum wells with intentionally altered indium distribution profiles, computed from the growth regime data; the compositions are listed sequentially along the growth direction. In addition, Table I also lists data obtained for undoped multilayered periodic structures with the same quantum wells (structures 2234–2237).

TABLE I. Parameters of $In_xGa_{1-x}As/GaAs$ structures. (QW–quantum-well layer; MPS–multilayer periodic structure.)

Structure No.	Type of structure	x	$h\nu_A$, eV	P, %
2246	QW	0.13	1.434	35
2247	QW	0.15/0.10	1.447	9
2248	QW	0.11/0.16	1.454	31
2249	QW	0.9/0.14/0.9	1.440	36
2234	MPS	0.16	1.416	33
2235	MPS	0.23/0.15	1.439	10
2236	MPS	0.13/0.21	1.428	22
2237	MPS	0.13/0.21/0.13	1.412	32

In fact, it turns out that the highest degree of polarization of the edge emission is observed in control samples and samples with an increased concentration of indium at the center of the quantum well. Increasing the indium concentration near one of the heterojunctions decreases the degree of polarization and is accompanied by a rather small shift in the energy maximum (by 0.01–0.02 meV) in the direction of higher energies. The lowest degree of polarization is observed for increased indium concentration near the boundary with the substrate. This can be understood if we take into account that segregation of indium at the growth temperatures used leads to penetration of a certain amount of indium into the cap layer,[16] which results in a decrease in the potential barrier from this side of the quantum well. Therefore, the potential profile is not completely symmetric relative to the center of the well even in the control sample. Shifting the layer with increased indium concentration towards the substrate tends to make the potential profile closer to triangular in shape. Similar layers located on the opposite side act in the opposite direction. The results obtained for a multilayered periodic structure and an isolated quantum-well layer are in agreement (Table I).

Thus, measurements of the polarization of edge PL from a quantum well with a nonrectangular potential profile confirm the dependence of the degree of polarization on the symmetry of the profile.

2. In(Ga)As/GaAs multilayer periodic structures

The PL of multilayer In(Ga)As/GaAs structures is also polarized parallel to the plane of the layer. The degree of polarization for a quantum well (at the wavelength of the maximum in the spectrum) turns out to be about 30% in this case. For the same sample parameters, the PL from quantum dots was polarized much more strongly: 50–100%. Figure 3 shows the dependence of the PL intensity from multilayer In(Ga)As/GaAs structures at the spectrum maximum on the angle of rotation of the polarizer. The parameters of the structures under study are listed in Table II.

Figure 3 shows that when thermalized carriers with ground-state energies of the quantized layers recombine, the angular dependence of the PL intensity has the form of a figure eight in the plane of the structure layers and perpendicular to the optical axis. This is in keeping with the selection rules.[17] However, the degree of polarization is not 100%, and depends on the layer structure. As the degree of polarization decreases, the shape of the figure eight is dis-

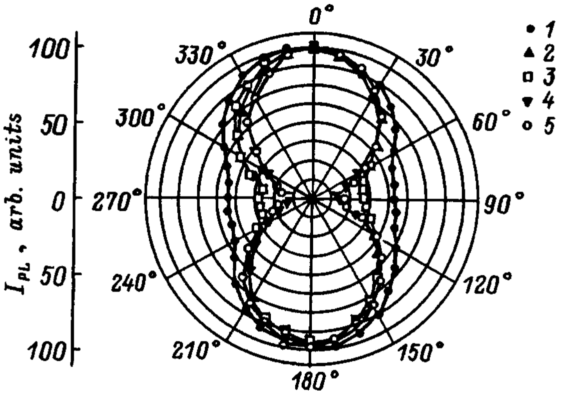

FIG. 3. Dependences of the PL intensity (normalized) at the spectral maximum of multilayer $In_xGa_{1-x}As$ / GaAs structures with quantum wells and quantum dots on the angle of rotation of the polarization. Sample numbers (see Table II): *1* — 1848, *2* — 1966, *3* — 1959, *4* — 1960, *5* — 2065.

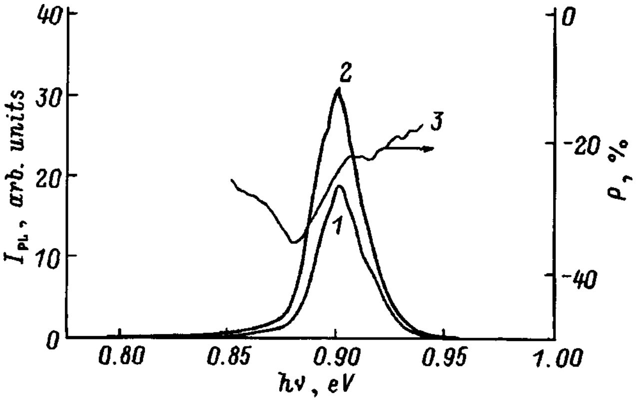

FIG. 4. Spectral dependences of the intensity (*1*,*2*) and degree of polarization (*3*) of PL from a $In_{0.535}Ga_{0.465}As$ / InP quantum well. Polarization: *1* — 0°, *2* — 90°.

torted due to additions at the minimum of light from other polarizations (samples 1848, 1966, 1959). This result is easy to explain if we postulate that the small-area regions of the quantum-well layers, with strongly asymmetric profiles of the indium distribution or a high degree of intermixing atoms at the heterojunction, are responsible for the 90° polarization, whereas the primary region of the In(Ga)As quantum-well layers is occupied by the quantum-well or a quantum-dot layer with 0° polarization. This is possible, e.g., as a result of local segregation of indium[16] or some electrically active impurity at one of the heterostructures.

3. MULTILAYER InAs / $In_{0.5}Ga_{0.5}As$ / InP STRUCTURES

It has been reported in the literature that the sign of the PL polarization from InGaAsP / InP structures with quantum wells corresponds to the sign of mechanical strain.[4] It has also been reported that the photosensitivity of $In_xGa_{1-x}As$ / InP structures depends on the polarization, and that the direction of polarization corresponding to the largest photosensitivity agrees in sign with the mechanical strain in the solid solution.[7] However, the changes in signal reported were considerably smaller than 100%.

The results of our investigations of the polarization PL from $In_xGa_{1-x}As$ / InP and InAs / $In_{0.53}Ga_{0.47}As$ / InP multilayer periodic structures reveal new features about the polarization of edge PL. We found that even when the *x*-ray diffraction curves indicated that the solid solution was under compressive strain, its edge PL was often polarized along the normal to the plane of the layers (90°, vector **E** along [001]).

TABLE II. Parameters of multilayer $In_xGa_{1-x}As$ / GaAs structures. (QW–quantum well; QD–quantum dot.)

Structure No.	Type of structure	x	InGaAs thickness, nm	Carrier concentration (per period) n,p, cm^{-2}	$h\nu_A$, eV
1848	QW	0.2	4.5	p, 10^{11}	1.389
1966	QD	1	0.65	p, 10^{11}	1.412
1959	QD	1	0.76	n, 10^{11}	1.395
1960	QD	1	0.73	p, 10^{12}	1.393
2065	QD	0.5	3.4	n, 3×10^{10}	1.282

Figure 4 shows the spectrum of 0°- (curve *1*) and 90°-PL (curve *2*) for a multilayer periodic structure with 8-nm-thick $In_xGa_{1-x}As$ quantum wells, $x=0.535$. Despite the fact that the *x*-ray diffraction curves indicate the presence of a tetragonal compressive strain of no more than 4.4×10^{-4}, we observed strong polarization at the maximum of the spectrum: $P=-25\%$. As the excitation intensity decreased, the maximum of the PL shifted slightly towards low energies and the degree of polarization increased to $P=-60\%$.

This degree of polarization is predicted by light-hole selection rules.[17] The shift of the maximum with changes in the level of excitation indicates screening of electric fields in the quantum well by the excited carriers. Increasing the level of excitation decreases the asymmetry of the quantum-well potential profile. Therefore, we propose to interpret the presence of 90° polarization as an indication that electric fields are present in the quantum well during growth, which lead to strongly nonrectangular potential wells (recall that in $In_xGa_{1-x}As$ / GaAs quantum wells the surface electric field also shifts the direction of polarization). The appearance of these electric fields could be a consequence of segregation of electrically active impurities.

The InAs layer makes a potential well within the InGaAs quantum well. Because it serves as an effective sink for excited carriers, the features of the fundamental PL line of the sample should correspond to its structure. Actually, the primary PL line of the InAs / $In_{0.53}Ga_{0.47}As$ / InP multilayer periodic structures is shifted towards lower energies and when the nominal thickness of the InAs layer is increased to 7.5 monolayers, the PL line shifts to 1.8 μm (77 K). The magnitude of this shift corresponds to data obtained in Ref. 18 for samples grown by molecular beam epitaxy. The absolute value of our PL maximum is located 0.04 eV higher in energy than in that paper. (Because our growth temperature was higher than that reported in Ref. 18, the effective thickness of our strained layer was somewhat decreased due to reverse evaporation.) The photoconductivity spectrum is in agreement with this PL data. We did not investigate the sur-

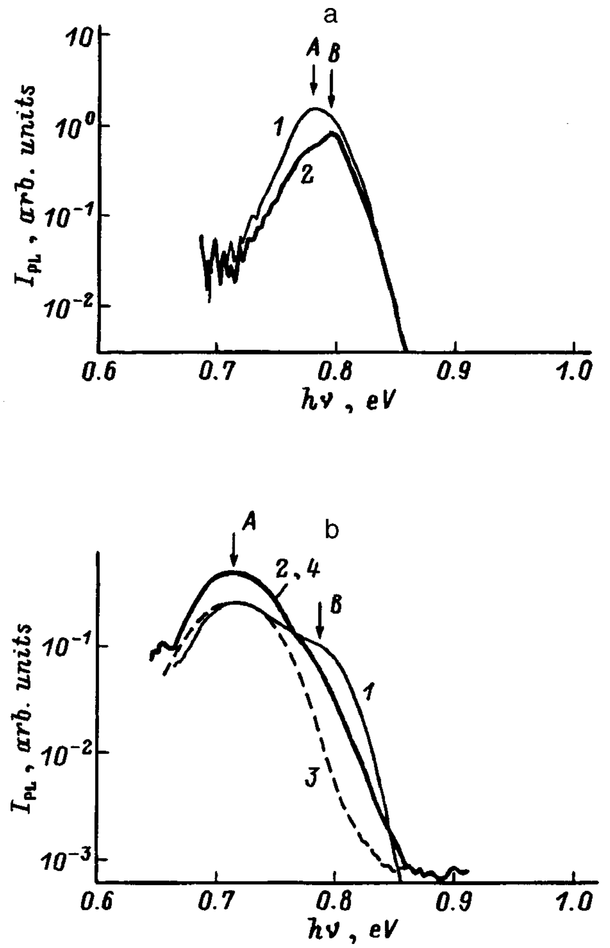

FIG. 5. PL spectra of InAs / $In_{0.537}Ga_{0.463}As$ / InP structures. a — 25-nm-InGaAs quantum well, 2.5 monolayers of InAs; polarization: *1* — 0°, *2* — 90°. b — 25-nm-InGaAs quantum well, 5 monolayers of InAs; *1, 2* and *3, 4* correspond to mutually perpendicular end facets; polarization: *1, 3* — 0°; *2, 4* — 90°.

faces of the quantum-well layers in these structures by atomic-force microscopy; however, the Gaussian form of the ground-state PL line is evidence of the formation of zero-dimensional states characteristic of quantum dots.

In InAs / $In_{0.53}Ga_{0.47}As$ / InP structures, like structures on a GaAs substrate, the InAs layer is subject to strong tetragonal compressive strain. (The mismatch in lattice parameters of InAs and InP is on the order of 3%.) Therefore, we expect that the edge PL will be polarized along the plane of the layer, i.e., at 0°. In a sample with small InAs thickness this is in fact observed. However, studies of a number of samples show that the maximum of the PL corresponding to recombination in the InAs layer can nevertheless have 90° polarization.

Figure 5a shows edge PL spectra of an $In_{0.537}Ga_{0.463}As$ / InP heterostructure with thin (2.5 monolayer) InAs layers at the center of an $In_{0.537}Ga_{0.463}As$ (25 nm) quantum well. It has 0° polarization. Peak A ($h\nu = 0.78$ eV) corresponds to recombination of carriers trapped by the InAs layer, while peak B ($h\nu = 0.8$ eV) corresponds to recombination in the layer of $In_{0.537}Ga_{0.463}As$ solid solution. Peak A is polarized more stongly than B: $P = 50\%$ and 20%, respectively.

When the thickness of the stressed layer is increased to five monolayers, the direction of the polarization changes (Fig. 5b). This figure shows spectra of 0°- (curves *1* and *3*) and 90°- (curves *2* and *4*) PL emitted from two mutually perpendicular cleaveage planes (curves *1*, *2*, *3*, and *4*). It is clear that at the PL maximum (A) we observe a strong 90° polarization, for which $P = 30\%$.

This change in the direction of the polarization is evidence of the existence of structural features that lead to participation of light-hole states in the recombination. One such feature could be a decrease in the symmetry of atomic bonds at the heterojunction, which leads to a higher degree of mixing of the states than in In(Ga)As / GaAs. Another is stratification or the presence of regions of structural order in the solid solution,[19] which can also lead to effects such as capture of nonequilibrium holes by inclusions and indirect recombination (in real space). In real-space indirect recombination, the participation of tunneling implies that the primary role is played by states that penetrate far into the barrier. Both effects are associated with the structure of the solid state solution layer.

The properties of line B (Fig. 5b) give information about the complicated structure of the solid solution. When we measured PL from the two perpendicular ends, the directions of the polarization in the region of line B did not coincide: curves *1* and *2* exhibit 0°, while curves *3* and *4*, which were obtained by measuring from the other end, exhibit 90° polarization. This is characteristic of an ordered solid solution.[20]

CONCLUSIONS

We have experimentally observed the effect of asymmetry of In(Ga)As / GaAs quantum-well structures on the degree of polarization of edge PL, and an increase in the degree of linear polarization of edge PL when quantum dots form in the structures.

In InAs / $In_{0.5}Ga_{0.5}As$ / InP structures the direction of polarization of PL from stressed quantum wells and from the solid solution itself varies in a more complicated way.

This work was supported by RFFI (Grant 95-02-05610), the ministry of science (Program FTNS, Grants 95-2004, 97-1089), and CRDFRESC02.

[1] R. Sooryakumar, D. S. Chemla, A. Pinchuk, A. C. Gossard, W. Wiegmann, and L. J. Sham, Solid State Commun. **54**, 859 (1985).
[2] K. Fujiwara, N. Tsukada, N. Nakayama, and T. Nishino, Solid State Commun. **69**, 63 (1989).
[3] D. Gershoni, I. Brener, G. A. Baraff, S. N. G. Chu, L. N. Pfeiffer, and K. West, Phys. Rev. B **44**, 1930 (1991).
[4] K. Uppal, D. Tishinin, and P. D. Dapkus, J. Appl. Phys. **81**, 390 (1997).
[5] G. Malkina, V. Ya. Aleshkin, B. N. Zvonkov, and Yu. N. Saf'yanov, Phys. Low-Dimens. Semicond. Struct. **1/2**, 61 (1997).
[6] X. Marie, J. Barrau, B. Brousseau, Th. Amand, M. Brousseau, E. V. K. Rao, and F. Alexandre, J. Appl. Phys. **69**, 812 (1991).
[7] D. Gershoni and H. Temkin, J. Lumin. **44**, 381 (1989).
[8] G. L. Bir and G. E. Pikus, *Symmetry and Strain-Induced Effects in Semiconductors* (Wiley, New York, 1975; Nauka, Moscow, 1972).
[9] S. Jorda and U. Rössler, Superlattices Microstruct. **8**, 481 (1990).
[10] E. L. Ivchenko, A. Yu. Kaminski, and U. Rössler, Phys. Rev. B **54**, 5852 (1996).

[11] W. L. Wang, J. L. Liao, B. Xu, Zh. Zhu, and B. Yang, Appl. Phys. Lett. **66**, 1080 (1995).
[12] B. N. Zvonkov, I. G. Malkina, E. R. Lin'kova, V. Ya. Aleshkin, I. A. Karpovich, and D. O. Filatov, Fiz. Tekh. Poluprovodn. **31**, 1100 (1997) [Semiconductors **31**, 1051 (1997)].
[13] B. N. Zvonkov, E. R. Lin'kova, I. G. Malkina, D. O. Filatov, and A. L. Chernov, JETP Lett. **63**, 439 (1996).
[14] G. A. Maksimov and D. O. Filatov, in *Proceedings of the 2nd All-Union Symposium SZM-98*, p. 105 [in Russian] (Nizhniĭ Novgorod, 1998).
[15] A. Chandra, C. E. C. Wood, D. W. Woodard, and L. F. Eastman, Solid-State Electron. **22**, 645 (1979).
[16] O. Dehaese, X. Wallart, and F. Mollot, Appl. Phys. Lett. **66**, 52 (1995).
[17] G. Bastard, C. Delalande, Y. Guldner, and P. Voisin, Adv. Electron. Electron Phys. **72**, 1 (1988); C. Weisbuch and B. Vinter, in *Quantum Semiconductor Structures*, edited by H. B. Jovanovich (Academic Press, San Diego, CA, 1991).
[18] V. M. Ustinov, A. E. Zhukov, A. F. Tsatsul'nikov, A. Yu. Egorov, A. R. Kovsh, M. V. Maksimov, A. A. Suvorova, N. A. Bert, and P. S. Kop'ev, Fiz. Tekh. Poluprovodn. **31**, 1256 (1997) [Semiconductors **31**, 1132 (1997)].
[19] A. Zunger and S. Mahajan, in *Handbook on Semiconductors* (Elsevier, Amsterdam, 1994), Vol. 3.
[20] G. S. Horner, A. Mascarenhas, R. G. Alonso, D. G. Friedman, K. Sinha, K. A. Bertness, J. G. Zhu, and J. M. Olson, Phys. Rev. B **48**, 4944 (1993).

Translated by Frank J.Crowne

SEMICONDUCTORS VOLUME 32, NUMBER 10 OCTOBER 1998

AMORPHOUS, GLASSY, AND POROUS SEMICONDUCTORS

Doping and impurity compensation by ion implantation in *a*-SiGe films

A. V. Ershov, A. I. Mashin, and A. F. Khokhlov

N. I. Lobachevsky State University at Nizhnii Novgorod, 603600 Nizhnii Novgorod, Russia

(Submitted March 16, 1998; accepted for publication March 23, 1998)
Fiz. Tekh. Poluprovodn. **32**, 1260–1262 (October 1998)

This paper discusses the electrical properties of *a*-SiGe films ($N_{\mathrm{Ge}}\sim 2.2$ at. %) prepared by co-evaporation of Si and Ge from separate sources and doped by ion implantation of substitutional impurities (B^+ and P^+), as well as the results of controlled impurity compensation by ion-beam doping. It was found that B^+ and P^+ implantation into *a*-SiGe films in the dose range $1.3\times 10^{14}-1.3\times 10^{17}$ cm^{-2}, followed by annealing at 350 °C, increased the conductivity of these films from 10^{-9} to 10^{-4} and to 10^{-5} S/cm for B^+ and P^+, respectively. The position of the Fermi level could be varied from $(E_v+0.27)$ to $(E_c-0.19)$ eV. These investigations indicate that compensation of pre-doped *a*-SiGe films by ion implantation is feasible and reproducible. It is also found that higher doping efficiency of *a*-SiGe films is obtained by using boron than by using phosphorus. © *1998 American Institute of Physics.* [S1063-7826(98)02410-7]

At this time, there is much interest in studying the properties of amorphous hydrogenated silicon (*a*-Si:H) as a promising material for making thin-film, large-area, solar-cell elements, field-effect transistors, etc.[1] Interest in studying the electrical properties of films of amorphous hydrogenless silicon, which contains small additives of an isovalent impurity like germanium (*a*-SiGe), arises from the possibility of obtaining a material with properties similar to *a*-Si:H but with more stable characteristics.[2–4]

In this paper, whose topic is investigating the possibility of doping these films with substitutional impurities, we present the results of ion-implanting boron and phosphorus into a layer of *a*-SiGe obtained by co-evaporation of Si and Ge. Our work demonstrates the possibility of compensating impurities in films that are previously doped.

Thin (~100 nm) films of *a*-SiGe with Ge content $N_{\mathrm{Ge}}\sim 2\%$ were obtained by combined evaporation of Si and Ge from different sources in a VU-1A vacuum setup under conditions similar to those we described in Ref. 4. The amount of isovalent Ge impurity in the layers was varied by varying the rate of evaporation of the germanium, and was determined from *x*-ray spectral fluorescence analysis according to the method of Ref. 5. The *a*-SiGe films were doped by implantation of B^+ and P^+ ions with energies E = 15 and 40 keV, respectively, at room temperature. The ion dose was varied from $\Phi=1.3\times 10^{14}$ to 1.3×10^{17} cm^{-2}. In order to compensate the ''impurity'' conductivity of *n*-type samples that were previously irradiated with phosphorus, we irradiated these samples with B^+ ions at E = 15 keV in doses of $\Phi=1.5\times 10^{15}-4.4\times 10^{16}$ cm^{-2}. In order to compensate the *p*-type conductivity of *a*-SiGe:B, we irradiated with phosphorus ions at E = 40 keV in doses of $\Phi=1.5\times 10^{15}-3\times 10^{17}$ cm^{-2}. In both cases, the preliminary irradiation doses were $\Phi=1.3\times 10^{17}$ cm^{-2} (leading to a concentration of $\sim 2\times 10^{21}$ cm^{-3}).

In order to avoid the incorporation of hydrogen in the films, the impurity ions were obtained by ionizing BF_3 and PCl_3 gases. The samples were then annealed in vacuum at a residual pressure of no more than 5×10^{-5} Torr and temperature 350 ± 5 °C for 30 minutes.

Aluminum contacts were deposited on the samples in a coplanar configuration in order to measure their electrical conductivity. The measurements were made in a vacuum cryostat in the temperature range from 100 to 420 K. The field intensity between the contacts did not exceed 10^3 V/cm. The conductivity mechanism was identified on the basis of a modified Mott–Davis model of the density of localized states.[6] The correctness of this model for layers of *a*-SiGe was discussed previously.[3,6]

Under the conditions described in Ref. 4, we obtained a series of *a*-SiGe films with germanium concentrations of 2.2 at. %. Measurements of the electrical conductivity of the films after annealing at 350 °C showed good agreement with the data of Ref. 4, which is evidence that our method of obtaining *a*-SiGe is highly reproducible. The films obtained by us had a conductivity of 1×10^{-9} S/cm, which at room temperature comes about via transport in the conduction band with an activation energy of 0.63 eV. The width of the optical gap of the films had a value of 1.58 eV, and the ratio of the photoconductivity measured from the source close to AM1 to the dark conductivity was 62.

Figure 1 shows the dose dependence of the conductivity $\sigma(\Phi)$ measured in the dark at room temperature and its activation energy $E_a(\Phi)$ for *a*-SiGe films ion-dosed with phosphorus and boron and annealed at a temperature of 350°.

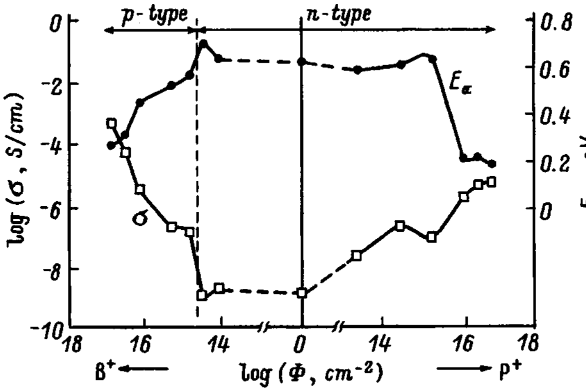

FIG. 1. Magnitude of the electrical conductivity activation energy versus dose for *a*-SiGe films ion-doped with boron and phosphorus and annealed at 350 °C.

Introducing boron ions in doses from 1.3×10^{15} to 1.3×10^{17} cm^{-2} leads to considerable increase in the conductivity—from 1×10^{-9} to 5×10^{-4} S/cm, i.e., more than five orders of magnitude. In this case, measurements of the sign of the thermoelectric power indicate that the conductivity is hole-like in nature, starting with a dose of 1.3×10^{15} cm^{-2}, which is evidence that type of majority carriers has changed compared with the unirradiated sample in which electron transport dominated. Thus, doping takes place even at these low doses of boron. Boron compensates the electron transport of the *n*-type original samples for boron-ion doses in the interval $0<\Phi\leqslant1.3\times10^{15}$ cm^{-2}.

Ion doping the films with phosphorus increases their conductivity by four orders of magnitude to values as high as $\sigma\approx1\times10^{-5}$ S/cm.

Measurements of the temperature dependences of the conductivity show that in the entire range of boron and phosphorus doses the contribution of electrical transport along delocalized states to the conductivity of the film at room temperature is dominant. There is an appreciable contribution to the conductivity from hopping transport via localized states near the Fermi level in the temperature range below 250 K for films doped with these impurities at doses greater than 6×10^{16} cm^{-2}.

With regard to the behavior of the activation energy, the function $\sigma(\Phi)$ is in qualitative agreement with data on the sign of the thermoelectric power. However, it is noteworthy that for doping with P$^+$ ions the behavior of the activation energy $E_a=E_c-E_F$ (where E_c is the edge of the conduction band, and E_F is the Fermi level) is less monotonic than for irradiation by B$^+$, and begins to decrease strongly for $\Phi>6\times10^{15}$ cm^{-2}. Apparently, the reason for the nonmonotonic portion of the function $E_a(\Phi)$ is the presence of peaks in the density of localized states near E_c (similar to X), which ''hinder'' the motion of the Fermi level toward the edge E_c at small doses. This fact, and also the weaker increase in σ with P$^+$ dose, are evidence that the efficiency of doping with phosphorus is lower than with boron. We estimated the efficiency of doping *a*-SiGe with boron and phosphorus atoms using the method described in Ref. 7. In this method, we first estimate the magnitude of the density of localized states near the Fermi level from those segments of the temperature dependences of the electrical conductivity that involve hopping transport of carriers (along states near the Fermi level) for films doped in doses greater than 6×10^{16} cm^{-2}, under the assumption that the localization radius for the carriers equals 1 nm. This density of states turned out to be $\sim(3-9)\times10^{21}\,\mathrm{eV}^{-1}\cdot\mathrm{cm}^{-3}$ for impurity doses of $\sim10^{17}$ cm^{-2}, which is in good agreement with values for *a*-Si : H, in which doping places the Fermi level in the region corresponding to the band tail.[6] Then, based on the magnitude of the shift of the Fermi level with increasing dose, we determine the impurity dose at which electrical activity equal to the ratio of concentrations of ionized to incorporated impurities appears. For B$^+$ and P$^+$ ions in doses of 1×10^{17} cm^{-2} this quantity is 0.14 and 0.09, respectively. It is clear that the efficiency of doping with boron ions is almost 1.5 times higher than for phosphorus ions. Comparison of these results for the efficiency of ion doping of *a*-SiGe and *a*-Si : H films give comparable results for concentrations of boron and phosphorus impurities: $N_{\mathrm{B,P}}\geqslant10^{20}$ cm^{-3} (Ref. 7).

Thus, films of *a*-SiGe obtained by the method of co-evaporation can indeed be doped. In this range of acceptor and donor impurity ion doses, the position of the Fermi level

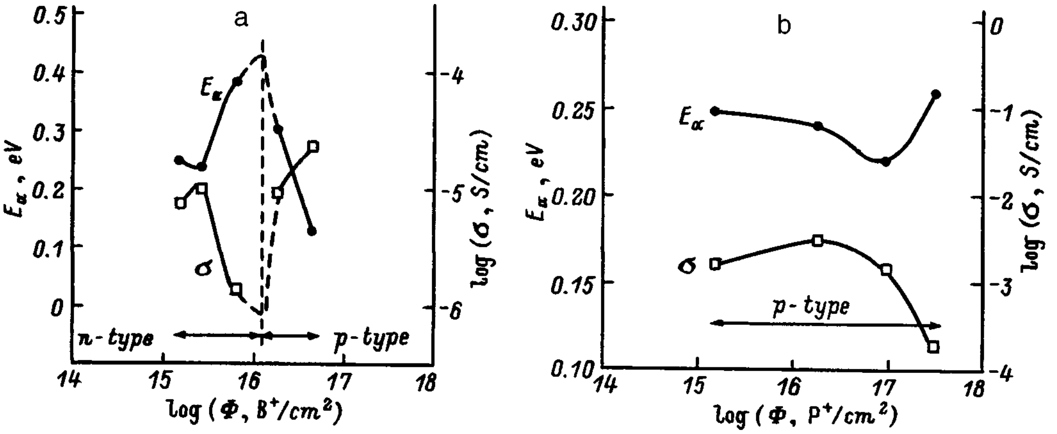

FIG. 2. Magnitude and activation energy of the electrical conductivity of *a*-SiGe : P films versus additional dose of incorporated boron ions (a), and the same for films of *a*- SiGe : B versus additional dose of incorporated phosphorus ions (b), after annealing at 350 °C.

can be controllably varied from $E_v+0.27$ (E_v at the edge of the valence band) to $E_c-0.19$ eV.

Figure 2 shows the dose dependence of the magnitude and activation energy of the conductivity of *n*-type films compensated with impurities boron (a) and *p*-type films compensated by phosphorus ions (b).

Let us first consider the results of our attempt to compensate the electrical conductivity of *a*-SiGe : P by additional incorporation of boron (Fig. 2a). Increasing the boron ion dose to 6×10^{15} cm^{-2} (for a concentration of $\sim4\times10^{20}$ cm^{-3}) decreases σ from 1×10^{-5} to 1.5×10^{-6} S/cm; in this case, E_a increases to 0.38 eV. Further increasing the dose leads to a change in the sign of the thermoelectric power, to an increase in the conductivity, and to a decrease in the activation energy to 0.1 eV. These data indicate that compensation is occurring. Here a transition of the sample to ''intrinsic'' behavior occurs in the dose range near $\Phi=1\times10^{16}$ cm^{-2}. This corresponds to a boron concentration $N_{\mathrm{B}}\sim8\times10^{20}$ cm^{-3}, which is somewhat smaller than the original phosphorus concentration. Obviously, doping with boron initially shifts the Fermi level from the bottom of the conduction band to the center of the mobility gap, after which the conductivity of the sample converts to *p*-type. Further changes in E_a reflect a shift in the Fermi level away from the edge of the valence band.

The process by which *a*-SiGe : B films are compensated by phosphorus atoms (Fig. 2b) differs somewhat from the case described above. We observed no change in conductivity type due to ion implantation with phosphorus in the dose range we studied; i.e., the films retained their original hole-like conductivity. Moreover, increasing the phosphorus dose to 10^{17} cm^{-2} leaves the magnitude and activation energy of the conductivity unchanged. A tendency toward compensation is observed only at the maximum phosphorus dose. In this case the conductivity decreases by roughly an order of magnitude and the activation energy E_F-E_v increases to 0.25 eV. The low electrical activation of phosphorus in *a*-SiGe films is also revealed in experiments on compensation. It is difficult to identify the reason for this because of the absence of exact information regarding the distribution of the density of states in the mobility gap of *a*-SiGe obtained by co-evaporation of Si and Ge. We probably should anticipate that in this material the peak in the density of states near E_c is considerably sharper than the peak near the edge of the valence band.

In summary, we have shown that films of amorphous silicon with small additives (~2 at. %) of germanium obtained by co-evaporation from separate sources of Si and Ge can be successfully doped with boron and phosphorus ions. The electrical properties of the doped *a*- SiGe films can be controlled by introducing opposite-type impurities to bring about compensation.

This work was carried out with the support of a grant from Goskombuz for fundamental and applied investigations in the area of materials for electronic technology under the direction of ''Electronic Technology Materials,'' in the ''Promising Materials'' division of MNTP (No. 01.9.60012617).

[1] A. Madan and M. Shaw, *The Physics and Applications of Amorphous Semiconductors* (Academic Press, Boston–San Diego–N.Y.–London–Sydney– Tokyo–Toronto, 1988; Mir, Moscow, 1991).

[2] A. F. Khokhlov, A. I. Mashin, A. V. Ershov, and Yu. A. Mordvinova, Phys. Status Solidi A A **94**, 379 (1986).

[3] A. V. Ershov, A. A. Ezhevskiĭ, A. F. Khokhlov, D. A. Khokhlov, A. I. Mashin, and N. I. Mashin, Nucl. Instrum. Methods Phys. Res. B **106**, 257 (1995).

[4] A. V. Ershov, V. Yu. Zverev, A. I. Mashin, A. F. Khokhlov, and N. I. Mashin, in *Proceedings of the Russian conference on "Structure and Properties of Crystalline and Amorphous Materials"*, 12–14 March 1996, Nizhniĭ Novgorod (Nizhniĭ Novgorod State Univ., Nizhniĭ Novgorod, 1996), p. 67.

[5] A. F. Khokhlov, A. I. Mashin, A. V. Ershov, N. I. Mashin, and E. V. Larina, Fiz. Tekh. Poluprovodn. **19**, 2204 (1985) [Sov. Phys. Semicond. **19**, 1360 (1985)].

[6] N. F. Mott and E. A. Davis, *Electronic Processes in Non-Crystalline Materials* [Clarendon Press, Oxford, (1979); Mir, Moscow, (1982)].

[7] H.-J. Hoffman, J. Appl. Phys. **18**, 427 (1979).

Translated by Frank J. Crowne

Long-term structural relaxation and photoinduced degradation in *a*-Si:H

K. V. Kougia

Pediatric Medical Academy, 194100 St. Petersburg, Russia

A. B. Pevtsov

A. F. Ioffe Physicotechnical Institute, Russian Academy of Sciences, 194021 St. Petersburg, Russia

(Submitted May 20, 1998; accepted for publication May 20, 1998)
Fiz. Tekh. Poluprovodn. **32**, 1272–1276 (October 1998)

The effect of heating-illumination cycling on the electrical properties of *a*-Si:H fabricated in a glow discharge was investigated. Comparison of experimental and theoretical results shows that photostimulated degradation of *a*-Si:H (the Staebler–Wronski effect) may occur due to long-term degradation of structural defects generated by preliminary heating. © *1998 American Institute of Physics.* [S1063-7826(98)02510-1]

1. Studies of the photoinduced degradation of *a*-Si:H (the Staebler–Wronski effect[1]) always incorporate the following two ideas: 1) nearly all the experiments require that the sample first be heated to a temperature of $T_A \sim 500\,\mathrm{K}$, and then cooled to a temperature T_0 at which the measurements are made; it is assumed without comment that this annealed state (state *A*) is also the ground state of the material that possesses the lowest internal energy; 2) despite the multitude of proposed interpretations of the Staebler–Wronski effect, all of them in general outline can be reduced to a phenomenological model that postulates a set of defect-formation centers, each of which can be in two stable states separated by a potential barrier. The model of such a center can be represented schematically as a double-well potential with parameters U and ΔE that fluctuate randomly (Fig. 1).[2]

In this paper we will analyze the behavior of an ensemble of random double-well potentials during thermal treatment as applied to investigation of the Staebler–Wronski effect, compare the results of calculations with the experimental data, and draw conclusions about possible mechanisms for this effect.

2. The samples under study were prepared by high-frequency decomposition of silane-containing gas mixtures in a system with capacitive coupling, and equipped with contacts deposited in a coplanar configuration for measuring dark conductivity and photoconductivity.

3. Figure 2a shows the temperature dependence of the electrical conductivity measured before (*1*) and after (*3*) illumination at 100 mW/cm^2 for 2 hours at 293 K. The measurements were made after the customary preliminary ''anneal'' at 500 K. Point (*2*) corresponds to the electrical conductivity of the material after ~7 years of being kept in the dark.

If we concede that the variations observed in the electrical conductivity are associated with transitions of defect-formation centers from one stable state to another, then these variations should be correlated with variations in the populations of wells of the double-well potentials used to model these centers. Let us calculate the temperature dependence of the average occupation coefficient of the upper wells of an ensemble consisting of 50 double-well potentials with barrier (U_i) and asymmetry (ΔE_i) parameters distributed according to a normal law around average values U and ΔE with mean-square deviations δU_i and $\delta \Delta E_i$. The occupation of each of the potentials is calculated from the equation

$$dn_i/dt = -n_i p_\downarrow + (1-n_i) p_\uparrow, \tag{1}$$

where n_i is the occupation coefficient of the ith upper well, and $p_\downarrow$ and $p_\uparrow$ are rates of transitions from the upper well to the lower and vice versa:

$$p_\downarrow = \nu \exp((U_i - \Delta E_i)/kT) \quad \text{and} \quad p_\uparrow = \nu \exp(U_i/kT), \tag{2}$$

where $\nu = 10^{12}$ Hz is a phonon frequency. As an initial condition we use the equilibrium condition at T = 500 K:

$$n_i(500\,\mathrm{K}) = p_\uparrow(500\,\mathrm{K})/(p_\uparrow(500\,\mathrm{K}) + p_\downarrow(500\,\mathrm{K})). \tag{3}$$

When temperature T is a linear function of time, Eq. (1) can only be solved numerically. The temperature dependence of each occupation coefficient n_i is calculated separately and the results are then summed so as to average over all the potentials of the ensemble.

The initial parameters of the calculation were chosen by looking for the best agreement between calculation and experiment according to the procedure described later in this text:

$$U = 1.22\,\mathrm{eV} \quad \delta U = 0.14\,\mathrm{eV},$$

$$\Delta E = 0.08\,\mathrm{eV} \quad \delta\Delta E = 0.02\,\mathrm{eV}. \tag{4}$$

The results of this calculation are shown in Fig. 2b. Curve *1* corresponds to an initial cooling of the ensemble from its equilibrium state achieved at T=500 K. The ''plateau'' observed for $T<300$ K indicates that the excess population of the upper well has become ''frozen,'' because under equilibrium conditions the population should follow curve *4.* At room temperature this ''frozen'' population can relax both under the action of temperature and other factors. The calculations show that the ensemble parameters given above hinder purely thermal relaxation, which is illustrated by point

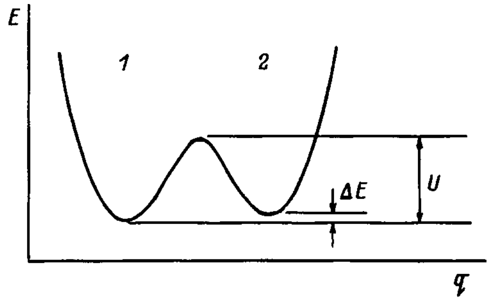

FIG. 1. Schematic illustration of the two-state model of a defect-formation center. E is the center energy, q is the configuration coordinate.

2 in Fig. 2b, which corresponds to a time interval of 7 years. It is clear that the system is still far from its equilibrium state even after being held for such a long time.

Let us assume, however, that we have found a way to stimulate relaxation of this system and have lowered the frozen population by a factor 100. Curve *3* (Fig. 2b) will then describe the temperature dependence of the average population when the system is heated. Let us now turn to the problem of an optimal choice of model parameters. These parameters were chosen so as to ensure the best agreement between calculation and experiment as follows. Since the conductivity in a-Si : H takes place via delocalized states, we have

$$\sigma(T)=\sigma_0 \exp(-(E_c-\mu)/kT), \tag{5}$$

where $E_c-\mu$ is the distance from the mobility edge in the conduction band to the Fermi level. Hence, features of the temperature dependence $\sigma(T)$ can be associated with motion of the Fermi level during the structural reconfiguration. Assuming the shift in the Fermi level is directly proportional to the change in occupation of the potential wells, i.e.,

$$|\Delta\mu| \propto |\Delta n|, \tag{6}$$

where $\Delta\mu$ is the shift in the Fermi level, and Δn is the change in occupation coefficient, and comparing Eqs. (4) and (5), we may conclude that over a rather limited temperature range the derivatives with respect to temperature (or some function of it) of n and $\ln(\sigma)$ will differ by no more than a constant; normalization by some ‘‘reference’’ functions $\sigma(T)$ and $n(T)$ will allow us to eliminate this factor as well. An example of this procedure is shown in Fig. 2c, where we compare $\sigma(T)$ and $n(T)$ differentiated with respect to inverse temperature and normalized by the functions $\sigma(T)$ and $n(T)$ obtained during the initial cooling of the sample (curve *1* in Figs. 2a and 2b). It should be noted that the choice of other reference functions leads to a change in the shape of the resulting curves shown in Fig. 2c, but the optimum values of the parameters of the calculations themselves will be unchanged and will coincide with those given previously.

We next consider the mechanism for relaxation of the frozen population (transition from curve *1* to curve *3*). As we have already shown, this role could be played by thermal excitation (point *2*), but the latter is insufficiently effective. Therefore, in our view another mechanism is more likely, which is also connected with excitation of lattice vibrations: nonradiative recombination of nonequilibrium carriers. Evidence in favor of this mechanism comes from experiments in which the parameters of the material are changed by passing a current through a diode structure. In these experiments it was shown that the degradation is minimal when only electrons are injected, is somewhat accelerated by injection of a few holes, and increases greatly when carriers of both signs

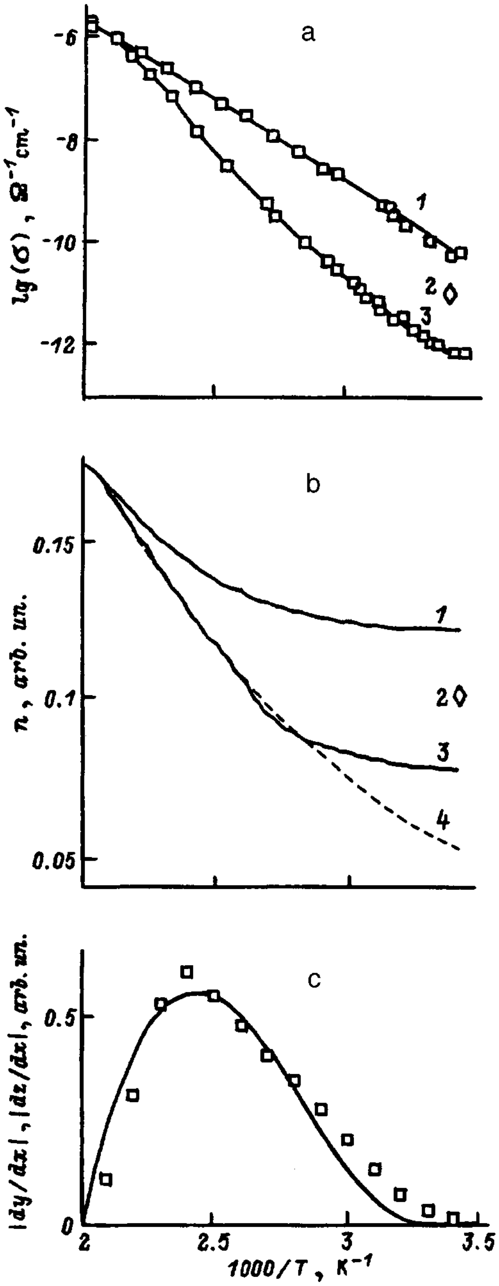

FIG. 2. a—Temperature dependence and electrical conductivity of a-Si : H annealed and unirradiated (*1*) and subjected to illumination by AM1 for 1 hour (*3*). Point (*2*) corresponds to electrical conductivity of annealed and unilluminated a-Si : H held at room temperature and in the dark for 7 years. b—Temperature dependences of the average occupation of upper wells of an ensemble of double-well potentials (n) as it is cooled from 500 K (*1*) and heated after stimulated relaxation of the frozen population (*3*). Point (*2*) is the average occupation at room temperature after a preliminary anneal followed by a 7-year stay in the dark. Curve (*4*) corresponds to equilibrium occupation with no freeze-out effects. c—Comparison of experimental (points) and calculated (solid curves) results. The procedure for comparison is described in the text of the article. Notation: $y=\sigma_3(T)/\sigma_1(T)$; $z=y=n_3(T)/n_1(T)$; $x=100/T$.

are injected, i.e., when recombination takes place.[3] The absence of a threshold in the spectral dependence of the Staebler–Wronski effect for ''device''-quality samples of *a*-Si : H also suggests that it is impossible to directly excite defect formation centers, and so an intermediate mechanism must exist for transferring energy from light quanta to these defects. Recombination of nonequilibrium carriers also provides such a mechanism.[4]

Thus, relaxation of the system under the action of light from the upper frozen state to the lower can be a manifestation of the Staebler–Wronski effect. To what extent is this identification justifiable? It is obvious that such a transition is connected with a decrease in the system energy, which agrees with the increase in activation energy of the dark conductivity, and consequently with the decrease in the Fermi level for undoped *a*-Si : H. The increase in defect concentration observed during the Staebler–Wronski effect is also in agreement with transition $2 \rightarrow 1$ (Fig. 1), because according to the results of Ref. 2, this frozen state of the system corresponds to the decreased defect concentration.

In conclusion, let us discuss the parameter values for the model obtained by us. The quantity $U = 1.22$ eV apparently can be associated with hydrogen diffusion, since it is in reasonable agreement with the results of other authors regarding the magnitude of the potential barrier for this process in material of ''device'' quality.[5] As for the value of $\Delta E = 0.08$ eV, its interpretation is not so obvious, especially since we have used a simple approximation of immobile potential wells. If we take into account the possibility that the extrema of the double-well potential can shift as the temperature changes, then we can only assert that the difference in energies of states *1* and *2* (Fig. 1) is on the order of few hundredths or at the most few tenths of an eV, which in itself is an interesting result since it forces us to resist identifying states *1* and *2* (Fig. 1) as states of an isolated dangling bond either saturated or unsaturated with hydrogen, because in this case the energy difference should be at a minimum an order of magnitude higher. Therefore, one probable explanation we must consider for the photoinduced effect is rearrangement of the hydrogen subsystem, evidence for which comes from experiments in which changes occur in the infrared spectrum corresponding to collective vibrations of hydrogen atoms.[6]

[1] D. L. Staebler and C. R. Wronski, Appl. Phys. Lett. **31**, 292 (1977).

[2] S. B. Aldabergenova, V. G. Karpov, K. V. Kougiya, A. V. Pevtsov, V. N. Solov'ev, and N. A. Feoktistov, Fiz. Tverd. Tela (Leningrad) **32**, 3599 (1990) [Sov. Phys. Solid State **32**, 2087 (1990)].

[3] L. Xu, G. Winboume, M. Silver, V. Canella, and T. McGill, Phil. Mag. B **57**, 715 (1988).

[4] S. B. Aldabergenova, A. A. Andreev, A. Ya. Vinogradov, K. V. Kougiya, and T. A. Sidorova, in *International Conference on Noncrystalline Semiconductors–89* [in Russian] (Uzhgorod, 1988), p. 222.

[5] R. A. Street, C. C. Tsai, and J. Kakalious, Phil. Mag. B **56**, 305 (1987).

[6] G. L. Kong, D. L. Zhang, Y. P. Zhao, and X. B. Liao, Sol. St. Phenomena **44–46**, 677 (1995).

Translated by Frank J. Crowne

SEMICONDUCTORS VOLUME 32, NUMBER 10 OCTOBER 1998

Heterogeneity and photoconductivity kinetics in amorphous hydrogenated silicon

K. V. Kougia

St. Petersburg State Pediatric Medical Academy, 194100 St. Petersburg, Russia

E. I. Terukov

A. F. Ioffe Physicotechnical Institute, Russian Academy of Sciences, 194021 St. Petersburg, Russia

V. Fus

Hahn-Meither Institute, D-12489 Berlin, Germany

(Submitted January 20, 1998; accepted for publication April 3, 1998)
Fiz. Tekh. Poluprovodn. **32**, 1266–1268 (October 1998)

A model of the decay kinetics of photoconductivity in amorphous hydrogenated silicon, in which recombination of excess carriers is assumed to occur via tunnelling, is proposed. It is shown that study of the decay shape after flash illumination can be a very effective way to detect structural inhomogeneities in amorphous or disordered semiconductors. © *1998 American Institute of Physics.* [S1063-7826(98)02610-6]

1. A characteristic feature of the nonstationary photoconductivity of disordered semiconductors, including amorphous hydrogenated silicon (a-Si:H), is the presence of a long-period ''tail'' in the photoconductivity that persists after switching off the illumination. Two possible mechanisms can give rise to this tail. The first is thermally stimulated emptying of traps (localized states) distributed with respect to energy in the band gap (mobility gap) of the semiconductor. In this case, the shape of the photoconductivity decay curve can be used to infer the distribution of localized states with respect to energy $N(E)$, since at a given temperature the decay time will characterize the depth of the localized states being emptied, and the magnitude of the photoconductivity will depend on their concentration. That possibility was mentioned for the first time in Ref. 1 as applied to semiconductors in powder form. Subsequently, analogous ideas for determining $N(E)$ were developed for chalcogenide-glass semiconductors[2,3] and recently a similar method was proposed for a-Si:H as well.[4,5]

A second possible mechanism for the appearance of a tail in the photoconductivity (or photoluminescence) is recombination of nonequilibrium carriers via tunneling. In this case, the slowing of the photoconductivity decay is connected with recombination of more and more distant pairs, and the magnitude of the photoconductivity is proportional to the concentration of carriers that have not yet recombined. This phenomenon is observed both in doped and compensated semiconductor crystals[6,7] and in a- Si:H.[8,9]

It is obvious that at sufficiently low temperatures the second mechanism becomes the mechanism of choice. As the temperature increases, it is usually assumed that thermally activated processes begin to overwhelm it. However, there is rather weighty evidence that even at ''high'' temperatures (above room temperature) recombination can take place via below-barrier tunneling.[10–13]

In this paper we will show that the data reported in Refs. 4 and 5 on photoconductivity kinetics in a-Si:H after excitation with short light pulses at room temperature can be explained and modeled by postulating the tunneling recombination of nonequilibrium carriers in a two-phase heterogeneous material.

2. It has been established experimentally that photoconductivity of undoped a-Si:H obtained by rf decomposition of silane is caused primarily by thermally activated motion of nonequilibrium electrons, whereas holes are considerably less mobile.[14] If we assume that after an initial thermalization (which occurs within times of order of the inverse phonon frequency, i.e., $<10^{-11}$ s) the long-period decay of the photoconductivity is connected with a drop in the concentration of nonequilibrium carriers due to tunneling recombination, then by analogy with donor-acceptor recombination in crystalline semiconductors we can assert that this drop in the concentration is connected with successive emptying of ''recombination channels'' consisting of ''donor- like localization center-closest electron capture center'' pairs. The characteristic lifetime of an electron-hole pair trapped in one of these channels is

$$\tau(r)=\nu_0^{-1}\exp(2r/q), \tag{1}$$

where r is the distance between a localized electron and hole, $\nu_0=1.4\times10^{11}\,\mathrm{s}^{-1}$ (Ref. 15) and $a\approx 12\,\text{Å}$ is the radius of localization of the least localized carrier, i.e., an electron.[16]

If N_{h1} and N_{e1} are concentrations of localization centers for electrons and holes, respectively, and if their spatial distribution is uncorrelated, then for the distribution of recombination channels with respect to distance we may use the formula[17]

$$g(r)=\frac{3r^2}{R^3}\exp\left(-\frac{r^3}{R^3}\right), \tag{2}$$

where $R^3=3/4\pi N_{e1}$.

After a short (in the limit an infinitely short) optical pulse, nonequilibrium carriers are trapped at localized states at a rate determined by the capture cross section σ_1. If only one type of recombination channel is assumed, then the initial occupation of the channels will be approximately uniform:

$$f(r)=N_0/N_{h1}, \tag{3}$$

where N_0 is the total concentration of electron-hole pairs created by the optical pulse. Then the decay of the concentration of nonequilibrium holes will be described by the expression

$$p(t)=\int_0^\infty f(r)g(r)\exp(-t/\tau(r))dr, \tag{4}$$

which can be related to the decay of the photoconductivity

$$\sigma(t)=\mu_D n(t)=\mu_D p(t) \tag{5}$$

by virtue of the condition of electrical neutrality, and if the electron drift mobility μ_D is time-independent. Expression (5) allows us to compare calculated curves for the decay of the photoconductivity with experiment, using the quantities μ_D, N_{h1}, and N_{e1} as fitting parameters. As we showed previously for the case of photoconductivity decay from a stationary state, even this simple model gives good agreement with experimental data over a wide interval of time and experimental temperatures.[13] However, for a short optical pulse a model with one type of recombination channel does not satisfy the experimental data and requires the introduction of a second type of channel characterized by concentrations N_{h2}, N_{e2} and hole capture cross section σ_2. Then

$$p(t)=\sum_{i=1}^{2}\int_0^\infty f_i(r)g_i(r)\exp(-t/\tau(r))dr, \tag{6}$$

where $g_i(r)=\dfrac{3r^2}{R_i^3}\exp(-\dfrac{r^3}{R_i^3})$, $R_i^3=3/4\pi N_{ei}$, while

$$f_i(r)=N_0\frac{\sigma_i N_{hi}}{\sigma_1 N_{h1}+\sigma_2 N_{h2}}, \tag{7}$$

where σ_1 and σ_2 are the cross sections for capture of nonequilibrium holes.

Equations (6) and (7) can be transformed as follows:

$$\sigma(t)=e\mu_D p(t)\sim\int_0^\infty f_1(r)g_1(r)\exp(-t/\tau(r))dr$$
$$+\beta\int_0^\infty f_2(r)g_2(r)\exp(-t/\tau(r))dr, \tag{8}$$

where $\beta=(\sigma_2 N_{h2})/(\sigma_1 N_{h1})$.

Expression (8) allows us to calculate the decay of the photoconductivity and compare it with experimental data. An example of a comparison with data obtained in Ref. 4 is shown in Fig. 1 for two *a*-Si : H samples deposited at different substrate temperatures. The fitting parameters that ensure best agreement between calculation and experiment are listed in Table I.

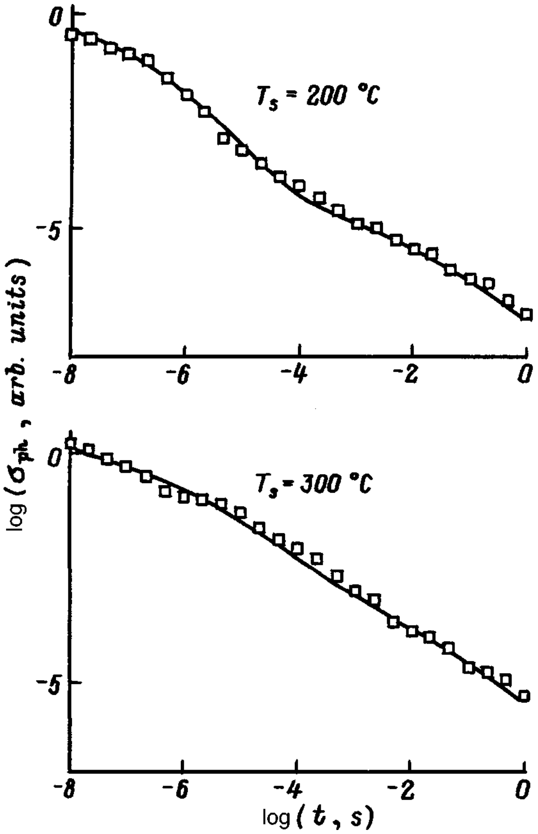

FIG. 1. Time dependence of the photoconductivity decay after pulsed excitation of samples of *a*-Si : H obtained at various substrate temperatures T_s (the squares are experimental data and the solid curves are the result of calculations).

3. In discussing these results several questions arise, above all: How can two sets of independent recombination channels coexist? It is obvious that they should be separated either in energy or in space. Attempts to construct a model with energy differences (e.g., the first set made up of deep states, the second of shallow) must postulate the near-complete absence of thermally activated transitions, which is doubtful at the experimental temperatures. Therefore, we prefer the second model, in which a set of recombination channels is separated in space, possibly concentrated in different phases of the *a*- Si : H. This point of view is confirmed by the results of our experimental studies, in which we showed that *a*-Si : H is structurally quite nonuniform, containing at least two phases, one hydrogen-enriched and one hydrogen-depleted.[18] In this model, the decrease of β and N_{e2} with increasing deposition temperature is entirely natural, because it reflects the increase in degree of uniformity of material obtained at higher substrate temperatures due to a decrease in the concentration of the hydrogen-rich phase. In order to identify the phases of the material we must also investigate the stability of values of N_{e1}, and ask whether they are in fact identical to values that we obtained in Ref. 13

TABLE I.

T_s, °C	$\beta=\dfrac{\sigma_2 N_{h2}}{\sigma_1 N_{h1}}$	N_{e_1} cm^{-3}	N_{e_2} cm^{-3}
200	4000	4.7×10^{17}	2.2×10^{18}
300	110	4.7×10^{17}	1.2×10^{18}

for our intrinsic materials. This kind of stability implies that the phase labeled 1 is a certain ‘‘intrinsic’’ characteristic of the material, and does not depend as strongly on the conditions under which it is obtained, which is entirely characteristic of the phase of a-Si:H that is hydrogen-depleted.[18]

Thus, studies of the shape of the photoconductivity decay under pulsed optical excitation can be effectively used to observe structural nonuniformities in amorphous or disordered semiconductors. This is especially interesting with regard to materials such as microcrystalline, nanocrystalline, and porous silicon.

[1] H. B. DeVore, RCA Rev. **20**, 79 (1959).
[2] J. G. Simmons and M.C. Tam, Phys. Rev. B **7**, 3706 (1973).
[3] J. Orenstein and M. Kastner, Phys. Rev. Lett. **46**, 1421 (1981).
[4] H. Naito, Solid State Phenom. **44–46**, 647 (1995).
[5] H. Oheda, Researches of the Electrotechnical Laboratory, 886 (1987).
[6] V. P. Dobrego and S. M. Ryvkin, Fiz. Tverd. Tela (Leningrad) **4**, 553 (1962) [Sov. Phys. Solid State **4**, 402 (1962)].
[7] R. Rentzch and I. S. Shilimak, Phys. Status Solidi A (A) **43**, 231 (1977).
[8] A. A. Andreev, A. V. Zherzdev, A. I. Kosarev, K. V. Koughia, and I. S. Shilimak, Solid State Commun. **52**, 589 (1984).
[9] B. I. Shklovskii, E. I. Levin, H. Fritzche, and S.D. Baranovskii, in *Advances in Disordered Semiconductors*, *Vol. 3: Correlation and Structural Defects*, edited by H. Fritzche (World Scientific, 1990), p. 161.
[10] K. V. Koughia and I. S. Shilimak, in *Advances in Disordered Semiconductors*, *Vol. 3: Correlation and Structural Defects*, edited by H. Fritzche (World Scientific, 1990), p. 213.
[11] H. Dersch, L. Shweitzer, and J. Stuke, Phys. Rev. B **28**, 4678 (1983).
[12] V. S. L’vov, L. S. Mima, and O. V. Tret’yak, Preprint No. 182, Institute of Automation and Electrometry, Siber. Dept., USSR Acad. Sci. (Novosibirsk, 1982).
[13] K. V. Koughia, E. I. Terukov, and V. Fus, Fiz. Tekh. Poluprovodn. (in press).
[14] T. Tiedje, in *The Physics of Hydrogeneted Amorphous Silicon*. Vol. II: *Electronic and Vibrational Properties*, edited by J. D. Jonnopoulos and G. Lucovsky (Springer-Verlag, Berlin-Heidelberg-N.Y.-Tokyo, 1984), p. 329.
[15] V. Chech, F. Schauer, and J. Stuchlik, J. Non-Cryst. Solids (in press).
[16] C. Tsang and R. A. Street, Phys. Rev. B **19**, 3027 (1979).
[17] H. Reiss, J. Chem. Phys. **25**, 400 (1956).
[18] J. Knights, in *The Physics of Hydrogenated Amorphous Silicon*. Vol. I, edited by J. D. Jonnopoulos and G. Lucovsky (Springer-Verlag, Berlin, 1984).

Translated by Frank J. Crowne

Relaxation of photoinduced metastable states in *a*-Si:H films deposited at high temperatures

I. A. Kurova and N. N. Ormont

M.V. Lomonosov Moscow State University, 119899 Moscow, Russia

O. A. Golikova and M. M. Kazanin

A. F. Ioffe Physicotechnical Institute, Russian Academy of Sciences, 194021 St. Petersburg, Russia

(Submitted April 10, 1998; accepted for publication April 15, 1998)
Fiz. Tekh. Poluprovodn. **32**, 1269–1271 (October 1998)

The results of an experimental study of dark-conductivity kinetics in *a*-Si:H after short-term and long-term illumination, are presented. The films were deposited at temperatures in the range $T_s = 300-390\,^\circ\mathrm{C}$. Data on relaxation of the photoinduced metastable states were found to correlate with the Fermi-level position. *© 1998 American Institute of Physics.* [S1063-7826(98)02710-0]

The kinetics of formation and relaxation of photoinduced metastable states in *a*-Si:H films have been investigated in a number of papers.[1,2] In recent years attention of investigators has focused on photoinduced metastable states in films obtained under various growth conditions.[3,4] In this paper we study the kinetics of formation and relaxation of photoinduced metastable states in *a*-Si:H films obtained by rf glow discharge at high substrate temperatures: $T_s \geqslant 300\,^\circ\mathrm{C}$ (Ref. 5).

The kinetics of time-dependent changes in the concentration of photoinduced metastable states in *a*-Si:H films after switching off illumination are determined by the method described in Ref. 6. It is assumed that the density of states near the Fermi level is constant while the dark conductivity $\sigma_d(t)$ changes with time t. In this case the motion of the Fermi level, which is proportional to the logarithm of the ratio of dark current to its equilibrium value at a given temperature σ_{d0}, is determined by the concentration of photoinduced metastable states:

$$\Delta F(t) = kT \ln[\sigma_d(t)/\sigma_{d0}] = N(t)/\rho_0(E_F), \qquad (1)$$

where ρ_0 is the constant density of states in the neighborhood of $F_0 + \Delta F$ (where F_0 is the initial Fermi level), and N is the concentration of photoinduced metastable states.

The sign of ΔF, i.e., the direction of motion of the Fermi level up or down within the band gap, is determined by where the photoinduced metastable states are located relative to the initial equilibrium Fermi level. Thus, in undoped films the formation of photoinduced metastable states (in this case, neutral photoinduced dangling bonds) near the center of the band gap for F_0 in the upper half of the latter leads to lowering of the Fermi level and a decrease in the dark conductivity;[1] The annealing of photoinduced dangling bonds after switching off the light then leads to an increase in σ_d. The increase in the number of electrically active impurity states under illumination gives rise to an increase in the dark conductivity in doped films as a result of the motion of the Fermi level towards the corresponding bands. Deactivation of the impurities is accompanied by a decrease in the dark conductivity. It should be noted that processes connected with activation and deactivation of impurities are slower, and therefore are actually observed at higher temperatures than processes connected with photoinduced dangling bonds.[7] When formation or relaxation of several types of photoinduced metastable states can take place at various energy intervals in the band gap above and below F_0, the kinetics of changes in the dark conductivity can be nonmonotonic. In Table I we show several parameters of the films we studied, which have different activation energies E_σ for the dark conductivity.[8] The position of the Fermi level is given at T = 370 K, and is determined from the value of $\sigma_{\min} = 2\times10^2\,\Omega^{-1}\cdot\mathrm{cm}^{-1}$ in the relation $E_c - F_0 = kT\ln(\sigma_{\min}/\sigma_{d0})$, where σ_{d0} is the dark conductivity of the film at that temperature.

Figure 1 shows the kinetics of the change in dark conductivity of films 1–3 after illumination at T = 405 K for 15 s with white light at an intensity $W = 90$ mW/cm^2. It is clear that the relaxation curves for σ_d for films 1 and 2 are nonmonotonic, i.e., after an initial increase there is a slow decrease in σ_d as a function of time t. For film 3 the decrease in σ_d is observed to be monotonic. The character of the relaxation curves corresponds to changes in σ_d for these films under illumination. Figure 2 shows the kinetics of σ_d during illumination: a monotonic increase of σ_d with illumination time t_{ill} for film 3, and nonmonotonic changes in σ_d for film 1.

For film 3 we observed monotonic relaxation of σ_d, and consequently photoinduced metastable states, for illumination times t_{ill} up to 2×10^3 s over the entire temperature range 360–430 K investigated. In this case the relaxation of the photoinduced metastable states is described by a single ''stretched'' exponential $N = A\exp(-t/\tau)^\beta$, where the parameters τ and β depend on temperature (Figs. 3 and 4). The nonmonotonic relaxation of σ_d, and consequently the photoinduced metastable states for films 1 and 2, is described by a sum of two ''stretched'' exponentials with different param-

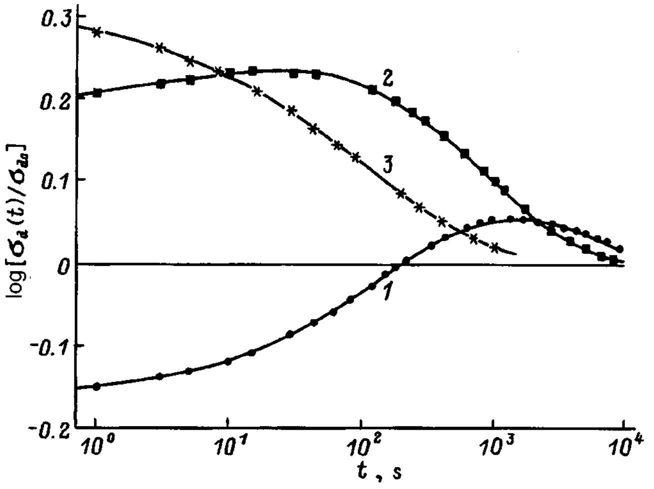

FIG. 1. Relaxation kinetics of the dark conductivity of films 1, 2, and 3 (curves *1*, *2*, and *3*, respectively) after illumination at T=405 K for 15 s.

eters τ_1, β_1 and τ_2, β_2. Label 1 refers to the short-time relaxation of the photoinduced metastable states, during which σ_d increases, while label 2 refers to the long-period relaxation of these states as σ_d decreases to its equilibrium value. As we already pointed out, the first of these processes is probably connected with photoinduced dangling bonds, while the second is connected with impurities.

Figures 3 and 4 show temperature dependences of τ and β for films 1–3 determined from the relaxation kinetics of σ_d. It is clear that for all the films the values of the parameter τ depend exponentially on temperature, i.e., $\tau \sim \exp(-E/kT)$, and the energy for the short-time anneal of the photoinduced metastable states (E_1) in films 1 and 2 is smaller than the energy for the long-period anneal (E_2): $E_1 \approx 1.1-1.0$ eV and $E_2 \approx 1.5$ eV (see Table I). For film 3, with its monotonic relaxation of the photoinduced metastable states, the annealing energy comes to 1.1 eV, i.e., it coincides with the values of E_1 obtained for curves *1* and *2*. Moreover, the temperature dependence of the parameter β for film 3 is analogous to the temperature dependence of β for films 1 and 2. Thus, the monotonic relaxation of photoinduced metastable states in film 3 is a fast process connected with photoinduced broken bonds. We note that for film 3, in contrast to films 1 and 2, the dark conductivity increases during the formation of photoinduced dangling bonds, while it decreases as these states relax. We assume that this is determined by the deeper location of the equilibrium Fermi level F_0 in the band gap of film 3 (see Table I). Because of this circumstance, neutral photoinduced dangling bonds form above F_0 and act as donors, giving up electrons. As a result, the Fermi level moves upward towards the conduction band and the dark conductivity in film 3 increases under illumination, and accordingly the relaxation of the photoinduced dangling bonds is accompanied by a decrease in σ_d. In film 1 the Fermi level is located above the photo-

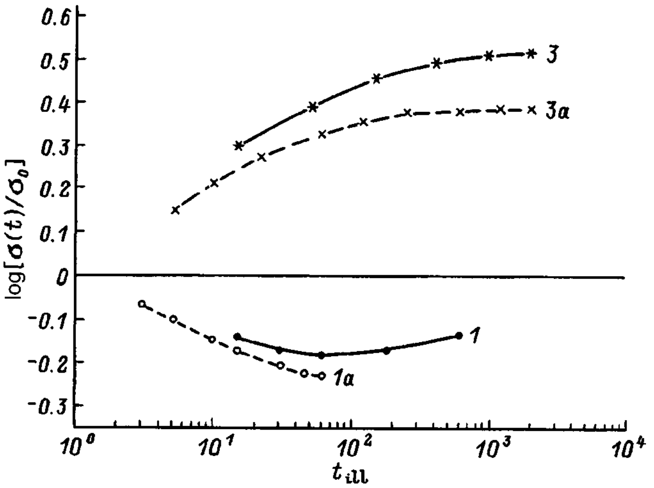

FIG. 2. Kinetics of the change in dark conductivity of films 1 and 3 (*1*, *3*) and their photoconductivity (*1a*, *3a*) under illumination at 405 K.

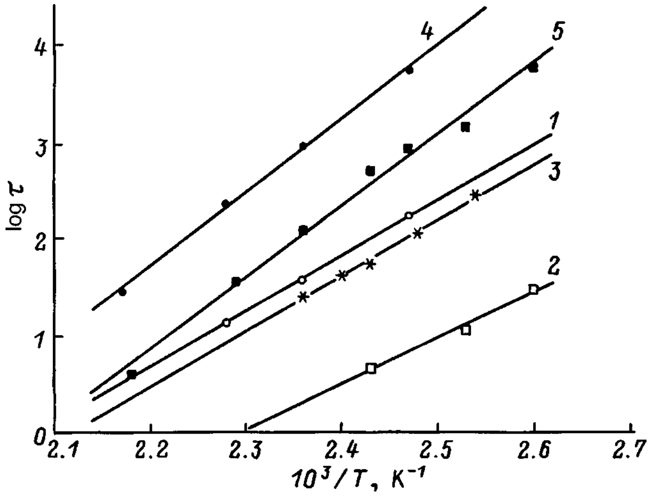

FIG. 3. Temperature dependences of the parameters τ for the relaxation processes of photoinduced metastable states in films 1, 2, 3. *1,2*—τ_1, *4,5*—τ_2, determined for σ_d of films 1 and 2, respectively. Curve *3* describes the monotonic relaxation of the photoinduced metastable states in film 3. Illumination time t_{ill}= 15 s.

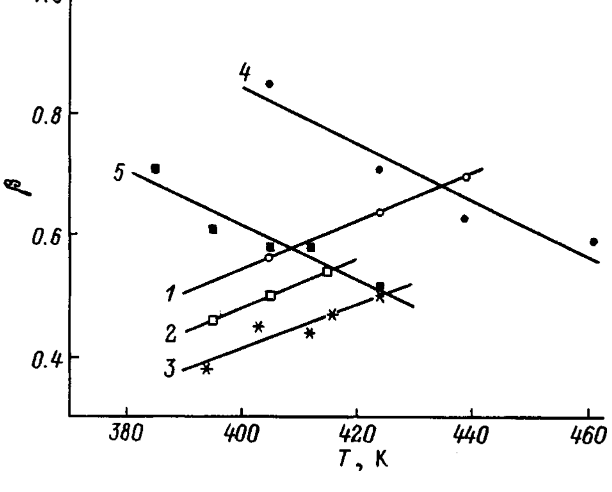

FIG. 4. Temperature dependence of parameters β for relaxation processes of photoinduced metastable states in films 1, 2, 3. *1,2*—β_1, *4,5*—β_2, determined for σ_d of films 1 and 2, respectively. Curve *3* describes the monotonic relaxation of photoinduced metastable states in film 3. Illumination time t_{ill}= 15 s.

TABLE I. Parameters of *a*-Si:H films.

Film number	T_s, °C	E_σ, eV	E_c-F_0, eV (T=370 K)	E_1, eV	E_2, eV
1	300	0.71	0.57	1.1	1.5
2	340	0.82	0.64	1.0	1.5
3	390	0.87	0.70	1.1	–

induced dangling bond energy levels, which in this case act as acceptors. As a result, during illumination of film 1 the Fermi level moves downward and the dark conductivity decreases. The change in photoconductivity of films 1 and 3 in the process of illumination also has different signs: The change in photoconductivity for film 1 has a negative sign, while for film 3 the sign is positive (Fig. 2). Thus, the photoconductivity of film 3 also changes anomalously, i.e., it increases with time, which is explained by the upward motion of the Fermi level.

The slow change in σ_d for films 1 and 2 under illumination and after it is switched off can be explained by activation and deactivation of uncontrolled impurities of donor type, probably O, N, and C. Such processes are not observed to operate in film 3, which may be due to the lower concentration of uncontrolled impurities, a consequence of the higher growth temperature for this film.

This work was supported by a grant from INTAS N 931916.

[1] M. Stutzmann, W. B. Jackson, and C. C. Tsai, Phys. Rev. B **32**, 23 (1985).

[2] R. S. Crandal, Phys. Rev. B **43**, 4057 (1991).

[3] N. Nata and A. Matsuda, J. Non-Cryst. Solids **164–166**, 231 (1993).

[4] D. Caputo, G. De Cesare, F. Irrera *et al.*, J. Non-Cryst. Solids **170**, 278 (1994).

[5] O. A. Golikova, Fiz. Tekh. Poluprovodn. **25**, 517 (1991) [Sov. Phys. Semicond. **25**, 690 (1991)].

[6] J. K. Ratl, W. Fuhs, and H. Mell, J. Non-Cryst. Solids **137–138**, 279 (1991).

[7] I. A. Kurova, E. V. Larina, N. N. Ormont, and D. V. Senashenko, Fiz. Tekh. Poluprovodn. **31**, 1455 (1997) [Semiconductors **31**, 1506 (1997)].

[8] I. A. Kurova, N. N. Ormont, O. A. Golikova, and V. Kh. Kudoyarova, Fiz. Tekh. Poluprovodn. **31**, 536 (1997) [Semiconductors **31**, 484 (1997)].

Translated by Frank J. Crowne

PHYSICS OF SEMICONDUCTOR DEVICES

Molecular beam epitaxy of alternating-strain ZnSe-based multilayer heterostructures for blue-green lasers

S. V. Ivanov, A. A. Toropov, S. V. Sorokin, T. V. Shubina,
N. D. Il'inskaya, A. V. Lebedev, I. V. Sedova, P. S. Kop'ev,
and Zh. I. Alferov

A.F. Ioffe Physicotechnical Institute, Russian Academy of Sciences, 194021 St. Petersburg, Russia

H.-J. Lugauer, G. Reuscher, M. Keim, F. Fischer, A. Waag,
and G. Landwehr

Physikalisches Institut, Universität Würzburg, Germany
(Submitted May 20, 1998; accepted for publication May 20, 1998)
Fiz. Tekh. Poluprovodn. **32**, 1272–1276 (October 1998)

High-quality ZnSe-based heterostructures are grown by uninterrupted molecular beam epitaxy using the concept of strain compensation and alternating-strain multilayers. To verify the advantages of this technique, optically pumped ZnSSe/ZnCdSe laser structures containing short-period superlattices or multiple quantum wells have been grown and studied. A room-temperature injection laser diode with a BeZnSe/ZnSe superlattice waveguide is described.
[S1063-7826(98)02810-5]

1. INTRODUCTION

Despite the considerable progress in increasing the lifetime of blue and violet lasers based on (In,Ga)N quantum wells,[1] interest in lasers based on II–VI compounds[2] continues, in particular, with regard to the green region of the spectrum where the human eye has its maximum sensitivity. Because this spectral region remains unreachable by other semiconductor material systems at present, the search for new solutions that could improve the emission characteristics of heterostructures based on ZnSe is still a topic of active research. Among the many fundamental problems that limit device use of these structures we may list the appearance of metastable compensating centers in doped *p*-layers, sizable lattice-constant mismatches between epitaxial layers and growth substrates, and the relatively low energy of formation and evolution of extended defects.

The most familiar recipe for making ZnSe separate- confinement laser diode heterostructures uses a single quantum well as the active region, placed at the center of an optical waveguide consisting of ZnSSe (Ref. 3) or BeZnSe solid solutions[4] enclosed by layers of wider-gap quaternary solid solutions. From the point of view of molecular beam epitaxy technology it is important that different contents of sulfur (in ZnSSe and ZnMgSSe) and beryllium (in BeZnSe and BeMgZnSe) are required to lattice- match the ternary and quaternary layers to a GaAs substrate, which imposes certain limitations on the technological processes involved in obtaining pseudomorphic heterostructures. The authors of Ref. 5 investigated various ways of providing the changes in sulfur content needed for lattice-matched growth of separate- confinement laser diode heterostructures, including: 1) increasing the substrate temperature during growth of the active and waveguiding regions compared to the growth temperature for the emitters, and 2) changing the intensity of the ZnS flux (i.e., the temperature of the ZnS source) at the ZnSSe / ZnMgSSe boundary. We note that both methods require stopping the growth near the active region, which can lead to uncontrollable loss of fabrication parameters and the formation of additional defects. As an alternative approach we have proposed an uninterrupted-growth regime characterized by cutting off only the Mg flux at a constant growth temperature.[6] As we showed experimentally, this decreases the content of sulfur in the ZnSSe layers by only 1.5–2% compared to the quaternary solid solutions, and as a result the waveguiding layers undergo a considerable tensile strain.

In order to ensure a total balance of the stresses in the structure, we proposed an approach that replaces the relatively thick layers of ternary solid solution (e.g., ZnSSe and BeZnSe) by short-period superlattices whose parameters are chosen so as to completely compensate for the stresses.[7] The idea of stress compensation, which is not new (see, e.g., Ref. 8), is to compensate for the stress due to mismatch in lattice constants of a layer and its substrate by introducing another layer of corresponding thickness that possesses the opposite sign of the lattice parameter mismatch. In addition to alternating layers with different-polarity stresses (tension-compression), the growth of pseudomorphic heterostructures also requires that the thickness of both individual layers and of the entire structure as a whole not exceed a critical value. The possibility of using alternating-stress layers of binary compounds in laser structures was considered in Ref. 9, where ZnSe / MgSe / ZnSe / ZnS short-period superlattices were used as the equivalent of ZnMgSSe emitters. However,

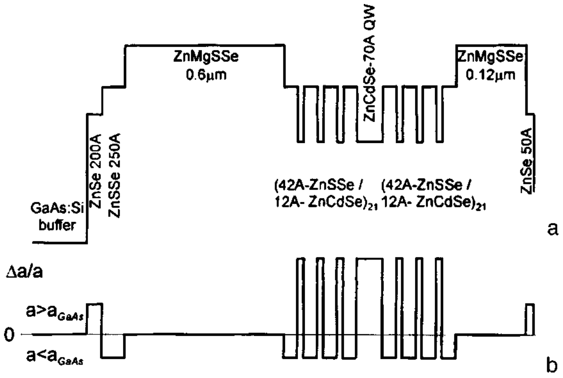

FIG. 1. a—Schematic band diagram of an optically pumped laser with a waveguide region based on a ZnSSe / ZnCdSe superlattice; b—profile of the variation in mismatch of bulk lattice parameters with thickness, illustrating compensation of stresses in the structure.

the large mismatch in lattice parameters of the binary compounds and the small critical thickness of the individual component layers imposes strict requirements on constancy of the growth rate, and consequently the intensity of the molecular fluxes and substrate temperatures. As a result, the authors of Ref. 9 reported making only light- emitting diodes, and not laser diodes.

In our study we have emphasized the use of ternary solid solution superlattices, and also stress compensation in the active and waveguiding regions (not just in the emitter and contact regions) of the laser structure. In order to determine the limits of applicability of this method and to study the optical and structural properties of alternating-stress multilayer heterostructures, we grew laser structures for optical pumping in the system ZnMgSSe / ZnSSe / ZnCdSe. In addition to structures with superlattices whose total thickness was less than the critical value, we investigated systems with multiple quantum wells whose total thickness was in the critical range,[7] in particular, between computed values of the critical thickness obtained in the Matthews–Blakeslee model[10] and the People–Bean model.[11]

There is particular interest in extending the method of stress compensation to the growth of heterostructures that include layers of new beryllium-containing solid solutions, which possess the highest hardness and stability against defect formation of all the II-VI compounds. Furthermore, the use of these compounds simplifies the problem of effective acceptor doping, which is necessary to create injection lasers that operate at room temperature.[12] In this paper we show for the first time that it is possible to make BeMgZnSe / ZnCdSe separate- confinement laser diodes with a waveguiding region in the form of an alternating-stress BeZnSe / ZnSe short-period superlattice.

2. EXPERIMENT

The structures were grown by MBE on a GaAs(001) substrate with a GaAs buffer layer grown in a separate III–V MBE chamber. Peculiarities of MBE technology for ternary and quaternary compounds in the systems (Zn,Mg,Cd)(S,Se) and (Be,Mg,Zn)Se, and also methods for controlling their

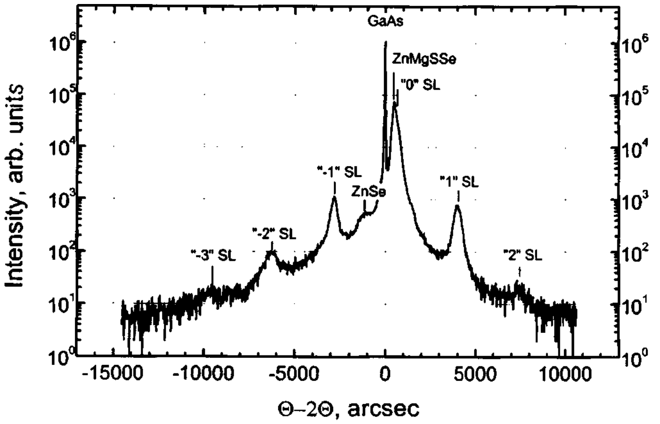

FIG. 2. Double-crystal x-ray rocking curve of a ZnMgSSe / (ZnSSe / ZnCdSe superlattice) / ZnCdSe separate-confinement laser structure grown by the method of overlapping molecular fluxes.

composition, stoichiometry, and growth rates were published previously.[4–6,12–15]

A schematic band diagram for an optically pumped laser with a waveguiding region based on a short-period superlattice is shown in Fig. 1a. The structure contains a 0.6- μm-layer of $Zn_{0.93}Mg_{0.07}S_{0.17}Se_{0.83}$, whose lattice parameter is close to that of GaAs with a low- temperature value of the band gap $E_g \sim 2.95$ eV, a 70 Å – $Zn_{0.87}Cd_{0.13}Se$ quantum well bounded by superlattices (42 Å – $ZnS_{0.15}Se_{0.85}$/12 Å – $Zn_{0.87}Cd_{0.13}Se_{21}$) on both sides, and a 0.12-μm-thick capping layer of ZnMgSSe. The sketch in Fig. 1b shows the change in mismatch of bulk lattice parameters with thickness, and illustrates the compensation of stresses in the structure. The structure with a central region of multiple ZnSSe / ZnCdSe quantum wells has an analogous construction and contains 30 pairs (170 Å–$ZnS_{0.1}Se_{0.9}$/50 Å–$Zn_{0.82}Cd_{0.18}Se$) with a total thickness of 0.66 μm. A BeMgZnSe / ZnCdSe structure for a separate-confinement quantum-well laser diode contained a 40 Å – $Zn_{0.63}Cd_{0.37}Se$ quantum well in the center of a (10 Å – $Be_{0.05}Zn_{0.95}Se$/15 Å – ZnSe)$_{82}$ waveguide superlattice, wide-gap emitter layers of *n*- and *p*-type $Be_{0.05}Mg_{0.06}Zn_{0.89}Se$ doped with iodine and nitrogen, respectively, and a ZnSe / BeTe modulation-doped graded superlattice with a 10-nm p^+-type BeTe layer for forming low-resistance ohmic contacts.

In order to characterize these structures we used double-crystal x-ray diffractometry and transmission electron microscopy. The photoluminescence (PL) spectra, excitation of photoluminescence, and light absorption in free epitaxial layers were recorded in a circulating helium cryostat in the temperature range 5–300 K using an STL-2 setup. As sources of excitation we used a He–Cd laser with an emission wavelength of 325 nm or a halogen lamp. The laser characteristics were studied under conditions of pulsed optical pumping (a nitrogen laser with pulse duration 8 ns) and injection pumping (with a pulse duration of 100 ns). Cavity laser mesastructures were fabricated by the usual photolithography, using Al_2O_3 as a dielectric and depositing Pd / Pt / Al contacts to the doped *p*- layers. Free epitaxial films were obtained after removal of the GaAs substrate by selective chemical etching.

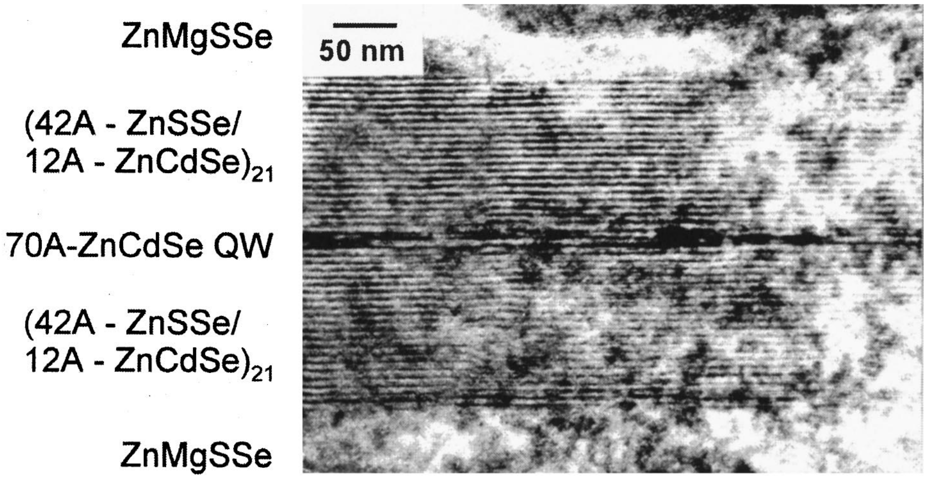

FIG. 3. TEM image of a cleavage plane of a ZnMgSSe / (ZnSSe / ZnCdSe superlattice) / ZnCdSe heterostructure.

3. RESULTS AND DISCUSSION

Double-crystal x-ray rocking curves of a typical structure with a ZnSSe / ZnCdSe superlattice are shown in Fig. 2. The position of the zero-reflection peak from the $ZnS_{0.15}Se_{0.85}/Zn_{0.87}Cd_{0.13}Se$ superlattice nearly coincides with the ZnMgSSe peak, and both these peaks are located near the GaAs substrate peak. In images of the structure obtained by TEM from a cleavage plane of a sample (Fig. 3) one can observe distinct boundaries, and in fact the absence of misfit dislocations. Figure 4 is revealed in the PL and excited- state PL spectra of this structure at 77 K. The half-width of the PL line was 14 meV (10 meV at 5 K). The solid curve also shows the absorption spectrum of a free film in which the heavy-hole exciton peak from the isolated quantum well is clearly resolved. The exciton peaks for heavy and light holes in the superlattice coincide with the absorption spectra of free films and excited-state PL of the original structure, which attests to the pseudomorphic nature of the growth and the absence of uncompensated stresses in the epitaxial structure. The solid-solution content of the ZnCdSe quantum well in this sample corresponds to luminescence at a wavelength near 490 nm at 300 K. Calculation of band parameters taking into account the pseudomorphic stresses in the layers confirm that the confinement of holes in such a quantum well is comparable to structures with a corresponding ZnSSe waveguide, along with better optical confinement determined by the small effective width of the superlattice band band, which is comparable to E_g for ZnSe (see Ref. 16). Laser oscillation under optical pumping is observed in this sample at wavelengths of 473 and 491 nm at 77 and 300 K, respectively, and the measured value of the threshold pump power density is less than 20 kW/cm^2 , which is one of the best values published for lasers based on ZnSe with oscillation wavelengths near 490 nm at 300 K. The threshold pump power density changes by less than a factor of 3 when the temperature rises from 77 to 300 K, which confirms the presence of good electronic confinement.

The optical properties of a structure with multiple quantum wells were investigated both in initial samples and in free films. In the absorption spectra of free films clearly marked exciton peaks were tracked up to temperatures of 300 K. Comparison of low-temperature absorption spectra and excited-state PL spectra measured on the same sample with the substrate removed show that freeing the epitaxial structure from the substrate leads to a rather small shift (~ 8 meV) in the heavy-hole exciton peak and a larger shift in the light- hole exciton peak (~ 15 meV). These values are in good agreement with calculations for pseudomorphically stressed heterostructures, which also indicates the absence of significant relaxation via misfit dislocations.

Laser oscillation in a structure with multiple quantum wells under optical pumping was studied in fourfold-cleaved samples (in the usual waveguide geometry) and in surface-emitting lasers made from free films, and was observed for both types of samples up to room temperature. Surface-emitting lasers were made by placing a free film in a resonator based on a quartz film with a metal mirror deposited on it. The characteristic form of the laser oscillation spectrum (77 K) under illumination from the surface and from the backside is shown in Fig. 5. The points show the shape of the absorption spectrum. Lasers with the usual waveguide geom-

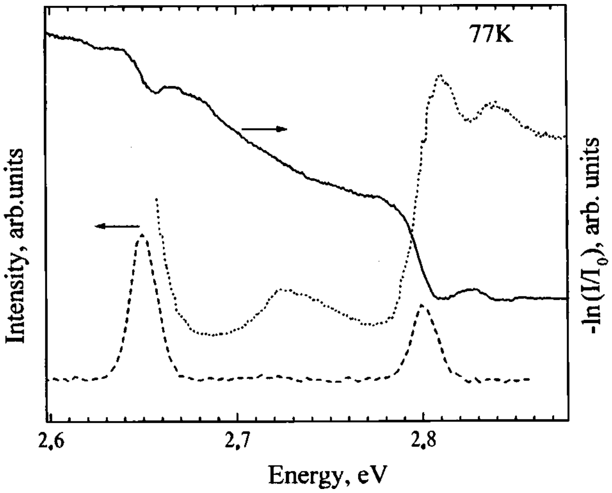

FIG. 4. Absorption spectrum of a free film (solid curve) and also PL (dashed curve) and excited-state PL (dots) spectra of the original sample of a ZnMgSSe / (ZnSSe / ZnCdSe superlattice) / ZnCdSe structure measured at 77 K.

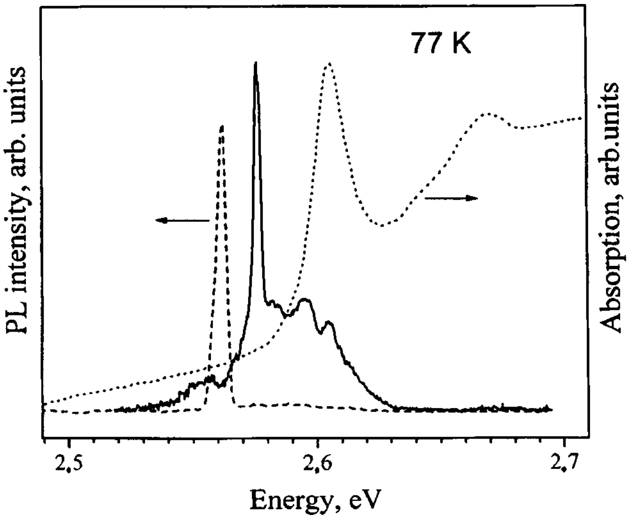

FIG. 5. Laser oscillation spectra at 77 K of ZnMgSSe / ZnSSe / ZnCdSe multiquantum-well laser samples. The solid curve corresponds to a surface-emitting laser and the dashed curve corresponds to a laser with waveguide geometry. The absorption spectrum of a free film is shown by dots.

etry demonstrated threshold pump densities of 11 kW/cm^2 at 77 K and ~ 22 kW/cm^2 at 300 K. The values of threshold pump density for the surface- emitting lasers was 65 and 110 kW/cm^2 at 77 and 300 K, respectively.

Typical electroluminescence and laser oscillation spectra at 300 K for BeMgZnSe / ZnCdSe separate-confinement quantum-well laser structures with BeZnSe / ZnSe superlattice waveguides are shown in Fig. 6. The average value of the threshold current density was 750 A/ cm^2, with a characteristic temperature T_0 of 307 K. Despite the lack of doping, waveguiding superlattices provide good carrier collection and confinement in the quantum well. We note that the optical confinement, and consequently the threshold characteristics, of the laser structures can be further improved if superlattices based on BeZnSe / ZnCdSe are used, due to the increase in the refractive index difference between the waveguide and quaternary solid solution that makes up the emitter layers.

CONCLUSIONS

We have proposed and experimentally tested our uninterrupted-growth MBE technology for making laser heterostructures based on ZnSe. High-quality alternating- strain superlattice and multi-quantum-well structures were made over a wide range of quantum-well compositions and emitter compositions by simply changing the ratio of well and barrier thicknesses. The use of short-period superlattices as waveguides for optically pumped ZnMgSSe / ZnSSe / ZnCdSe lasers leads to a decrease in the threshold pump-power density. For the example of a structure with multiple quantum wells we show that it is possible to make structures with a low level of misfit dislocations at thicknesses close to the critical thickness.

For the first time we have shown the usefulness of the concept of alternating-strain superlattices for the material system (Be,Mg,Zn)Se, and we have obtained laser diodes with waveguides based on BeZnSe / ZnSe superlattices operating at room temperature.

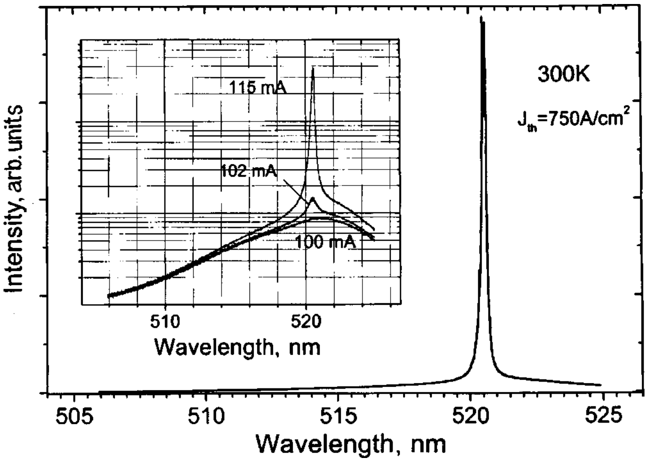

FIG. 6. Laser oscillation spectrum of a BeMgZnSe / ZnCdSe separate-confinement quantum-well laser diode with a waveguiding region based on a BeZnSe / ZnSe superlattice, measured at 300 K.

The authors are grateful to N. N. Faleev and A. A. Sitnikova for making the x-ray structural and TEM studies.

This work was supported by a grant from RFFI No. 97-02- 18269 (a), and also the Science Ministry of the Russian Federation under the program ''Physics of Solid-State Nanostructures'' Nos. 97-2014 and 97-1035.

[1] S. Nakamura, M. Senoh, S. Hagahama, N. Iwasa, T. Yamada, T. Matsushita, Y. Sugimoto, and H. Kiyoku, Appl. Phys. Lett. **70**, 1417 (1997).
[2] S. Taniguchi, T. Hino, S. Itoh, K. Nakano, N. Nakayama, A. Ishibashi, and M. Ikeda, Electron. Lett. **32**, 552 (1996).
[3] J. M. Gaines, R. R. Drenten, K. W. Haberern, T. Marshell, D. Mensz, and J. Petruzzello, Appl. Phys. Lett. **62**, 2462 (1993).
[4] A. Waag, F. Fischer, K. Schüll, T. Baron, H.-J. Lugauer, Th. Litz, U. Zehnder, W. Ossau, T. Gerhardt, M. Keim, G. Reuscher, and G. Landwehr, Appl. Phys. Lett. **70**, 1 (1997).
[5] E. S. Oh, S. D. Lee, H. D. Jung, J. R. Kim, M. D. Kim, B. J. Kim, J. K. Ji, H. S. Park, T. I. Kim, S. V. Ivanov, A. A. Toropov, and T. V. Shubina, J. Appl. Phys. **80**, 5951 (1996).
[6] S. V. Ivanov, S. V. Sorokin, P. S. Kop'ev, J. R. Kim, H. D. Jung, and H. S. Park, J. Cryst. Growth **159**, 16 (1996).
[7] T. V. Shubina, S. V. Ivanov, A. A. Toropov, G. N. Aliev, M. G. Tkatchman, S. V. Sorokin, N. D. Il'inskaya, and P. S. Kop'ev, J. Cryst. Growth **184/185**, 596 (1998).
[8] D. C. Houghton, M. Davies, and M. Dion, Appl. Phys. Lett. **64**, 505 (1994).
[9] B. J. Wu, L. H. Kuo, J. M. DePuydt, G. M. Haugen, M. A. Haase, and L. Salamanca-Riba, Appl. Phys. Lett. **68**, 379 (1996).
[10] J. W. Matthews and A. S. Blakeslee, J. Cryst. Growth **27**, 118 (1974).
[11] R. People and J. C. Bean, Appl. Phys. Lett. **47**, 322 (1985).
[12] A. Waag, Th. Litz, F. Fischer, H.-J. Lugauer, T. Baron, K. Schüll, U. Zehnder, T. Gerhardt, U. Lunz, M. Keim, G. Reuscher, and G. Landwehr, J. Cryst. Growth **184/185**, 1 (1998).
[13] S. V. Ivanov, R. N. Kyutt, G. N. Mosina, L. M. Sorokin, S. V. Sorokin, and P. S. Kop'ev, in *Proceedings 23rd International Symposium on Compound Semiconductors, St. Petersburg, 1996* (Inst. Phys. Conf. Ser. No. 155: Chapter 3, p. 223).
[14] S. Sorokin, S. Ivanov, A. Toropov, T. Shubina, I. Sedova, M. Tkatchman, P. Kop'ev, and Zh. Alferov, in *Proceedings International Symposium on Nanostructures: Physics and Technology* (St. Petersburg, Russia, 1997), p. 206.
[15] S. V. Ivanov, S. V. Sorokin, I. L. Krestnikov, N. N. Faleev, B. Ya. Ber, I. V. Sedova, and P. S. Kop'ev, J. Cryst. Growth **184/185**, 70 (1998).
[16] A. A. Toropov, S. V. Inanov, T. V. Shubina, A. V. Lebedev, L. M. Sorokin, S. V. Sorokin, G. N. Aliev, M. G. Tkatchman, N. D. Il'inskaya, and P. S. Kop'ev, in *Proceedings International Symposium on Nanostructures: Physics and Technology* (St. Petersburg, Russia, 1997), p. 210.

Translated by Frank J. Crowne